Doctoral theses at NTNU, 2022:30

Philip Erik Buschmann

On the role of symmetry and degeneracy in nonlinear thermoacoustic eigenproblems with application to can-annular combustors

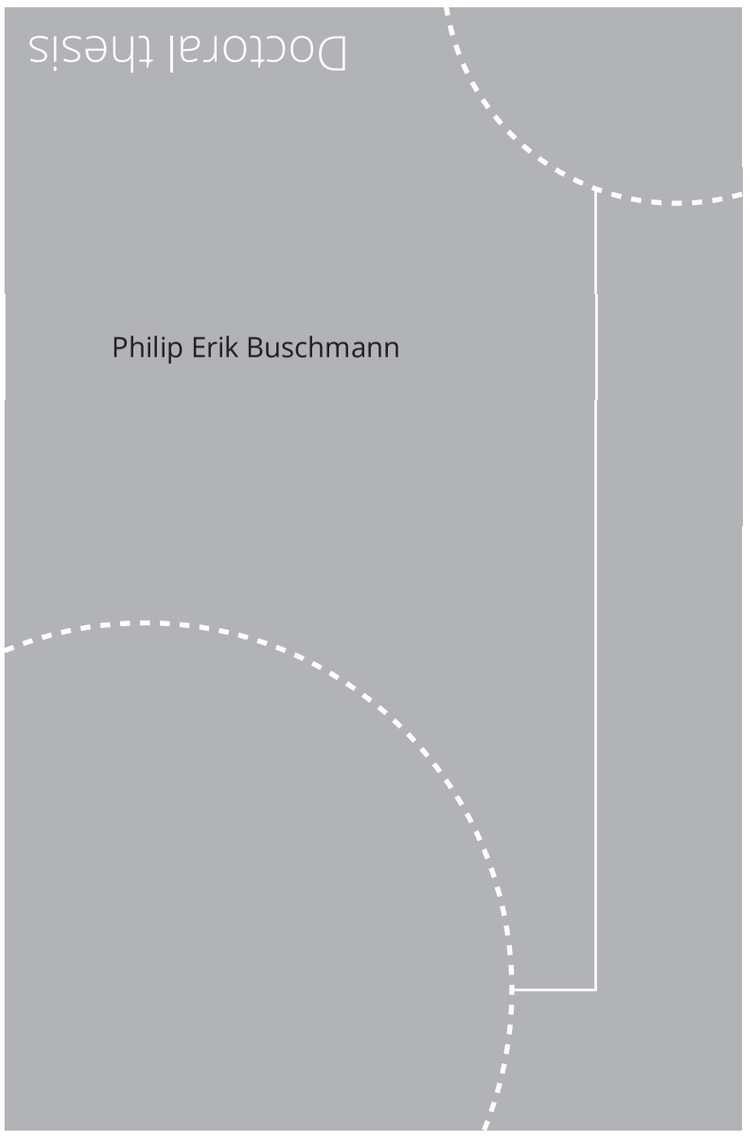

ISBN 978-82-326-6927-1 (printed ver.)
ISBN 978-82-326-6125-1 (electronic ver.)
ISSN 1503-8181 (printed ver.)
ISSN 2703-8084 (electronic ver.)

NTNU
Norwegian University of
Science and Technology

NTNU
Norwegian University of
Science and Technology
Thesis for the degree of
Philosophiae Doctor
Faculty of Engineering
Department of Energy and Process Engineering

Doctoral theses at NTNU, 2022:30

NTNU
Norwegian University of
Science and Technology

Doctoral theses at NTNU, 2022:30

NTNU

Philip Erik Buschmann

On the role of symmetry and degeneracy in nonlinear thermoacoustic eigenproblems with application to can-annular combustors

Thesis for the degree of Philosophiae Doctor

Trondheim, February 2022

Norwegian University of Science and Technology
Faculty of Engineering
Department of Energy and Process Engineering

NTNU
Norwegian University of
Science and Technology

NTNU
Norwegian University of Science and Technology

Thesis for the degree of Philosophiae Doctor

Faculty of Engineering
Department of Energy and Process Engineering

ISBN 978-82-326-6927-1 (printed ver.)
ISBN 978-82-326-6125-1 (electronic ver.)
ISSN 1503-8181 (printed ver.)
ISSN 2703-8084 (electronic ver.)

Doctoral theses at NTNU, 2022:30

PRINTED IN NORWAY
NO - 1598

NORDIC SWAN ECOLABEL
Printed matter
2041 0731

Printed by Skipnes Kommunikasjon AS

Abstract

The subject of this dissertation are thermoacoustic instabilities in combustion chambers with discrete rotational and reflective symmetries. Designing thermoacoustically stable combustors is one of the principal challenges in the engineering of modern gas turbines operating with low NOx emissions. This thesis contributes to the research in the field from three perspectives: numerical, theoretical and experimental.

Combustion experiments are costly and hence the design phase needs accurate computational models to cut development costs. Frequency-domain models in the form of network models, or as finite-element discretizations of the thermoacoustic Helmholtz equation, have proven highly successful in predicting thermoacoustic stability. From a mathematical point of view, the models lead to nonlinear eigenvalue problems which need to be solved numerically. The first achievement of this thesis is to provide fast and reliable solution algorithms that are tailored to thermoacoustic problems. The methods have the capability to compute all relevant solutions – a crucial property to determine stability of a combustor. One of the methods based on contour integration proved essential in computing intrinsic thermoacoustic modes in annular geometries for the first time and it is explained why these modes appear in clusters. These modes cannot be computed with methods that were the de-facto standard in the thermoacoustic field at the beginning of this PhD, which is subsequently proven in work that is part of this thesis. Part of this thesis is also a strategy with which the high dimension of the discrete problems can be drastically reduced – permitting parameter studies of large-scale problems.

Combustion chambers in modern industrial applications mainly come in

two types: annular or can-annular layouts. Both designs exhibit discrete spatial symmetries, i.e. certain reflections and rotations leave the combustors invariant. The presence of the discrete symmetries has implications for the type of oscillations that occur. Most prominently, standing and spinning azimuthal modes originate from a degenerate mode pair. The second achievement of this work is to interpret the thermoacoustic nonlinear eigenvalue problem from the formal viewpoint of symmetry group theory for the first time. With this powerful framework it can be predicted which physical objects show degenerate modes and how these degeneracies split as the symmetries are lowered by perturbations. This has important implications for industrial combustors, which exhibit high symmetries and consequently a large number of degenerate modes. Moreover, a number of thermoacoustic configurations are discussed, which exhibit non-trivial symmetries with surprising degeneracies. In thermoacoustics, Bloch waves have been used successfully to reduce computational cost of solving the nonlinear eigenvalue problem. Bloch waves exploit exclusively the rotational symmetry. A major result of this work is that even when an additional mirror symmetry is present, a further reduction is only possible for simple eigenvalues. Related to this work on eigenvalue multiplicity is a result on so-called exceptional points in thermoacoustic spectra. For the first time it is shown that for certain parameter combinations two eigenvalues can coalesce and form a defective point.

Can-annular combustors have received little experimental attention in academia. Unlike the annular design, the can-annular design exhibits so-called clustered modes, i.e. multiple modes within narrow frequency bands due to the presence of a weak coupling. From an engineering perspective there are many advantages to this design. However, the closely spaced modes lead to thermoacoustic effects that differ starkly from those observed in annular combustion chambers – which have been well-researched in the past two decades. The third achievement of this thesis is to establish a new can-annular model combustor to explore the complex dynamics of can-annular combustors in well-defined and accessible lab experiment. The design permits to adjust the can-to-can coupling and study its effect on clustered modes. Several tightly packed clusters are observed, which contain modes of different azimuthal mode orders. In addition, the frequencies and amplitudes of the observed limit cycle oscillations show a strong sensitivity to changes in the cross talk size. Thus, the results confirm recent theoretical work in the literature. The observed transient dynamics show that interactions between multiple unstable modes in a cluster are complex and it is difficult to predict which mode will form the limit cycle oscillation.

Preface

This thesis is submitted to the Norwegian University of Science and Technology (NTNU) for partial fulfilment of the requirements for the degree of philosophiae doctor. The doctoral work has been carried out in the Thermo Fluids Group at the Department of Energy and Process Engineering (EPT), from November 2017 until November 2021. The research work has been supervised by Associate Professor Jonas P. Moeck and Associate Professor Nicholas Worth. This thesis consists of six chapters and nine scientific papers, which are summarized in Chap. 5 and included in full text at the end of the thesis. Of the nine papers seven have been published or presented at scientific conferences, while two are in a draft state. Listed in chronological order of publication, the articles are:

Article 1
Exceptional points in the thermoacoustic spectrum
Georg A. Mensah, Luca Magri, Camilo F. Silva, Philip E. Buschmann and Jonas P. Moeck
Journal of Sound and Vibration, Volume 433, Pages 124-128, 2018

Author contributions: PEB, GAM and JPM formulated the problem and its solution. CFS and LM contributed to the analysis. GM wrote an early draft of the letter, which was subsequently extended and polished by all authors.

Article 2

Solution of Thermoacoustic Eigenvalue Problems with a Noniterative Method

Philip E. Buschmann, Georg A. Mensah, Franck Nicoud and Jonas P. Moeck
Journal of Engineering for Gas Turbines and Power, 142(3): 031022 (11 pages), 2020

Author contributions: PEB conducted analysis and numerical computations. GAM, FN and JPM supervised the work. PEB wrote the draft and presented the paper at the ASME 2019 conference in Phoenix, Arizona. All authors commented on the draft and proofread the final version.

Article 3

Intrinsic thermoacoustic modes in an annular combustion chamber

Philip E. Buschmann, Georg A. Mensah and Jonas P. Moeck
Combustion and Flame, Volume 241, Pages 251-262, 2020

Author contributions: PEB developed the theory and performed the numerical computations. JPM encouraged PEB to investigate the origin of the intrinsic modes and supervised the work. PEB wrote the manuscript with support from GAM and JPM. All authors commented on the draft and proofread the final version.

Article 4

Iterative Solvers for the Thermoacoustic Nonlinear Eigenvalue Problem and Their Convergence Properties

Georg A. Mensah, Philip E. Buschmann and Alessandro Orchini
Presented at SOTIC-2021 conference and invited for publication to the International Journal of Spray and Combustion Dynamics; authors intend to submit it.

Author contributions: PEB and GAM conceived the idea. All authors developed the theory. GAM and AO performed numerical computations. GAM wrote the first draft of the manuscript. All authors contributed to the final manuscript and proofread the final draft. PEB presented the paper at the SOTIC-2021 conference in Munich, Germany.

Article 5

Experimental study of thermoacoustic modes in a can-annular model combustor

Philip E. Buschmann, Nicholas Worth and Jonas P. Moeck

Presented at SOTIC-2021 conference and invited for publication to the International Journal of Spray and Combustion Dynamics (SCD); authors do not intend to submit it but extend the paper and submit it to a suitable journal.

Author contributions: JPM conceived the idea. PEB designed and performed the experiment and analysed all data. NW contributed with ideas to the experimental design and the data acquisition setup. JPM supervised the post-processing of the experimental data. PEB performed all numerical computations and wrote the manuscript. NW and JPM proofread the final draft. PEB presented the paper at the SOTIC-2021 conference in Munich, Germany.

Article 6

Reduced-order modelling of thermoacoustic instabilities in can-annular combustors

Alessandro Orchini, Tiemo Pedergnana, Philip E. Buschmann,
Jonas P. Moeck and Nicolas Noiray

Presented at SOTIC-2021 conference. An extended version of the paper is currently under review with the Journal of Sound and Vibration.

Author contributions: AO formulated the theoretical model and performed all numerical computations. TM contributed with experimental data to the theoretical model. PEB contributed with experimental data to the numerical model for validation purposes. AO wrote the paper, which was proofread by JPM and NN. AO presented the paper at the SOTIC-2021 conference in Munich, Germany.

Article 7
A subspace-accelerated method for solving nonlinear thermoacoustic eigenvalue problems
Georg A. Mensah, Alessandro Orchini, Philip E. Buschmann and Luka Grubišić
As of Monday 10th January, 2022 accepted for publication in the Journal of Sound and Vibration

Author contributions: GAM conceived of the idea. GAM, AO and PEB developed the theory under the supervision of LG. GAM and AO implemented the numerical test case. GM wrote the first draft and PEB, AO and LG finalized the manuscript. All authors contributed to the final manuscript and proofread the final draft.

Draft Article 8
Symmetry groups in thermoacoustics
Philip E. Buschmann and Jonas P. Moeck
This article is in draft state with planned submission in late 2021 to a suitable journal.

Author contributions: PEB developed the theory, implemented all numerical models and wrote the manuscript. JPM supervised the work and helped in shaping the research. Both authors proofread the final draft of the manuscript.

Draft Article 9
Symmetry perturbations in a can-annular model combustor
Philip E. Buschmann, Nicholas Worth and Jonas P. Moeck
This article is in draft state with planned submission to the 39th International Symposium of Combustion.

Author contributions: JPM conceived the idea. PEB performed the experiments, analysed the data, derived the theory and writes the manuscript. JPM and NW supervise the research.

Acknowledgements

First and foremost, I would like to thank my supervisor Jonas Moeck for his mentorship, guidance and patience. I feel honored to have been his first PhD student in Norway and I could not have dreamt of a better supervisor. I have learned tremendously from his multiphysics approach to science and the research work together has been exhilarating. I am also very thankful for the great freedom he has given me in exploring subjects on my own.

The PhD being the final milestone in my academic studies, I would like to thank my many teachers who have inspired me over the years. Gudrun Tisch's mathematics teachings in high school instilled a deep love for the subject in me, which led me to study Engineering. During my Bachelor's, Thoralf Reichel took me under his wings and introduced me to the experimental side of combustion research. The work in the laboratory was a great introduction to the research at the Hermann-Föttinger-Institut at TU Berlin. Later, in my Master's I was lucky that I could join Georg Mensah as a student assistant. That period has sparked a very productive collaboration that continues to this day and I have to thank him for his continuing mentoring and the inspiring conversations over the years. Much of my work builds on top of the results he has obtained in his exemplary research. Thanks go also out to Alessandro Orchini with whom Georg and I form a productive trio and I hope the collaboration will continue.

My experiments have greatly benefited from the help of Sam Wiseman, Francesco Di Sabatino, Yi Hao Kwah, Dirren Govender, Thomas Indlekofer and Eirik Æsøy. Their door was always open for my questions. Sam Wiseman has been a tremendous help with his sheer endless knowledge of

small tips and tricks that he always happily shared. Special thanks go out to Yi Hao Kwah who designed two electrical distributor boxes to supply all eight PMTs from two amplifiers – even though he himself only needed one but wanted to make sure that other experiments run smoothly. In addition, he provided his notes to compute the aperture and helped tremendously with the PMT setup. The experiments would not have been possible without the technicians of the Department of Energy and Process Engineering and major thanks go out to Stein Skånøy who has been invaluable and always ready to help on short notice. None of the research would have been possible without the combustion lab that James Dawson and Nicholas Worth built up from scratch at NTNU. They have fostered a great working atmosphere and it has been a pleasure to be part of the group. Plus, the university administration has been a huge help. Especially, Trond Kvilhaug, Elin Steen, Ingrid Wiggen, Wenche Nygård and Debbie Koreman van den Bergh who have greatly helped with purchasing, organisation and administrative challenges.

Moving to a new country for PhD studies is marked by great uncertainty but a number of friends made me feel right at home in Trondheim. I would like to thank Marek Mazur who went out of his way to welcome me and taught me how to enjoy cross-country skiing. The Åsnes Amundsen race in 2019 that we completed together is one of my favorite memories. Eirik Æsøy and Thomas Indlekofer have been my partners in crime for many climbing and skiing adventures in Trøndelag – luckily they have not been my downfall, even though I surely tried to knock on the doors of Valhalla for entry. Thomas I have to thank for introducing me to the world of rock- and ice climbing, and Eirik for being my trusted rope partner. My Norwegian group of friends consisting of Håkon Nygård, Anna Knutsen, Benjamin Smeltzer, Øyvind Hanssen-Bauer and Andreas Akselsen has been warm and welcoming. We have been on many great trips, where they showed me their majestic country. A highlight of 2021 has surely been the long week spent together freezing and climbing with Andreas and Ben in Flatanger. Moreover, I would like to thank my friends and office mates Loïc Duffo, Dirren Govender, Yi Hao Kwah, Harish Subramanian Gopalakrishnan, Frida Cronqvist and Olav Rømcke for the chats that brightened up my days and the good time outside the office. A special thanks go out to my two long term flatmates Jose Aguilar and Leon Li. The three years together in the Persaunet house have been splendid. I greatly enjoyed their company, our cooking and the conversations.

Finally, my biggest thanks go out to my family and my girlfriend. The

pandemic-induced travelling restrictions severely reduced the time I could spend with either of them and I wished it would have been easier. My parents and my brothers have always supported me in going to Norway and strengthened my resolve when it came to difficult decisions. Words cannot express how much your support means to me.

Even though we have been separated by pandemic-induced travelling restrictions, the past 3 years have been the happiest of my life thanks to you, Davita.

Friday 19th November, 2021

Philip E. Buschmann

Contents

List of Tables

List of Figures

Nomenclature

The nomenclature in the attached publications at the end of the thesis can differ from the one given here and can include items that are not listed here.

Abbreviations

CH_4	methane
CO_2	carbon dioxide
H_2	hydrogen
NOx	nitrogen oxides
DNS	direct numerical simulation
EU	European Union
FEM	finite element method
FTF	flame transfer function
LC	limit cycle
LEE	linearized Euler equations
LES	large eddy simulation
NLEVP	nonlinear eigenvalue problem
PDE	partial differential equation

PMT	photomultiplier
PSD	power spectral density
TAI	thermoacoustic instability
XT	cross-talk

Greek symbols

$\boldsymbol{\varepsilon}$	vector of perturbations
ε	perturbation
α_j	integration weight
$\boldsymbol{\tau}$	stress tensor
Δ_{sp}	spin ratio
Γ	Jordan curve in complex plane containing a domain $\Omega \subset \mathbb{C}$
γ	heat capacity ratio
Γ_0	boundary of computational domain with homogeneous Dirichlet boundary conditions
κ	bulk viscosity
λ	thermal conductivity
μ	viscosity
Ω	domain of integration, or only in Chap. 3 domain in complex plane
ω	angular frequency
ω_{I}	growth rate defined as $-\mathrm{Im}\,(\omega)$
ϕ	arbitrary physical quantity
ϕ_i	azimuthal coordinate with index i
Ψ	source term in acoustic energy balance
ψ	shape function

ρ	density, or only in Chap. 3 resolvent set
σ	spectrum
σ_v	reflection operation along a vertical plane v
τ	time delay in n–τ model
θ	phase angle between two oscillations

Latin symbols

$\bar{R}$	mass-specific gas constant
$\dot{w}_i$	rate of production/consumption of species i
$\hat{p}$	right pressure eigenfunction of the continuous problem; thermoacoustic mode shape
$\hat{p}_h$	trial function from a discrete space V_h
i	imaginary unit
$\mathbb{S}$	triangles
$\mathbb{T}$	tetrahedra
$\mathcal{D}$	flame describing function which maps $\mathcal{D} : \mathbb{C} \times V \to \mathbb{C}$
$\mathcal{F}$	flame transfer function which maps $\mathcal{F} : \mathbb{C} \to \mathbb{C}$
$\mathcal{S}$	triangle
$\mathcal{T}$	tetrahedron
$\mathfrak{m}_a$	algebraic multiplicity
$\mathfrak{m}_g$	geometric multiplicity
$\mathrm{C_S}$	group with reflection symmetry
C_N	cyclic point group of order N
C_{Nv}	cyclic point group of order N with reflection symmetry; also known as pyramidal symmetry group
G	symmetry group

Ma	Mach number
A	generic matrix
C	boundary mass matrix
I	identity matrix
K	stiffness matrix
M	mass matrix
Q	flame matrix
R	residual matrix function
T	discrete operator in Kato's example
A_p	moment matrix of order p
B_N	projection matrix
b_N	column in projection matrix B_N
L	discrete linear operator family, abbreviating the discretized thermoacoustic Helmholtz equation
$\mathcal{A}, \mathcal{M}$	linear operators
$\mathcal{I}$	identity operators
$\mathcal{L}$	continuous linear operator family, abbreviating the thermoacoustic Helmholtz equation
$\mathcal{P}_0$	projection operator
$\tilde{V}$	rectangular matrix with random entries
f_i	vector of external body forces
n	unit normal vector
p	discrete right eigenvector
q	heat flux vector
u	velocity

V_i	diffusive velocity of species i
w_k	discrete left eigenvector
p_m	matrix with recorded pressure signals
u_1	velocity fluctuation
x	discrete location vector
a	number of eigenvalues
a_m^+, a_m^-	modal coefficient for clockwise and anti-clockwise spinning mode of azimuthal order m
a_m^s, a_m^c	modal coefficient for sine and cosine components of a mode of azimuthal order m
A_{can}	cross-section area of a can
A_{LC}	amplitude of limit cycle
A_{XT}	cross-section area of cross-talk
b_p	filtering function
c	speed of sound
c_p	specific heat capacity at constant pressure
c_v	specific heat capacity at constant volume
d	dimension of discrete (nonlinear) eigenvalue problem; degrees of freedom in chosen discretization
d_{can}	diameter of a can
e	internal energy
e_1	acoustic fluctuation energy
f	frequency
f_i	function of boundary impedances for boundary i
f_{s}	sampling frequency
H	Hilbert space

h	enthalpy
h°	enthalpy of formation
h^s	sensible enthalpy
L^2	space of square-integrable functions
M	number of different species in a mixture
m	azimuthal mode order
N	number of can combustors
n	interaction index in n–τ model
N_I	number of integration points along the contour Γ
P	thermal power
p	pressure
p_1	pressure fluctuation
P_j	expansion coefficients
q	volumetric heat-release rate
Q_0	mean global heat release
q_1	heat-release rate fluctuation
s	number of eigenvalues inside of Γ
T	temperature
t	time coordinate
T_ac	acoustic period of oscillation
u_0	mean flow velocity
V	function space
v	test function
V_C	control volume
V_F	volume of heat-release zone

V_h	discrete function space
v_h	test function from a discrete space V_h
$W^{1,2}$	Sobolev space of order 1 with finite norm of order 2
w_i	weight i for projection
x	space coordinate
Y_i	mass fraction of species i
Z	impedance
z	complex argument

Modifiers

$\hat{(\cdot)}$	Fourier-transformed quantity
$(\cdot)_1$	temporally fluctuating quantity
$(\cdot)^{-1}$	inverse
$(\cdot)^{\dagger}$	hermitian transpose
$(\cdot,\cdot)$	inner product
$(\cdot)^{*}$	complex conjugate
$(\cdot)^{T}$	transpose
$(\cdot)_0$	mean quantity

Chapter 1

Introduction

1.1 Motivation

The topic of this thesis are thermoacoustic instabilities in annular and can-annular combustors from an experimental, theoretical and numerical angle. Thermoacoustic instabilities are self-excited pressure oscillations that can occur in combustion chambers of rocket engines (Culick and Yang, 1995) and gas turbines (McManus et al., 1993; Dowling and Stow, 2003; Lieuwen and Yang, 2005a). Modern stationary gas turbines for power generation are particularly susceptible to these unwanted pressure oscillations and a considerable amount of engineering and research has been expended to understand, predict and tame them.

Combustion of fossil fuels and biofuels produces greenhouse gases that are dangerous to the climate. The most recent report from the Intergovernmental Penal on Climate Change (Masson-Delmotte et al., 2021) strongly underlines the need to reduce greenhouse gas emissions. Stationary gas turbines for power generation certainly contribute to climate change. However, until energy can be reliably obtained from sustainable or renewable sources exclusively, gas turbines are a promising bridging technology. Gas turbines have quick response times and can employ a mix of different fuels. Gas turbine technology is well-matured owing to a century of developments since the Norwegian Ægidius Elling build the first gas turbine that produced excess power in 1903 (Leksikon, 2021). These features make them ideally suited to fill supply gaps of renewable energies. Therefore, current combustion research aims at reducing emissions to the necessary minimum that is physically possible.

Reducing emissions in the form of nitrogen oxides, or short NOx, is one of the main challenges for cleaner gas turbines. Nitrogen is a natural component of atmospheric air and under high temperatures it forms NOx. As an unwanted byproduct it reduces the thermodynamic efficiency of the gas turbine, but more importantly NOx causes acid rain, damages the ozone layer, harms the human respiratory system and damages the soil (Boningari and Smirniotis, 2016). Hence, the reduction is a focus of the EU Commission, see Directive (EU) 2015/2193 (EU Commission, 2015) which imposes stringent limits for the gas turbine industry. In a push to reduce NOx emissions, gas turbine manufacturers switched from diffusion to premixed flames, which reduces the occurrence of local hot spots in the combustion zone. Since NOx-formation has an exponential dependence on temperature, this measure proved highly effective in decreasing NOx emissions.

The switch to premixed flames came with a price: thermoacoustic instabilities. Premixed flames that are kinematically stabilized are especially prone to this type of instability. Hereby an unstable feedback loop between flames and pressure waves causes a growth in amplitude until levels dangerous to the structure and the operation are reached: a thermoacoustic instability manifests itself and the engine needs to be shutoff to prevent structural damage.

Recently, the German government (Bundesministerium für Wirtschaft und Energie, 2020) and a joint initiative from the private and public sector under the auspices of the EU Commission (The Fuel Cells and Hydrogen Joint Undertaking, 2019) have announced their plans to make hydrogen the key of the future energy economy. Hydrogen can be burned in gas turbine engines but its addition exasperates the susceptibility to instabilities due to the high burning velocity which increases sensitivity to fluctuations (Indlekofer et al., 2021a).

Consequently, there is an urgent need to understand thermoacoustic instabilities and develop methods to predict them such that stable combustors can be designed that contribute to a cleaner energy economy. This thesis contributes to this goal in a threefold manner: i) algorithms and methods are developed to solve the linear stability problem of thermoacoustics – a so-called nonlinear eigenvalue problem – fast and effectively; ii) theoretical properties of annular and can-annular combustors related to mode degeneracy are derived by analysing the thermoacoustic stability problem from the perspective of the mathematical language of symmetry groups; iii) a can-annular model combustor experiment is established to explore

the role of closely-spaced eigenvalues in a well-defined and accessible lab environment.

1.2 Basic concepts of thermoacoustic instabilities

Flames need to be placed into confined domains to extract work from combustion in the Brayton cycle. The combustion process is unsteady and involves the interaction of acoustic, hydrodynamic and chemical processes. In its simplest form, the velocity-coupled thermoacoustic feedback loop is depicted in Fig. 1.1(a): a flame emits pressure waves that travel upstream and downstream. As they are reflected at the walls and propagate through the combustion chamber, they excite hydrodynamic structures upstream of the flame. These structures propagate to the flame and trigger a response and, thus, close the loop. If the feedback is positive, an acoustic pressure wave grows in amplitude and a thermoacoustic instability (TAI) manifests itself in the system. Such an instability can be observed in the experimental data recorded in Fig. 1.2(a): after an initially stable state, characterized by a low amplitude, the amplitude grows and the self-excited oscillation reaches a stable limit cycle (LC) (Strogatz, 2018).

The amplitude of a TAI can reach dangerously high levels. Figure 1.1(b) shows the structural damage to a combustion chamber after a TAI has occurred. On one hand the large amplitude pressure waves can damage the encasing of the combustion chamber but on the other hand they can lead to flow-reversal. This is extremely dangerous for combustors operating with premixed flames or technically premixed flames: as the combustible mixture at the injectors is slowed down due to an incoming pressure wave, the flame can propagate upstream to components that are not sufficiently protected against thermal stresses. As a consequence, flashback can occur that melts components. Due to their damaging effect, industrial designs try to avoid thermoacoustic instabilities as much as possible. Data from real engines is scarce, but industrial manufacturers are willing to accept certain small amplitude limit cycle oscillations during operation (Bothien et al., 2019b).

The feedback loop depicted in Fig. 1.1(a) is only valid for propagation-stabilized flames, i.e. flames that are stabilized in a region of low velocity created with bluff-bodies and/or swirlers or by other suitable flame holders. Lieuwen (2012) scrutinizes the interaction mechanism in more detail in Chap. 12 of his book. Lieuwen gives a detailed account of the interactions between flame structures, hydrodynamical modes and pressure waves. For the fully premixed flames considered in this thesis, the loop of

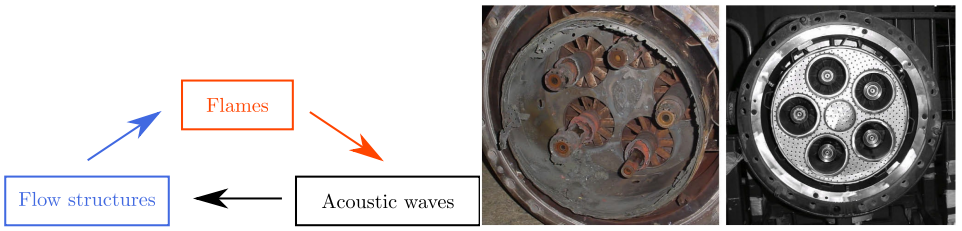

Figure 1.1: a) Schematic depiction of the velocity-coupled thermoacoustic feedback loop, adapted from Lieuwen (2012). b) The left and right images depict a combustor after and before operation, respectively. During the operation a thermoacoustic instability occurred which caused significant structural damage. Image is taken from the book of Lieuwen and Yang (2005b).

Fig. 1.1(a) is sufficient.

1.2.1 Rayleigh's criterion

For the confined domain of a combustion chamber one can formulate an energy balance (Poinsot and Veynante, 2005; Lieuwen, 2012) for the energy of the acoustic fluctuation, and it will be derived in Sec. 2.1.7. The only source term Ψ in the balance, after integration over the combustion chamber volume and averaging over one acoustic period, reads

$$\Psi = \int_{V_C} \int_0^{T_{ac}} q_1 p_1 \, \mathrm{d}t \, \mathrm{d}x \,. \tag{1.1}$$

The source term contains the unsteady volumetric heat-release rate fluctuation q_1 and the pressure fluctuation p_1. Here, T_{ac} is the acoustic period of oscillation and V_C the control volume – the combustion chamber. In the following, fluctuations are denoted as $(\cdot)_1$ quantities. The source term is positive depending on the phase relationship between p_1 and q_1. If both p_1 and q_1 oscillate harmonically, the product in the kernel of Eq. (1.1) is positive if the quantities are in phase, i.e. $0 < \left|\theta_{p_1 q_1}\right| < \pi/2$. If it holds that the contribution from the source term Ψ is larger than losses occurring at the boundaries

$$\Psi > \text{acoustic losses over boundaries}\,, \tag{1.2}$$

acoustic energy is added to the system. Hence, Equation (1.2) is a stability criterion, which is prominently known as *Rayleigh criterion*. Lord Rayleigh (Rayleigh, 1878) was the first to explain the stability of a thermoacoustic

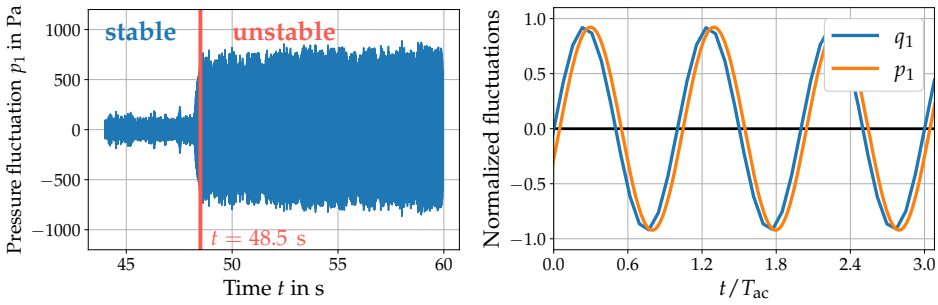

(a) (b)

Figure 1.2: a) Pressure signal recorded during an experimental run that is part of Article 5. A limit cycle oscillation ($t > 48.5\,\mathrm{s}$) manifests itself and persists until the end of the measurement. Parameters are kept constant and the instability is triggered by turbulent background noise. The entire recorded measurement is depicted in Fig. 1.3(a). b) Normalized pressure p_1 and heat-release fluctuation q_1 recorded during an experiment. Both signals show an oscillation at 770 Hz. The heat-release signal q_1 is extracted from OH^* camera data. The data was recorded during experiments presented in Article 5 but does not belong to the data presented in a).

systems via phase relation between p_1 and q_1 in 1878. Figure 1.2(b) shows p_1 and q_1 during a thermoacoustic instability and the phase difference is $\theta_{pg} = 0.158\,\mathrm{rad}$ or 9°.

The criterion is derived from a first-order expansion of the conservation equations and neglects interactions between acoustics and hydrodynamics. Under these assumptions, acoustic losses only occur at boundaries. As the criterion (1.2) states, the integral over the combustor volume needs to result in a net positive value. Since losses outside the flame zone only occur at boundaries, conditions often favor instabilities, as formulated by Culick and Yang (1995) (p. 3, 1st paragraph) for rocket engines

> *Indeed, because of the high density of energy release in a volume having relatively low losses, conditions normally favor excitation and sustenance of oscillations in any combustion chamber intended for a propulsion system.*

For some gas turbines – in particular for aero engines – the situation is not quite as severe as for rocket engines, since the walls contain plenty of cooling holes (Zhao et al., 2019) that can contribute to the acoustic losses.

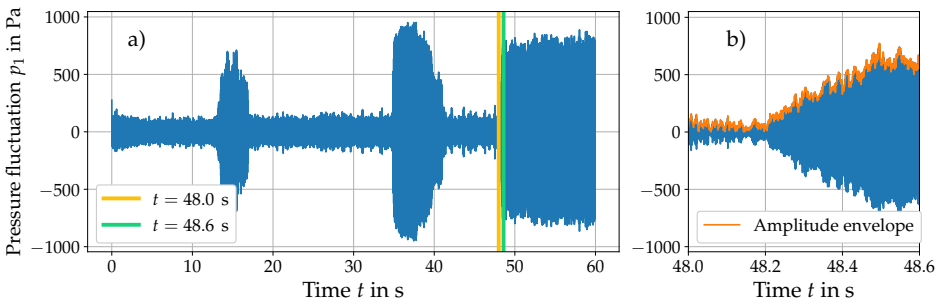

Figure 1.3: a) The full pressure signal recording of which the final bit is depicted in Fig. 1.2(a). The interval marked with vertical lines is shown in b). The full signal shows that there are two bursts where the combustor turns unstable temporarily, but these do not reach a steady state. b) The amplitude of the pressure oscillation grows steadily, until it reaches a steady state at approximately 500 Pa.

Polifke (2004) (p. 5) and Lieuwen (2012) (p. 36) give a very intuitive interpretation of Rayleigh's criterion: for a gas under constant pressure a heat addition results in an expansion. Hence, work is performed on the surroundings akin to "$p\,\mathrm{d}V$". Therefore, an in-phase oscillation of q_1 and p_1 adds work to the fluctuation, like combustion does in the compressed stage in a piston engine. The reader might notice that this is a perfect metaphor to give a first-year PhD student as advice: when the pressure is high, you have to turn up the 'heat' to maximize the productive output but don't exhaust yourself, when it is not.

1.2.2 Transition to instability and thermoacoustic modes

Figure 1.2(b) shows that in an experiment, an instability grows in amplitude until it reaches a steady state – a limit cycle with an associated amplitude and frequency. A competition between driving and damping forces occurs, see the schematic depiction in Fig. 1.4(a): in an unstable linear state, the amplifying forces are larger than the damping forces. Consequently, the oscillation grows in amplitude until the two forces reach an equilibrium. The equilibrium state is defined by a limit cycle amplitude A_{LC} and an associated frequency, which is given in Fig. 1.4(b) for the considered experimental data. The growth of the mode is fed from energy due to the Rayleigh criterion (1.2). In an experiment, damping does not only occur due to losses at the boundaries, as suggested by Eq. (1.2), but also via the interaction between hydrodynamic and acoustic fluctuations (Hofmeister et al., 2019).

A thermoacoustic oscillation is, in essence, an acoustic oscillation that is fed with energy from the heat-release. Thus, it has an associated frequency, amplitude and mode shape. In the present example, Fig. 1.4(a), the unstable linear state is an unstable thermoacoustic mode. Prediction of the linear stability by using numerical methods is conducted by determining if all modes are damped, i.e. have a negative growth rate. Section 1.3.1 reviews different modelling strategies in the literature to do so. In this thesis, stability is assessed by means of the thermoacoustic Helmholtz equation. The equation is derived from first principles in Chap. 2.

Importantly, linear stability only determines the initial exponential growth or decay of a mode at a given frequency. As the mode grows in amplitude, the growth rate will change. A growth in amplitude is usually limited by reaching a certain saturation level in the heat-release response, i.e. there is a limit to how much acoustic energy the heat-release can supply. Other nonlinear factors can be the competition or synchronization between multiple unstable modes. The growth is usually also accompanied by a shift in frequency, see the numerical study by Noiray et al. (2008) and Orchini et al. (2019) that agrees well with experiments. The sign of the growth rate is of special importance, but the value itself is highly useful to determine if certain modes are on the border of instability and which modes are amplified the strongest. The transient growth of an unstable mode, interaction between multiple unstable modes (Moeck and Paschereit, 2012) and the final state in a limit cycle cannot be determined from a linear stability analysis. It is commonly assumed, that the linearly most unstable mode will result in a limit cycle oscillation and, hence, needs to be damped. This is not necessarily true, as counter-examples exist (Bourgouin et al., 2015a). The primary engineering objective is that all modes are linearly stable to ensure a smooth operation.

In the opening of this section it was explained that a flame emits acoustic waves, which are reflected at the boundaries of the combustor and return to an upstream location of the flame where they excite a hydrodynamic response that subsequently triggers a response in the flame. Modes of this feedback mechanism are of *acoustic* origin, since they belong to acoustic resonance frequencies of the combustor. Due to the presence of a flame, the frequencies are slightly shifted with respect to the purely acoustic frequencies. The so-called *intrinsic* mechanism is based exclusively on upstream propagating waves. Hoeijmakers (2014) showed with a network model that a combustor with anechoic terminations – which dampen all resonance frequencies – can become unstable. The mechanism was ex-

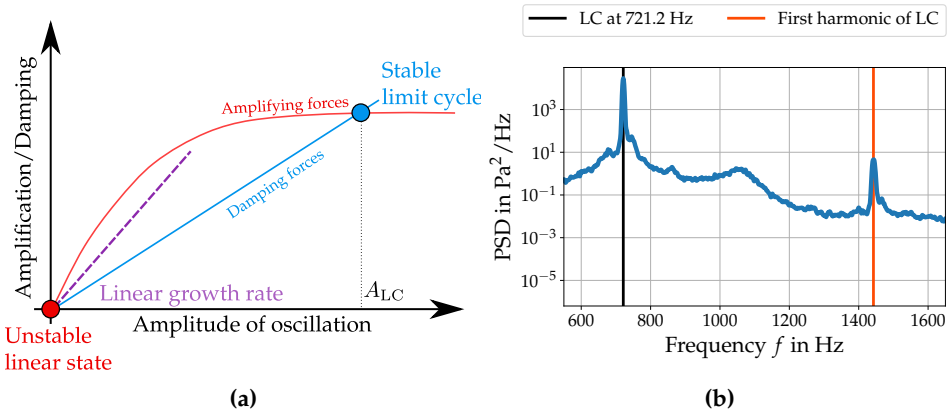

Figure 1.4: a) Schematic depiction of the growth of an unstable oscillation until it reaches a stable limit cycle. The figure is an adjusted and annotated version of the one in Lieuwen and Yang (2005b)(p. 38). b) Spectral content of the last 16 s (depicted in Fig. 1.2(a)) computed with Welch's method. The limit cycle oscillation shows one dominant peak. The second peak is of the first harmonic of the LC oscillation.

plained by Bomberg et al. (2015) and Emmert et al. (2015). In a combustor with non-anechoic boundaries, an intrinsic instability is usually distinguished from an acoustic one by not occurring at any purely acoustic resonance frequencies. The intrinsic mechanism is a fairly recent discovery of the previous decade and has received ample attention in recent years, see Hoeijmakers et al. (2014); Bomberg et al. (2015); Emmert et al. (2015); Mukherjee and Shrira (2017); Ghani et al. (2019). Courtine et al. (2015) conducted a direct numerical simulation that shows the intrinsic mechanism. The aforementioned work considered the intrinsic mechanism mainly in isolation, i.e. with anechoic terminations. Work by Silva and co-authors (Silva et al., 2015, 2019; Orchini et al., 2020) gives a detailed discussion of intrinsic modes for models with non-anechoic boundary conditions.

Figure 1.3 a) shows that the final limit cycle oscillation is preceded by two smaller bursts, where the combustor turns temporarily unstable. Such a phenomenon is triggered due to the presence of turbulent background noise that can turn a combustor unstable or stable if the combustor is marginally stable, i.e. one or more thermoacoustic modes are very close to having positive growth rates. Bonciolini and co-authors (Bonciolini et al., 2016, 2017, 2018; Bonciolini and Noiray, 2019) have combined thermoacoustic models with stochastic terms to model these effects.

1.3 Thermoacoustic subjects considered in this thesis

In this section three specific topics in thermoacoustics are motivated. Each section concludes with a concrete objective to which this thesis contributes to.

1.3.1 Predicting thermoacoustics instabilities

Thermoacoustic instabilities need to be reliably predicted to build stable gas turbines. Different modelling strategies have been proposed to achieve this goal. These strategies differ in the trade-offs they make between numerical cost and physical simplifications. The most detailed – but also most expensive – analysis can be conducted for industrial configurations with reactive large eddy simulations (LES) (Wolf et al., 2012, 2009; Schulz et al., 2019). Direct numerical simulation (DNS) of combustion instabilities – with next to no simplifications – is computationally too expensive and can only be conducted for laminar flames, see Courtine et al. (2015) for a simulation of an intrinsic instability.

DNS and LES are both time-domain methods and costly. A simulation needs to be integrated forward in time and then observed if an instability grows. It is more efficient to formulate a linearized problem of the governing equations in frequency space. In the following, Fourier-transformed quantities are denoted by $\hat{(\cdot)}$. Solving these linearized problems yields, at a minimum, a set of tuples $(\omega, \hat{p})$ – the thermoacoustic *modes* – described by a frequency of oscillation $f = \text{Real}(\omega)/2\pi$, growth rate[1] $\omega_\text{I} = -\text{Imag}(\omega)$ and acoustic mode shape $\hat{p}$. If all thermoacoustic modes are damped (negative growth rate), a combustor will be *linearly* stable. In addition, the mode shape $\hat{p}$ is necessary to determine where to place acoustic damping elements in a combustion chamber (Bellucci et al., 2005; Zhao and Morgans, 2009; Mensah and Moeck, 2017a).

Linearized formulations have been proposed in the form of the linearized Navier–Stokes equations (LNSE) (Gikadi et al., 2012; Avdonin et al., 2019; Meindl et al., 2021), linearized Euler equations (LEE)(Hofmeister et al., 2020) or the thermoacoustic Helmholtz equation (Nicoud et al., 2007). The former two require input in the form of a mean field solution for all primitive variables (the number of which depends on the chosen formulation). Mean fields can be obtained from measurement data but are usually obtained from solving the Reynolds-averaged Navier–Stokes equations. LNSE and LEE retain the interaction between acoustic and hydrodynamic

[1] The Fourier transformation that dictates this sign will be defined later in Sec. 2.2

effects, unlike the thermoacoustic Helmholtz equation where the pressure fluctuation p_1 and velocity u_1 are algebraically related due to a linearized momentum balance, see Chap. 2 for details.

The main equation utilized in this thesis is the thermoacoustic Helmholtz equation. It is derived in the next chapter (Chap. 2), where all assumptions and simplifications are detailed. The equation is written as

$$\nabla \cdot \left(c^2 \nabla \hat{p} \right) + \omega^2 \hat{p} = -(\gamma - 1)\, \hat{q}\,(\omega)\, \nabla \hat{p}_{\mathrm{ref}} \cdot \mathrm{n}_{\mathrm{ref}}\,, \tag{1.3}$$

where c is the speed of sound and γ the heat capacity ratio. The right hand side of Eq. (1.3) contains the heat-release effect $\hat{q}$, which is related to the upstream gradient $\nabla \hat{p}_{\mathrm{ref}}$ at a reference location and in a reference direction $\mathrm{n}_{\mathrm{ref}}$. For this section it is assumed that $\hat{q}$ is expressed as a known function of ω such that the equation is closed. The dependence on $\hat{p}$ is linear and the dependence on ω potentially nonlinear. The equation is an inhomogeneous wave equation; hence, it lends itself to a network based solution approach (Dowling and Stow, 2003). This and related approaches are not the subject of this thesis and instead finite-element discretizations (FEM) of Eq. (1.3), as first proposed by Pankiewitz (2004) and later by Nicoud et al. (2007), are.

Equation (1.3) neglects any mean flow effects. This is not always a good approximation, since the mean flow has an effect on the thermoacoustic frequencies and mode shapes. Bauerheim et al. (2015) show this in annular combustion chambers with a mean swirl, which is a flow in tangential direction. Two co- and counter-rotating modes with the same azimuthal order are affected differently by this mean field. Compared to the case without any mean field, the co-rotating wave is shifted to a higher frequency and the counter-rotating one to a lower frequency.

Figure 1.5 shows a computational result of Eq. (1.3) for the can-annular combustor investigated in this thesis with an experimental result overlayed. As the figure depicts, there is good agreement between numerical and experimental frequencies. However, the numerics predict that two entirely different modes would be unstable[2]. If there are several unstable modes a linear analysis alone cannot predict, which mode(s) will be observed experimentally. Nonetheless, equation (1.3) has proven to be a successful tool for industrial applications, see the study by Wolf et al. (2012) on an industrial chamber where the result compares favorably to an LES

[2]See Article 5 where the result is taken from for a discussion on the limits of the numerical model with respect to this experiment.

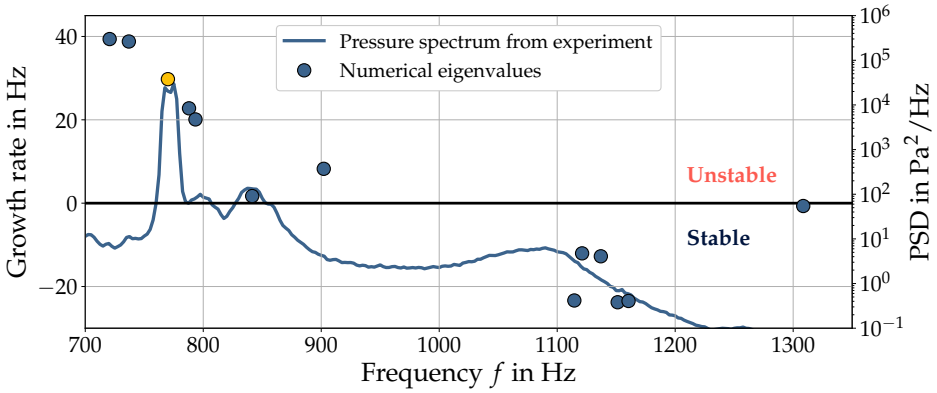

Figure 1.5: Result of a linear stability analysis of solving the thermoacoustic Helmholtz equation for the can-annular model combustor. The result is taken from Article 5. The circles are eigenvalues in the complex plane and the solid line is an experimentally obtained spectrum. The eigenvalue marked in gold agrees well with the experimentally observed limit cycle oscillation.

computation. One of its key advantages is that boundary conditions and the effect of the flame $\hat{q}$ can be measured experimentally. Equation (1.3) can be abbreviated in operator notation as

$$\mathcal{L}(\omega)\,\hat{p} = 0\,, \tag{1.4}$$

and after discretization with the finite-element or finite-volume method as

$$\mathrm{L}(\omega)\,\mathrm{p} = 0\,, \quad \mathrm{L} \in \mathbb{C}^{d\times d}\,. \tag{1.5}$$

Equations (1.4) and (1.5) both constitute a nonlinear eigenvalue problem (NLEVP). L is the discrete one with solutions in the form of eigenpairs (ω, p), where $d \approx 10^3 - 10^6$ is the dimension of the chosen discretization. Only nontrivial solutions $\mathrm{p} \neq 0$ (or $\hat{p} \neq 0$) are of interest. Importantly, the nonlinearity is restricted to the eigenvalue ω – the dependence on the eigenvector p is linear. This is also the case for the continuous problem. Solution of discrete NLEVPs is inherently more difficult than their linear counterparts. Linear eigenvalue problems have at most as many distinct eigenvalues as their system dimension (Saad, 2011). This is not the case for NLEVPs and they can have a countable infinite number of eigenvalues. Most importantly, *all* of the unstable eigenvalues in Fig. 1.5 need to be computed to assess stability of a combustor.

Recently, advancements have been made to employ adjoint perturbation methods (Silva et al., 2017a; Juniper, 2018; Magri, 2019; Mensah et al., 2020;

Orchini et al., 2021) to thermoacoustic NLEVPs. The adjoint formulation permits a numerically cheap computation of derivatives of the eigenpairs (ω, p) with respect to physical parameters of the model. These adjoint methods together with optimization strategies permit to alter geometries and physical parameters of combustors such that a stable design can be computed automatically (Aguilar and Juniper, 2020). Such strategies require not just precise but also fast NLEVP solvers.

It is possible to remove nonlinear dependencies in Eq. (1.3), for instance by expanding the (generally) nonlinear function $q(\omega)$ in terms of rational functions. The re-cast problem is then linear in ω and can be solved using established linear methods. In the thermoacoustic community this approach (and variants thereof) are called state space methods and they have been successfully used in applications, see work by Schuermans et al. (2003) or Meindl et al. (2016, 2020) and references therein. However, this approach necessarily introduces an approximation error in the form of *spurious modes*. These are modes which are solutions to the approximated problem, but not of the original NLEVP. A technical discussion for general NLEVPs can be found in Sec. 6 of Güttel and Tisseur (2017). The work in this thesis does not consider this approach and retains the nonlinearity in ω to preclude any possible approximation error.

NLEVPs have received plenty of attention in the mathematical community. A review article by Güttel and Tisseur (2017) covers their properties and the many solution methods that have been proposed. However, these advances had never entered the codes employed in the thermoacoustics community. At the start of this thesis, only fixed-point methods as proposed by Nicoud et al. (2007), were employed in the field of thermoacoustics to compute eigenvalues *and* mode shapes for large-scale NLEVPs. In his thesis Miguel-Brebion (2017) proposed a method that is able to compute all eigenvalues and eigenvectors of small NLEVPs ($d < 10^2$). Miguel-Brebion's method cannot be applied to the large problems considered in this thesis, since it computes the determinant of the operator $\mathrm{L}(\omega)$. Due to numerical rounding errors this is not feasible for large problems. A so-called Nyquist criterion (Sattelmayer and Polifke, 2003) can be evaluated to determine if a system is linearly stable or not, but it does not yield the mode shape. Fixed-point methods suffer from many drawbacks, including slow convergence and not being able to guarantee finding all eigenvalues – which is crucial in determining stability of a combustor. In his thesis, Mensah (2019) recognized this shortcoming and made a step forward by focusing on faster iterative strategies. The work in this thesis builds on Mensah's work. Devel-

opment of fast and reliable solution strategies for thermoacoustic NLEVPs constitutes Objective 1 of this thesis. This objective benefits thermoacoustic NLEVPs in general, but also NLEVPs of can-annular combustors in particular, since these exhibit closely neighbouring eigenvalues that are hard to compute. The origin of these tightly packed eigenvalues will be detailed below.

1.3.2 The relationship between symmetry groups and eigenvalue degeneracy in combustion chambers

Annular and can-annular combustors are often invariant with respect to discrete symmetry operations. In Figure 1.6(a) the top view of a simplified can-annular combustor is depicted. A rotation by any multiple of $2\pi/8$ leaves the combustor invariant as well as reflection along certain planes of which two are depicted as σ_v and σ_d. All geometric operations that leave a combustor invariant form a *group* G (a group that is denoted by the name C_{8v} for the example in Fig. 1.6(a)) and it is assumed that the mathematical operator that describes linear stability of the system

$$\mathcal{L}(\omega)\,\hat{p} = 0\,, \quad \hat{p} \neq 0\,, \tag{1.6}$$

is also invariant with respect to the same geometric operations. In the following, a few properties of symmetry groups are motivated briefly to give an idea of the importance for thermoacoustic problems. A more comprehensive introduction is given in Draft Article 8. The first five pages of Inui et al. (2012) are also a gentle introduction to this formal subject.

A group is a set of elements for which a group multiplication "$*$" is defined and which fulfills four group axioms: (G1) closure under multiplication, (G2) associativity, (G3) existence of identity element and (G4) existence of inverse element. One of the simplest groups possible is the one of a combustor with reflection symmetry, depicted in Fig. 1.7(b) and 1.7(c), which contains two elements only

$$C_S = \{E, \sigma_v\}\,, \tag{1.7}$$

where E is the identity element and σ_v a reflection operation. One could represent the elements of C_S by matrices. Then, the group multiplication "$*$" can be defined as matrix multiplication. This leads to the theory of group representations (Inui et al., 2012). Even without choosing a concrete representation and simply by using a geometric understanding, it is clear

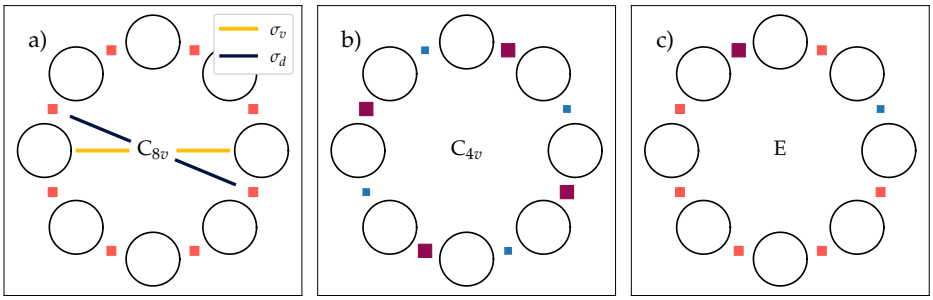

Figure 1.6: a) – c) Schematic top view of a can-annular combustion chamber. The circles are the cans and the squares are blocking elements that are inserted to vary the acoustic communication between adjacent cans, see Sec. 1.3.3. The color of each square signifies a blocking element with a certain diameter. The combustor in a) has the same blocking element inserted in all eight gaps. This is changed for the configurations b) and c) in a way to reduce the symmetry of the configuration. The combustor in a) is left invariant by eight rotations (multiples of $2\pi/8$) and reflection along eight reflection planes of which two are depicted as σ_v and σ_d. For the combustor in b) there are only four rotations (as multiples of $2\pi/4$) and four reflection operations. No symmetry exists for c). The formal name of every associated symmetry group is given in the center, e.g. C_{8v}.

that

$$E * E^{-1} = E\,, \tag{1.8}$$

$$E * \sigma_v = \sigma_v\,, \tag{1.9}$$

$$\sigma_v * E = \sigma_v\,, \tag{1.10}$$

$$\sigma_v * \sigma_v^{-1} = E\,, \tag{1.11}$$

where σ^{-1} refers to the inverse element of σ_v, which is the element itself in this case. Hence, the group axioms G1–G4 are fulfilled. The letter "S" in the group name C_S and the convention of using **s**igma σ as the symbol for reflection stems from the German word "*S*piegelung" for the reflection operation, as noted in Inui et al. (2012) on p. 2.

Once the symmetry group G of a system is known, a number of conclusions can be drawn on the eigenvalues ω and eigenvectors $\hat{p}$ without conducting any computations or experiments. Importantly, an annular and a can-annular combustion chamber can have the same symmetry group. Hence, both cases can be considered identical from a group-theoretical perspective: if G is the group for both, then statements derived from knowing G hold for both. First and foremost, all practical groups have been tabulated

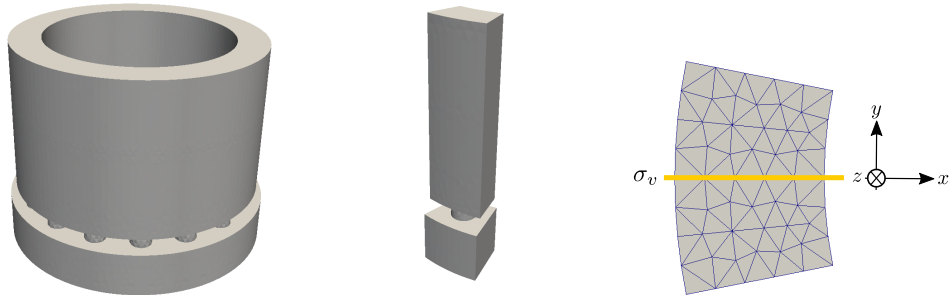

Figure 1.7: a) Annular combustion chamber with 16 identical combustors. b) One of the sixteen combustors, a so-called unit cell. c) Top view of the single cell with the reflection plane highlighted. The reflection operation (not the plane itself) is denoted by σ_v.

by means of their character tables (Inui et al., 2012, App. A) – in a sense a barcode of the group, which can be consulted to gather properties of the group.

In a character table the *irreducible representations* or short "irreps." of the group are given. For the example in Eq. (1.7) it was mentioned that the operations could be represented by three-dimensional matrices. If σ_v is a reflection operation along the xz plane, then the matrix would be written as

$$\sigma_v \doteq \begin{pmatrix} 1 & 0 & 0 \\ 0 & -1 & 0 \\ 0 & 0 & 1 \end{pmatrix}, \tag{1.12}$$

while E is simply represented by the identity matrix. The symbol "$\doteq$" denotes "represented by". However, such a representation would be "too big". Instead, one could represent the elements of C_S simply by numbers, i.e.

$$\Gamma_2 : \begin{matrix} E \doteq 1 \\ \sigma_v \doteq -1 \end{matrix} . \tag{1.13}$$

Then the relations Eqs. (1.9)–(1.11) would still hold, when "$*$" is chosen as ordinary multiplication. This representation cannot be further reduced – it is irreducible – and it has dimension one. One could also choose

$$\Gamma_1 : \begin{matrix} E \doteq 1 \\ \sigma_v \doteq 1 \end{matrix} . \tag{1.14}$$

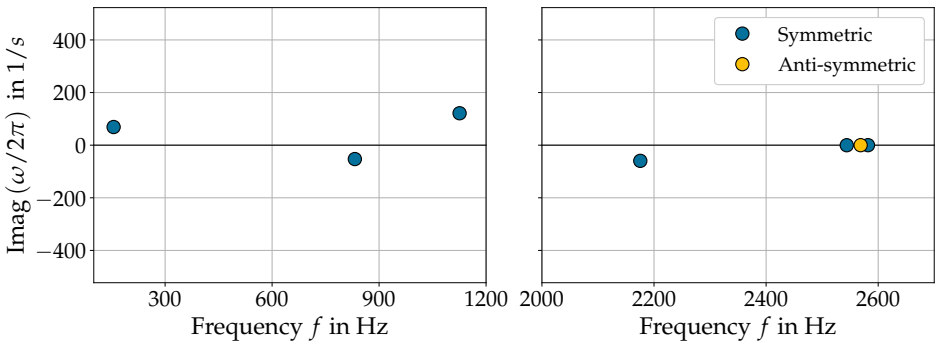

Figure 1.8: Thermoacoustic eigenvalues of a single cell combustor below 2300 Hz with reflection symmetry. The eigenfunctions belonging to the depicted eigenvalues are either symmetric or anti-symmetric with respect to the mirroring plane. There are no frequencies outside the depicted range below 2600 Hz. The result is from Draft Article 8.

which is the *trivial* irrep. and Eq. (1.9)–(1.11) would also hold. The representations Γ_1 (1.14) and Γ_2 (1.14) are the only two for C_S. By convention the trivial one is always listed as the first one. Both of the representations are one-dimensional. Bloch numbers, as used by Mensah and Moeck (2015) are also labels for irreps., but for a group called C_N with elements that are only discrete rotations.

The central importance of symmetry group theory to eigenvalue problems Eq. (1.6) is that every eigenpair $(\omega, \hat{p})$ must belong to one irrep. Accordingly, the irreps. can be used to label modes. In the above example of C_S modes are either 'symmetric' (belong to the first irreducible representation Γ_1) or 'anti-symmetric' (belong to the second irreducible representation Γ_2). This, means that if the thermoacoustic NLEVP (1.6) is solved on the unit cell (Fig. 1.7(b)) all computed eigenfunction $\hat{p}$ are either symmetric or anti-symmetric with respect to the reflection plane. Figure 1.8 show the result of a linear stability analysis for a combustor with group C_S.

The dimension of an irrep. determines the geometric multiplicity of an eigenvalue. Together with the algebraic multiplicity it can then be determined if a combustor exhibits simple or degenerate eigenvalues. Any combustor with a symmetry group that has at least one two-dimensional irrep. must exhibit a degenerate eigenvalue. For C_S both irreps. Γ_1 and Γ_2 are one-dimensional. Then degenerate eigenvalues can only occur for reasons unrelated to symmetry – so-called accidental degeneracies. Draft Article 8 goes deeper into detail and explains the theorems that govern irreps.,

mode degeneracy and under which conditions symmetry group theory can be applied to thermoacoustic problems.

As a quick reminder, eigenvalues have a geometric and an algebraic multiplicity. For the familiar case of a linear matrix eigenvalue problem

$$\mathrm{A}\mathrm{p} = \omega\mathrm{p}\,, \quad \mathrm{A} \in \mathbb{C}^{d\times d}\,, \quad d < \infty\,, \quad \mathrm{p} \in \mathbb{C}^{d} \neq 0\,, \tag{1.15}$$

the algebraic multiplicity is the order of the root of the characteristic polynomial at the eigenvalue

$$\det\left(\mathrm{A} - \omega\mathrm{I}\right) = 0\,, \tag{1.16}$$

and the geometric multiplicity is the dimension of the space spanned by the associated eigenvectors p. An eigenvalue is said to be degenerate if the algebraic multiplicity is larger than one. Chapter 3 gives definitions of algebraic and geometric multiplicity for the infinite-dimensional problem (1.6) that are generalizations of the definitions for ordinary matrices.

Degenerate eigenvalues in thermoacoustics are encountered in the form of azimuthal modes in annular and can-annular combustion chambers (Krebs et al., 1999; Stow and Dowling, 2001; Moeck et al., 2010). Figure 1.9 shows a degenerate mode pair of azimuthal order $m = 1$ belonging to the same eigenvalue in an annular combustion chamber. Due to the presence of the degenerate pair azimuthal modes can assume spinning, standing and mixed (intermediate state between the two pure cases of spinning and standing) states. Considerable research has been invested in previous years to characterise the states in annular combustion chambers, see the selected works by Evesque et al. (2003); Ghirardo and Juniper (2013); Worth and Dawson (2013); Bothien et al. (2015); Bourgouin et al. (2015b); Bauerheim et al. (2016b); Prieur et al. (2017); Mazur et al. (2021); Faure-Beaulieu et al. (2021), among a vast number of publications in the thermoacoustic field.

Symmetry can be lowered by perturbing the original system. Any symmetry group of the perturbed system must be a subgroup of the original group G. The loss of all symmetry leads to the trivial identity group E. Importantly, some perturbations conserve degenerate modes, while others cause degenerate modes to split. Figures 1.6(b) and (c) depict configurations that exhibit a lower symmetry than the case in Fig. 1.6(a). For instance, the combustor in Fig. 1.6(b) (with group C_{4v}) is not invariant with respect to a rotation by $2\pi/8$ but instead only by $2\pi/4$. The combustor in Fig. 1.6(c) does not exhibit any symmetries; hence the symmetry group is E – the identity group.

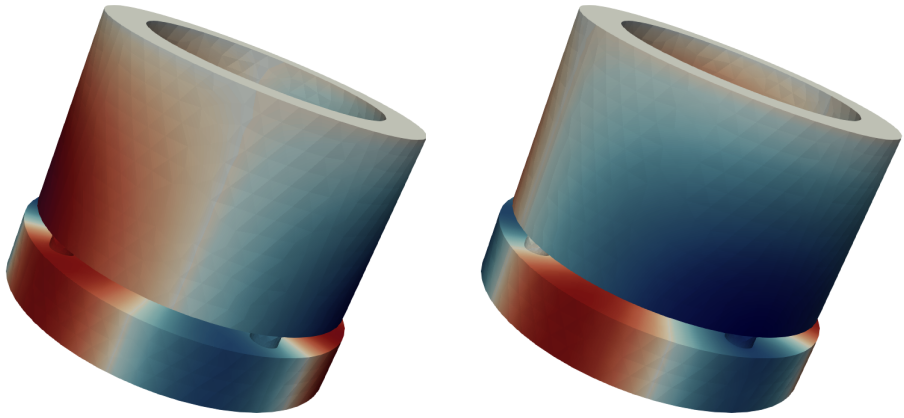

(a) **(b)**

Figure 1.9: Two modes in a degenerate pair belonging to an azimuthal mode order of $m = 1$. The normalized real part is depicted, where red areas correspond to a high value and areas in blue to a low value. The modes are orthogonal to each other. The result is from a computation in Draft Article 8.

No real combustor is perfectly symmetric. But it is the proximity to this idealized symmetric configuration that is responsible for the observed dynamics. Importantly, combustors with N cans (or burners in an annular combustor) that have C_{Nv} symmetry must exhibit degenerate modes. But the implication only goes this way. A combustor can also exhibit degenerate modes without C_{Nv}. However, even if the lower symmetry C_N – which by itself does not have degenerate modes – is present, the combustor can be close enough to C_{Nv} to show near-degenerate modes. It depends on how strong the symmetry breaking effect is that reduces the symmetry from C_{Nv} to C_N.

In thermoacoustics it has long been known that underlying symmetries imply degenerate modes. Ghirardo et al. (2016) identify the symmetry group C_{Nv} and discuss degenerate azimuthal modes. Mensah and Moeck (2015) successfully employed the so-called Bloch theory – a subject from symmetry group theory – to reduce computational costs in solving the eigenvalue problem Eq. (1.5). Bauerheim et al. in two papers (Bauerheim et al., 2014, 2016a) discuss the splitting of degenerate eigenvalues from a quantitative perspective using a network model of an annular combustor.

There remain a few open questions on the properties of thermoacoustic modes that can be answered by analyzing the problem from the perspective of symmetry groups. Most importantly, symmetry group theory natur-

ally permits to predict how and if degenerate modes split as the symmetry is lowered by perturbations. In addition, Bloch theory as employed by Mensah and Moeck (2015) exploits the C_N symmetry to reduce computational cost. It is shown that if the higher symmetry C_{Nv} is present, a further reduction is possible – but only for simple eigenvalues. Objective 2 consists in analyzing the thermoacoustic eigenvalue problem in the language of symmetry groups and applying its machinery to a number of problems.

1.3.3 Thermoacoustic instabilities in can-annular combustors

A can-annular arrangement of combustion chambers is one of two types of designs found in modern industrial gas turbines, see the portfolio of several major manufacturers (General Electric Power, 2021; Ansaldo Energia, 2021; Mitsubishi Power, 2021). The second type is an annular design. In an industrial can-annular design, compressed air is fed to individual, isolated combustion chambers that are arranged around a circumference, see Fig. 1.10(a). In the cans, combustion takes place. The hot products exit the combustion chamber at its downstream end, where the circular cross-section of the can is merged to an annular gap – the inlet of the turbine (Pennell et al., 2017). This small gap, depicted in Fig. 1.10(b), is the so-called acoustic cross-talk (XT). It permits acoustic waves to travel between neighbouring cans. Since the gap is small, the coupling is generally understood to be weak (Ghirardo et al., 2019, 2020). This has consequences for the modes of thermoacoustic instabilities that are unique to this type of combustor.

Industrial combustors for stationary power generation employ an even number N of cans. This is a manufacturing necessity, since the combustor casing consists of two halves and only with an even N is the flange not located inside a burner, according to Ghirardo et al. (2019). For industrial-scale engines the number of cans is in the range of eight to sixteen.

The major advantage of a can-design is that a significant amount of engineering can be conducted on a single can. A number of important features, such as air-fuel mixing, flame location, flashback and blow-off sensitivity can be simulated and experimented on a single can – which reduces development time and costs compared to an annular combustion chamber, where either a full rig or an annular segment are necessary. Disadvantages come in the form of an increased weight, larger size, more surface area that requires cooling, and thermoacoustic instabilities strongly affected by the cross-talk.

Figure 1.11 depicts, in a schematic way, the basic building blocks of the can-annular model combustor that is later presented in detail in Chap. 4. The design shares key ideas of its industrial counterparts, while a number of constraints necessitate differences. The model combustor is fed from a joint plenum with perfectly premixed reacting mixture, from where it enters individual injectors. At the downstream end of the injectors, bluff bodies are positioned, which provide a recirculation zone inside the can combustors where the flames are stabilized. Far downstream of the flame zone, a cross-talk element is mounted, which permits acoustic communication between adjacent cans. Due to the downstream location of the cross-talk element, there is no flame-to-flame interaction.

The reason why can-annular combustors exhibit a unique type of instabilities is the presence of so-called mode clusters. These are groups of modes within a narrow frequency band that have different azimuthal mode orders. Figure 1.12 depicts a computational result where two such clusters can be observed with modes of orders $m = 0, 1, 2, 3, 4$. Figure 1.5 also depicts clustered modes in the group between 700 Hz and 900 Hz, but the frequency band over which the clusters extend is much wider.

The clustering is due to the weak coupling via the cross-talk areas. In the idealized case that the strength of the communication is reduced to zero, all of the clustered modes in Fig. 1.12 would merge into an eightfold degenerate eigenvalue. This corresponds to a state where every can would oscillate in a standalone fashion with no synchronization. All eight eigenvalues exhibit the same axial order.

Due to the non-vanishing cross-talk the eightfold degenerate eigenvalue splits into the orders observed here. After the split the clustered modes still have the same axial order. This feature can then be used to group modes into clusters, say when they are obtained from a linear stability analysis. After the split, the degeneracy is conserved: $m = 0, 4$ are simple while $m = 1, 2, 3$ are twofold degenerate. In principle, mode orders that differ from the ones given here can be realized, and that is the case for clusters at higher frequencies. For the low frequencies usually observed in experiments, this is not the case. Then, the heuristic that a combustor with N (even) cans has modes of orders

$$m \in \left\{0, 1, \ \ldots \ , \frac{N}{2} - 1, \frac{N}{2}\right\}, \tag{1.17}$$

in a cluster can be used. Modes of orders $m = 0$ and $m = N/2$ are simple while the remainder is degenerate. In the literature (Ghirardo et al., 2019)

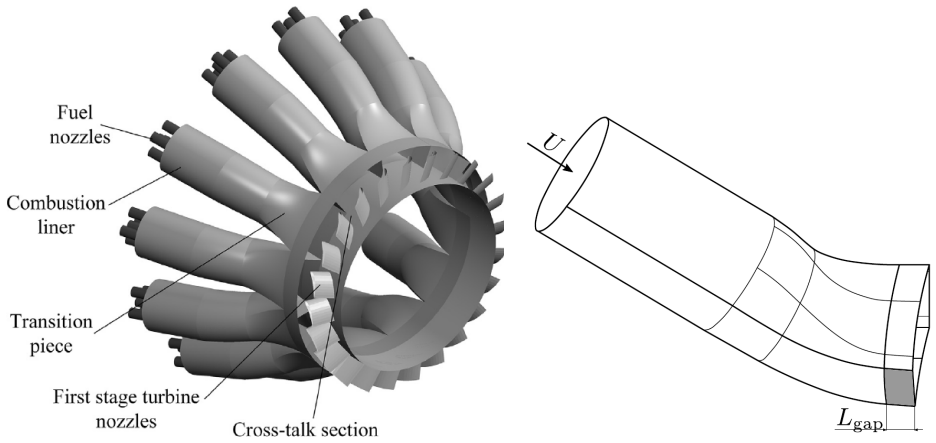

Figure 1.10: a) Can-annular combustor in an industrial application. The cans merge at their respective downstream ends onto an annular cross-section. The figure is taken from Moon et al. (2020a) who added the annotations to a figure originally due to Luque et al. (2015). b) Sketch of a single can. In gray the cross-talk area is visible via which acoustic communication between adjacent cans takes place. The figure is taken from Ghirardo et al. (2019).

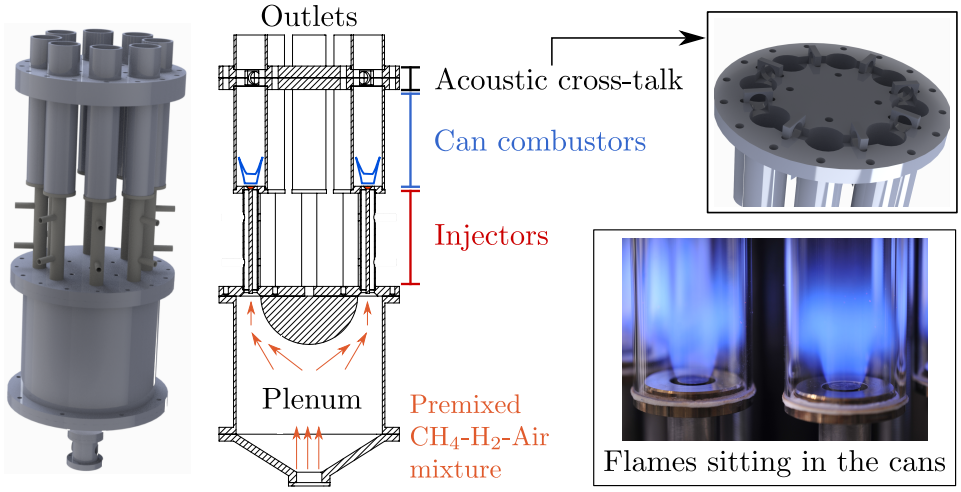

Figure 1.11: A rendering, a simplified cut-through and a picture during operation of the can-annular test rig that is described in detail in Chap. 4. Perfectly premixed mixture enters a plenum from where the individual cans are fed. Towards the outlet, a coupling ring is mounted, which permits acoustic waves to travel between adjacent cans. By inserting blocking elements, the surface area of the cross-talk cavity, and hence the strength of the cross-talk, can be adjusted.

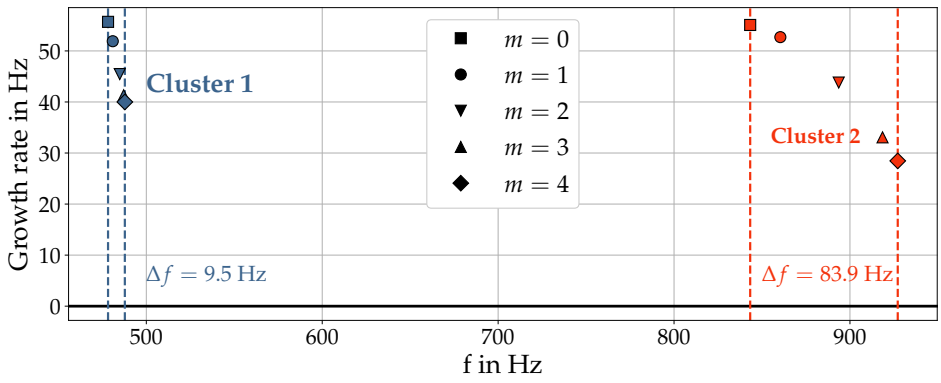

Figure 1.12: Eigenvalues for the can-annular model combustor of Article 5, when a sintered plate is mounted to decouple the upstream plenum. Two clusters of eigenvalues can be identified in which modes of different azimuthal mode orders are present. At the bottom of the figure the width of the bands Δf of the clusters are given. The computed eigenvalues only agree qualitatively with the experimentally observed modes, because the numerical setup cannot replicate all of the features of the actual experiments. For example, the installed sintered plate is modelled as an impedance boundary condition that stops all communication via the plenum. However, Article 5 shows that some communication through the plate is still possible. The numerical model cannot account for this.

the mode $m = 0$ is usually referred to as a *push-push* mode, while the $m = N/2$ mode is called a *push-pull* mode.

Since the coupling via the XT is weak, the post-split modes remain in a narrow frequency band. This introduces interesting dynamics if the single isolated "progenitor" mode is unstable. The cluster that originates from this unstable mode can contain several unstable modes. This is the case for the modes in Fig. 1.12, which are all unstable. Two important questions are: Which cluster dominates the system? Or is it a combination of or synchronization between modes? Moreover, multiple modes can be unstable.

An additional effect called *mode localization* (Hodges, 1982) can take place as well. Hereby, a significantly increased oscillation amplitude is observed in only a few cans, while the remainder remain silent. This phenomenon is caused by the fact the closely neighbouring eigenvalues – as they are occurring in a cluster – cause a significant sensitivity of the associated eigenvectors to perturbations (Pierre, 1988). Thus, small asymmetries in the system have large effects on the eigenfunctions which results into shapes with a strong localization. From the engineering perspective this is a severe

problem, since pressure transducers need to be mounted in every single can to assess stability – unlike in annular combustion chambers where an instability is active in the entire chamber.

Existing theoretical and experimental work

There has been significant research on instabilities in annular combustion chambers, see the many references in the review articles of Bauerheim et al. (2016b) and Poinsot (2017). In comparison, the research on thermoacoustic instabilities in can-annular combustors has not reached the same depth. Kaufmann et al. (2008) computed modes with alternating and pairwise alternating patterns for a Siemens SGT5-8000H gas turbine. In two papers Farisco et al. (2015, 2017) investigated the acoustic communication via a cross-talk between two adjacent cans and found it to play a major importance for synchronization of modes.

Ghirardo et al. (2019, 2020) revealed the existence of clustered modes. von Saldern et al. (2020) predicted the splitting of N-fold degenerate modes as the XT size is increased from zero. Both show that the $m = 0$ mode before and after the split stays in place and that higher order modes are further offset from $m = 0$. Unlike in these models, in experiments a XT has a finite volume and thus the mode $m = 0$ experiences a minor shift from the uncoupled can if the XT size is varied. Furthermore, in the aforementioned studies it is also show that clustered modes are ordered by increasing frequency according to their mode order and that modes of higher order are more sensitive to the coupling strength, i.e. more offset from $m = 0$.

Experimentally, Moon et al. (2020a,b, 2021) give a first proof of these properties and report a variety of oscillation patterns in a model can-annular combustor. The model combustor they employed with $N = 4$ cans has two predecessors: single can (Kim, 2016, 2017) and a twin can setup (Jegal et al., 2019; Moon et al., 2019). The same weak coupling in the twin setup is employed in the can-annular layout. Throughout the publications, the size of the XT is kept constant. In the can-annular combustor of Moon and coauthors an equivalence ratio can be prescribed for every burner individually. Hence, the work explores how asymmetries affect the thermoacoustic stability states.

In Moon et al. (2020a) the authors vary the length of a single combustor to determine for which lengths instabilities are observed. Equipped with this knowledge, the four-can combustor is operated with different lengths, and symmetric and asymmetric equivalence ratios. Opposite cans have the

same equivalence ratio whenever an asymmetry is realized. The observed modes are of orders $m = 0, 1, 2$. For a number of cases the combustor shows a stochastic nature with respect to the attained limit cycles: under the same operating conditions different modes reach a stable limit cycle. For one specific case all three modes of orders $m = 0, 1, 2$ are attained and it can be observed that these are arranged by increasing frequency – confirming theoretical results. For the $m = 1$ mode only one location of the nodal line is observed, that is inside cans. A purely acoustic analysis confirms the mode clusters.

In Moon et al. (2020b) the same equivalence ratio is employed in neighbouring cans, unlike in the preceeding paper (Moon et al., 2020a) which uses opposite cans, to realize an asymmetry. The result is a richer variety in instability states: the $m = 1$ mode shows different nodal line locations and a spinning state. It is also observed how two very closely neighbouring modes (which form a degenerate pair in the symmetric case) are active as standing modes simultaneously at slightly different frequencies (260 Hz vs. 258 Hz). Plus, first concrete evidence for mode localization is given in the form of a high amplitude oscillation in one can with the remainder silent.

In the two papers (Moon et al., 2020a,b) pure CH_4–air mixture is employed. For the third paper (Moon et al., 2021) four novel hydrogen combustors are employed. Each combustor uses a large number (97 nozzles) of very small (nozzle diameter is 3 mm) hydrogen flames. The design is similar to the one employed by Lee and Kim (2020), but employs more and smaller individual nozzles. The combustor is operated with pure H_2–air mixture but there are no changes in geometry: the same combustor lengths and cross-talks are employed. The hydrogen flames have a decidedly different response and excite instabilities at higher frequencies that the CH_4–air mixtures. Mode types are similar to the ones observed in the previous two paper (Moon et al., 2020a,b), but more types of mode localization are observed: a) push-push localization involving three and two cans and b) push-pull localization involving two and three cans.

Transient phenomena have been studied by von Saldern et al. (2020) using a reduced order model with a nonlinear flame response. The results show that competition between multiple unstable modes of a cluster occurs. The mode with the linearly largest growth rate, $m = 2$, grows strongest in amplitude, but does not dominate the limit cycle. After a transient the mode dies down and the push-pull mode dominates. The result highlights how difficult it is to predict the mode order and frequency of limit cycle oscilla-

tions in can-annular combustors.

On notational differences concerning azimuthal modes

There is a certain notational difference concerning the naming of modes between this work and the work by Moon et al. (Moon et al., 2020a,b, 2021). In this work, modes of lowest order ($m = 0$) are referred to as push-push, while those of highest ($m = 4$ here, $m = 2$ in Moon et al.) are push-pull modes. The mode orders in-between are degenerate and can be of standing, spinning or mixed type. Moreover, for standing modes the location of the nodal is understood to be variable. For instance, for standing modes $m = 1, 2$, the nodal lines can be located inside opposite cans or between cans, i.e. in the XTs. This notation differs from the one in Moon et al. who refer to an $m = 1$ mode as 'push-pull (pairwise)' or 'push-pull (2-cans)', depending on the location of the nodal line. Table 1.1 compares the notations.

For one case Moon et al. label a mode as degenerate, which this work would argue is incorrect. "Case D" in Moon et al. (2021) exhibits an unstable push-pull mode at 559 Hz. An FEM analysis confirms the 559 Hz but also reveals an $m = 2$ mode at 557 Hz, which is only active in the XT segment. The experimentally observed mode shapes agree with the FEM partially, i.e. the mode shape of the numerical mode at 559 Hz agrees with the experiments in the cans but not in the XT – vice versa for the 557 Hz mode. Moon et al. argue that these two modes, since they have the same azimuthal order and are in close vicinity, belong to a degenerate pair. From the standpoint of the work in this thesis, these modes correspond to simple eigenvalues, respectively. A push-pull mode is necessarily simple. The proximity of the two is just coincidence due to the geometrical dimensions. Hence, they do not form a degenerate pair.

The need for more experimental results

At the time of writing of this thesis, the can-annular combustor employed by Kihun Moon and coauthors (Moon et al., 2020a,b, 2021) is the only other can-annular experiment in academia besides the one presented in this thesis at NTNU. A new experiment has the prospect to confirm existing studies but also to give new insights on thermoacoustics of can-annular combustors. Therefore, Objective 3 constitutes the design and operation of a new can-annular model combustor that permits a detailed study of the effect of cross-talk strength on the thermoacoustic modes. The design pursued in this thesis has several key differences to the design by Kihun Moon and co-authors, namely

Table 1.1: Comparison of the notation in Moon et al. (2020a) and Moon et al. (2020a) with the notation employed in this thesis for azimuthal modes in can-annular combustors.

Moon et al.	Azi. order m	This thesis
push-push	0	push-push or $m = 0$
push-pull (4 cans) push-pull (alternating)	4	push-pull or $m = 4$
push-pull (2 cans) push-pull (2 cans only)	1	$m = 1$, nodal lines in cans
push-pull pairwise	1	$m = 1$, nodal lines in XTs
azimuthal (spinning)	1	$m = 1$, spinning

- The number of cans is higher, with $N = 8$ compared to $N = 4$. Thus, clusters consist of more modes with the orders $m = 0, 1, 2, 3, 4$. The higher number is also more representative of the number encountered in real engines.

- A major conceptual difference is that the cross-talk strength is not varied in Moon's combustor, but the overall length of the combustor is. Changing the length of the combustor directly alters the thermoacoustic frequencies and makes it difficult to isolate the effect of the cross-talk communication.

- Both combustors can be operated with nominally symmetric operating conditions. However, the mixture injection for every combustor is controlled individually in Moon's combustor. In the combustor in this thesis, all cans can only be fed with the same mixture from the shared plenum.

- Moon's combustor does not have a plenum – as is realistic for actual gas turbines. Hence, there is no acoustic coupling between cans via the plenum. Moreover, the outlet boundary condition is decidedly different: a water-cooled piston realizes a sound hard boundary. Due to the opening to the atmosphere, the combustor in this thesis has a pressure node there.

1.4 Summary of objectives of this thesis

The objectives have been motivated in the previous sections. Here, they are summarized and a road map is given that details where the objectives are achieved by giving references to chapters in this thesis and papers that are part of this thesis. In Chaps. 2 and 3 two fundamental topics from the thermoacoustic literature are reviewed, since they are relevant to the content of this thesis. Chapter 2 derives the thermoacoustic Helmholtz equation as the governing PDE for linear stability analysis from the Navier–Stokes equations and formulates the continuous and discrete nonlinear eigenvalue problem. Chapter 3 discusses nonlinear eigenvalue problems and eigenvalue degeneracy, while Chap. 4 described the experimental setup in detail. The thesis concludes with the summary of the scientific contributions in Chap. 5 and the conclusions in Chap. 6. Starting from p. 99 the nine papers that form the thesis are collected. Appendix A contains the technical drawings.

Objective I.

Develop fast solvers for the nonlinear thermoacoustic eigenvalue problem that return all relevant eigenvalues.

Chapter 3 reviews aspects of nonlinear eigenvalue problems as they are relevant to thermoacoustic problems. Article 4 shows that fixed-point methods – the first and most popular methods used in thermoacoustics – are inadequate to compute intrinsic thermoacoustic modes. Numerical experiments by the author had shown this at the beginning of the PhD work, a proof using Banach's fixed-point theorem was obtained later. Article 2 presents a global solution strategy that guarantees to find all eigenvalues inside a specified contour in the complex plane, and the work is based on a method due to Beyn (2012). This global method was instrumental in finding intrinsic thermoacoustic modes in an annular combustion chamber, and the results are published in Article 3. The aforementioned article Article 4 also contains work on fast iterative solution strategies for NLEVPs. Article 7 presents a subspace-projection strategy that significantly reduces the dimensions of FEM-discretized NLEVPs and permits to use the previously developed solvers.

Objective II.

Analyze the thermoacoustic eigenvalue problem from the perspective of symmetry groups and use the machinery to solve open questions in thermoacoustics.

The relation between symmetry and degeneracy is the central subject of this thesis. This relation is explored in Draft Article 8. Symmetry group theory can only be employed to determine geometric multiplicity (for continuous and discrete problems); hence Chap. 3 contains a brief discussion of algebraic multiplicity both for the discrete and continuous case to complete the picture. Article 1 explores a case in a thermoacoustic system where the algebraic multiplicity is higher than the geometric multiplicity of an eigenvalue, a so-called exceptional point.

Objective III.

Establish an atmospheric can-annular model combustor to study the effect of cross-talk variation.

The can-annular model combustor is described in Chap. 4. Article 5 contains the first set of experiments performed on the combustor. In addition, linear stability analysis is performed on the combustor using the numerical tools developed in Objective 1. Article 6 contains a network model, where the geometry and parameters of the can-annular combustor are employed to propose an acoustic model for the coupling via the cross-talk gap.

Objective IV.

Analyze eigenvalue degeneracy of the can-annular model combustor from the perspective of symmetry groups.

This objective applies the theoretical results from Objective 2 to the experimental combustor in Objective 3, which has symmetry group C_{8v}. A Draft Article 9 that will soon be submitted contains these results.

Chapter 2

Fundamentals I – Linear stability analysis with the thermoacoustic Helmholtz equation

In this chapter the thermoacoustic Helmholtz equation is derived from the Navier–Stokes equations. In a first step, the conservation equations are simplified using physical arguments to derive a wave equation for $\ln(p)$. In a second step, the $\ln(p)$ wave equation is linearized to obtain the thermoacoustic Helmholtz equation. This strategy is originally due to Phillips (1960) and found in Poinsot and Veynante (2005). In a third step, the equation is transformed into frequency domain and a suitable closure of the heat-release rate $\hat{q}$ is formulated in terms of flame transfer functions. In a fourth step, the variational problem associated with the numerical solution of the equation is defined – a so-called nonlinear eigenvalue problem, which is discussed in Chap. 3.

2.1 Acoustic wave equation derived from the Navier–Stokes equations

The compressible and reactive Navier–Stokes equations are given by the continuity, momentum, species and energy balances (Law, 2010, p. 163). In this section, physical arguments from Law (2010), Poinsot and Veynante (2005) and Lieuwen (2012) are employed to simplify the balance equations.

In the following, vector and tensor-valued quantities are denoted in bold, e.g. u and $\boldsymbol{\tau}$. An equation placed inside a box signifies that all necessary simplifications for that section have been applied and that the equation will be employed at a later point in the derivation.

2.1.1 Mass conservation

The continuity equation, or mass balance, is written as

$$\frac{\partial \rho}{\partial t} + \nabla \cdot (\rho \mathrm{u}) = 0\,, \tag{2.1}$$

$$\tag{2.2}$$

with the density ρ and velocity u. With the material derivative for an arbitrary quantity ϕ defined as

$$\frac{\mathrm{D}\phi}{\mathrm{D}t} = \frac{\partial \phi}{\partial t} + \mathrm{u} \cdot \nabla \phi\,, \tag{2.3}$$

the continuity equation can be re-written into

$$\boxed{\frac{\mathrm{D}\rho}{\mathrm{D}t} = -\rho \nabla \cdot \mathrm{u}} \tag{2.4}$$

2.1.2 Species mass conservation

Conservation of M different species is governed by

$$\frac{\partial \rho Y_i}{\partial t} + \nabla \cdot [\rho Y_i \, (\mathrm{u} + \mathrm{V}_i)] = \dot{w}_i\,, \quad i = 1, \ldots, M\,, \tag{2.5}$$

where Y_i is the mass fraction of species i, V_i is the diffusive velocity and $\dot{w}_i$ is the rate of production/consumption of a chemical species. Since the total mass is constant, the mass fractions are governed by

$$\sum_{i=1}^{M} Y_i = 1\,. \tag{2.6}$$

The diffusive velocities are defined as

$$\mathrm{V}_i = \mathrm{u}_i - \mathrm{u}\,, \tag{2.7}$$

and it holds

$$\rho \mathrm{u} = \sum_{i=1}^{M} \rho_i \mathrm{u}_i\,. \tag{2.8}$$

Multiplying Eq. (2.7) by Y_i and summing over all indices yields

$$\sum_{i=1}^{M} Y_i \mathrm{V}_i = \sum_{i=1}^{M} Y_i \mathrm{u}_i - \sum_{i=1}^{M} Y_i \mathrm{u}\,, \tag{2.9}$$

Together with Eq. (2.8) one obtains

$$\boxed{\sum_{i=1}^{M} Y_i \mathrm{V}_i = 0} \tag{2.10}$$

Formally, for the diffusive velocities a constitutive relation (Law, 2010) needs to be specified. However, this is omitted since the term where the constitutive relations appears later in the energy balance equation will be eliminated by assuming equal heat capacities $c_{p,i} = c_p$.

2.1.3 Momentum balance

The momentum balance is formulated as

$$\frac{\partial \mathrm{u}}{\partial t} + \mathrm{u} \cdot \nabla \mathrm{u} = -\frac{\nabla p}{\rho} + \frac{\nabla \cdot \boldsymbol{\tau}}{\rho} + \sum_{i=1}^{M} Y_i \mathrm{f}_i\,, \tag{2.11}$$

where $\boldsymbol{\tau}$ is the stress tensor and f_i a vector of external body forces acting on the species. The constitutive relation for the stress tensor is given as

$$\boldsymbol{\tau} = \left[p + \left(\frac{2}{3}\mu - \kappa\right)(\nabla \cdot \mathrm{u})\right] \mathrm{I} - \mu\left[(\nabla \mathrm{u}) + (\nabla \mathrm{u})^T\right]\,, \tag{2.12}$$

which assumes that the medium behaves as a Newtonian fluid. Besides the pressure p, the stress tensor depends on the velocity u, and contains the two viscosities μ and κ as parameters. Similar to the diffusive velocities in the species mass balance Eq. (2.5), the stress tensor $\boldsymbol{\tau}$ will be neglected at a later stage.

For thermoacoustic applications, body forces f_i are negligible. Hence, in the momentum balance (2.11) the contribution of the individual species Y_i can be discarded. Since the left hand side of Eq. (2.11) constitutes the material derivative, one obtains the simpler form

$$\frac{\mathrm{D}\mathrm{u}}{\mathrm{D}t} = -\frac{1}{\rho}\nabla p + \frac{1}{\rho}\nabla \cdot \boldsymbol{\tau}\,. \tag{2.13}$$

As a constitutive relation for the pressure p, the ideal gas law is employed

$$p = \rho \bar{R} T\,. \tag{2.14}$$

Here, $\bar{R}$ is the mass-specific gas constant and T the temperature. The ideal gas model is justified since the gases considered in this thesis are at low pressures and at high temperatures. The combustion chambers that are modelled in this thesis are exclusively operated with CH_4–H_2–air mixtures under atmospheric conditions. These gases can be considered ideal for pressures below 100 bars and temperatures above 300 K. However, even for industrial gas turbines with pressures of up to 50 bars the ideal gas model would still be valid for CH_4–H_2–air mixtures.

For an ideal gas the speed of sound c is defined as

$$c^2 = \gamma \bar{R} T \,, \tag{2.15}$$

and Eq. (2.13) can then be formulated as

$$\frac{\mathrm{D}\mathrm{u}}{\mathrm{D}t} + \frac{c^2}{\gamma}\frac{1}{p}\nabla p = \frac{1}{\rho}\nabla \cdot \boldsymbol{\tau} \,. \tag{2.16}$$

An application of the chain rule of differentiation gives

$$\frac{\mathrm{D}\mathrm{u}}{\mathrm{D}t} + \frac{c^2}{\gamma}\nabla \ln(p) = \frac{1}{\rho}\nabla \cdot \boldsymbol{\tau} \,. \tag{2.17}$$

By taking the divergence of Eq. (2.17) an equation is obtained

$$\boxed{\nabla \cdot \frac{\mathrm{D}\mathrm{u}}{\mathrm{D}t} + \nabla \cdot \left[\frac{c^2}{\gamma}\nabla \ln(p)\right] = \nabla \cdot \left(\frac{1}{\rho}\nabla \cdot \boldsymbol{\tau}\right)} \tag{2.18}$$

which is later combined with a suitable formulation of the energy equation to obtain the wave equation in $\ln(p)$.

2.1.4 Energy balance

The balance equation for the internal energy e (chemical and sensible) is given as

$$\frac{\partial \rho e}{\partial t} + \nabla \cdot (\rho \mathrm{u}\, e) = -\nabla \cdot \mathrm{q} - \boldsymbol{\tau} : \nabla \mathrm{u} + \rho \sum_{j=1}^{M} Y_i \mathrm{f}_i \cdot \mathrm{u} \,, \tag{2.19}$$

where the colon operator denotes tensor contraction and the heat flux vector q takes the form

$$\mathrm{q} = -\lambda \nabla T + \rho \sum_{i=1}^{M} h_i Y_i \mathrm{V}_i \,, \tag{2.20}$$

where λ is the thermal conductivity and h the enthalpy. The term "$-\lambda\nabla T$" is Fourier's law for heat conduction. This simplified form already assumes that the Dufour effect (transfer of heat due to concentration gradients) and radiation are neglected. The Dufour effect is very small (Palle et al., 2005) and since the flames considered in this thesis are low in soot, the radiative losses can be neglected as well.

Again, body forces are neglected $\mathrm{f}_i = 0$ and the contribution of the stress tensor simplifies to

$$\boldsymbol{\tau} : \nabla \mathrm{u} = p\mathrm{I} : \nabla u = p\nabla \cdot \mathrm{u}\,, \tag{2.21}$$

for low-speed subsonic flows, where viscous heating is far lower than heating due to other sources (Law, 2010, p. 170). Thus, Equation (2.19) simplifies to

$$\frac{\partial \rho e}{\partial t} + \nabla \cdot (\rho \mathrm{u}\, e) = -\nabla \cdot \mathrm{q} - p\nabla \cdot \mathrm{u}\,. \tag{2.22}$$

Substituting $e = h - \frac{p}{\rho}$ yields

$$\begin{aligned} \frac{\partial (\rho h - p)}{\partial t} + \nabla \cdot (\rho \mathrm{u}\, h - \mathrm{u}\, p) = -\nabla \cdot (-\lambda \nabla T) \\ -\nabla \cdot \left(\rho \sum_{i=1}^{M} h_i Y_i \mathrm{V}_i \right) - p\nabla \cdot \mathrm{u}\,. \end{aligned} \tag{2.23}$$

The equation can be re-arranged into

$$\frac{\partial (\rho h)}{\partial t} + \nabla \cdot \left[\rho \mathrm{u}\, h - \lambda \nabla T + \rho \sum_{i=1}^{M} h_i Y_i \mathrm{V}_i \right] = \frac{\partial p}{\partial t} + \nabla \cdot (\mathrm{u}\, p) - p\nabla \cdot \mathrm{u}\,. \tag{2.24}$$

The chain rule of differentiation gives for the right hand side

$$\frac{\partial p}{\partial t} + p\nabla \cdot \mathrm{u} + \mathrm{u} \cdot \nabla p - p\nabla \cdot \mathrm{u} = \frac{\partial p}{\partial t} + \mathrm{u} \cdot \nabla p = \frac{\mathrm{D}p}{\mathrm{D}t}\,. \tag{2.25}$$

Thus, Eq. (2.24) simplifies to

$$\frac{\partial (\rho h)}{\partial t} + \nabla \cdot \left[\rho \mathrm{u}\, h - \lambda \nabla T + \rho \sum_{i=1}^{M} h_i Y_i \mathrm{V}_i \right] = \frac{\mathrm{D}p}{\mathrm{D}t}\,. \tag{2.26}$$

The enthalpy is governed by $h = \sum_{i=1}^{M} Y_i h_i$, and hence

$$\frac{\partial}{\partial t} \left(\rho \sum_{i=1}^{M} Y_i h_i \right) + \nabla \cdot \left[\rho \sum_{i=1}^{M} Y_i h_i \left(\mathrm{u} + \mathrm{V}_i \right) - \lambda \nabla T \right] = \frac{\mathrm{D}p}{\mathrm{D}t}\,. \tag{2.27}$$

The enthalpy h_i can be written as the sum of the enthalpy of formation h_i° and the sensible enthalpy h_i^s as

$$h_i = h_i^\circ + h_i^s \tag{2.28}$$

and this will be used to re-write Eq. (2.27). Multiplying the species balance (2.5) by h_i° and summing over all indices gives

$$\frac{\partial}{\partial t}\rho \sum_{i=1}^{M} Y_i h_i^\circ + \nabla \cdot \rho \sum_{i=1}^{M} h_i^\circ Y_i \left(\mathrm{u} + \mathrm{V}_i\right) = \sum_{i=1}^{M} h_i^\circ \dot{w}_i \,. \tag{2.29}$$

Subtracting Eq. (2.29) from Eq. (2.27) yields

$$\frac{\partial}{\partial t}\left(\rho \sum_{i=1}^{M} Y_i h_i^s\right) + \nabla \cdot \left[\rho \sum_{i=1}^{M} Y_i h_i^s \left(\mathrm{u} + \mathrm{V}_i\right) - \lambda \nabla T\right] = \frac{\mathrm{D}p}{\mathrm{D}t} - \sum_{i=1}^{M} h_i^\circ \dot{w}_i \,, \tag{2.30}$$

where the sum of the enthalpies (2.28) is used. The sums can be simplified further into

$$\frac{\partial}{\partial t}\left(\rho h^s\right) + \nabla \cdot \left(\rho \mathrm{u} h^s + \rho \sum_{i=1}^{M} Y_i h_i^s \mathrm{V}_i - \lambda \nabla T\right) = \frac{\mathrm{D}p}{\mathrm{D}t} - \sum_{i=1}^{M} h_i^\circ \dot{w}_i \,. \tag{2.31}$$

Assuming equal heat capacities $c_{p,i} = c_p$ for all species gives $h_i^s \equiv h^s$, since for an ideal gas it holds $\mathrm{d}h = c_p \mathrm{d}T$. Then, Equation (2.10) allows to eliminate the term with the diffusive velocities

$$\frac{\partial}{\partial t}\left(\rho h^s\right) + \nabla \cdot \left(\rho \mathrm{u}\, h^s - \lambda \nabla T\right) = \frac{\mathrm{D}p}{\mathrm{D}t} - \sum_{i=1}^{M} h_i^\circ \dot{w}_i \,. \tag{2.32}$$

Assuming equal heat capacities is justified here, by noting that air is used as oxidizer, hence N_2 dominates as a species. The volumetric heat-release rate due to combustion is defined as

$$q = -\sum_{i=1}^{M} h_i^\circ \dot{w}_i \,. \tag{2.33}$$

and contains only the chemical contribution of the enthalpy. In the thermoacoustic literature, the term is often denoted by $\dot{q}$ but in this thesis the convention of Law (2010) is followed. By eliminating the continuity equation (2.1) from Eq. (2.32), one obtains

$$\rho \frac{\mathrm{D}h^s}{\mathrm{D}t} - \nabla \cdot \left(\lambda \nabla T\right) = \frac{\mathrm{D}p}{\mathrm{D}t} + q \,. \tag{2.34}$$

By writing $\mathrm{d}h^s = c_p \mathrm{d}T$ the material derivative can be re-written into

$$\boxed{\rho c_p \frac{\mathrm{D}T}{\mathrm{D}t} - \nabla \cdot \left(\lambda \nabla T\right) = \frac{\mathrm{D}p}{\mathrm{D}t} + q} \tag{2.35}$$

2.1.5 A wave equation for $\ln(p)$

The equation will be re-cast into a formulation for $\ln p$ following Poinsot and Veynante (2005)(p. 425). In a first step, division by $\rho c_p T$ and re-arrangement yields

$$\frac{1}{T}\frac{\mathrm{D}T}{\mathrm{D}t} - \frac{1}{\rho c_p T}\frac{\mathrm{D}p}{\mathrm{D}t} = \frac{1}{\rho c_p T}\left[\nabla\cdot(\lambda\nabla T) + q\right] . \tag{2.36}$$

The material derivative for T can be written as

$$\frac{\mathrm{D}T}{\mathrm{D}t} = \left(\frac{\partial T}{\partial p}\right)_{\rho,\bar{R}}\frac{\mathrm{D}p}{\mathrm{D}t} + \left(\frac{\partial T}{\partial \rho}\right)_{\bar{R},p}\frac{\mathrm{D}p}{\mathrm{D}t} + \left(\frac{\partial T}{\partial \bar{R}}\right)_{p,\rho}\frac{\mathrm{D}\bar{R}}{\mathrm{D}t} \tag{2.37}$$

and with the ideal gas law (2.14) the total derivative is written as

$$\frac{\mathrm{D}T}{\mathrm{D}t} = \frac{1}{\rho\bar{R}}\frac{\mathrm{D}p}{\mathrm{D}t} - \frac{p\bar{R}}{(\rho\bar{R})^2}\frac{\mathrm{D}\rho}{\mathrm{D}t} - \frac{p\rho}{(\rho\bar{R})^2}\frac{\mathrm{D}\bar{R}}{\mathrm{D}t} . \tag{2.38}$$

The ideal gas law (2.14) applied again gives

$$\frac{\mathrm{D}T}{\mathrm{D}t} = \frac{1}{\rho\bar{R}}\frac{\mathrm{D}p}{\mathrm{D}t} - \frac{T}{\rho}\frac{\mathrm{D}\rho}{\mathrm{D}t} - \frac{T}{\bar{R}}\frac{\mathrm{D}\bar{R}}{\mathrm{D}t} . \tag{2.39}$$

For the left hand side of Eq. (2.36) one obtains

$$\frac{1}{T}\frac{\mathrm{D}T}{\mathrm{D}t} - \frac{1}{\rho c_p T}\frac{\mathrm{D}p}{\mathrm{D}t} = \frac{1}{p}\frac{\mathrm{D}p}{\mathrm{D}t} - \frac{1}{\rho c_p T}\frac{\mathrm{D}p}{\mathrm{D}t} - \frac{1}{\rho}\frac{\mathrm{D}\rho}{\mathrm{D}t} - \frac{1}{\bar{R}}\frac{\mathrm{D}\bar{R}}{\mathrm{D}t} . \tag{2.40}$$

and re-arrangement yields

$$\frac{1}{T}\frac{\mathrm{D}T}{\mathrm{D}t} - \frac{1}{\rho c_p T}\frac{\mathrm{D}p}{\mathrm{D}t} = \frac{\mathrm{D}p}{\mathrm{D}t}\left[\frac{1}{p} - \frac{1}{\rho c_p T}\right] - \frac{1}{\rho}\frac{\mathrm{D}\rho}{\mathrm{D}t} - \frac{1}{\bar{R}}\frac{\mathrm{D}\bar{R}}{\mathrm{D}t} . \tag{2.41}$$

The coefficients of the first term on the right hand side can be re-written as

$$\frac{1}{p} - \frac{1}{\rho c_p T} = \frac{\rho c_p T - p}{\rho c_p T p} = \frac{\rho c_p T - \rho\bar{R}T}{\rho c_p T p} = \frac{1}{p}\frac{c_p - \bar{R}}{c_p} = \frac{1}{\gamma p} , \tag{2.42}$$

where the isentropic exponent $\gamma = c_p/c_v$ and $c_p = c_v + \bar{R}$ is used. Thus, Equation (2.36) is written as

$$\frac{1}{\gamma p}\frac{\mathrm{D}p}{\mathrm{D}t} - \frac{1}{\rho}\frac{\mathrm{D}\rho}{\mathrm{D}t} - \frac{1}{\bar{R}}\frac{\mathrm{D}\bar{R}}{\mathrm{D}t} = \frac{1}{\rho c_p T}\left[\nabla\cdot(\lambda\nabla T) + q\right] . \tag{2.43}$$

Following Kotake (1975) and using Eq. (2.4) the equation is formulated as

$$\frac{1}{\gamma}\frac{\mathrm{D}\ln(p)}{\mathrm{D}t} + \nabla\cdot\mathrm{u} - \frac{\mathrm{D}\ln(\bar{R})}{\mathrm{D}t} = \frac{1}{\rho c_p T}\left[\nabla\cdot(\lambda\nabla T) + q\right]. \tag{2.44}$$

Taking the material derivative of the previous equation gives the final formulation of the energy equation that is necessary to derive the wave equation

$$\begin{aligned}\frac{\mathrm{D}}{\mathrm{D}t}\left[\frac{1}{\gamma}\frac{\mathrm{D}\ln(p)}{\mathrm{D}t}\right] + \frac{\mathrm{D}}{\mathrm{D}t}\left[\nabla\cdot\mathrm{u}\right] - \frac{\mathrm{D}}{\mathrm{D}t}\left[\frac{\mathrm{D}\ln(\bar{R})}{\mathrm{D}t}\right] = \\ \frac{\mathrm{D}}{\mathrm{D}t}\left[\frac{1}{\rho c_p T}\left[\nabla\cdot(\lambda\nabla T) + q\right]\right].\end{aligned} \tag{2.45}$$

Subtracting Eq. (2.45) from Eq. (2.18)

$$\begin{aligned}\nabla\cdot\left[\frac{c^2}{\gamma}\nabla\ln(p)\right] - \frac{\mathrm{D}}{\mathrm{D}t}\left[\frac{1}{\gamma}\frac{\mathrm{D}\ln(p)}{\mathrm{D}t}\right] = \nabla\cdot\left[\frac{1}{\rho}\nabla\cdot\boldsymbol{\tau}\right] - \frac{\mathrm{D}}{\mathrm{D}t}\left[\frac{\mathrm{D}\ln(\bar{R})}{\mathrm{D}t}\right] \\ -\frac{\mathrm{D}}{\mathrm{D}t}\left[\frac{1}{\rho c_p T}\left[\nabla\cdot(\lambda\nabla T) + q\right]\right] - \nabla\mathrm{u} : \nabla\mathrm{u}.\end{aligned} \tag{2.46}$$

Equation (2.18) contains a term $\nabla\cdot\mathrm{D}\mathrm{u}/\mathrm{D}t$ and Eq. (2.45) a term $\mathrm{D}\left(\nabla\cdot\mathrm{u}\right)/\mathrm{D}t$. These two terms are not equal and instead a computation shows

$$\nabla\cdot\frac{\mathrm{D}\mathrm{u}}{\mathrm{D}t} - \frac{\mathrm{D}\left(\nabla\cdot\mathrm{u}\right)}{\mathrm{D}t} = \nabla\cdot\left(\mathrm{u}\cdot\nabla\mathrm{u}\right) - \mathrm{u}\cdot\nabla\left(\nabla\cdot\mathrm{u}\right) = \nabla\mathrm{u} : \nabla\mathrm{u}. \tag{2.47}$$

According to Kotake (1975), the terms on the right hand side of Eq. (2.46) related to viscosity $\boldsymbol{\tau}$, $\bar{R}$ and temperature T are of smaller order than the terms related to combustion q and velocity $\nabla\mathrm{u}$. In this work, the velocity term is neglected as well and Eq. (2.46) simplifies to

$$\nabla\cdot\left[\frac{c^2}{\gamma}\nabla\ln(p)\right] - \frac{\mathrm{D}}{\mathrm{D}t}\left[\frac{1}{\gamma}\frac{\mathrm{D}\ln(p)}{\mathrm{D}t}\right] = -\frac{\mathrm{D}}{\mathrm{D}t}\left[\frac{1}{\rho c_p T}q\right]. \tag{2.48}$$

If constant γ is assumed, the wave equation in $\ln(p)$ is then written as

$$\boxed{\nabla\cdot\left[c^2\nabla\ln(p)\right] - \frac{\mathrm{D}}{\mathrm{D}t}\left[\frac{\mathrm{D}\ln(p)}{\mathrm{D}t}\right] = -\gamma\frac{\mathrm{D}}{\mathrm{D}t}\left[\frac{1}{\rho c_p T}q\right]} \tag{2.49}$$

2.1.6 Linearization and formulation of wave equation in p

Before performing a linearization, it is assumed that the flow has zero Mach number $\mathrm{Ma} = 0$, which implies $\mathrm{u}_0 = 0$. A discussion by Nicoud et al. (2007)(App. A) suggests that this assumption is valid if the spatial extension of the flame is small compared to the acoustic wavelength – also referred to as an *acoustically compact* flame in the thermoacoustic literature. In physical terms, this implies that a resulting equation is only valid for low frequencies and flames with short flame brushes. However, a study by Nicoud and Wieczorek (2009) suggests that the assumption could be problematic for Mach numbers as low as $\mathrm{Ma} = 0.05$.

For all primitive variables an ansatz in terms of mean quantities $(\cdot)_0$ and fluctuations $(\cdot)_1$ is formulated

$$p = p_0 + \varepsilon p_1 \,, \tag{2.50}$$
$$\rho = \rho_0 + \varepsilon \rho_1 \,, \tag{2.51}$$
$$\mathrm{u} = \varepsilon \mathrm{u}_1 \,, \tag{2.52}$$
$$q = q_0 + \varepsilon q_1 \,, \tag{2.53}$$

where fluctuations of heat capacities are ignored ($\bar{R} = \bar{R}_0$) and $\varepsilon \ll 1$. Furthermore, it is assumed that all mean quantities only depend on space. As a consequence of these assumptions, the material derivative for a fluctuation ϕ_1 simplifies to

$$\frac{\mathrm{D}\phi_1}{\mathrm{D}t} \approx \frac{\partial \phi_1}{\partial t} + \varepsilon \mathrm{u}_1 \cdot \nabla \phi_1 \,, \tag{2.54}$$

and the material derivative for an arbitrary quantity ϕ

$$\frac{\mathrm{D}\phi}{\mathrm{D}t} = \underbrace{\frac{\partial \phi_0}{\partial t}}_{=0} + \varepsilon \left[\frac{\partial \phi_1}{\partial t} + \mathrm{u}_1 \cdot \nabla \phi_0 \right] + O\left(\varepsilon^2\right) \,. \tag{2.55}$$

To prepare, it is demonstrated that $q_0 = 0$ (which is consistent with $\mathrm{u}_0 = 0$), by setting the elliptic temperature term in Eq. (2.35) zero (as done in the previous section) and inserting ansatz (2.50)–(2.53) plus Eq. (2.55)

$$(\rho_0 + \varepsilon \rho_1)\; c_p\, \varepsilon \left[\frac{\partial T_1}{\partial t} + \mathrm{u}_1 \cdot \nabla T_0 \right] = \varepsilon \left[\frac{\partial p_1}{\partial t} + \mathrm{u}_1 \cdot \nabla p_0 \right] + q_0 + \varepsilon q_1 + O\left(\varepsilon^2\right) \,, \tag{2.56}$$

since T_0 and p_0 do not vary in time. Clearly, the only term to zeroth order is

$$\varepsilon^0 : \quad 0 = q_0 \,. \tag{2.57}$$

For the present purposes this is acceptable, since a formulation for the fluctuation quantities is of interest – it does stipulate the absence of any combustion, though (Nicoud et al., 2007, p. 8). To obtain the term of order ε^1 of the $\ln(p)$ equation (2.49) directly, the Gateaux derivative (Ciarlet, 2013) is computed. For the left hand side of Eq. (2.49) this amounts to

$$\begin{aligned} \frac{\mathrm{d}}{\mathrm{d}\varepsilon}\nabla\cdot\left[c^2\nabla\ln\left(p_0+\varepsilon p_1\right)\right] - \frac{\mathrm{d}}{\mathrm{d}\varepsilon}\frac{\mathrm{D}}{\mathrm{D}t}\left[\frac{\mathrm{D}\ln\left(p_0+\varepsilon p_1\right)}{\mathrm{D}t}\right] = \\ \nabla\cdot\left[c^2\nabla\left(\frac{p_1}{p_0+\varepsilon p_1}\right)\right] - \frac{\mathrm{D}^2}{\mathrm{D}t^2}\left[\frac{p_1}{p_0+\varepsilon p_1}\right], \end{aligned} \tag{2.58}$$

and setting $\varepsilon = 0$ yields

$$\nabla\cdot\left[c^2\nabla\left(\frac{p_1}{p_0}\right)\right] - \frac{\mathrm{D}^2}{\mathrm{D}t^2}\left[\frac{p_1}{p_0}\right] . \tag{2.59}$$

Likewise, one obtains for the right hand side of equation (2.49)

$$-\gamma\frac{\mathrm{D}}{\mathrm{D}t}\left[\frac{\bar{R}}{c_P}\left(\frac{q_1}{p_0}-\frac{q_0}{p_0^2}p_1\right)\right] . \tag{2.60}$$

The second term is zero, since $q_0 = 0$ and thus the formulation is

$$\nabla\cdot\left[c^2\nabla\left(\frac{p_1}{p_0}\right)\right] - \frac{\mathrm{D}^2}{\mathrm{D}t^2}\left[\frac{p_1}{p_0}\right] = -\gamma\frac{\mathrm{D}}{\mathrm{D}t}\left[\frac{\bar{R}}{c_P}q_1\right] \tag{2.61}$$

Technically speaking, in this equation only the $\ln(p)$ terms have been linearized – not yet the material derivatives. Hence, it is an incomplete linearization but tedious algebra can be avoided by first formulating another necessary assumption: For deflagration flames the isobaric assumption (Law, 2010; Poinsot and Veynante, 2005) is valid. By this assumption, the spatial dependence of p_0 is neglected. Inserting Eq. (2.54) into Eq. (2.61) and keeping only zeroth order terms[1] yields

$$\nabla\cdot\left(c^2\nabla p_1\right) - \frac{\partial^2 p_1}{\partial t^2} = -\frac{\partial}{\partial t}\left[\frac{\gamma\bar{R}}{c_P}q_1\right] , \tag{2.62}$$

[1] Due to the incomplete linearization from before, zeroth order terms where the material derivative has been re-written correspond to first order terms globally.

where the entire equation has been multiplied by the constant p_0. The result can be re-written with the identity

$$\frac{\gamma \bar{R}}{c_p} = \frac{\bar{R}}{c_v} = \frac{c_p - c_v}{c_v} = \gamma - 1 \tag{2.63}$$

into

$$\boxed{\frac{\partial^2 p_1}{\partial t^2} - \nabla \cdot \left(c^2 \nabla p_1 \right) = -(\gamma - 1) \frac{\partial q_1}{\partial t}} \tag{2.64}$$

the time domain formulation of the thermoacoustic Helmholtz equation, as commonly encountered in the literature. To summarize, all assumptions that have been employed are:

- Linear dependence of stress tensor $\boldsymbol{\tau}$ on p and u (p. 31)
- External body forces are neglected $\mathrm{f}_i = 0$ (p. 31)
- Ideal gas law $p = \rho \bar{R} T$ (p. 31)
- Fourier's law for heat conduction (p. 32)
- No heating due to radiation (p. 32)
- Dufour effect neglected (p. 32)
- Low speed subsonic flow, where viscous heating can be neglected (p. 33)
- Equal heat capacities $c_{p,i} = c_p$ for all species (p. 34)
- Neglection of viscosity $\boldsymbol{\tau}, \bar{R}$ and T terms following an order of magnitude analysis due to Kotake (1975) (p. 36)
- Neglection of the velocity term $\nabla \mathrm{u} : \nabla \mathrm{u}$ (p. 36)
- Constant heat capacity ratio γ (p. 36)
- Zero Mach number flow $\mathrm{Ma} = 0$ (p. 37)
- Acoustic perturbations are small (p. 37)
- Fluctuations in heat capacities are neglected (p. 37)
- Mean quantities only depend on space (p. 37)
- Isobaric assumption for deflagration flames (p. 38)

2.1.7 Acoustic energy balance equations and Rayleigh's criterion

The simplified balance equations from the previous sections can be used to formulate a balance equation for a fluctuation energy, where the source term appears in the Rayleigh criterion Eq. (1.1). In a first step, the inviscid ($\boldsymbol{\tau} = 0$) momentum balance (2.13) is linearized under the zero Mach number assumption of Sec. 2.1.6 to give

$$(\rho_0 + \varepsilon\rho_1)\,\frac{\mathrm{D}\mathrm{u}_1}{\mathrm{D}t} = -\nabla\,(p_0 + \varepsilon p_1)\;, \tag{2.65}$$

and employing Eq. (2.54) gives

$$(\rho_0 + \varepsilon\rho_1)\,\varepsilon\frac{\partial \mathrm{u}_1}{\partial t} = -\nabla\,(p_0 + \varepsilon p_1) + O\left(\varepsilon^2\right)\;. \tag{2.66}$$

Sorting by powers of ε and neglecting terms ε^2 or higher yields

$$\varepsilon^0: \qquad 0 = -\nabla p_0\,, \tag{2.67}$$

$$\varepsilon^1: \quad \rho_0\frac{\partial \mathrm{u}_1}{\partial t} = -\nabla p_1\,. \tag{2.68}$$

Taking the scalar product of Eq. (2.68) with u_1 gives

$$\frac{\partial}{\partial t}\left[\frac{1}{2}\rho_0\mathrm{u}_1^2\right] = -\nabla p_1\cdot\mathrm{u}_1\,. \tag{2.69}$$

In a second step, Equation (2.44) is simplified by neglecting variations in heat capacities $\bar{R} = \bar{R}_0$ and the elliptic temperature term "$\nabla\cdot(\lambda\nabla T)$" – as before – to give

$$\frac{1}{\gamma}\frac{\mathrm{D}\ln(p)}{\mathrm{D}t} + \nabla\cdot\mathrm{u} = \frac{1}{\rho c_p T}q\,. \tag{2.70}$$

As before, the Gateaux derivative to linearize the $\ln(p)$ term gives

$$\frac{1}{\gamma p_0}\frac{\mathrm{D}p}{\mathrm{D}t} + \nabla\cdot\mathrm{u}_1 = \frac{\bar{R}}{c_p}q_1\,, \tag{2.71}$$

whereby constant p_0 is assumed. Keeping only terms of lowest order in ε in the material derivatives results in

$$\frac{1}{\gamma p_0}\frac{\partial p_1}{\partial t} + \nabla\cdot\mathrm{u}_1 = \frac{(\gamma-1)}{\gamma p_0}q_1\,. \tag{2.72}$$

After multiplication with p_1 and using $\gamma p_0 = \rho_0 c_0^2$ one obtains the second necessary component

$$\frac{\partial}{\partial t}\left[\frac{1}{2}\rho_0 c_0^2 p_1^2\right] + \nabla \cdot \mathrm{u}_1 p_1 = \frac{(\gamma-1)}{\gamma p_0} q_1 p_1 \,. \tag{2.73}$$

Adding Eq. (2.69) and Eq. (2.73) gives a balance equation for an acoustic fluctuation energy e_1

$$\boxed{\frac{\partial}{\partial t}\left(e_1\right) + \nabla \cdot \left(\mathrm{u}_1 p_1\right) = \frac{(\gamma-1)}{\gamma p_0} q_1 p_1} \tag{2.74}$$

with the definition

$$e_1 = \frac{1}{2}\frac{p_1^2}{\rho_0 c_0^2} + \frac{1}{2}\rho_0 {\mathrm{u}_1}^2 \,. \tag{2.75}$$

The source term on the right hand side of Eq. (2.74) appears in the Rayleigh criterion, which was introduced in Chap. 1.2.1. Chu (1965) and Nicoud and Poinsot (2005) derived a more general formulation for a fluctuation energy.

2.2 Formulation in frequency space and closure of the equation

If the fluctuations are assumed to oscillate harmonically in time

$$p_1 = \hat{p}\, e^{\mathrm{i}\omega t} \,, \tag{2.76}$$

$$q_1 = \hat{q}\, e^{\mathrm{i}\omega t} \,, \tag{2.77}$$

the frequency-domain formulation for Eq. (2.64) is

$$\boxed{\nabla \cdot \left(c^2 \nabla \hat{p}\right) + \omega^2 \hat{p} = -\left(\gamma - 1\right)\hat{q}} \tag{2.78}$$

Equation (2.78) is the basis of the stability analysis conducted in this thesis. Solutions are given in the form of the eigenvalues ω and eigenfunctions $\hat{p}$. Together, these form eigenpairs $(\omega, \hat{p})$. The choice of the fluctuation quantities Eq. (2.76)–(2.77) corresponds to the definition of the Fourier transformation as

$$\hat{f}\left(\omega\right) \equiv \mathcal{F}\left\{f\right\} = \frac{1}{\sqrt{2\pi}} \int_{-\infty}^{+\infty} f\left(t\right) e^{-\mathrm{i}\omega t}\, \mathrm{d}t \,. \tag{2.79}$$

The eigenvalue is a complex number $\omega \in \mathbb{C}$ and hence,

$$e^{-\mathrm{i}\omega t} = e^{\mathrm{i}\omega_\mathrm{R} t}\, e^{-\omega_\mathrm{I} t}\,, \tag{2.80}$$

where ω_R and ω_I are the real and imaginary parts of ω, respectively. The real part of ω corresponds to the angular frequency of oscillation with unit $1/s$. The oscillation frequency is defined as $f = \mathrm{Real}\,(\omega)\,/2\pi$ with unit Hz. Equation (2.80) states that growth of a mode $(\omega, \hat{p})$ in time is given for

$$\mathrm{Imag}\,(\omega) < 0\,. \tag{2.81}$$

Conversely, damping is given if $\mathrm{Imag}\,(\omega) > 0$. Suitable boundary conditions and expressions for the heat-release term in the form $\hat{q} = \hat{q}\,(\omega, \hat{p})$ to close the equation are discussed next.

2.2.1 Closure of the heat-release rate $\hat{q}$

The heat-release response $\hat{q}$ can be linked to an upstream velocity fluctuation at a reference location $\hat{\boldsymbol{u}}|_\mathrm{ref}$ in a reference direction $\boldsymbol{n}|_\mathrm{ref}$ via a flame transfer function (FTF) $\mathcal{F}\,(\omega)$

$$\hat{q} = \frac{Q_0}{u_0 V_\mathrm{F}} \mathcal{F}\,(\omega)\; \hat{\boldsymbol{u}}|_\mathrm{ref} \cdot \boldsymbol{n}|_\mathrm{ref}\;. \tag{2.82}$$

Here, Q_0 is the mean global heat-release, u_0 the mean flow at the reference position and V_F the volume of the heat-release zone. FTFs can be obtained via measurements (Durox et al., 2009), large-eddy simulations (Giauque et al., 2005) or from analytic considerations (Ducruix et al., 2000; Schuller et al., 2003). A very simple time-delay model was suggested by Crocco and Cheng (1956)

$$\mathcal{F}\,(\omega) = n e^{-\mathrm{i}\omega\tau}\,, \tag{2.83}$$

where n is the so-called interaction index describing the gain of the flame response, and τ is a time delay – hence the name: n–τ model. Crocco's model is simple but frequently employed as a generic flame model in thermoacoustic studies (McManus et al., 1993; Dowling and Morgans, 2005; Huang and Yang, 2009; Hield et al., 2009; Courtine et al., 2014).

Expression (2.82) contains implicitly two assumptions: i) $\hat{q}$ depends on an upstream velocity fluctuation and ii) that the dependence is linear. Kinematically stabilized flames, as considered in this work, are sensitive to upstream velocity fluctuations. This is in contrast to flames stabilized by autoignition, which are predominantly sensitive to upstream temperature

fluctuations (Bothien et al., 2019a). The review article by Schuller et al. (2020) collects the current state of scientific knowledge on kinematically stabilized flames. If finite amplitude effects are to be considered, the linear dependence on $\hat{u}$ is replaced with a dependence on the amplitude $|\hat{u}|$, see Stow and Dowling (2004); Noiray et al. (2008). However, such a formulation introduces a nonlinear dependence on the eigenvector. The work in this thesis does not consider this type of problem.

In order to close the problem, the velocity fluctuation $\hat{\boldsymbol{u}}|_{\mathrm{ref}}$ in Eq. (2.82) can be expressed via the linearized momentum balance (2.68) as

$$-\mathrm{i}\omega\hat{\boldsymbol{u}} = \frac{1}{\rho_0}\nabla\hat{p}\,. \tag{2.84}$$

By closing Eq. (2.78) with Eqs. (2.82) and (2.84) the eigenvalue problem is expressed only in the unknown eigenpairs $(\omega, \hat{p})$

$$\boxed{\nabla\cdot\left(c^2\,\nabla\hat{p}\right) + \omega^2\hat{p} = (\gamma-1)\,\frac{Q_0}{\rho_0 u_0 V_{\mathrm{F}}}\mathcal{F}\,(\omega)\,\nabla\hat{p}|_{\mathrm{ref}}\cdot\boldsymbol{n}|_{\mathrm{ref}}} \tag{2.85}$$

Equation (2.85) is a nonlinear eigenvalue problem. The problem has a nonlinear dependence on the eigenvalue ω and a linear dependence on the eigenvector $\hat{p}$. Then the problem is commonly abbreviated into operator form as

$$\boxed{\mathcal{L}\,(\omega)\,\hat{p} = 0} \tag{2.86}$$

The operator $\mathcal{L}$ contains the equation and its boundary conditions.

2.2.2 Boundary conditions

Boundary conditions for the acoustic problem can be expressed by means of the specific impedance Z (Rienstra and Hirschberg, 2004), which is the ratio of acoustic and velocity fluctuations at a boundary

$$Z = \frac{\hat{p}}{\rho c\,\hat{\mathrm{u}}\cdot\mathrm{n}_{\mathrm{BC}}}\,, \tag{2.87}$$

here n_{BC} specifies the unit normal vector pointing outward at the boundary surface. The specific impedance is either a complex scalar or a function of the eigenvalue $Z : \mathbb{C} \to \mathbb{C}$. Using the linearized momentum balance (2.84), the impedance (2.87) can be expressed as a Robin-type boundary condition

$$Z\,c\,\nabla\hat{p}\cdot\mathrm{n}_{\mathrm{BC}} - \mathrm{i}\omega\hat{p} = 0\,. \tag{2.88}$$

Table 2.1: Acoustic boundary conditions for the thermoacoustic Helmholtz equation.

Description	Impedance	Physics
Anechoic	$Z = 1$	-
Pressure release	$Z = 0$	$\hat{p} = 0$
Rigid wall	$Z = \infty$	$\nabla\hat{p} \cdot \mathrm{n}_{\mathrm{BC}} = 0$

Table 2.1 collects three important cases for thermoacoustics. A detailed discussion for thermoacoustics can be found in Silva et al. (2014). A rigid wall boundary condition is also referred to as *sound hard* and it constitutes a homogeneous Neumann boundary condition. This is the most common boundary condition since it is prescribed on all combustion chamber walls and it will enter the variational formulation as a natural boundary condition. Non-pressurized combustion chambers in academia are usually open to the atmosphere at the outlet. Hence, a pressure release or pressure node $\hat{p} = 0$ is prescribed there. In addition, academic model combustors are commonly fed with reactant mixtures from small diameter pipes. Hence, there are chocked or close to chocked conditions and sound hard boundary conditions are prescribed there as well.

Anechoic boundary conditions $Z = 1$ have played a major role in a recent series of experiments and theoretical analysis related to intrinsic thermoacoustic modes. An ideal anechoic termination eliminates all acoustic resonance frequencies of a geometry – prohibiting any thermoacoustic instabilities related to these resonance frequencies. However, a series of authors (Hoeijmakers, 2014; Hoeijmakers et al., 2014; Emmert et al., 2015; Courtine et al., 2015; Silva et al., 2015, 2017b; Ghani et al., 2019) showed that a combustor with anechoic terminations can still exhibit thermoacoustic instabilities. The research revealed that an instability can be triggered by a purely upstream travelling pressure wave emitted from a flame. Such an instability is independent of the acoustic properties of the combustor and hence *intrinsic* to the flame. Article 3 focuses on these modes extensively in an annular combustion chamber.

In industrial applications, or when using materials or components that are known to exhibit complex scattering behaviour, impedances are measured or modelled to accurately describe the properties of the considered components. Then the impedance is a function of ω and an additional source of nonlinearity for the NLEVP in Eq. (2.85).

2.3 Variational formulation

The variational formulation for Eq. (2.78) is derived in this section. The closure (2.82) is inserted later for reasons of readability. In a first step, the function spaces are defined, then the variational formulation is derived and finally a finite-element ansatz formulated to obtain the discrete nonlinear eigenvalue problem. The discretization goes back to Nicoud et al. (2007).

2.3.1 Preparation

The computation domain Ω, i.e. the combustor without the boundaries, is an open subset of $\mathbb{R}^N$ with piecewise smooth boundary. The $L^2(\Omega)$ scalar product is defined as

$$(\hat{p}, v)_{L_2} := \int_\Omega \hat{p}(x)\, v(x)^* \, \mathrm{d}x\,, \tag{2.89}$$

which consists of all functions $\hat{p}$ and v that are square-integrable in Ω. Here, the asterix $(\cdot)^*$ denotes the complex-conjugate. Equipped with its natural norm

$$||\hat{p}||_{L^2} := \sqrt{(\hat{p}, \hat{p})_{L_2}}\,, \tag{2.90}$$

the space $L^2(\Omega)$ becomes a Banach space, when the norm is finite $||\hat{p}||_{L^2} < \infty$. For the thermoacoustic Helmholtz equation, only the Sobolev-space $W^{1,2}$ is relevant to derive the weak formulation and this space is constructed using the L^2 spaces. The space $W^{1,2}$, is equipped with the scalar product

$$(v, \hat{p})_1 = (v, \hat{p}) + (\nabla v, \nabla \hat{p}) = \int_\Omega \left(v\hat{p}^* + \sum_{k=1}^{N} \frac{\partial v}{\partial x_k} \frac{\partial \hat{p}^*}{\partial x_k} \right) \mathrm{d}x\,, \tag{2.91}$$

and norm

$$||\hat{p}||^2_{W^{1,2}} = ||\hat{p}||^2_2 + ||\nabla \hat{p}||^2_2\,. \tag{2.92}$$

With the norm (2.92) $W^{1,2}$ becomes a Hilbert space denoted by H^1. The norm requires that $\hat{p}^2$ and $|\nabla \hat{p}|^2$ have finite integrals over Ω (Logg et al., 2012). Using the finite-element method a finite-dimensional vector space V_h will be constructed s.t. $V_h \subset V = H^1$, where H^1 is the vector space of the weak formulation.

2.3.2 Weak formulation

A variational formulation for Eq. (2.78) is derived by multiplying the equations with a test function v from the right and integrating over the computational domain Ω to obtain

$$\int_\Omega \nabla \cdot \left(c^2 \nabla \hat{p}\right) v^* \,\mathrm{d}x + \int_\Omega \omega^2 \hat{p} v^* \,\mathrm{d}x = -i\omega\,(\gamma - 1) \int_\Omega \hat{q}\, v^* \,\mathrm{d}x\,. \tag{2.93}$$

Setting $\mathrm{w} = c^2 \nabla \hat{p}$ the elliptic term in Eq. (2.93) can be recast with the identity

$$\nabla \cdot (\phi \mathrm{w}) = \phi\,(\nabla \cdot \mathrm{w}) + (\nabla \phi) \cdot \mathrm{w}\,, \tag{2.94}$$

which can be re-arranged into

$$\phi\,(\nabla \cdot \mathrm{w}) = \nabla \cdot (\phi \mathrm{w}) - (\nabla \phi) \cdot \mathrm{w}\,. \tag{2.95}$$

Replacing the elliptic term leads to

$$\begin{aligned}\int_\Omega \nabla \cdot \left(v^*\, c^2 \nabla \hat{p}\right) \,\mathrm{d}x - \int_\Omega \nabla v^* \cdot c^2 \nabla \hat{p} \,\mathrm{d}x + \omega^2 \int_\Omega \hat{p}\, v^* \,\mathrm{d}x = \\ -i\omega\,(\gamma - 1) \int_\Omega \hat{q}\, v^* \,\mathrm{d}x\,,\end{aligned} \tag{2.96}$$

and applying the divergence theorem to the left hand side

$$\begin{aligned}\int_{\partial\Omega} v^*\, c^2 \nabla \hat{p} \cdot \mathrm{n} \,\mathrm{d}s - \int_\Omega \nabla v^* \cdot c^2 \nabla \hat{p} \,\mathrm{d}x + \omega^2 \int_\Omega \hat{p}\, v^* \,\mathrm{d}x = \\ -i\omega\,(\gamma - 1) \int_\Omega \hat{q}\, v^* \,\mathrm{d}x\,,\end{aligned} \tag{2.97}$$

gives a formulation with lowered regularity requirements on the functions. The variational problem then reads

$$\textit{Find } \omega \in \mathbb{C} \textit{ and } \hat{p} \in V \textit{ such that} \tag{2.98}$$

$$\int_{\partial\Omega} c^2 \nabla \hat{p} \cdot \mathrm{n}\, v^* \,\mathrm{d}x - \int_\Omega c^2 \nabla \hat{p} \cdot \nabla v^* \,\mathrm{d}x + \omega^2 \int_\Omega \hat{p}\, v^* \,\mathrm{d}x = -\,\mathrm{i}\omega\,(\gamma - 1) \int_\Omega \hat{q}\, v^* \,\mathrm{d}x$$

$$\textit{holds for all } v^* \in \hat{V},$$

where $V = \hat{V}$ and

$$V = \left\{ w \in H^1(\Omega) : w = 0 \;\text{ on }\; \Gamma_0 \right\}. \tag{2.99}$$

The boundaries Γ_0 are all the boundaries where pressure nodes $\hat{p} = 0$ are prescribed. If the closure (2.82) for $\hat{q}$ is employed, the right hand side of Eq. (2.98) reads

$$-\mathrm{i}\omega\,(\gamma-1)\int_\Omega \hat{q}\,v^*\,\mathrm{d}x = (\gamma-1)\,\frac{Q_0}{\rho_0 u_0 V_\mathrm{F}}\int_\Omega \mathcal{F}\,(\omega)\,\nabla\hat{p}|_\mathrm{ref}\cdot\boldsymbol{n}|_\mathrm{ref}\,v^*\,\mathrm{d}x\,. \quad (2.100)$$

Boundary conditions enter the variational problem (2.98) via the surface integral term, where impedances can be prescribed. The surface integral is split into the different segments and individual, potentially ω-dependent impedance, are prescribed.

2.3.3 Discretization of variational formulation

The weak formulation can be discretized using the finite element method. A discrete space $V_h \subset V$ is chosen in which a solution is sought.

$$\textit{Find } \omega_h \in \mathbb{C} \textit{ and } \hat{p}_h \in V_h \textit{ such that} \quad (2.101)$$

$$\int_{\partial\Omega} c^2\nabla\hat{p}_h\cdot\mathrm{n}\,v_h^*\,\mathrm{d}x - \int_\Omega c^2\nabla\hat{p}_h\cdot\nabla v_h^*\,\mathrm{d}x + \omega^2\int_\Omega \hat{p}\,v_h^*\,\mathrm{d}x = -\mathrm{i}\omega\,(\gamma-1)\int_\Omega \hat{q}_h v_h^*\,\mathrm{d}x \quad (2.102)$$

$$\textit{holds for all } v_h^* \in \hat{V}_h,$$

The function $\hat{p}_h$ is the finite dimensional approximation of $\hat{p}$ – likewise for $\hat{q}_h$ and ω_h. After this section the subscript "h" is dropped for brevity. For V_h and $\hat{V}_h$ the space of all piecewise linear functions on a mesh of tetrahedra is chosen. For the function $\hat{p}_h$ a finite dimensional expansion is chosen

$$\hat{p}_h = \sum_{j=1}^{d} P_j\psi_j\,, \quad (2.103)$$

where the shape functions ψ_j have local support and d is the dimension of the space, which is identical to the degrees of freedom (DOF). The P_j are expansion coefficients which are to be computed. The resulting problem is written for the left hand side of Eq. (2.101) as

$$-\sum_{\mathcal{T}\in\mathbb{T}}\int_\mathcal{T} c^2\nabla\psi_i\cdot\nabla\psi_j^*\,P_j\,\mathrm{d}x + \sum_{\mathcal{S}\in\mathbb{S}}\int_\mathcal{S} c^2\psi_i^*\nabla\psi_j\cdot\mathrm{n}\,P_j\,\mathrm{d}x + \omega^2\sum_{\mathcal{T}\in\mathbb{T}}\int_\mathcal{T}\psi_i^*\psi_j\,P_j\,\mathrm{d}x\,, \quad (2.104)$$

and the right hand side as

$$(\gamma - 1)\,\frac{Q_0}{\rho_0 u_0 V_\mathrm{F}} \sum_{\mathcal{T}\in\mathbb{T}} \int_{\mathcal{T}} \frac{1}{\rho_0} \mathcal{F}\,(\omega)\,\psi_i^* \nabla\psi_j|_{\mathrm{x_{local}}} \cdot \mathrm{n_{ref}}\, P_j \mathrm{d}x\,, \tag{2.105}$$

where Ω and its surface $\partial\Omega$ have been segmented into tetrahedra $\mathbb{T}$ and triangles $\mathbb{S}$, respectively. Care is taken that the segmentation conserves underlying symmetries. The actual numerical discretization is performed in the package developed by Mensah and Orchini (2021) and its predecessor (Mensah et al., 2018). The latter of which this author was a co-developer. A detailed description of the solver-specific implementation can be found in the thesis of Mensah (2019).

With p as the vector of the expansion coefficients P_j, then the discretized problem reads in a general form

$$\left[\mathrm{K} + \omega \sum_i f_i\,(\omega)\,\mathrm{C}_i + \omega^2 \mathrm{M} + \sum_i \mathcal{F}_i\,(\omega)\,\mathrm{Q}_i\right] \mathrm{p} = 0\,, \tag{2.106}$$

which is the discrete nonlinear eigenvalue problem. Matrix K is the stiffness matrix, C_i are matrices corresponding to boundary conditions with prescribed impedances $f_i\,(\omega)$, M is the mass matrix and Q is the matrix corresponding a heat-release effect $\mathcal{F}_i\,(\omega)$ – multiple flames are possible. All constant coefficients have been absorbed into the discretization matrices. In abbreviated form, the problem is written as

$$\boxed{\mathrm{L}\,(\omega)\,\mathrm{p} = 0\,,\quad \mathrm{L} \in \mathbb{C}^{d\times d}} \tag{2.107}$$

Chapter 3

Fundamentals II – Nonlinear Eigenvalue Problems

In the previous chapter the thermoacoustic Helmholtz equation was derived and subsequently formulated as a nonlinear eigenvalue problem, or short NLEVP, which reads

$$\boxed{\mathcal{L}(\omega)\,\hat{p} = 0\,,\quad \hat{p} \neq 0} \tag{3.1}$$

The problem always has homogeneous boundary conditions. These can be prescribed either in the form of a velocity node ($\nabla\hat{p} \cdot \mathrm{n} = 0$), pressure node ($\hat{p} = 0$) or as an impedance.

Outside of thermoacoustics, nonlinear eigenvalue problems arise in a variety of disciplines, including: stability analysis of vibrational systems (Voss, 2002), engineering of electromagnetic waveguides (Jorkowski and Schuhmann, 2020) and stability analysis of delay differential equations (Meerbergen et al., 2013). For more examples see Chap. 2 in Effenberger (2013). A review by Mehrmann and Voss (2004) focuses on NLEVPs from the perspective of industrial applications and solution algorithms. A collection of example problems to test solution algorithms is published in Betcke et al. (2013).

The purpose of this chapter is to review and collect a select few mathematical properties of NLEVPs that have implications for practical thermoacoustic problems. A comprehensive review on NLEVPs can be found in Güttel and Tisseur (2017). The problem is defined in Sec. 3.1 and basic properties are reviewed in Sec. 3.2. Section 3.3 elaborates on eigenvalue de-

generacy and the overlapping concept of a derogatory eigenvalue. In Sec. 3.4 a solution strategy employed in Article 2 is presented from a so-called filtering perspective.

3.1 Definitions, basic assumptions and selected properties

Equation (3.1) expresses that the linear operator $\mathcal{L}$ maps the eigenpairs $(\omega, \hat{p})$ into the null space. Here, $\mathcal{L} : \mathbb{C} \times V \to V$, where V is a suitable Sobolev space. The set of all eigenvalues forms the spectrum $\sigma \in \Omega \subset \mathbb{C}$. The complementary set is the resolvent set $\rho = \Omega \setminus \sigma$. Importantly, for an arbitrary $z \neq \omega$ the operator $\mathcal{L}(z)$ is invertible. The argument z in $\mathcal{L}(z)$ denotes that the operator is parameter-dependent. Thus, the only solution to the problem

$$\mathcal{L}(z)\,\hat{h} = 0\,, \quad z \neq \omega\,, \tag{3.2}$$

is $\hat{h} = 0$. Only at eigenvalues ω the inverse $\mathcal{L}^{-1}$ does not exist. Linear eigenvalue problems

$$\mathcal{A}\hat{p} = \omega\hat{p}\,, \quad \hat{p} \neq 0\,, \tag{3.3}$$

are a special case of Eq. (3.1) if they are re-cast into the form

$$(\mathcal{A} - \omega\mathcal{I})\,\hat{p} = 0\,, \tag{3.4}$$

where $\mathcal{I}$ is the identity operator from the same space as the linear operator $\mathcal{A}$. If the differential operator $\mathcal{L}$ is discretized, the problem is denoted as

$$\mathrm{L}(\omega)\,\mathrm{p} = 0\,, \quad \mathrm{L} \in \mathbb{C}^{d\times d}\,, \quad \mathrm{p} \in \mathbb{C}^{d}\,. \tag{3.5}$$

where d are the degrees of freedom in the chosen discretization method. Most of the theory in this chapter focuses on discrete NLEVPs (3.5), but the theory of symmetry groups in the Draft Article 8 is valid for discrete and continuous formulations.

Throughout this chapter and this thesis, $\mathcal{L}$ is assumed to be a Fredholm operator of index 0. The discrete equivalent of this condition is that L is non-singular, i.e. $\det \mathrm{L}(z) \neq 0$ for all $z \in \mathbb{C}$. For a singular operator the resolvent set is empty.

$\mathcal{L}$ is also assumed to have an analytic dependence on z in a simply connected domain surrounding any eigenvalue ω. In this thesis this condition is necessary since contour integration in Article 2, and also featured in Sec. 3.4, is applied. Contour integration due to Beyn (2012) employs Cauchy's theorem which requires such an analytic dependence.

3.2 Basic properties of NLEVPs and implications for solution algorithms

The entries of NLEVPs can be rational, polynomial or any other arbitrary functions. Thus, a problem such as

$$\mathrm{L}(\omega)\,\mathrm{p} = \begin{pmatrix} \sin(\omega) & 0 \\ 0 & \cos(\omega) \end{pmatrix} \mathrm{p} = 0\,, \tag{3.6}$$

has countably infinitely many eigenvalues

$$\omega_k^0 = \pi k\,, \quad \text{and} \quad \omega_k^1 = \pi k - \frac{\pi}{2} \quad k \in \mathbb{Z}\,, \tag{3.7}$$

and an eigenvector for all ω_k^0 eigenvalues is

$$\mathrm{p}_k = \begin{pmatrix} 1 \\ 0 \end{pmatrix}. \tag{3.8}$$

Hence, all eigenvectors to ω_k^0 are identical. These two features are both in stark contrast to linear eigenvalue problems, where at most $d = \dim \mathrm{L}$ distinct eigenvalues are possible and all eigenvectors are linearly independent. These properties alone make the numerical solution difficult. Linear problems have a wealth of methods (Saad, 2011) that can exploit the finiteness of the number of eigenvalues and the orthogonality of eigenvectors. One example is the implicitly restarted Arnoldi method (Lehoucq et al., 1998), which is used in the linear eigenvalue solver of SCIPY (Virtanen et al., 2020).

The thermoacoustic eigenvalue problem has a general structure, as formulated in Eq. (2.106), as

$$\left[\mathrm{K} + \omega \sum_i f_i(\omega)\,\mathrm{C}_i + \omega^2 \mathrm{M} + \sum_i \mathcal{F}_i(\omega)\,\mathrm{Q}_i\right] \mathrm{p} = 0\,, \tag{3.9}$$

The three sources of nonlinearities are the boundary conditions, expressed by the coefficient functions $f_i(\omega)$, the quadratic nonlinearity ω^2 due to the time derivative of the original wave equation, and the flame terms $\mathcal{F}_i(\omega)$. The quadratic nonlinearity can simply be removed via doubling of the system size by introducing a vector

$$\hat{\mathrm{p}} = \begin{pmatrix} \mathrm{p} \\ \omega \mathrm{p} \end{pmatrix}, \tag{3.10}$$

to re-write the problem as

$$\begin{bmatrix} 0 & -\mathrm{I} \\ \mathrm{K} + \sum_i \mathcal{F}_i(\omega)\,\mathrm{Q}_i & \sum_i f_i(\omega)\,\mathrm{C}_i \end{bmatrix} \begin{bmatrix} \mathrm{p} \\ \omega\mathrm{p} \end{bmatrix} = -\omega \begin{bmatrix} \mathrm{I} & 0 \\ 0 & \mathrm{M} \end{bmatrix} \begin{bmatrix} \mathrm{p} \\ \omega\mathrm{p} \end{bmatrix}, \tag{3.11}$$

which has the form of generalized linear eigenvalue problem if the values for ω in $f_i(\omega)$ and $\mathcal{F}_i(\omega)$ are fixed. This strategy was used by Nicoud et al. (2007) to formulate a fixed-point algorithm to solve the problem iteratively. In Article 4 shortcomings of this fixed-point method are detailed and better solution algorithms, so-called Householder iterations, are proposed.

The nonlinearities in $f_i(\omega)$ and $\mathcal{F}_i(\omega)$ are more difficult, since these can involve data from measurements. It is possible to expand these nonlinearities in the form of rational functions, see the discussion in Sec. 6 of Güttel and Tisseur (2017). However, such an expansion can incur *spurious* modes, which are defined as eigenvalues of an approximation $\tilde{\mathrm{L}}(\omega) \approx \mathrm{L}(\omega)$, which are not eigenvalues of the original problem $\mathrm{L}(\omega)$ (Güttel and Tisseur, 2017).

3.3 Classification of eigenvalues

Eigenvalues ω of operators $\mathcal{L}$ and L can be classified by their multiplicities. In the finite dimensional case the definitions are standard and addressed first. In addition, the terms *derogatory* and *non-derogatory* are put into context. In the continuous case, the geometric multiplicity is implied by properties of the governing symmetry groups as detailed in Draft Article 8. For completeness, an algebraic multiplicity for operators is defined as well.

3.3.1 Algebraic and geometric multiplicity in finite dimensions

The *algebraic multiplicity* of an eigenvalue is defined as the highest integer $\mathfrak{m}_a$ for which it holds

$$\frac{\partial^{\mathfrak{m}_a - 1}}{\partial \omega^{\mathfrak{m}_a - 1}} \det \mathrm{L}(\omega) = 0 \quad \text{and} \quad \frac{\partial^{\mathfrak{m}_a}}{\partial \omega^{\mathfrak{m}_a}} \det \mathrm{L}(\omega) \neq 0, \tag{3.12}$$

i.e. the order of the pole of $\det \mathrm{L}(\omega)$ at an eigenvalue ω. The *geometric multiplicity* is defined as the dimension of the null space of the eigenvalue

$$\mathfrak{m}_g = \dim\left[\operatorname{null} \mathrm{L}(\omega)\right]. \tag{3.13}$$

The algebraic multiplicity bounds the geometric multiplicity from above

$$\mathfrak{m}_a \geq \mathfrak{m}_g, \tag{3.14}$$

which is well-known for the linear case and proven by Szyld and Xue (2014) for the nonlinear case.

3.3.2 Algebraic multiplicity for continuous operators

For linear operators $\mathcal{L}$ the geometric multiplicity $\mathfrak{m}_g$ is also defined as the dimension of the null space as in Eq. (3.13) as

$$\mathfrak{m}_g = \dim\left[\operatorname{null}\mathcal{L}\left(\omega\right)\right], \tag{3.15}$$

and it is a major subject of Draft Article 8 to relate $\mathfrak{m}_g$ to the properties of the symmetry group of $\mathcal{L}$. For general continuous operators $\mathfrak{m}_g$ is not necessarily finite, but for the Fredholm operators in this thesis it is. In contrast, an algebraic multiplicity cannot rely on the determinant operation as required in Eq. (3.12). The book by López-Gómez and Mora-Corral (2007) considers algebraic multiplicities for linear operators in depth.

To give an idea, consider the operator $\mathcal{L}$ as a function of its complex variable. For every value z a new operator is obtained, hence the expression operator family. Consider only those values of z, the eigenvalues ω, where the operator family is not invertible. The algebraic multiplicity $\mathfrak{m}_a$ is then a unique map $\mathfrak{m}_a\left[\mathcal{L},\omega_0\right]$ that returns a number in the real interval $[0,\infty]$ for $\mathcal{L}$ at ω. This map is based on two axioms: for the product of two operators $\mathcal{L}$ and $\mathcal{M}$ with the same eigenvalue ω

$$\mathfrak{m}_a\left[\mathcal{L}\mathcal{M},\omega\right] = \mathfrak{m}_a\left[\mathcal{L},\omega\right] + \mathfrak{m}_a\left[\mathcal{M},\omega\right], \tag{3.16}$$

the algebraic multiplicity must be the sum of the individual multiplicities. In addition, there exists a unique rank one projection P_0 (from the same space of operators as $\mathcal{L}$) such that

$$\mathfrak{m}_a\left[\tilde{\mathcal{L}},\omega\right] = 1, \tag{3.17}$$

for a newly defined operator

$$\tilde{\mathcal{L}}\left(z\right) = \left(z-\omega\right)\mathcal{P}_0 + \mathcal{I}_V - \mathcal{P}_0, \tag{3.18}$$

where I_V is the identity operator in the given space. An example for such a map $\mathfrak{m}_a\left[\mathcal{L},\omega\right]$ that is valid in the discrete and continuous case is given in López-Gómez and Mora-Corral (2007)(Chap. 9) as

$$\mathfrak{m}_a\left[\mathcal{L},\omega\right] = \operatorname{tr}\frac{1}{2\pi\mathrm{i}}\int_\gamma \mathcal{L}'\left(z\right)\mathcal{L}^{-1}\left(z\right)\,\mathrm{d}z, \tag{3.19}$$

where γ is a positively oriented contour in the complex plane that contains *one* ω and the trace operator needs to be defined carefully for operators. $\mathcal{L}'$ is the derivative of $\mathcal{L}$ with respect to the argument. Equation (3.19) has

been employed by Maeda et al. (2011) to estimate the number of eigenvalues inside a contour for discrete problems.

In the finite-dimensional case $V = \mathbb{C}^m$, the function

$$\mathfrak{m}_a\left[\mathcal{L}, \omega\right] = \operatorname{ord}_\omega \det \mathrm{L}\,, \tag{3.20}$$

defined in Eq. (3.12) has these properties. As can be shown following the computation in Chap. 6.5 of López-Gómez and Mora-Corral (2007)

$$\begin{aligned}\mathfrak{m}_a\left[\mathcal{L}\mathcal{M}, \omega\right] &= \operatorname{ord}_\omega \det\left(\mathcal{L}\mathcal{M}\right) = \operatorname{ord}_\omega\left[\det \mathcal{L} \cdot \det \mathcal{M}\right]\,, &(3.21)\\ &= \operatorname{ord}_\omega \det \mathcal{L} + \operatorname{ord}_\omega \det \mathcal{M}\,, &(3.22)\\ &= \mathfrak{m}_a\left[\mathcal{L}, \omega\right] + \mathfrak{m}_a\left[\mathcal{M}, \omega\right]\,. &(3.23)\end{aligned}$$

Notice that Eq. (3.16) does not mean that the product of two matrices that have the same eigenvalue yields a matrix with a twofold eigenvalue. It clearly holds that,

$$\begin{pmatrix}1 & 0\\ 0 & 2\end{pmatrix}\begin{pmatrix}1 & 0\\ 0 & 1\end{pmatrix} = \begin{pmatrix}1 & 0\\ 0 & 2\end{pmatrix}, \tag{3.24}$$

and $\mathfrak{m}_a\left[\cdot, \omega = 1\right] = 1 \neq 3$. Instead, the operator families have to be considered

$$\left[\begin{pmatrix}1 & 0\\ 0 & 2\end{pmatrix} - z\,\mathrm{I}_2\right]\left[\begin{pmatrix}1 & 0\\ 0 & 1\end{pmatrix} - z\,\mathrm{I}_2\right] = \begin{pmatrix}(1-z)^2 & 0\\ 0 & (1-z)\,(2-z)\end{pmatrix}, \tag{3.25}$$

and $\mathfrak{m}_a\left[\cdot, \omega = 1\right] = 3$ becomes evident. Now, what is the purpose of Eq. (3.18)? This is a normalization property, since Eq. (3.16) alone only ensures that $\mathfrak{m}_a$ is defined up to a multiplicative constant. In the current example Eq. (3.18) would take the form

$$\tilde{\mathcal{L}}\left(z\right) = \left(z - \omega\right)\begin{pmatrix}1 & 0\\ 0 & 0\end{pmatrix} + \mathrm{I}_2 - \begin{pmatrix}1 & 0\\ 0 & 0\end{pmatrix} = \begin{pmatrix}z-\omega & 0\\ 0 & 1\end{pmatrix}, \tag{3.26}$$

and $\mathfrak{m}_a\left[\tilde{\mathcal{L}}, \omega\right] = 1$. In a sense, $\tilde{\mathcal{L}}$ is one of the simplest operators in the space where $\mathcal{L}$ is from. Hence, for this one the value of $\mathfrak{m}_a$ is fixed to one.

3.3.3 Simple, degenerate and defective eigenvalues

An eigenvalue with $\mathfrak{m}_a = 1$ is called *simple* and $\mathfrak{m}_a > 1$ *degenerate*. Additionally, any eigenvalue with $\mathfrak{m}_a > \mathfrak{m}_g$ is called *defective*, while those with $\mathfrak{m}_a = \mathfrak{m}_g > 1$ are *semi-simple*. Table 3.1 contains this classification. In a previous section it was stated that operators $\mathcal{L}$ (and L) must have Fredholm index 0. Being a Fredholm operator guarantees that the dimension of the kernel, and thus $\mathfrak{m}_g$, is finite.

Table 3.1: Classification of eigenvalues by their multiplicities.

Multiplicities	classification	sub-classification
$\mathfrak{m}_a = 1$	simple	–
$\mathfrak{m}_a > 1$	degenerate	–
$\mathfrak{m}_a = \mathfrak{m}_g > 1$	degenerate	semi-simple
$\mathfrak{m}_a > \mathfrak{m}_g \geq 1$	degenerate	defective

3.3.4 Defective eigenvalues in thermoacoustics: Exceptional Points

Article 1 explores the occurrence of a defective point in a thermoacoustic system. Hereby the eigenvalue problem is considered a function of a vector of parameters $\boldsymbol{\varepsilon}$

$$\mathrm{L}\left(\omega, \boldsymbol{\varepsilon}\right) \mathrm{p} = 0\,, \tag{3.27}$$

and consequently, the eigenvalues (and eigenfunctions) are functions of the parameters $\omega = \omega\left(\boldsymbol{\varepsilon}\right)$. Those values of the parameters for which $\mathfrak{m}_a > \mathfrak{m}_g$ are called an *exceptional point* (EP), see p. 66 in Kato (1980) and the review by Heiss (2012). For a complex-valued problem L, an EP requires at least two parameters, i.e. $\boldsymbol{\varepsilon} = (\varepsilon_1, \varepsilon_2)$.

To visualize an exceptional point in a linear algebra setting and demonstrate the implications for thermoacoustics, Tosio Kato's example (Kato, 1980)(p. 64) is reproduced, which considers a simple model problem

$$\mathrm{T}\left(\varepsilon\right) \mathrm{p} = \begin{pmatrix} 1 & \varepsilon \\ \varepsilon & -1 \end{pmatrix} \mathrm{p} = \omega \mathrm{p}\,, \tag{3.28}$$

which is written in operator notation as

$$\mathrm{L}\left(\omega, \varepsilon\right) = \mathrm{T}\left(\varepsilon\right) - \omega \mathrm{I} = \begin{pmatrix} 1-\omega & \varepsilon \\ \varepsilon & -1-\omega \end{pmatrix}. \tag{3.29}$$

The characteristic polynomial is $\omega^2 - \left(1 + \varepsilon^2\right) = 0$ with two distinct eigenvalues that are dependent on ε

$$\omega_{1,2} = \pm\sqrt{1+\varepsilon^2}\,. \tag{3.30}$$

These eigenvalues merge for $\varepsilon_{\mathrm{EP}} = \pm\mathrm{i}$ to $\omega_{\mathrm{EP}} = 0$, forming two separate exceptional points. Notice that $\det \mathrm{T}\left(\varepsilon_{\mathrm{EP}}\right) = 0$ and thus the matrix is permanently degenerate. A quick computation gives the eigenvectors as functions

of ε

$$\mathrm{p}_1 = \begin{pmatrix} -\frac{\varepsilon}{1-\sqrt{1+\varepsilon^2}} \\ 1 \end{pmatrix} \text{ and } \mathrm{p}_2 = \begin{pmatrix} -\frac{\varepsilon}{1+\sqrt{1+\varepsilon^2}} \\ 1 \end{pmatrix}, \tag{3.31}$$

which are identical at either EP

$$\mathrm{p}_{\mathrm{EP}}^{\pm} = \begin{pmatrix} \mp i \\ 1 \end{pmatrix}, \tag{3.32}$$

thus, giving the necessary geometric multiplicity of one. The sensitivity of the eigenvalue to a change in the perturbation parameter ε at an EP is computed as

$$\frac{\partial \omega_{1,2}}{\partial \varepsilon} = \pm \frac{\varepsilon}{\sqrt{1+\varepsilon^2}}, \tag{3.33}$$

which shows that the infinite sensitivity of an eigenvalue to ε at the exceptional point is due to the square root in the numerator.

The implications for thermoacoustics are that in the vicinity of an EP, the eigenvalues are strongly sensitive to changes in parameters. If the parameters of the n–τ model are the parameters $\boldsymbol{\varepsilon} = (n, \tau)$, then a minor variation in either can result in large changes in the oscillation frequency $f = \mathrm{Real}\,(\omega)\,/2\pi$ and/or growth rates.

3.3.5 Derogatory and non-derogatory eigenvalues

The notion of a derogatory eigenvalue overlaps with the classification in terms of simple/degenerate/defective. The distinction is mainly important for perturbation studies of eigenvalues, see work in Mensah et al. (2020); Orchini et al. (2021); Kirillov (2010); Seyranian and Mailybaev (2003); Kirillov (2013). Following Definition 5.4. on p. 322 of Bernstein (2009), an eigenvalue is derogatory if

$$\mathfrak{m}_g > 1, \tag{3.34}$$

and non-derogatory otherwise. Degenerate and derogatory both imply $\mathfrak{m}_a > 1$, see Tab. 3.2. However, these are independent properties, see the note in Gregory (1960) for examples.

What's the difference? Consider the examples in Tab. 3.3. Defectiveness always implies that the geometric multiplicity is smaller than the algebraic multiplicity, which is not the case for a derogatory matrix, see Example 3. However, this is the case if the matrix is simultaneously defective, see

Table 3.2: Classification employed in Seyranian and Mailybaev (2003) in the analysis of eigenvalue perturbations.

Multiplicities	classification
$\mathfrak{m}_a \geq \mathfrak{m}_g > 1$	derogatory
$\mathfrak{m}_a \geq \mathfrak{m}_g = 1$	non-derogatory

Example 1. The exceptional point of Article 1 has $\mathfrak{m}_a = 2$ and $\mathfrak{m}_g = 1$ and is, hence, defective and non-derogatory.

Example 1 describes a derogatory exceptional point. Moeck et al. (2018) showed that this case exists in thermoacoustics. In an annular combustion chamber a semi-simple eigenvalue of an acoustic origin merges with a semi-simple eigenvalue of intrinsic origin to form an exceptional point with $\mathfrak{m}_a = 4$ and $\mathfrak{m}_g = 2$. Consequently, the eigenvalue is derogatory and defective.

Table 3.3: Examples of multiplicities of an eigenvalue and its respective classification.

Example	$\mathfrak{m}_a$	$\mathfrak{m}_g$	Classification	
1.	3	2	defective	derogatory
2.	3	1	defective	non-derogatory
3.	2	2	semi-simple	derogatory

3.4 Contour integration from the filtering perspective

In Article 2 Beyn's contour integral method (Beyn, 2012) is employed to solve thermoacoustic NLEVPs. The power in the method lies in the fact that it returns *all* eigenvalues and eigenvectors inside a user-specified contour Γ in the complex plane. Beyn's method is based on a theorem due to Keldysh (1971) that the inverse of a discrete L can be expanded into

$$\mathrm{L}(z)^{-1} = \sum_{k=1}^{a} \mathrm{p}_k \, \mathrm{w}_k^{\dagger} \frac{1}{(z-\omega_k)} + \mathrm{R}(z) \; . \tag{3.35}$$

In the equation a is an unknown number of eigenvalues, w a right eigenvector and R an analytic, matrix-valued function. Article 2 contains a complete description of Beyn's method. To summarize, Eq. (3.35) is integrated along a closed contour Γ in the complex plane

$$\oint_{\Gamma} \mathrm{L}(z)^{-1} \, \mathrm{d}z = \oint_{\Gamma} \sum_{k=1}^{s} \mathrm{p}_k \, \mathrm{w}_k^{\dagger} \frac{1}{(z-\omega_k)} \, \mathrm{d}z + \oint_{\Gamma} \mathrm{R}(z) \, \mathrm{d}z \, . \tag{3.36}$$

The number $s < a$ corresponds to the number of eigenvalues inside of Γ. Since R is analytic in all of $\mathbb{C}$, the term last term in the equation is zero. In addition, the sum over all eigenvalues ω_k is split into those inside the contour and those outside

$$\begin{aligned}\oint_\Gamma \mathrm{L}(z)^{-1}\,\mathrm{d}z = \oint_\Gamma \sum_{k\,:\,\omega_k\in\sigma(\Gamma)}^{s} \mathrm{p}_k \mathrm{w}_k^\dagger \frac{1}{(z-\omega_k)}\,\mathrm{d}z \\ + \oint_\Gamma \sum_{k\,:\,\omega_k\notin\sigma(\Gamma)} \mathrm{p}_k \mathrm{w}_k^\dagger \frac{1}{(z-\omega_k)}\,\mathrm{d}z\,.\end{aligned} \tag{3.37}$$

Again, the second sum is analytic since its poles lie outside Γ. Cauchy's theorem from analytic function theory permits to lift all zeros of the first sum

$$\oint_\Gamma \mathrm{L}(z)^{-1}\,\mathrm{d}z = 2\pi\mathrm{i}\sum_{k=1}^{s} \mathrm{p}_k\,\mathrm{w}_k^\dagger\,. \tag{3.38}$$

Numerical mathematics enter the algorithm now as the continuous integral is discretized. In essence, two so-called moment matrices

$$\mathrm{A}_p = \frac{1}{2\pi\mathrm{i}}\oint_\Gamma z^p \mathrm{L}(z)^{-1}\,\tilde{\mathrm{V}}\,\mathrm{d}z\,, \tag{3.39}$$

$$\approx \sum_{j=0}^{N_\mathrm{I}-1} \alpha_j z_j^p \mathrm{L}\left(z_j\right)^{-1}\tilde{\mathrm{V}},\quad p\in\{0,1\}\,. \tag{3.40}$$

have to be computed and in Beyn (2012) and Article 2 it is demonstrated how the eigenvalues can be recovered from the moment matrices A_p. While the algebra is straightforward, it is worthwhile to consider a different perspective: filtering. Beyn's method performs a filtering of a part of the spectrum in the complex plane. Hereby, the numerical integral approximates an ideal filter. This perspective is useful to understand shortcomings of the method. Barel and Kravanja (2016) consider the filtering perspective in detail.

To obtain a formulation that contains a so-called filter function, Keldysh's theorem Eq. (3.35) is evaluated at a concrete z_j and multiplied with $\hat{V}$ from the right to yield

$$\mathrm{L}\left(z_j\right)^{-1}\hat{V} = \sum_{k=0}^{s} \mathrm{p}_k\,\mathrm{w}_k^\dagger \frac{1}{\left(z_j-\omega_k\right)}\hat{V} + \mathrm{R}\left(z_j\right)\hat{\mathrm{V}}\,. \tag{3.41}$$

With this expression, the term $\mathrm{L}\left(z_j\right)^{-1}\tilde{\mathrm{V}}$ in Eq. (3.40) can be replaced

$$\bar{\mathrm{A}}_p = \sum_{k=0}^{s} \mathrm{p}_k \mathrm{w}_k^{\dagger} \hat{\mathrm{V}} \sum_{j=0}^{N_\mathrm{I}-1} \frac{\alpha_j z_j^p}{\left(z_j - \omega_k\right)} + \sum_{j=0}^{N_\mathrm{I}-1} \alpha_j z_j^p \mathrm{R}\left(z_j\right) \hat{\mathrm{V}}, \quad p = 0, 1. \tag{3.42}$$

Following Barel and Kravanja (2016), the filter function is defined as the term

$$b_0\left(z\right) = \sum_{j=0}^{N_\mathrm{I}-1} \frac{\alpha_j z_j^p}{\left(z_j - z\right)}. \tag{3.43}$$

The term 'filter function' stems from its purpose to approximate an ideal filter, which would be

$$b_p\left(z\right) = \begin{cases} 1, & z \text{ is inside } \Gamma \\ 0, & z \text{ is outside } \Gamma \end{cases}. \tag{3.44}$$

Ideally, it holds $b_p\left(\omega_k\right) = 0$ for eigenvalues ω_k not inside a contour Γ and thus the contribution would vanish in the computation of the moment matrices

$$\bar{\mathrm{A}}_p = \sum_{k=0}^{s} \mathrm{p}_k \mathrm{w}_k^{\dagger} \hat{\mathrm{V}}\, b_p\left(\omega_k\right) + \sum_{j=0}^{N_\mathrm{I}-1} \alpha_j z_j^p \mathrm{R}\left(z_j\right) \hat{\mathrm{V}}, \quad p = 0, 1. \tag{3.45}$$

However, b_p only approximates this ideal filter due to the numerical discretization of the contour integral. If Γ is a unit circle and trapezoid integration is performed, the discrete sampling points on the contour are written as

$$z_j = e^{2\pi \mathrm{i} \frac{j}{N}}, \tag{3.46}$$

with integration weights

$$\alpha_j = \frac{z_j}{N_\mathrm{I}}. \tag{3.47}$$

Then, the filtering function Eq. (3.43) simplifies to

$$b_p\left(z\right) = \frac{1}{N_\mathrm{I}} \sum_{j=0}^{N_\mathrm{I}-1} \frac{z_j^{p+1}}{z_j - z} = \frac{z^p}{1 - z^{N_\mathrm{I}}}, \tag{3.48}$$

and it can be seen how an increase in the number of sampling points N_I results in an increasingly better filter, see the depiction in Fig. 3.1.

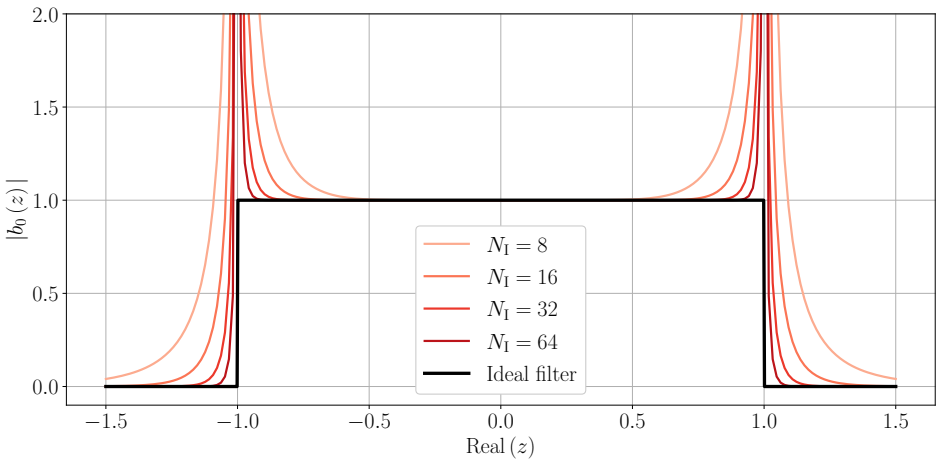

Figure 3.1: The filter function $b_0(z)$ of Eq. (3.48) depicted on the real axis. For higher values of N_I the function approximates the ideal filter increasingly better. However, an eigenvalue potentially located inside the side tails is not entirely removed and thus 'pollutes' the solution, which is discussed in Article 2.

Beyn's method is one of many algorithms for NLEVPs that integrate a suitable variation of L along a contour Γ to find all eigenvalues inside. Güttel and Tisseur (2017) review these different strategies including work by a Japanese Group (Asakura et al., 2009; Yokota and Sakurai, 2013; Sakurai and Sugiura, 2003) that also focused on contour integration.

Chapter 4

Experimental Setup and Methods

This chapter gives details on the experimental setup that is featured in Article 5 and Draft Article 9. It goes more into detail than the description in the papers.

4.1 Technical design documentation

The baseline configuration of the combustor is depicted in Fig. 4.1 and Fig. 4.2 shows the rig during operation. The combustor consists of eight cans that are fed with perfectly premixed mixture from a shared plenum. Combustion takes place in isolated cans. Towards the outlet a coupling segment is mounted that permits acoustic waves to travel between adjacent cans. The outlets are open to the atmosphere. In this section, the components are detailed.

Up until the end of the injector section, the combustor is identical to the atmospheric annular combustor employed by Worth and Dawson (2013); Mazur et al. (2019) and Indlekofer et al. (2021b). In the cited works, twelve or more injectors were employed and such a high number is not possible for the can-annular combustor due to geometric constraints, since the individual cans are made similar in diameter to the quartz tubes employed in the single sector experiments of Æsøy et al. (2020). By keeping the diameters comparable, FTFs can be measured on the same single sector setup as Æsøy et al. and then used for modelling of linear stability.

A design was sought that gives a lot of flexibility to adjust the geometries,

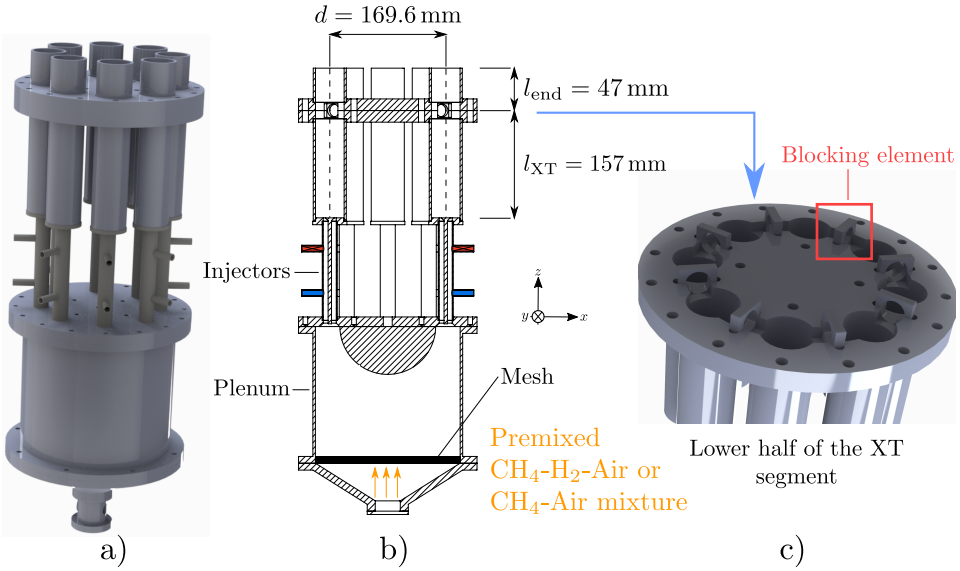

Figure 4.1: a) Rendering of the can-annular rig. From the plenum, injectors feed mixture into individual cans. Pressure transducers are mounted in the injectors. Each can consists of a lower and an upper part, with the two-part XT-ring sandwiched in between. b) Axial cut through the rig. Dimensions upstream of the base of the cans and of the bluff bodies can be found in Indlekofer et al. (2021b). Pressure transducers are mounted in the lower ports (blue), while the upper ones (red) are blocked. Steel wool is inserted into the conical section at the inlet and closed with a mesh to suppress any large-scale asymmetries in the inflow. c) Lower half of the XT with the blocking elements mounted. An identical plate is mounted from above. The revolving groove is 10 mm deep (in each plate) and has outer and inner diameters 189.6 mm and 149.6 mm, respectively.

especially with respect to the length of the cans and varying the strength of the acoustic communication between adjacent cans. The objective was to build a cost effective setup that re-uses as much as possible from the existing setups in the combustion laboratory at NTNU in order to minimize the number of new components that had to be manufactured. Concretely, this means that the plenum and injectors of the annular combustor are employed. Only three major components had to be manufactured: a base plate to hold the eight injectors, and two plates that constitute the cross-talk. The technical drawings are listed in A.1.

4.1.1 Steel cans and quartz tubes for the combustion chambers

For the cans, steel pipes available from stock with inner diameter $d_{\mathrm{can}} = 41.9\,\mathrm{mm}$ are used. With respect to diameter this stock pipe is closest to

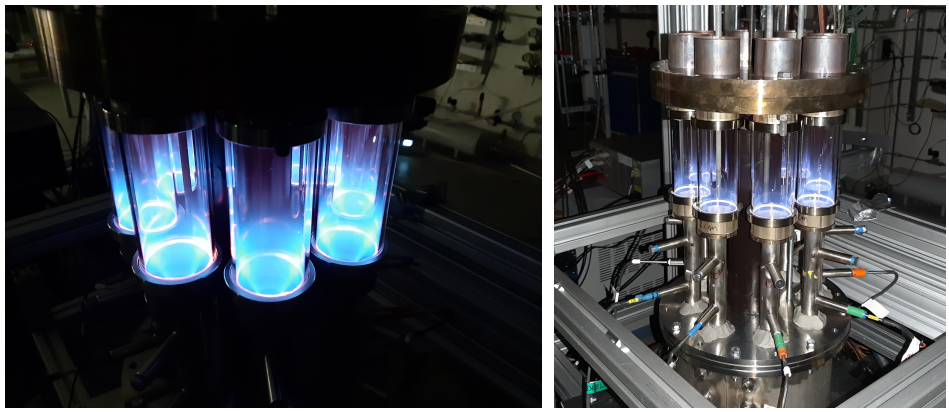

(a) (b)

Figure 4.2: Photos of the can-annular model combustor during operation with individual blue flames visible in the cans.

the quartz tubes employed by Æsøy et al. (2020) with inner diameter of 44 mm. Each can consists of a lower and upper piece of steel pipe. Different lengths have been cut to experiment with different axial positions of the cross-talk segment, and to vary the total length. Most of the experiments are conducted with lengths 150 mm and 40 mm for the lower and upper segment, respectively.

Figures 4.3, 4.4(b) and 4.8 also depict a setup where quartz tubes are inserted to give optical access to the flames in the cans. Due to manufacturing tolerances, the quartz tubes have a slightly different dimension than the steel pipes, with inner diameter $d_{\text{can}} = 45\,\text{mm}$. Figure 4.3(b) shows possible ways to mount a quartz tube using transition pieces and short pipe segments. The technical descriptions of the raw material (as ordered) of the steel pipes and the quartz tubes are given in Tab. A.2.

4.1.2 Cross-talk segment to realize weak coupling between adjacent cans

Figure 4.4(b) shows a photo of the lower plate of the XT segment. In the upper and lower XT segment, a groove runs circumferentially. In-between cans there are slots in the groove which point towards the center. In these slots blocking elements of cuboidal shape with a central bore can be inserted to vary the strength of the acoustic coupling, see Fig. 4.1(c). In Figure 4.4(a) the blocking elements can be seen as they are sitting in the mounted rig.

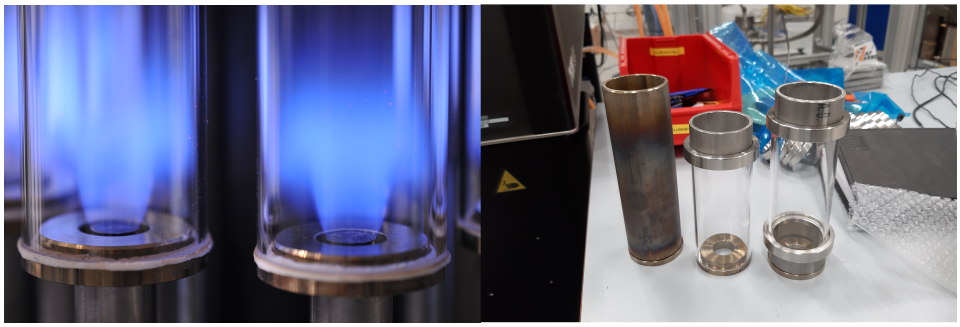

(a) (b)

Figure 4.3: a) Photo of the can-annular combustor during operation. The flames are located inside the quartz tubes and stabilized at a bluff body. Ceramic wool (in white) is used as a sealing. b) A can combustion chamber and two possible setups to mount a quartz tube.

Apart from inserting no element at all, blocking elements with five different bore sizes are available, see Tab. 4.1. An example of such a blocking element is depicted in Fig. 4.6(b). If no element is inserted, the cross-section is square, otherwise it is circular. For comparison, the can-annular combustor of Moon et al. (2020a,b, 2021) has a ratio $A_{XT}/A_{can} = 0.24$, while the two-can combustor of Venkatesan et al. (2019) has a ratio of $A_{XT}/A_{can} = 0.29$. However, both combustors have a chocked outlet unlike the combustor in this thesis. Thus, a direct comparison with respect to interaction strength is difficult.

Table 4.1: Dimensions of the blocking elements. For 'Open' the edge length of the square cross-section is given. A range was chosen that is comparable to the ratios employed in Moon et al. (2020a,b, 2021).

Name	Tiny	Small	Medium	Large	Huge	Open
d_{XT} in mm	9.4	13.2	16.2	18.7	20.0	20.0
A_{XT}/A_{can}	0.05	0.10	0.15	0.20	0.23	0.29

4.1.3 Acoustic decoupling at the inlet and the outlet

In order to inhibit acoustic communication via the outlets, loose sheet metal plates are put on top of the combustor to decouple acoustic communication via the outlets, Fig. 4.6(a). An end correction (Levine and Schwinger, 1948) gives $0.61 d_{can}/2 = 12.78\,\text{mm}$ for the location of the pressure node downstream of each outlet. The length of the pipe segment is 45 mm to yield

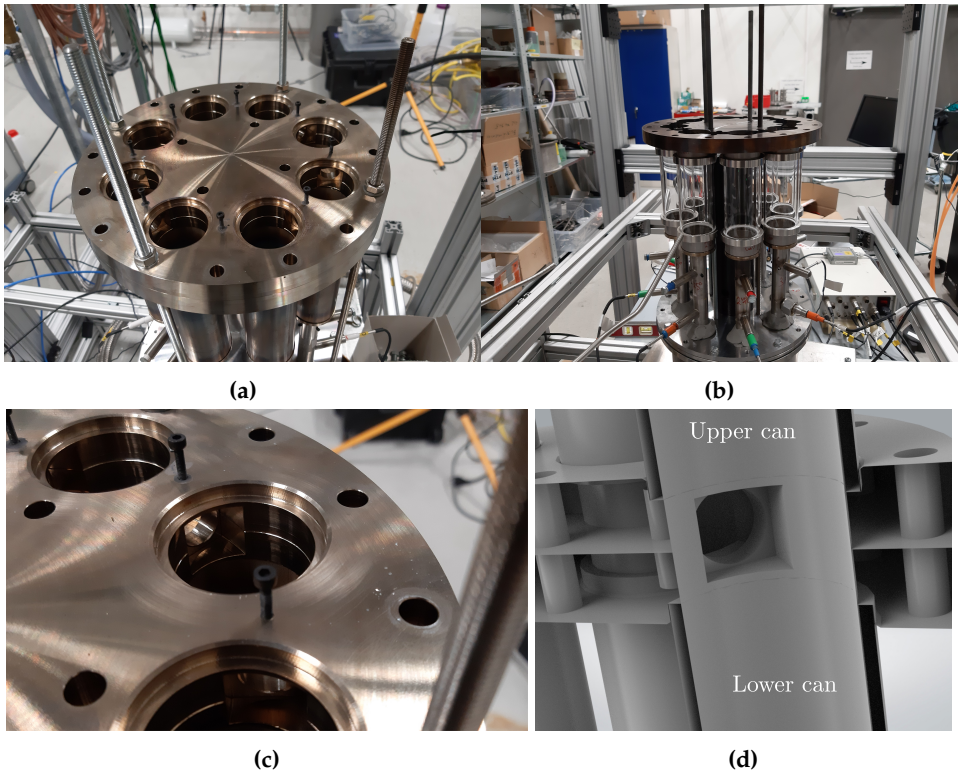

Figure 4.4: Pictures of the setup during re-configuration. a) The upper steel tubes are removed and a view into the coupling segment is possible where blocking elements are installed – see the detailed view in c). b) The upper half of the coupling segment is removed and the circumferential groove with slots for the blocking elements is visible. The threaded rods are used to compress the entire rig and ensure minimal leakage. For the configuration with quartz tubes, the coupling segments rests on nuts on the threaded rods. This measure is taken to avoid that the quartz tubes are compressed and potentially break under thermal stresses. c) Detailed view into the cross-talk area of a). d) Rendering of a cut view through the combustor. The lower and upper can are visible with the opening for the cross-talk in-between.

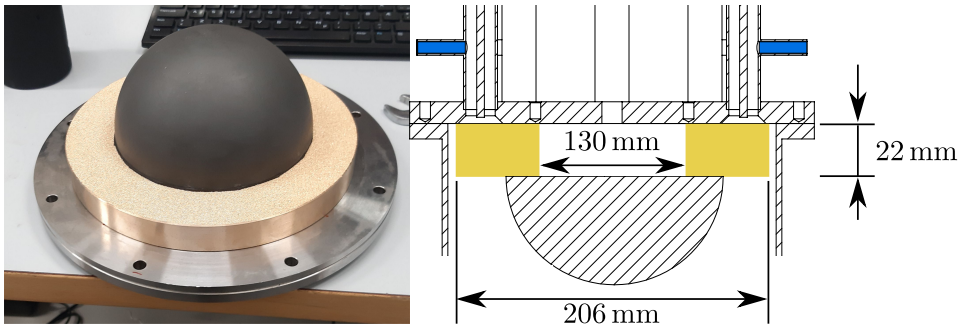

Figure 4.5: a) Photo of the sintered plate mounted on the base plate, just upstream of the injectors. b) Detailed cut view of the plenum in Fig. 4.1 with the sintered plate (yellow) mounted upstream of the injectors.

a total of 57.78 mm, which is significantly shorter then the sheet metal of height 150 mm.

For some experiments, a sintered plate is installed upstream of the injectors to decouple the plenum and confine acoustic communication to the cross-talk segment. The mounted plate is schematically depicted in Fig. 4.5. The sintered plate is of type SIKA-B200 with a porosity of 51% and pore size 124 μm. The plate has a high pressure drop and is highly acoustically reflective. Figure 4.7 shows that the communication between adjacent cans is minimal and that a strong decoupling is achieved.

4.1.4 Operation of the combustor

Perfectly premixed mixtures of CH_4–H_2–air are employed. The baseline configuration is unstable for a pure CH_4–air mixture at power $P = 4$ kW per burner and for equivalence ratios $\phi = 0.75, \ldots, 1.0$. For the same conditions the configuration with a sintered plate is stable. Hence, hydrogen is added to the mixture to achieve an unstable state. A H_2 content of 8% by power (20.09% by volume) was set and the overall power was increased to 8.3 kW per burner. With the sintered plate, the combustor is usually stable for $\phi = 0.75$ and unstable for higher values of ϕ.

Measurements are usually taken for a duration of 60 s. To monitor whether all flames are stabilised as intended on the bluff body flame holders rather than lifted, an overhead Photron SA1.1 CMOS camera is employed. Together with a LaVision Intensified Relay Optics unit and a Cerco 2178 UV lens equipped with a D20-VG0035942 filter (centre wavelength 310 nm, full

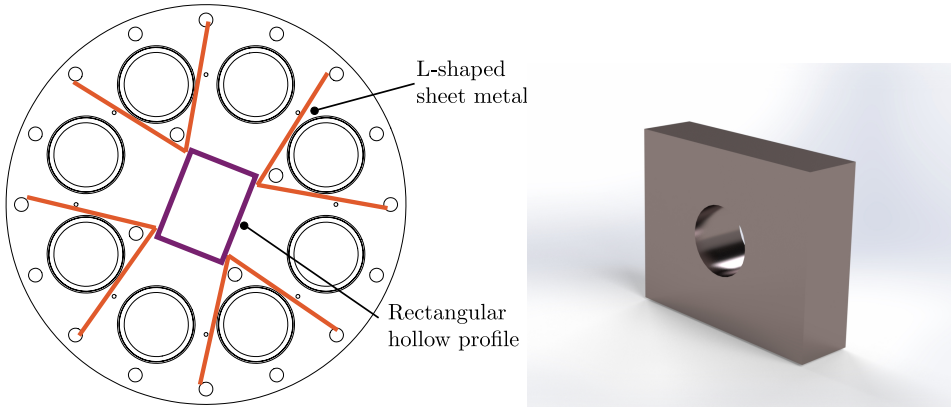

Figure 4.6: a) Schematic top view of the combustor with sheet metals placed loosely on top to suppress acoustic communication via the outlets. b) Rendering of a blocking element with a central bore.

width half maximum 10 nm) the camera images the OH^* chemiluminescence in the heat release zone. The concentration of OH^* radicals scales linearly with the actual heat release (Higgins et al., 2001). A setup with mirrors overhead of the combustion rig is used to take images from the top. The setup was devised by Håkon Nygaard for the atmospheric annular rig and is depicted on p. 37 of his thesis (Nygård, 2021). Apart from monitoring, the camera data is not used for data analysis. If the bluff body is not visible on the OH^* images, then the flame has not stabilized properly. Hydrogen content is then increased to trigger an upstream propagation of the flame. Otherwise the ignition procedure is repeated.

An Optris CTlaser 3MHCF4 pyrometer is aimed at the inside wall of the outlet of one can to record the temperature. A new experimental run is commenced once the outlet temperature has dropped to 350 °C. This approach is taken to improve repeatability of the experiments.

4.2 Experimental diagnostics and post-processing

4.2.1 Data acquisition

In every injector tube one Kulite (XCS-093-05D) pressure transducer is mounted, see Fig. 4.1. The pressure transducers are located in the lower of the two ports with the upper one blocked. A 24-bit DAQ system (NI model 9174) is used for the signal recording. Ideally, two pressure transducers

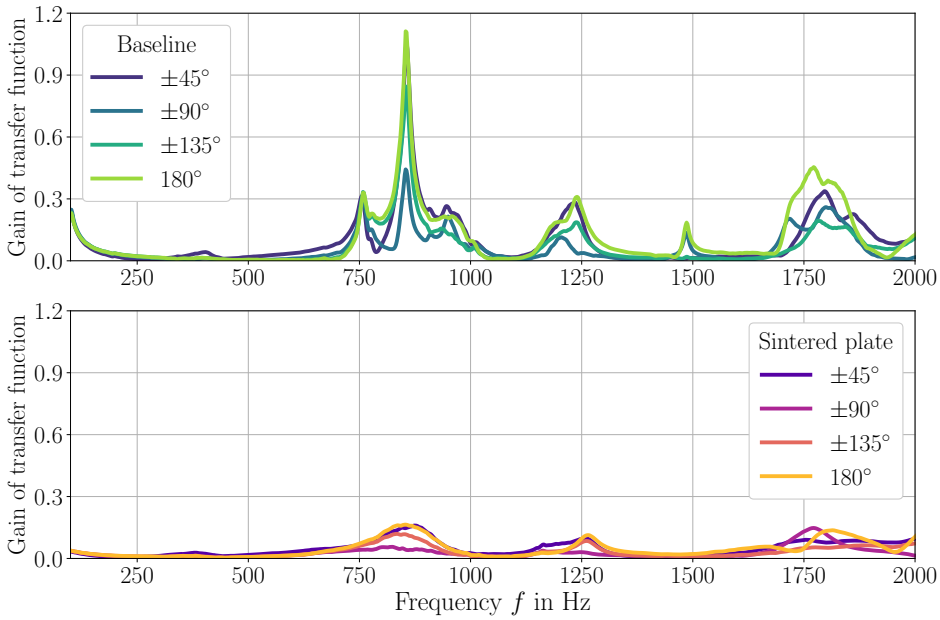

Figure 4.7: For the baseline case (without a sintered plate) and the case with a sintered plate, the XTs are closed and the cans are forced via the outlets with a loudspeaker in the range of 100 Hz to 2000 Hz. This yields seven transfer functions with respect to the microphones in the other cans. This is done for all eight cans and the average taken. Finally, transfer functions of cans at angles +45° and −45° are averaged (likewise for the other angles). The addition of the sintered plate significantly reduces communication via the plenum.

would be placed in every injector to permit a reconstruction of the fluctuation inside the can with a two-microphone method. However, during the experiments only eight pressure transducers were available. Pressure signals are recorded at f_s = 51.2 kHz and amplified with a FE-579-TA Bridge Amplifier from FYLDE set to a gain of 300 and using a built-in low-pass filter with cut-off at 20 kHz.

If quartz tubes are employed, the heat-release data is recorded using eight Hamamatsu H11901-113 photomultipliers (PMTs) and amplified with two Hamamatsu C7169 amplifiers set to a gain of 0.4 V. An optical bandpass filter of type "310nm CWL, 25mm Dia., Hard Coated OD 4.0 10nm" from Edmund optics is mounted in front of every PMT to reduce the optical spectrum to the range of OH^* radicals. The arrangement in Fig. 4.8 shows how the PMTs are arranged around the cans. A small laser, model PL202 from Thorlabs, is used to align every PMT with the center of every can. Two

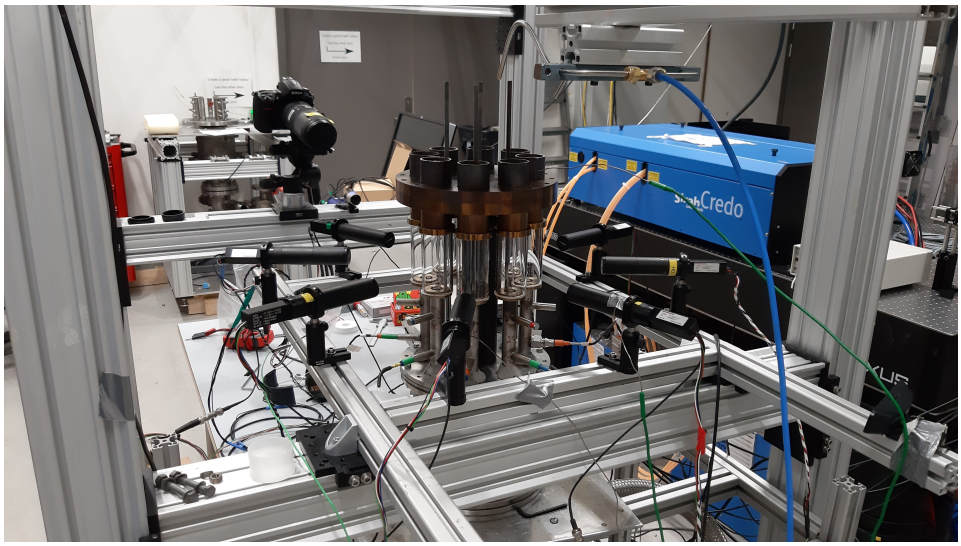

Figure 4.8: Picture of the experimental setup with quartz tubes installed. The mounted photomultipliers and pressure transducers are visible.

1 inch length tubes are mounted on every PMT. It is ensured that the opening of every PMT (with attached lens tubes) has a distance of 10.5 cm from the outer wall of the can it is aimed at. The main reason is to avoid damage to the PMTs from the heat of the combustor. For the chosen distances, a minor computation shows that the aperture for every PMT is approximately 40 mm – the inner diameter of every quartz tube can. Signals from the photomultipliers are recorded with the same frequency as the pressure signals.

4.2.2 Signal processing and data analysis

Short time Fourier transform is employed to identify dominant frequencies over time for a transient analysis. Hereby, the data is binned into segments of 400 ms with an overlap of 75%. Each segment is extended via zero padding to twice its length. If the transient analysis leads to the identification of a relevant window in time domain, the frequency content is computed with Welch's method. If necessary, an ideal band-pass filter is applied during the post-processing. Filter limits are chosen narrowly on a case-by-case basis to account for drifts in frequencies and mode switching. All given pressure amplitudes are taken as the root mean square value of the signals.

4.2.3 Projection onto modal bases and spin ratio

Information on the modal order m of an instability can be obtained from a projection onto a suitable modal basis. In the following, it is assumed that all eight pressure signals have been narrowly band-pass filtered around a frequency of interest. The signals are cast into a matrix $\mathrm{p} \in \mathbb{R}^{N\times l}$, where $N = 8$ is the number of pressure transducers and l is the number of samples – usually $l = f_\mathrm{s} \cdot 60\,\mathrm{s}$. In order to determine azimuthal mode orders m of a limit cycle oscillation, the signals are projected onto a set of circumferential basis functions, following Moeck (2010).

A standing wave basis is constructed in the form of a transformation matrix $\mathrm{B}_N \in \mathbb{R}^{N\times N}$ with columns

$$\mathrm{b}_n = \begin{pmatrix} w_0 1 \\ w_1 \cos\phi_n \\ w_1 \sin\phi_n \\ \cdots \\ w_{N/2} \cos N/2\phi_n \end{pmatrix}, \tag{4.1}$$

where the azimuthal coordinate takes discrete value

$$\phi_i = 0, \ldots, 2\pi\,(N-1)\,/N\,, \tag{4.2}$$

and weights are chosen as $w_0 = w_{N/2} = 1/\sqrt{N}$ and $w_1, \ldots, w_{N/2-1} = 1/\sqrt{N/2}$ to make B unitary. The matrix of modal coefficients $\mathrm{p}_m \in \mathbb{R}^{N\times l}$ is obtained via projection

$$\mathrm{p}_m = \mathrm{B}_N \mathrm{p}\,. \tag{4.3}$$

Columns of p_m contain the modal coefficients, which are termed a_m^s and a_m^c for sine and cosine basis, respectively. To represent the physical oscillation amplitudes, the modal coefficients need to be normalized by $\sqrt{N/2}$ for $m = 1, \ldots, N-1$ and $\sqrt{N}$ otherwise. Notice that for the $m = N//2$ mode (here $m = 4$) it cannot be determined whether the mode is of spinning or standing type due to aliasing.

From a standing basis, the modal coefficients of a spinning basis can be obtained. First, the analytic s_m of a_m is computed and then following Moeck (2010)

$$\begin{pmatrix} a_m^+ \\ a_m^- \end{pmatrix} = \frac{w_m}{2\sqrt{N}} \begin{pmatrix} 1 & \mathrm{i} \\ 1 & -\mathrm{i} \end{pmatrix} \begin{pmatrix} s_m^c \\ s_m^s \end{pmatrix}. \tag{4.4}$$

the modal coefficients of the spinning basis a_m^+, a_m^- are obtained. The amplitudes of either are computed as the root mean square.

A spin ratio is defined following Bourgouin et al. (2013) as

$$\Delta_{\mathrm{sp}} = \frac{\left|a_m^+\right| - \left|a_m^-\right|}{|a_m^+| + |a_m^-|} \in [-1, +1] \ , \tag{4.5}$$

where a_m^+ and a_m^- are spinning mode coefficients derived from the standing basis. Values +1 and −1 denote a spinning state in clockwise and counterclockwise directions, respectively. A spin ratio of zero corresponds to a standing mode.

Chapter 5

Summary of research articles

This thesis consists of nine research articles that have contributed to the objectives formulated in Sec. 1.4. In this chapter the articles are listed in chronological order of publishing and the scientific contributions are summarized in technical detail.

Article 1

Exceptional points in the thermoacoustic spectrum
Georg A. Mensah, Luca Magri, Camilo F. Silva, Philip E. Buschmann and Jonas P. Moeck
Journal of Sound and Vibration, Volume 433, 7 October 2018, Pages 124-128

Article 1 has the form of a rapid communication and shows that exceptional points occur in thermoacoustic systems by studying a generic Rijke tube model. The EP is computed by varying two parameters, the interaction index n and time delay τ, such that an acoustic and an intrinsic eigenvalue coalesce. By using the self-orthogonality of eigenvectors at an EP, a set of equations for the dispersion relation is derived to compute the EP explicitly. Furthermore, it is demonstrated how the high sensitivity of eigenvalues in the vicinity of an EP has grave implications for thermoacoustic stability: small changes in parameters can lead to large changes in growth rates and oscillation frequencies. Thus, a minor shift in operating conditions, that alters values akin to n or τ, can render a combustor unstable and potentially shift the frequency.

Article 2

Solution of Thermoacoustic Eigenvalue Problems with a noniterative Method
Philip E. Buschmann, Georg A. Mensah, Franck Nicoud and Jonas P. Moeck
Journal of Engineering for Gas Turbines and Power, Volume 142, Issue 3, March 2020

Article 2 applies a global solution method to NLEVPs in thermoacoustic applications. The presented contour integration method, originally due to Beyn (2012), returns all eigenvalues inside a specified contour in the complex plane. The method is applied to a network model of a Rijke tube and to the FEM-discretized MICCA combustor. The former employs an n–τ model for the flame response, while the latter uses an FTF extracted from experimental data. Eigenvalues computed with contour integration are confirmed with fixed-point methods. The global strategy is found to be advantageous to local, iterative solvers. Guidelines for choosing parameters for contour integration are given and it is recommended to confirm eigenpairs computed with contour integration with an iterative method. For the annular combustion chamber a large number of clustered modes are observed for the first time.

Article 3

Intrinsic thermoacoustic modes in an annular combustion chamber
Philip E. Buschmann, Georg A. Mensah and Jonas P. Moeck
Combustion and Flame, Volume 241, April 2020, Pages 251-262

Article 3 follows up on the clustered modes observed in an annular combustion chamber in Article 2. A computation with an n–τ model for an annular combustion chamber reveals tightly clustered modes of increasing azimuthal mode orders. The higher the azimuthal mode order, the stronger damped the modes – forming a near-vertical pattern in the complex plane. Clusters are separated by $\Delta f = 1/\tau$ on the real line and higher clusters deviate more from this vertical alignment. It is explained and proven, that the clustered modes are formed by intrinsic modes. These modes originate from the same intrinsic mechanism that is well-explored in 1D problems where the n–τ model is employed. For low frequencies, the intrinsic modes are cut-off and experience an environment similar to an anechoic termination, hence they are almost identical to intrinsic modes in an anechoic environment. However, for higher frequencies the modes become

cut-on and experience the outlet boundary condition, which yields strong shifts in frequency. Hence, cut-off modes are near identical in frequency and stack vertically, while cut-on or almost cut-on modes are positioned away from their respective clusters.

Article 4

Iterative Solvers for the Thermoacoustic Nonlinear Eigenvalue Problem and Their Convergence Properties
Georg A. Mensah, Philip E. Buschmann and Jonas P. Moeck
Presented at SOTIC-2021 conference and invited for publication to the International Journal of Spray and Combustion Dynamics; authors intend to submit it.

Article 4 presents several key advancements related to iterative, local solvers for thermoacoustic NLEVPs. First off, it is demonstrated with a numerical experiment that fixed-point methods are unable to compute intrinsic thermoacoustic modes for FEM-discretized problems. This is subsequently proven using Banach's fixed-point theorem by constructing an explicit criterion for the contraction properties of any iterative schemes based on adjoints. Evaluation of the criterion at eigenvalues shows that intrinsic modes are repellers for fixed-point methods. Consequently, generalized Newton methods of arbitrary order, so-called Householder iterations, are formulated using adjoints. For these methods all eigenvalues are attractors and they are shown to have advantageous convergence properties for thermoacoustic NLEVPs.

Article 5

Experimental study of thermoacoustic modes in a can-annular model combustor
Philip E. Buschmann, Nicholas Worth and Jonas P. Moeck
Presented at SOTIC-2021 conference and invited for publication to the International Journal of Spray and Combustion Dynamics (SCD); authors do not intend to submit it but extend the paper and submit it to a suitable journal.

Article 5 presents the first experimental results on the newly developed can-annular model combustor, where the strength of the acoustic cross-talk between adjacent cans is varied. The design of the combustor is presented and it is detailed how the cross-talk is realized. Results for two different

configurations are presented: a baseline configuration with an attached plenum and a setup with an installed sintered plate that decouples the plenum acoustically. The decoupling is shown by comparing measured transfer functions for both cases, which show a strong decoupling effect. The baseline configuration shows clustered modes in a band of approximately 150 Hz. Clusters are formed by modes of different azimuthal mode orders, $m = 0, 1, 2, 3, 4$ for the combustor with $N = 8$ cans. A gradual reduction in cross-talk strength is found to shift the frequencies to lower values, which is consistent with theoretical work in the literature. A linear stability analysis matches well with the experiments but also reveals that only one cluster exists, since at higher frequencies modes belonging to different clusters overlap. Decoupling of the plenum has a major effect on the thermoacoustic frequencies: two clusters within narrow bands of approximately 50 Hz are observed. These modes are highly sensitive to reduction in cross-talk size – again, confirming theoretical results. In addition, the azimuthal orders of the instabilities are described and certain transient phenomena, with mode switching and simultaneously active modes, are reported.

Article 6

Reduced-order modelling of thermoacoustic instabilities in can-annular combustors

Alessandro Orchini, Tiemo Pedergnana, Philip E. Buschmann, Jonas P. Moeck and Nicolas Noiray

Presented at SOTIC-2021 conference. An extended version of the paper is currently under review with the Journal of Sound and Vibration.

Article 6 formulates a reduced-order model for a can-annular combustor and employs geometries of the combustor presented in Article 5. The main focus of the work is the combination of a semi-empirical model for the acoustic communication via the cross-talk with a thermoacoustic network model. The reduced-order model is used to study eigenvalue clusters and their dependence on parameters and explores sensitivities with respect to the origin of individual modes. In addition, the role of outlet boundary conditions are studied. This is crucial for the comparison of experimental results in academia, where a pressure node $p = 0$ at the outlet is often found, to industrial configurations where a velocity node is encountered.

Article 7

A subspace-accelerated method for solving nonlinear thermoacoustic eigenvalue problems

Georg Mensah, Alessandro Orchini, Philip E. Buschmann and Luka Grubišić

Accepted for publication in the Journal of Sound and Vibration.

Article 7 has the form of a rapid communication and presents a projection strategy to massively reduce the size of NLEVPs in thermoacoustics originating from FEM-discretizations from $O\left(10^4\right)$ to $O\left(10^1\right)$. The strategy relies on random sampling in a domain of interest in the complex plane to assemble a suitable subspace. The subspace is automatically enlarged if a residual criterion is violated. The strategy shows a strong reduction in computational time for the so-called BRS combustor. A key advantage lies in the fact that the original problem is reduced to a smaller one, where the original parameter and eigenvalue-dependence are retained. Thus, the reduction strategy is independent from the solution step and any desired algorithm can be employed.

Draft Article 8

Symmetry groups in thermoacoustics

Philip E. Buschmann and Jonas P. Moeck

This article is in draft state with planned submission in late 2021 or early 2022 to a suitable journal.

Draft Article 8 analyses the thermoacoustic stability problem from the perspective of symmetry groups. An introductory example of a single combustor with reflection symmetry is motivated to explain basic group theory terminology and introduce the two major applications of symmetry group theory: reduction in computational cost of (nonlinear) eigenvalue problems with underlying symmetries and the prediction of eigenvalue degeneracies from the knowledge of the character table of a symmetry group alone. Two sections focus on the two most common groups in thermoacoustics of annular and can-annular combustors: the rotational group C_N and the rotation-reflection group C_{Nv}. For the group C_N it is elaborated why this group generally does not exhibit degenerate modes – unless under certain circumstances which introduce an additional symmetry in the

form of time symmetry. The character table of C_{Nv} is derived from scratch and the eigenvalue labels are discussed with respect to Bloch wave numbers – a label that is technically only correct for eigenvalues of group C_N – and azimuthal wave numbers. Finally, it is shown that a reduction in computational cost, akin to Bloch-wave theory, is possible for eigenmodes of a combustor with C_{Nv} symmetry but only for simple eigenvalues. The article concludes with a discussion of eigenvalue splitting as predicted by symmetry group theory for certain cases in the thermoacoustic literature.

Draft Article 9

Symmetry perturbations in a can-annular model combustor

Philip E. Buschmann, Nicholas Worth and Jonas P. Moeck
This article is in draft state with planned submission to the 39th International Symposium of Combustion.

Draft Article 9 focuses on the role of symmetry breaking in a can-annular model combustor. The combustor of Article 5 is operated with sets of asymmetric blocking elements for the XTs. Thus, a reduction in symmetry is achieved and the effect on mode localization is studied. Here, 'localization' refers to a phenomena where a minority of cans exhibit large amplitude pulsations, while the remainder remain silent. This effect is known for systems of weakly coupled oscillators. The reduction in symmetry is conducted in line with the results from Draft Article 8 and takes into account all possible symmetry groups with lower symmetry until full asymmetry is reached. Preliminary results indicate that strong localization in a minority of cans might have occurred.

Chapter 6

Conclusions and Outlook

Linear stability analysis is an essential design tool for engineers in the gas turbine industry. This thesis contributes to making this analysis more reliable by improving the numerical solution methods in a series of three papers consisting of Article 2, Article 4 and Article 7. The two papers Article 1 and Article 3 are closely related to this work. The former shows that eigenvalue trajectories can merge at special points in the parameter space. At these points an infinite sensitivity of the eigenvalues to perturbations in the parameters exists. The latter discusses eigenmodes that could – at that time[1] – only be attained computationally thanks to the methods developed in this thesis.

Can-annular and annular combustors are the principle designs employed in gas turbines for aircrafts or stationary power generation. These designs exhibit discrete symmetries. The importance of these symmetries has long been known in the thermoacoustic community. Draft Article 8 unravels the precise implications between the symmetries and properties of thermoacoustic eigenpairs in the language of group theory. The machinery of symmetry groups is established as a powerful mechanism to analyse thermoacoustic systems and in particular to predict eigenvalue splitting. Draft Article 9 uses the symmetry group formalism for a can-annular combustor experiment where the symmetry is lowered.

[1] For the state space framework (Emmert et al., 2016) it has since been demonstrated that it also yields these intrinsic eigenvalues Meindl et al. (2020). In the state space framework the original NLEVP is approximated by a linear surrogate problem, which can introduce an error.

The groundwork for Draft Article 9 is laid in Article 5, which contains the first set of experimental results on this combustor and confirms a number of theoretical predictions on eigenvalue clusters in can-annular combustors. As part of characterising the combustor a linear stability analysis is performed using methods developed in this work. The methods developed in this thesis were especially useful to compute the closely neighbouring modes in the clusters. Article 6 contains a first step in formulating a low-order model of the can-annular combustor in Article 5.

Brief outlook into nonlinear eigenvector problems

A closure of $\hat{q}$ with a finite amplitude response in the form of a flame describing function $\mathcal{D}$ (Noiray et al., 2008) introduces a dependency on the amplitude – a nonlinearity in the eigenvector – to the thermoacoustic Helmholtz equation (2.78) to yield

$$\mathcal{N}(\omega, \hat{p}) = \nabla \cdot \left(c^2 \nabla \hat{p}\right) + \omega^2 \hat{p} + \mathcal{D}(\omega, |\nabla \hat{p}|) = 0\,. \tag{6.1}$$

As in the linear case, a solution corresponds to those pairs $(\omega, \hat{p})$ where the inverse $\mathcal{N}^{-1}$ does not exist.

Finding an algorithm that returns a satisfactory closed-form solution to Eq. (6.1) is still an open problem in thermoacoustics. Contour integration and Householder iterations, as presented in Article 2 and Article 4, permit a rapid solution of thermoacoustic NLEVPs. Can a similar success can be achieved for problems that are nonlinear in the eigenvector? Ideally, such an algorithm would enable the direct computation of the frequency and amplitude of every unstable mode oscillating at a limit cycle. Several authors have been able to compute solutions to Eq. (6.1), including Noiray et al. (2008); Han et al. (2015); Laera et al. (2017); Mensah and Moeck (2017b); Yang and Morgans (2018); Orchini et al. (2019). However, these solution strategies rely on fixing the amplitude A at a reference location and iteratively solving an NLEVP for an eigenpair. The iterative strategy is launched from the eigenvalues of the linear stability analysis. Then, the amplitude is increased until a traced eigenvalue crosses the real line. The eigenvalue with $\mathrm{Im}(\omega) = 0$ is then the oscillation frequency of the limit cycle. Clearly, the eigenvalue is then a function of the amplitude and follows a trajectory through the complex plane. In (can)-annular combustion chambers solutions to standing or spinning limit cycles both originate from the same linearly unstable eigenvalue. The aforementioned authors compute spinning modes by prescribing the same amplitudes at all reference locations, and standing modes using delicate constraints.

Since the formulation of Eq. (6.1), without any constraints on the amplitude, contains standing and spinning trajectories as solutions, it might be possible to devise a strategy to compute these trajectories directly. In particular, it raises questions if the trajectories are unique, stable modes exhibit trajectories as well and how mixed modes fit into the picture. Moreover, it is questionable if a finite amplitude closure, as in Eq. (6.1) is justified from a physical perspective or if a finite amplitude equation, like the equation for $\ln(p)$ in Eq. (2.49), is required.

Open research questions with the can-annular model combustor

The employed setup has a pressure node $\hat{p} = 0$ located at the downstream end. Gas turbine combustors are chocked at the outlet, which is reasonably well modelled with a pressure anti-node $\nabla\hat{p} \cdot \mathrm{n} = 0$. Therefore, it could be beneficial to mount a converging diverging nozzle[2] to achieve this outlet boundary condition and repeat the experiments. Care would need to be taken not to increase the mean pressure too severely – the existing rig is neither designed nor certified for elevated pressures.

In the experiments only one pressure transducer was mounted per injector to record the pressure fluctuations. This choice was dictated by the available equipment. Ideally, at lest two pressure transducers would be mounted in every injector tube to permit a reconstruction of the velocity fluctuation inside the can or at the bluff body. Plus, one or more additional pressure transducers in the plenum could be beneficial to estimate the acoustic communication via the plenum during an instability.

Currently, there is no access to mount a pressure transducer into any of the cross-talk segments and an entirely new coupling segment would be required. However, with such a setup the exact level of communication – even during the transient of an instability – could be recorded. This data could be beneficial for analytic models for the acoustic can-to-can coupling.

A setup with $N = 9$ cans, while not relevant for industrial cases, could be designed and operated fairly straightforwardly based on the existing setup. Such a design would permit to confirm the existence and mode orders of eigenvalue clusters with an odd number of cans.

The sintered plate that is mounted upstream to decouple the plenum acoustically originally belongs to a different experimental setup. Hence, the can-annular combustor was not designed to employ it. Unfortunately, it is cur-

[2]Credit goes to Prof. Thomas Sattelmayer (TU Munich) for this suggestion during a private conversation.

rently not possible to measure the impedance of the employed plate. This is because the transfer matrix setup that is used for impedance measurements at NTNU, as conducted by Indlekofer et al. (2021a), requires a small sample and that sample was ordered not for the specific sintered plate that is employed in this thesis. In order to improve numerical models where the impedance is used as an inlet boundary condition, it is suggested to order such a sample.

During the ignition of the combustor it was observed that occasionally in one or more cans the flame did not stabilize at the bluff bodies, but instead approximately 15 cm downstream. The then lifted flame has a very long flame brush. The combustor is usually thermoacoustically stable with the lifted flame. Experience gained during the experiments suggests that the combustor turns unstable if the flame switches to the upstream location at the bluff-body. This switching happens stochastically but can also be triggered by increasing the H_2 content to raise the burning velocity. Hence, it could be worthwhile to investigate this effect in detail by devising a way to reliably control the location of the stabilization of the flame, without changing the operating conditions. The results could be compared with a linear stability analysis where FTFs for up- and downstream stabilized flames are employed.

Bibliography

Æsøy, E., Aguilar, J. G., Wiseman, S., Bothien, M. R., Worth, N. A., and Dawson, J. R. (2020). Scaling and prediction of transfer functions in lean premixed H_2/CH_4-flames. *Combustion and Flame*, 215:269–282.

Aguilar, J. G. and Juniper, M. P. (2020). Thermoacoustic stabilization of a longitudinal combustor using adjoint methods. *Physical Review Fluids*, 5(8):083902.

Ansaldo Energia (2021). Ansaldo GT36 specifications.

Asakura, J., Sakurai, T., Tadano, H., Ikegami, T., and Kimura, K. (2009). A numerical method for nonlinear eigenvalue problems using contour integrals. *JSIAM Letters*, 1:52–55.

Avdonin, A., Meindl, M., and Polifke, W. (2019). Thermoacoustic analysis of a laminar premixed flame using a linearized reactive flow solver. *Proceedings of the Combustion Institute*, 37(4):5307–5314.

Barel, M. V. and Kravanja, P. (2016). Nonlinear eigenvalue problems and contour integrals. *J. Comput. Appl. Math.*, 292:526 – 540.

Bauerheim, M., Cazalens, M., and Poinsot, T. (2015). A theoretical study of mean azimuthal flow and asymmetry effects on thermo-acoustic modes in annular combustors. *Proceedings of the Combustion Institute*, 35(3):3219–3227.

Bauerheim, M., Ndiaye, A., Constantine, P., Moreau, S., and Nicoud, F. (2016a). Symmetry breaking of azimuthal thermoacoustic modes: the UQ perspective. *Journal of Fluid Mechanics*, 789:534–566.

Bauerheim, M., Nicoud, F., and Poinsot, T. (2016b). Progress in analytical methods to predict and control azimuthal combustion instability modes in annular chambers. *Physics of Fluids*, 28(2):021303.

Bauerheim, M., Salas, P., Nicoud, F., and Poinsot, T. (2014). Symmetry breaking of azimuthal thermo-acoustic modes in annular cavities: a theoretical study. *Journal of Fluid Mechanics*, 760:431–465.

Bellucci, V., Schuermans, B., Nowak, D., Flohr, P., and Paschereit, C. O. (2005). Thermoacoustic modeling of a gas turbine combustor equipped with acoustic dampers. *J. Turbomach.*, 127(2):372–379.

Bernstein, D. S. (2009). *Matrix mathematics: theory, facts, and formulas*. Princeton university press.

Betcke, T., Higham, N. J., Mehrmann, V., Schröder, C., and Tisseur, F. (2013). NLEVP: A collection of nonlinear eigenvalue problems. *ACM Transactions on Mathematical Software (TOMS)*, 39(2):1–28.

Beyn, W.-J. (2012). An integral method for solving nonlinear eigenvalue problems. *Linear Algebra and its Applications*, 436(10):3839–3863.

Bomberg, S., Emmert, T., and Polifke, W. (2015). Thermal versus acoustic response of velocity sensitive premixed flames. *Proc. Combust. Inst.*, 35(3):3185–3192.

Bonciolini, G., Boujo, E., and Noiray, N. (2016). Effects of turbulence-induced colored noise on thermoacoustic instabilities in combustion chambers. In *International Symposium: Thermoacoustic Instabilities in Gas Turbines and Rocket Engines*. ETH Zürich.

Bonciolini, G., Boujo, E., and Noiray, N. (2017). Output-only parameter identification of a colored-noise-driven van-der-pol oscillator: thermoacoustic instabilities as an example. *Physical Review E*, 95(6):062217.

Bonciolini, G., Ebi, D., Boujo, E., and Noiray, N. (2018). Experiments and modelling of rate-dependent transition delay in a stochastic subcritical bifurcation. *Royal Society open science*, 5(3):172078.

Bonciolini, G. and Noiray, N. (2019). Bifurcation dodge: avoidance of a thermoacoustic instability under transient operation. *Nonlinear Dynamics*, 96(1):703–716.

Boningari, T. and Smirniotis, P. G. (2016). Impact of nitrogen oxides on the environment and human health: Mn-based materials for the nox abatement. *Current Opinion in Chemical Engineering*, 13:133–141.

Bothien, M., Lauper, D., Yang, Y., and Scarpato, A. (2019a). Reconstruction and analysis of the acoustic transfer matrix of a reheat flame from large-eddy simulations. *Journal of Engineering for Gas Turbines and Power*, 141(2):021018.

Bothien, M. R., Ciani, A., Wood, J. P., and Fruechtel, G. (2019b). Sequential combustion in gas turbines: The key technology for burning high hydrogen contents with low emissions. In *Turbo Expo: Power for Land, Sea, and Air*, volume 58615, page V04AT04A046. American Society of Mechanical Engineers.

Bothien, M. R., Noiray, N., and Schuermans, B. (2015). Analysis of azimuthal thermo-acoustic modes in annular gas turbine combustion chambers. *Journal of Engineering for Gas Turbines and Power*, 137(6).

Bourgouin, J.-F., Durox, D., Moeck, J., Schuller, T., and Candel, S. (2015a). A new pattern of instability observed in an annular combustor: The slanted mode. *Proceedings of the Combustion Institute*, 35(3):3237–3244.

Bourgouin, J.-F., Durox, D., Moeck, J. P., Schuller, T., and Candel, S. (2013). Self-sustained instabilities in an annular combustor coupled by azimuthal and longitudinal acoustic modes. In *Turbo Expo: Power for Land, Sea, and Air*, volume 55119, page V01BT04A007. American Society of Mechanical Engineers.

Bourgouin, J.-F., Durox, D., Moeck, J. P., Schuller, T., and Candel, S. (2015b). Characterization and modeling of a spinning thermoacoustic instability in an annular combustor equipped with multiple matrix injectors. *Journal of Engineering for Gas Turbines and Power*, 137(2).

Bundesministerium für Wirtschaft und Energie (2020). Die Nationale Wasserstoffstrategie.

Chu, B.-T. (1965). On the energy transfer to small disturbances in fluid flow (part i). *Acta Mechanica*, 1(3):215–234.

Ciarlet, P. G. (2013). *Linear and nonlinear functional analysis with applications*, volume 130. Siam.

Courtine, E., Selle, L., Nicoud, F., Polifke, W., Silva, C., Bauerheim, M., and Poinsot, T. (2014). Causality and intrinsic thermoacoustic instability modes. In *Proceedings of the summer program*, page 169. Center for Turbulence Research.

Courtine, E., Selle, L., and Poinsot, T. (2015). DNS of intrinsic thermoacoustic modes in laminar premixed flames. *Combust. Flame*, 162(11):4331–4341.

Crocco, L. and Cheng, S.-I. (1956). Theory of combustion instability in liquid propellant rocket motors. Technical report, Princeton Univ Nj.

Culick, F. E. and Yang, V. (1995). Overview of combustion instabilities in liquid-propellant rocket engines. *Liquid Rocket Engine Combustion Instability*, 169:3–37.

Dowling, A. P. and Morgans, A. S. (2005). Feedback control of combustion oscillations. *Annu. Rev. Fluid Mech.*, 37:151–182.

Dowling, A. P. and Stow, S. R. (2003). Acoustic analysis of gas turbine combustors. *Journal of propulsion and power*, 19(5):751–764.

Ducruix, S., Durox, D., and Candel, S. (2000). Theoretical and experimental determinations of the transfer function of a laminar premixed flame. *Proceedings of the Combustion Institute*, 28(1):765–773.

Durox, D., Schuller, T., Noiray, N., and Candel, S. (2009). Experimental analysis of nonlinear flame transfer functions for different flame geometries. *Proceedings of the Combustion Institute*, 32(1):1391–1398.

Effenberger, C. (2013). Robust solution methods for nonlinear eigenvalue problems. *Ecole polytechnique fédérale de Lausanne*.

Emmert, T., Bomberg, S., and Polifke, W. (2015). Intrinsic thermoacoustic instability of premixed flames. *Combust. Flame*, 162(1):75–85.

Emmert, T., Meindl, M., Jaensch, S., and Polifke, W. (2016). Linear State Space Interconnect Modeling of Acoustic Systems. *Acta Acustica united with Acustica*, 102(5):824–833.

EU Commission (2015). Directive (EU) 2015/2193 of the European Parliament and of the Council of 25 November 2015 on the limitation of emissions of certain pollutants into the air from medium combustion plants.

Evesque, S., Polifke, W., and Pankiewitz, C. (2003). Spinning and azimuthally standing acoustic modes in annular combustors. In *9th AIAA/CEAS Aeroacoustics Conference and Exhibit*, page 3182.

Farisco, F., Panek, L., and Kok, J. B. (2017). Thermo-acoustic cross-talk between cans in a can-annular combustor. *International Journal of Spray and Combustion Dynamics*, 9(4):452–469.

Farisco, F., Panek, L., Kok, J. B., Pent, J., and Rajaram, R. (2015). Thermo-acoustic coupling in can-annular combustors—a numerical investigation. In *ICSV22 International Congress on Sound and Vibration*.

Faure-Beaulieu, A., Indlekofer, T., Dawson, J. R., and Noiray, N. (2021). Experiments and low-order modelling of intermittent transitions between clockwise and anticlockwise spinning thermoacoustic modes in annular combustors. *Proceedings of the Combustion Institute*, 38(4):5943–5951.

General Electric Power (2021). General Electric Power Lineup.

Ghani, A., Steinbacher, T., Albayrak, A., and Polifke, W. (2019). Intrinsic thermoacoustic feedback loop in turbulent spray flames. *Combust. Flame*, 205:22–32.

Ghirardo, G., Di Giovine, C., Moeck, J. P., and Bothien, M. R. (2019). Thermoacoustics of can-annular combustors. *Journal of Engineering for Gas Turbines and Power*, 141(1):011007.

Ghirardo, G., Juniper, M., and Moeck, J. P. (2016). Weakly nonlinear analysis of thermoacoustic instabilities in annular combustors. *Journal of Fluid Mechanics*, 805:52–87.

Ghirardo, G. and Juniper, M. P. (2013). Azimuthal instabilities in annular combustors: standing and spinning modes. *Proceedings of the Royal Society A: Mathematical, Physical and Engineering Sciences*, 469(2157):20130232.

Ghirardo, G., Moeck, J., and Bothien, M. R. (2020). Effect of noise and nonlinearities on thermoacoustics of can-annular combustors. *Journal of Engineering for Gas Turbines and Power*, 142(4):041005.

Giauque, A., SELLE, L., Gicquel, L., Poinsot, T., Buechner, H., Kaufmann, P., and Krebs, W. (2005). System identification of a large-scale swirled partially premixed combustor using les and measurements. *Journal of Turbulence*, (6):N21.

Gikadi, J., Sattelmayer, T., and Peschiulli, A. (2012). Effects of the mean flow field on the thermo-acoustic stability of aero-engine combustion chambers. In *Turbo Expo: Power for Land, Sea, and Air*, volume 44687, pages 1203–1211. American Society of Mechanical Engineers.

Gregory, R. T. (1960). Defective and derogatory matrices. *SIAM Review*, 2(2):134–139.

Güttel, S. and Tisseur, F. (2017). The nonlinear eigenvalue problem. *Acta Numerica*, 26:1–94.

Han, X., Li, J., and Morgans, A. S. (2015). Prediction of combustion instability limit cycle oscillations by combining flame describing function simulations with a thermoacoustic network model. *Combustion and Flame*, 162(10):3632–3647.

Heiss, W. (2012). The physics of exceptional points. *Journal of Physics A: Mathematical and Theoretical*, 45(44):444016.

Hield, P. A., Brear, M. J., and Jin, S. H. (2009). Thermoacoustic limit cycles in a premixed laboratory combustor with open and choked exits. *Combustion and Flame*, 156(9):1683–1697.

Higgins, B., McQuay, M., Lacas, F., Rolon, J.-C., Darabiha, N., and Candel, S. (2001). Systematic measurements of oh chemiluminescence for fuel-lean, high-pressure, premixed, laminar flames. *Fuel*, 80(1):67–74.

Hodges, C. (1982). Confinement of vibration by structural irregularity. *Journal of sound and vibration*, 82(3):411–424.

Hoeijmakers, M., Kornilov, V., Arteaga, I. L., de Goey, P., and Nijmeijer, H. (2014). Intrinsic instability of flame–acoustic coupling. *Combust. Flame*, 161(11):2860–2867.

Hoeijmakers, P. (2014). *Flame-acoustic coupling in combustion instabilities*. PhD thesis, Technische Universiteit Eindhoven.

Hofmeister, T., Hummel, T., Berger, F., Klarmann, N., and Sattelmayer, T. (2020). Elimination of numerical damping in the stability analysis of non-compact thermoacoustic systems with linearized euler equations. In *Turbo Expo: Power for Land, Sea, and Air*, volume 84133, page V04BT04A037. American Society of Mechanical Engineers.

Hofmeister, T., Hummel, T., Schuermans, B., and Sattelmayer, T. (2019). Quantification of energy transformation processes between acoustic and hydrodynamic modes in non-compact thermoacoustic systems via a helmholtz-hodge decomposition approach. In *Turbo Expo: Power for Land, Sea, and Air*, volume 58615, page V04AT04A013. American Society of Mechanical Engineers.

Huang, Y. and Yang, V. (2009). Dynamics and stability of lean-premixed swirl-stabilized combustion. *Progress in energy and combustion science*, 35(4):293–364.

Indlekofer, T., Ahn, B., Kwah, Y. H., Wiseman, S., Mazur, M., Dawson, J. R., and Worth, N. A. (2021a). The effect of hydrogen addition on the amplitude and harmonic response of azimuthal instabilities in a pressurized annular combustor. *Combustion and Flame*, 228:375–387.

Indlekofer, T., Faure-Beaulieu, A., Noiray, N., and Dawson, J. (2021b). The effect of dynamic operating conditions on the thermoacoustic response of hydrogen rich flames in an annular combustor. *Combustion and Flame*, 223:284–294.

Inui, T., Tanabe, Y., and Onodera, Y. (2012). *Group theory and its applications in physics*, volume 78. Springer Science & Business Media.

Jegal, H., Moon, K., Gu, J., Li, L. K., and Kim, K. T. (2019). Mutual synchronization of two lean-premixed gas turbine combustors: Phase locking and amplitude death. *Combustion and Flame*, 206:424–437.

Jorkowski, P. and Schuhmann, R. (2020). Solving Nonlinear Eigenvalue Problems for Waveguide-Coupled Cavities Using an Integral Solver with Subspace Projection. *IEEE Transactions on Magnetics*, 56(1):1–4.

Juniper, M. P. (2018). Sensitivity analysis of thermoacoustic instability with adjoint helmholtz solvers. *Physical Review Fluids*, 3(11):110509.

Kato, T. (1980). *Perturbation theory for linear operators*. Springer Berlin/Heidelberg, New York, 2nd edition.

Kaufmann, P., Krebs, W., Valdes, R., and Wever, U. (2008). 3D thermoacoustic properties of single can and multi can combustor configurations. In *Turbo Expo: Power for Land, Sea, and Air*, volume 43130, pages 527–538.

Keldysh, M. V. (1971). On the completeness of the eigenfunctions of some classes of non-selfadjoint linear operators. *Russ. Math. Surv.*, 26(4):15.

Kim, K. T. (2016). Combustion instability feedback mechanisms in a lean-premixed swirl-stabilized combustor. *Combustion and Flame*, 171:137–151.

Kim, K. T. (2017). Nonlinear interactions between the fundamental and higher harmonics of self-excited combustion instabilities. *Combustion Science and Technology*, 189(7):1091–1106.

Kirillov, O. (2010). Eigenvalue bifurcation in multiparameter families of non-self-adjoint operator matrices. *Zeitschrift für angewandte Mathematik und Physik*, 61(2):221–234.

Kirillov, O. N. (2013). *Nonconservative stability problems of modern physics*. de Gruyter.

Kotake, S. (1975). On combustion noise related to chemical reactions. *Journal of Sound and Vibration*, 42(3):399–410.

Krebs, W., Walz, G., and Hoffmann, S. (1999). Thermoacoustic analysis of annular combustor. In *5th AIAA/CEAS Aeroacoustics Conference and Exhibit*, page 1971.

Laera, D., Schuller, T., Prieur, K., Durox, D., Camporeale, S. M., and Candel, S. (2017). Flame describing function analysis of spinning and standing modes in an annular combustor and comparison with experiments. *Combustion and Flame*, 184:136–152.

Law, C. K. (2010). *Combustion physics*. Cambridge university press.

Lee, T. and Kim, K. T. (2020). Combustion dynamics of lean fully-premixed hydrogen-air flames in a mesoscale multinozzle array. *Combustion and Flame*, 218:234–246.

Lehoucq, R. B., Sorensen, D. C., and Yang, C. (1998). *ARPACK users' guide: solution of large-scale eigenvalue problems with implicitly restarted Arnoldi methods*. SIAM.

Leksikon, N. B. (2021). Ægidius Elling.

Levine, H. and Schwinger, J. (1948). On the radiation of sound from an unflanged circular pipe. *Physical review*, 73(4):383.

Lieuwen, T. C. (2012). *Unsteady combustor physics*. Cambridge University Press.

Lieuwen, T. C. and Yang, V., editors (2005a). *Combustion Instabilities in Gas Turbine Engines*, volume 210 of *Prog. Astronaut. Aeronaut.* AIAA, Inc.

Lieuwen, T. C. and Yang, V. (2005b). *Combustion instabilities in gas turbine engines: operational experience, fundamental mechanisms, and modeling*. American Institute of Aeronautics and Astronautics.

Logg, A., Mardal, K.-A., and Wells, G. (2012). *Automated solution of differential equations by the finite element method: The FEniCS book*, volume 84. Springer Science & Business Media.

López-Gómez, J. and Mora-Corral, C. (2007). *Algebraic multiplicity of eigenvalues of linear operators*, volume 177. Springer Science & Business Media.

Luque, S., Kanjirakkad, V., Aslanidou, I., Lubbock, R., Rosic, B., and Uchida, S. (2015). A new experimental facility to investigate combustor–turbine interactions in gas turbines with multiple can combustors. *Journal of Engineering for Gas Turbines and Power*, 137(5).

Maeda, Y., Futamura, Y., and Sakurai, T. (2011). Stochastic estimation method of eigenvalue density for nonlinear eigenvalue problem on the complex plane. *JSIAM letters*, 3:61–64.

Magri, L. (2019). Adjoint methods as design tools in thermoacoustics. *Applied Mechanics Reviews*, 71(2).

Masson-Delmotte, V., Zhai, P., Pirani, A., Connors, S. L., Péan, C., Berger, S., Caud, N., Chen, Y., Goldfarb, L., Gomis, M. I., Huang, M., Leitzell, K., Lonnoy, E., Matthews, J. B. R., Maycock, T. K., Waterfield, T., Yelekçi, O., Yu, R., and Zhou, B. (2021). *IPCC, 2021: Climate Change 2021: The Physical Science Basis. Contribution of Working Group I to the Sixth Assessment Report of the Intergovernmental Panel on Climate Change*. Cambridge University Press. In Press.

Mazur, M., Kwah, Y. H., Indlekofer, T., Dawson, J. R., and Worth, N. A. (2021). Self-excited longitudinal and azimuthal modes in a pressurised annular combustor. *Proceedings of the Combustion Institute*, 38(4):5997–6004.

Mazur, M., Nygård, H. T., Dawson, J. R., and Worth, N. A. (2019). Characteristics of self-excited spinning azimuthal modes in an annular combustor with turbulent premixed bluff-body flames. *Proceedings of the Combustion Institute*, 37(4):5129–5136.

McManus, K., Poinsot, T., and Candel, S. M. (1993). A review of active control of combustion instabilities. *Progress in energy and combustion science*, 19(1):1–29.

Meerbergen, K., Schröder, C., and Voss, H. (2013). A Jacobi–Davidson method for two-real-parameter nonlinear eigenvalue problems arising from delay-differential equations. *Numerical linear algebra with applications*, 20(5):852–868.

Mehrmann, V. and Voss, H. (2004). Nonlinear eigenvalue problems: A challenge for modern eigenvalue methods. *GAMM-Mitteilungen*, 27(2):121–152.

Meindl, M., Albayrak, A., and Polifke, W. (2020). A state-space formulation of a discontinuous galerkin method for thermoacoustic stability analysis. *Journal of Sound and Vibration*, 481:115431.

Meindl, M., Emmert, T., and Polifke, W. (2016). Efficient calculation of thermoacoustic modes utilizing state-space models. In *23rd International Congress on Sound and Vibration, ICSV23, Athens, Greece*.

Meindl, M., Silva, C. F., and Polifke, W. (2021). On the spurious entropy generation encountered in hybrid linear thermoacoustic models. *Combustion and Flame*, 223:525–540.

Mensah, G. A. (2019). *Efficient computation of thermoacoustic modes*. PhD thesis, Technische Universität Berlin.

Mensah, G. A., Buschmann, P. E., Orchini, A., and Moeck, J. P. (2018). Pyholtz. https://bitbucket.org/pyholtzdevelopers/public.git.

Mensah, G. A. and Moeck, J. P. (2015). Efficient computation of thermoacoustic modes in annular combustion chambers based on bloch-wave theory. In *ASME Turbo Expo 2015: Turbine Technical Conference and Exposition*. American Society of Mechanical Engineers Digital Collection.

Mensah, G. A. and Moeck, J. P. (2017a). Acoustic damper placement and tuning for annular combustors: an adjoint-based optimization study. *Journal of Engineering for Gas Turbines and Power*, 139(6).

Mensah, G. A. and Moeck, J. P. (2017b). Limit cycles of spinning thermoacoustic modes in annular combustors: A bloch-wave and adjoint-perturbation approach. In *ASME Turbo Expo 2017: Turbomachinery Technical Conference and Exposition*. American Society of Mechanical Engineers Digital Collection.

Mensah, G. A. and Orchini, A. (2021). WavesAndEigenvalues. https://julholtzdevelopers.github.io/WavesAndEigenvalues.jl/dev/.

Mensah, G. A., Orchini, A., and Moeck, J. P. (2020). Perturbation theory of nonlinear, non-self-adjoint eigenvalue problems: simple eigenvalues. *Journal of Sound and Vibration*, 473:115200.

Miguel-Brebion, M. (2017). *Joint numerical and experimental study of thermoacoustic instabilities*. PhD thesis.

Mitsubishi Power (2021). Mitsubishi Power Gas Turbine Lineup.

Moeck, J., Orchini, A., Buschmann, P., Mensah, G., and Magri, L. (2018). Higher-order degenerate points in annular thermoacoustic systems. *Bulletin of the American Physical Society*, 63.

Moeck, J. P. (2010). *Analysis, modeling, and control of thermoacoustic instabilities*. PhD thesis, Technische Universität Berlin.

Moeck, J. P. and Paschereit, C. O. (2012). Nonlinear interactions of multiple linearly unstable thermoacoustic modes. *International Journal of Spray and Combustion Dynamics*, 4(1):1–27.

Moeck, J. P., Paul, M., and Paschereit, C. O. (2010). Thermoacoustic instabilities in an annular Rijke tube. In *Turbo Expo: Power for Land, Sea, and Air*, volume 43970, pages 1219–1232.

Moon, K., Choi, Y., and Kim, K. T. (2021). Experimental investigation of lean-premixed hydrogen combustion instabilities in a can-annular combustion system. *Combustion and Flame*, page 111697.

Moon, K., Jegal, H., Gu, J., and Kim, K. T. (2019). Combustion-acoustic interactions through cross-talk area between adjacent model gas turbine combustors. *Combustion and Flame*, 202:405–416.

Moon, K., Jegal, H., Yoon, C., and Kim, K. T. (2020a). Cross-talk-interaction-induced combustion instabilities in a can-annular lean-premixed combustor configuration. *Combustion and Flame*, 220:178–188.

Moon, K., Yoon, C., and Kim, K. T. (2020b). Influence of rotational asymmetry on thermoacoustic instabilities in a can-annular lean-premixed combustor. *Combustion and Flame*, 223:295–306.

Mukherjee, N. K. and Shrira, V. (2017). Intrinsic flame instabilities in combustors: Analytic description of a 1-D resonator model. *Combust. Flame*, 185:188–209.

Nicoud, F., Benoit, L., Sensiau, C., and Poinsot, T. (2007). Acoustic modes in combustors with complex impedances and multidimensional active flames. *AIAA Journal*, 45(2):426–441.

Nicoud, F. and Poinsot, T. (2005). Thermoacoustic instabilities: Should the rayleigh criterion be extended to include entropy changes? *Combustion and flame*, 142(1-2):153–159.

Nicoud, F. and Wieczorek, K. (2009). About the zero mach number assumption in the calculation of thermoacoustic instabilities. *International Journal of Spray and Combustion Dynamics*, 1(1):67–111.

Noiray, N., Durox, D., Schuller, T., and Candel, S. (2008). A unified framework for nonlinear combustion instability analysis based on the flame describing function. *J. Fluid Mech.*, 615:139–167.

Nygård, H. T. (2021). *Experimental Measurement of Flame Describing Functions in an Azimuthally Forced Annular Combustor*. PhD thesis, NTNU.

Orchini, A., Mensah, G. A., and Moeck, J. P. (2019). Effects of nonlinear modal interactions on the thermoacoustic stability of annular combustors. *Journal of Engineering for Gas Turbines and Power*, 141(2).

Orchini, A., Mensah, G. A., and Moeck, J. P. (2021). Perturbation theory of nonlinear, non-self-adjoint eigenvalue problems: Semisimple eigenvalues. *Journal of Sound and Vibration*, 507:116150.

Orchini, A., Silva, C. F., Mensah, G. A., and Moeck, J. P. (2020). Thermoacoustic modes of intrinsic and acoustic origin and their interplay with exceptional points. *Combustion and Flame*, 211:83–95.

Palle, S., Nolan, C., and Miller, R. S. (2005). On molecular transport effects in real gas laminar diffusion flames at large pressure. *Physics of Fluids*, 17(10):103601.

Pankiewitz, C. (2004). *Hybrides Berechnungsverfahren für thermoakustische Instabilitäten von Mehrbrennersystemen*. PhD thesis, Technische Universität München.

Pennell, D. A., Bothien, M. R., Ciani, A., Granet, V., Singla, G., Thorpe, S., Wickstroem, A., Oumejjoud, K., and Yaquinto, M. (2017). An introduction to the Ansaldo GT36 constant pressure sequential combustor. In *Turbo Expo: Power for Land, Sea, and Air*, volume 50855, page V04BT04A043. American Society of Mechanical Engineers.

Phillips, O. M. (1960). On the generation of sound by supersonic turbulent shear layers. *Journal of Fluid Mechanics*, 9(1):1–28.

Pierre, C. (1988). Mode localization and eigenvalue loci veering phenomena in disordered structures. *Journal of Sound and Vibration*, 126(3):485–502.

Poinsot, T. (2017). Prediction and control of combustion instabilities in real engines. *Proceedings of the Combustion Institute*, 36(1):1–28.

Poinsot, T. and Veynante, D. (2005). *Theoretical and numerical combustion*. RT Edwards, Inc.

Polifke, W. (2004). Combustion instabilities. *Advances in aeroacoustics and applications*, 5.

Prieur, K., Durox, D., Schuller, T., and Candel, S. (2017). A hysteresis phenomenon leading to spinning or standing azimuthal instabilities in an annular combustor. *Combustion and flame*, 175:283–291.

Rayleigh, L. (1878). The explanation of certain acoustical phenomena. *Roy. Inst. Proc.*, 8:536–542.

Rienstra, S. W. and Hirschberg, A. (2004). An introduction to acoustics. *Eindhoven University of Technology*, 18:19.

Saad, Y. (2011). *Numerical methods for large eigenvalue problems: Revised edition*. SIAM.

Sakurai, T. and Sugiura, H. (2003). A projection method for generalized eigenvalue problems using numerical integration. *Journal of Computational and Applied Mathematics*, 159(1):119 – 128. 6th Japan-China Joint Seminar on Numerical Mathematics; In Search for the Frontier of Computational and Applied Mathematics toward the 21st Century.

Sattelmayer, T. and Polifke, W. (2003). A novel method for the computation of the linear stability of combustors. *Combustion Science and Technology*, 175(3):477–497.

Schuermans, B., Bellucci, V., and Paschereit, C. O. (2003). Thermoacoustic Modeling and Control of Multi Burner Combustion Systems. volume 2 of *Turbo Expo: Power for Land, Sea, and Air*, pages 509–519.

Schuller, T., Durox, D., and Candel, S. (2003). A unified model for the prediction of laminar flame transfer functions: comparisons between conical and v-flame dynamics. *Combustion and Flame*, 134(1-2):21–34.

Schuller, T., Poinsot, T., and Candel, S. (2020). Dynamics and control of premixed combustion systems based on flame transfer and describing functions. *Journal of Fluid Mechanics*, 894.

Schulz, O., Doll, U., Ebi, D., Droujko, J., Bourquard, C., and Noiray, N. (2019). Thermoacoustic instability in a sequential combustor: large eddy simulation and experiments. *Proceedings of the Combustion Institute*, 37(4):5325–5332.

Seyranian, A. P. and Mailybaev, A. A. (2003). *Multiparameter stability theory with mechanical applications*, volume 13. World Scientific.

Silva, C. F., Duran, I., Nicoud, F., and Moreau, S. (2014). Boundary conditions for the computation of thermoacoustic modes in combustion chambers. *AIAA journal*, 52(6):1180–1193.

Silva, C. F., Emmert, T., Jaensch, S., and Polifke, W. (2015). Numerical study on intrinsic thermoacoustic instability of a laminar premixed flame. *Combustion and Flame*, 162(9):3370–3378.

Silva, C. F., Magri, L., Runte, T., and Polifke, W. (2017a). Uncertainty quantification of growth rates of thermoacoustic instability by an adjoint helmholtz solver. *Journal of Engineering for Gas Turbines and Power*, 139(1).

Silva, C. F., Merk, M., Komarek, T., and Polifke, W. (2017b). The contribution of intrinsic thermoacoustic feedback to combustion noise and resonances of a confined turbulent premixed flame. *Combustion and Flame*, 182:269–278.

Silva, C. F., Yong, K. J., and Magri, L. (2019). Thermoacoustic modes of quasi-one-dimensional combustors in the region of marginal stability. *Journal of Engineering for Gas Turbines and Power*, 141(2).

Stow, S. R. and Dowling, A. P. (2001). Thermoacoustic oscillations in an annular combustor. In *Turbo Expo: Power for Land, Sea, and Air*, volume 78514, page V002T02A004. American Society of Mechanical Engineers.

Stow, S. R. and Dowling, A. P. (2004). Low-order modelling of thermoacoustic limit cycles. In *Turbo Expo: Power for Land, Sea, and Air*, volume 41669, pages 775–786.

Strogatz, S. H. (2018). *Nonlinear dynamics and chaos with student solutions manual: With applications to physics, biology, chemistry, and engineering*. CRC press.

Szyld, D. B. and Xue, F. (2014). Several properties of invariant pairs of nonlinear algebraic eigenvalue problems. *IMA Journal of Numerical Analysis*, 34(3):921–954.

The Fuel Cells and Hydrogen Joint Undertaking (2019). Hydrogen Roadmap Europe: A sustainable pathway for the European Energy Transition.

Venkatesan, K., Cross, A., Yoon, C., Han, F., and Bethke, S. (2019). Heavy duty gas turbine combustion dynamics study using a two-can combustion system. In *Turbo Expo: Power for Land, Sea, and Air*, volume 58615, page V04AT04A020. American Society of Mechanical Engineers.

Virtanen, P., Gommers, R., Oliphant, T. E., Haberland, M., Reddy, T., Cournapeau, D., Burovski, E., Peterson, P., Weckesser, W., Bright, J., van der Walt, S. J., Brett, M., Wilson, J., Millman, K. J., Mayorov, N., Nelson, A. R. J., Jones, E., Kern, R., Larson, E., Carey, C. J., Polat, İ., Feng, Y., Moore, E. W., VanderPlas, J., Laxalde, D., Perktold, J., Cimrman, R., Henriksen, I., Quintero, E. A., Harris, C. R., Archibald, A. M., Ribeiro, A. H., Pedregosa, F., van Mulbregt, P., and SciPy 1.0 Contributors (2020). SciPy 1.0: Fundamental Algorithms for Scientific Computing in Python. *Nature Methods*, 17:261–272.

von Saldern, J. G., Moeck, J. P., and Orchini, A. (2020). Nonlinear interaction between clustered unstable thermoacoustic modes in can-annular combustors. *Proceedings of the Combustion Institute*, 38(4):6145–6153.

Voss, H. (2002). A rational spectral problem in fluid-solid vibration. *Preprints des Institutes für Mathematik*.

Wolf, P., Staffelbach, G., Gicquel, L., Müller, D., and Poinsot, T. (2012). Acoustic and large eddy simulation studies of azimuthal modes in annular combustion chambers. *Combust. Flame*, 159:3398–3413.

Wolf, P., Staffelbach, G., Roux, A., Gicquel, L., Poinsot, T., and Moureau, V. (2009). Massively parallel les of azimuthal thermo-acoustic instabilities in annular gas turbines. *Comptes Rendus Mecanique*, 337(6-7):385–394.

Worth, N. A. and Dawson, J. R. (2013). Modal dynamics of self-excited azimuthal instabilities in an annular combustion chamber. *Combustion and Flame*, 160(11):2476–2489.

Yang, D. and Morgans, A. S. (2018). Low-order network modeling for annular combustors exhibiting longitudinal and circumferential modes. In *ASME Turbo Expo 2018: Turbomachinery Technical Conference and Exposition*. American Society of Mechanical Engineers Digital Collection.

Yokota, S. and Sakurai, T. (2013). A projection method for nonlinear eigenvalue problems using contour integrals. *JSIAM Letters*, 5:41–44.

Zhao, D., Gutmark, E., and Reinecke, A. (2019). Mitigating self-excited flame pulsating and thermoacoustic oscillations using perforated liners. *Science Bulletin*, 64(13):941–952.

Zhao, D. and Morgans, A. S. (2009). Tuned passive control of combustion instabilities using multiple helmholtz resonators. *Journal of sound and vibration*, 320(4-5):744–757.

Publications in full text

Exceptional points in the thermoacoustic spectrum

Journal of Sound and Vibration 433 (2018) 124–128

Contents lists available at ScienceDirect

Journal of Sound and Vibration

journal homepage: www.elsevier.com/locate/jsvi

Exceptional points in the thermoacoustic spectrum

Georg A. Mensah [a], Luca Magri [b,*], Camilo F. Silva [c], Philip E. Buschmann [d], Jonas P. Moeck [d,a]

[a] Institut für Strömungsmechanik und Technische Akustik, Technische Universität Berlin, Berlin, Germany
[b] Engineering Department, University of Cambridge, Cambridge, UK
[c] Professur für Thermofluiddynamik, Technische Universität München, Munich, Germany
[d] Department of Energy and Process Engineering, Norwegian University of Science and Technology, Trondheim, Norway

ARTICLE INFO

Article history:
Received 17 April 2018
Revised 27 June 2018
Accepted 30 June 2018
Available online 20 July 2018
Handling Editor: A.V. Metrikine

Keywords:
Thermoacoustics
Defective eigenvalue
Eigenvalue sensitivity
Intrinsic thermoacoustic modes

ABSTRACT

Exceptional points are found in the spectrum of a prototypical thermoacoustic system as the parameters of the flame transfer function are varied. At these points, two eigenvalues and the associated eigenfunctions coalesce. The system's sensitivity to changes in the parameters becomes infinite. Two eigenvalue branches collide at the exceptional point as the interaction index is increased. One branch originates from a purely acoustic mode, whereas the other branch originates from an intrinsic thermoacoustic mode. The existence of exceptional points in thermoacoustic systems has implications for physical understanding, computing, modeling and control.

1. Introduction

At exceptional points (EPs), at least two eigenvalues and the associated eigenfunctions coalesce, and the eigenvalue sensitivity with respect to changes in the parameters becomes infinite [1,2]. Interesting physical phenomena associated with EPs appear across various disciplines from quantum mechanics through optics and acoustics [2–4]. To the best of the authors' knowledge, the role of exceptional points has not yet been explored in thermoacoustic systems, although points in the parameter space with infinite sensitivity were discussed in a recent review article [5]. In this letter, we show that these points in the thermoacoustic spectrum are exceptional, and that they can be found in a generic thermoacoustic system when two real parameters are varied.

1.1. Thermoacoustic instabilities

Thermoacoustic instabilities are a major challenge for the reliable operation of many technical combustion systems, as reviewed by Ref. [5] and references therein. For most practical applications with low-Mach number combustion, thermoacoustic phenomena can be modelled by an inhomogeneous Helmholtz equation, which reads

$$\nabla \cdot \left(\overline{c}^2 \nabla \widehat{p}\right) + \omega^2 \widehat{p} = -\mathrm{i}\omega(\gamma - 1)\widehat{q}, \tag{1}$$

* Corresponding author.
E-mail address: lm547@cam.ac.uk (L. Magri).

https://doi.org/10.1016/j.jsv.2018.06.069
0022-460X/

where ω is the complex frequency, $\overline{c}$ is the mean speed of sound, $\mathrm{i}^2 = -1$, and γ is the heat-capacity ratio. $\widehat{p}$ and $\widehat{q}$ are the Fourier-transformed fluctuations[1] of acoustic pressure and heat release rate, respectively. Quantities are non-dimensionalized with a characteristic length, speed of sound, and density. The heat release rate fluctuation is commonly related to a velocity fluctuation at a reference position by a time-delay model [5], i.e. $-\mathrm{i}\omega(\gamma-1)\widehat{q} = n\exp(-\mathrm{i}\omega\tau)\nabla\widehat{p}\,|_{x_{\mathrm{ref}}}$, where the parameters n and τ are the interaction index and the time delay, respectively. The thermoacoustic stability problem is generally non-Hermitian because of the flame response term and dissipative boundary conditions. On numerical discretization or travelling-wave decomposition [5], thermoacoustic stability is governed by a nonlinear eigenvalue problem [6,7]

$$\mathbf{L}(\omega;\boldsymbol{\varepsilon})\widehat{\mathbf{p}} = 0, \tag{2}$$

where the vector $\boldsymbol{\varepsilon} \in \mathbb{R}^M$ contains M parameters related to, for example, the mean speed of sound, the geometry, the flame response, and the boundary conditions. $\mathbf{L} \in \mathbb{C}^{N\times N}$ is an analytic function of $\boldsymbol{\varepsilon}$ and ω in some subdomain of $\mathbb{R}^M \times \mathbb{C}$, where N is the number of degrees of freedom of the discretized equations. For a given $\boldsymbol{\varepsilon}$, the stability of the linear system is characterized by the eigenvalues $\omega = \omega_r + \mathrm{i}\omega_i$, where $\omega_r \in \mathbb{R}$ is the angular frequency and $-\omega_i \in \mathbb{R}$ is the growth rate of the linear oscillation. With this convention, the system is linearly stable if $\omega_i > 0$. The associated thermoacoustic mode shapes are provided by the eigenvectors $\widehat{\mathbf{p}} \in \mathbb{C}^N$.

1.2. Eigenvalue classification

Eigenvalues can be classified according to their algebraic and geometric multiplicities, a and g. The algebraic multiplicity is the eigenvalue's multiplicity as a root of the dispersion relation, whereas the geometric multiplicity is the dimension of the associated eigenspace, i.e. the number of linearly independent eigenvectors. An eigenvalue of (2) can be either semi-simple, when $a = g$; or defective, when $a > g$. For the special case $a = g = 1$ an eigenvalue is called simple. Semi-simple eigenvalues with $g > 1$ and defective eigenvalues are referred to as degenerate eigenvalues. Defective eigenvalues that are branch-point singularities in the parameter space are called exceptional points (EPs). Eigenvalues of single-flame longitudinal thermoacoustic systems are typically simple [5,8]. Systems with discrete rotational symmetry, such as annular and can-annular combustors, feature semi-simple degenerate eigenvalues [6,9], with fewer simple eigenvalues.

1.3. Sensitivity at an exceptional point

Mathematically, in the neighborhood of an EP, the eigenvalue has a perturbation expansion in fractional powers of the parameter (Section II-2.2 in Ref. [1]), also known as Puiseux series. At an EP with $a = 2$ (hence $g = 1$), which is assumed in the remainder of this letter, the change of the eigenvalue due to a perturbation to the i-th parameter, ε_i, reads

$$\omega = \omega_{\mathrm{EP}} + \omega_1\sqrt{\varepsilon_i - \varepsilon_{i,\mathrm{EP}}} + O\left(\varepsilon_i - \varepsilon_{i,\mathrm{EP}}\right), \qquad \varepsilon_i \to \varepsilon_{i,\mathrm{EP}}, \tag{3}$$

where ω_1 is a constant. Thus, the first-order sensitivity $\partial\omega/\partial\varepsilon_i|_{\omega_{\mathrm{EP}},\varepsilon_{\mathrm{EP}}}$ with respect to any parameter, ε_i, is infinite[2] [2] because $(\omega - \omega_{\mathrm{EP}})/(\varepsilon_i - \varepsilon_{i,\mathrm{EP}}) \to \infty$ as $\varepsilon_i \to \varepsilon_{i,\mathrm{EP}}$. An equivalent expansion holds for the eigenfunction at the EP.

1.4. Calculation of exceptional points in thermoacoustics

We consider a thermoacoustic system with an $n-\tau$ flame model and calculate EPs as n and τ are varied. The eigenvalues are the roots of the dispersion relation

$$D(\omega; n, \tau) = 0, \tag{4}$$

where $D(\omega; n, \tau) \equiv \det[\mathbf{L}(\omega; n, \tau)]$ is the characteristic function, which is transcendental and analytic in ω in some subdomain of the complex plane. For an eigenvalue to have $a = 2$, (4) must be satisfied with the two following conditions

$$\frac{\partial D}{\partial\omega}(\omega; n, \tau) = 0, \tag{5}$$

$$\frac{\partial^2 D}{\partial\omega^2}(\omega; n, \tau) \neq 0. \tag{6}$$

The solution of the two complex-valued equations (4) and (5) is the set of parameters $(n_{\mathrm{EP}}, \tau_{\mathrm{EP}})$ and the defective eigenvalue ω_{EP}. Equations (4) and (5) would also be satisfied for degenerate semi-simple eigenvalues, such as those found in systems with rotational symmetry. However, in systems without symmetry, which we consider here, degenerate eigenvalues are generically defective [10]. The defective eigenvalue has algebraic multiplicity two, but there is only one associated eigenvector $\widehat{\mathbf{p}}_{\mathrm{EP}}$.

[1] e.g., a fluctuation evolves as $\widehat{(\cdot)}\exp(\mathrm{i}\omega t)$.

[2] This is in contrast to the semi-simple case, in which the first-order sensitivity is finite (Theorem II-2.3 in Ref. [1]).

Table 1
Acoustic eigenvalue (in grey) and some close-by exceptional points. The parameters n and τ are given to ten decimal places. With this precision, two eigenvalues are found to be identical up to four decimal places.

#	n	τ	real(ω)	imag(ω)
1	0.0	-	2.2273	0.0000
1.a	1.0332748434	0.9545158731	2.5967	0.7160
1.b	0.3397183716	3.6122221467	2.2766	0.2615
1.c	0.1367125262	9.2027775468	2.2357	0.1076
1.d	−0.0939726697	13.4231684179	2.2313	0.0741

2. A prototypical time-delayed thermoacoustic system

We consider a prototypical thermoacoustic system, which contains the essential physical mechanisms of many thermoacoustic systems [5]. We assume that (i) the frequency of the oscillation is smaller than the cut-off frequency of the duct, i.e. only plane acoustic waves propagate; (ii) the duct has a sound hard end at the upstream boundary (zero acoustic pressure gradient) and an open end at the downstream boundary (acoustic pressure node); (iii) the flame is compact, i.e. it imposes a discontinuity in the mean temperature and acts as a point source for the acoustic field. The flame is located at the non-dimensional location $x_{\mathrm{flm}} = 0.6$; the non-dimensional reference position, at which the acoustic velocity drives the flame, is $x_{\mathrm{ref}} = 0.5$; the ratio of the speeds of sound between the hot and cold side is 2. The reference quantities for non-dimensionalization are the length of the duct and the speed of sound/density of the cold side. The characteristic function for this classical thermoacoustic problem reads

$$D(\omega; n, \tau) = n \exp(-\mathrm{i}\omega\tau) \sin(\omega x_{\mathrm{ref}}) \sin\left((x_{\mathrm{flm}} - 1)\frac{\omega}{2}\right) + \sin(x_{\mathrm{flm}}\omega) \sin\left((x_{\mathrm{flm}} - 1)\frac{\omega}{2}\right) + 2\cos(x_{\mathrm{flm}}\omega) \cos\left((x_{\mathrm{flm}} - 1)\frac{\omega}{2}\right). \tag{7}$$

Table 1 lists the acoustic mode ($n = 0$) and the EPs found in the vicinity of it by solving Eqs. (4) and (5). The EPs approach the acoustic eigenvalue as τ increases, while the magnitude of the associated interaction index n decreases. Section 3 discusses the eigenvalue and eigenvector sensitivity in the vicinity of the EP #1.a. The results for the other EPs in Table 1 are qualitatively similar and not discussed in this letter.

3. Exceptional points in the thermoacoustic spectrum

Because the algebraic multiplicity of the EPs considered here is $a = 2$, two eigenvalues will be found in the vicinity of the defective eigenvalue as the parameters depart from the exceptional point. In combination with the extreme sensitivity close to the EP, the numerical computation of EPs is therefore challenging for algorithms based on fixed-point iteration, such as those commonly used in thermoacoustic analyses. In the present work, a global contour-integral-based method proposed by Beyn [7] is used. This method provides all the eigenvalues within a given circle in the complex plane, even if they are defective. The integration circle has been centered at the defective eigenvalue #1.a with unit radius. This circle encloses the acoustic eigenvalue $\omega_{\mathrm{ac}} \approx 2.2273 + 0\mathrm{i}$ (mode #1). Figure 1 (left panel) shows the eigenvalue trajectories in the vicinity of EP #1.a, which are parametrized by the interaction index n for different levels of τ. When $\tau = \tau_{\mathrm{EP}}$, while the interaction index n is varied from zero to $3n_{\mathrm{EP}}$, two eigenvalue trajectories (black lines) approach each other, coalesce at $n = n_{\mathrm{EP}}$ and diverge eventually. This is a manifestation of the branch-point singularity, which implies infinite parameter sensitivity. The acoustic eigenvalue ω_{ac} is the starting point of the trajectory labeled 'acoustic'. It is neutrally stable because the system without flame is conservative. The trajectory coming from the opposite direction starts far away from the circle with a large positive imaginary part, which, in contrast to the acoustic mode, corresponds to a highly damped mode. As observed in Ref. [8] (and references therein), the physical origin of this trajectory is an intrinsic thermoacoustic (ITA) mode, which, for $n \ll 1$, is highly damped and independent of the geometry. Almost all the trajectories in the vicinity of the EP, thus, originate from either an acoustic mode or an intrinsic mode. The exceptions to this rule are the branches I and II, which are of mixed type; thus, they cannot be unambiguously traced back further than the EP. The investigation of these branches is left for future work. The large parameter sensitivity becomes apparent when considering eigenvalue trajectories that do not pass across the EP. The curvature and spread of these lines show that the parameter sensitivity becomes larger as n and τ approach the EP. Figure 1 (right panel) shows the absolute value of the eigenvectors for different points along the exceptional branch ($\tau = \tau_{\mathrm{EP}}$). Because the exceptional point is a defective eigenvalue, the two mode shapes collapse at $n = n_{\mathrm{EP}}$, i.e. $g = 1$ (black line). A small perturbation to n significantly changes the mode shape around the EP.

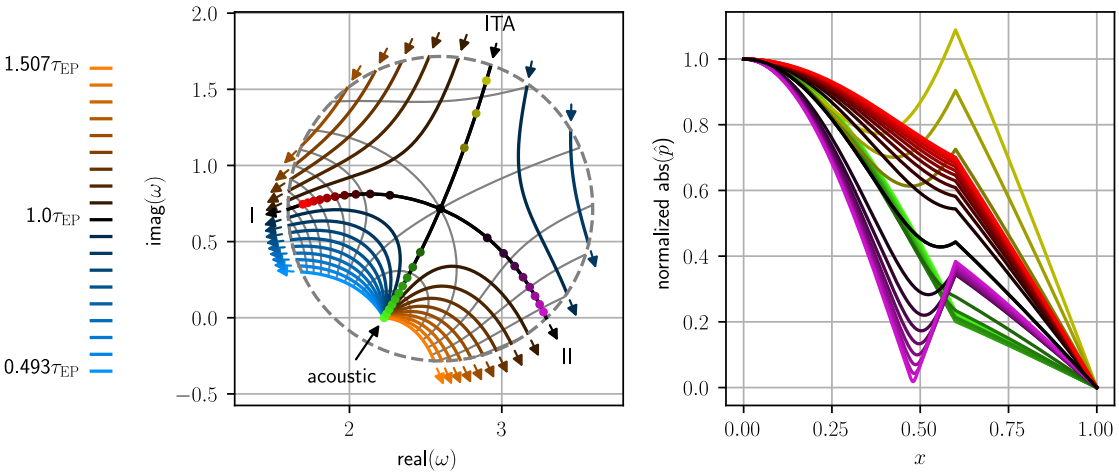

Fig. 1. Left: eigenvalue trajectories when n is varied from 0 to 3 times its exceptional value (mode #1.a in Table 1). Blue lines are for $\tau < \tau_{EP}$ while orange lines are for $\tau > \tau_{EP}$. τ varies equidistantly between $\tau_{EP} \pm 0.2\frac{2\pi}{\text{real}(\omega_{EP})}$. The darker the shading, the closer the values are to the exceptional point. The black lines represent the trajectories for $\tau = \tau_{EP}$; their intersection corresponds to the EP. The colored arrows indicate the direction of increasing n. The thin grey lines highlight solutions for constant n. The markers on the black line depict values of n ranging equidistantly from 0 to $2n_{EP}$. Only solutions inside the circle are shown. Right: the eigenvectors corresponding to the markers on the exceptional trajectories. Acoustic branch in green, intrinsic thermoacoustic branch in yellow, exceptional branch I in red, exceptional branch II in purple, EP in black. (For interpretation of the references to color in this figure legend, the reader is referred to the Web version of this article.)

4. Discussion

Exceptional points in the spectrum of a prototypical thermoacoustic system are found and investigated for the first time, to the best of the authors' knowledge. In contrast to semi-simple degenerate eigenvalues, which are found in the thermoacoustic analysis of annular combustors and have finite sensitivity, EPs do not stem from a geometric symmetry of the system. These points are branch-point singularities in the parameter space. They have fundamental and practical implications for thermoacoustic stability.

- Physics: Exceptional points occur when two eigenvalue trajectories with different physical nature collide. One trajectory originates from an acoustic mode, and the other trajectory originates from an intrinsic thermoacoustic mode.
- Numerical methods: Iterative methods based on fixed point algorithms, which are commonly used in thermoacoustic stability analysis, do not seem to be robust in the vicinity of exceptional points. A contour-integration-based approach [7] facilitates robust computations of the thermoacoustic spectrum.
- Modeling and control: The large sensitivity at an EP may help design new control schemes to mitigate thermoacoustic instabilities with small changes in the design variables. The appropriate expansion at the EP, which can be used to calculate sensitivities to the system's parameters for passive control, is in fractional powers of the parameters. Robust control schemes will be necessary around exceptional points because small uncertainties in the parameters are exceedingly amplified.

Future research will be aimed at establishing the universality of EPs in thermoacoustic systems, investigate the role of EPs in systems with discrete rotational symmetry, and exploit the properties of EPs, e.g. the large sensitivity to parameters, for control of instabilities.

Acknowledgements

L.M. gratefully acknowledges support from the Royal Academy of Engineering Research fellowship.

References

[1] T. Kato, Perturbation Theory for Linear Operators, second ed., Springer Berlin/Heidelberg, New York, 1980.
[2] W.D. Heiss, The physics of exceptional points, J. Phys. A Math. Theor. 45 (44) (2012) 444016, http://stacks.iop.org/1751-8121/45/i=44/a=444016.
[3] K. Ding, G. Ma, M. Xiao, Z.Q. Zhang, C.T. Chan, Emergence, coalescence, and topological properties of multiple exceptional points and their experimental realization, Phys. Rev. X 6 (2016) 021007https://doi.org/10.1103/PhysRevX.6.021007.
[4] V. Achilleos, G. Teocharis, O. Richoux, V. Pagneux, Non-Hermitian acoustic metamaterials: role of exceptional points in sound absorption, Phys. Rev. B 95 (2017) 144303https://doi.org/10.1103/PhysRevB.95.144303.
[5] M.P. Juniper, R. Sujith, Sensitivity and nonlinearity of thermoacoustic oscillations, Annu. Rev. Fluid Mech. 50 (1) (2018) 661–689, https://doi.org/10.1146/annurev-fluid-122316-045125.
[6] L. Magri, M. Bauerheim, M.P. Juniper, Stability analysis of thermo-acoustic nonlinear eigenproblems in annular combustors. Part I. Sensitivity, J. Comput. Phys. 325 (2016) 395–410, https://doi.org/10.1016/j.jcp.2016.07.032, http://www.sciencedirect.com/science/article/pii/S0021999116303278.

[7] S. Güttel, F. Tisseur, The nonlinear eigenvalue problem, Acta Numer. 26 (2017) 1–94, https://doi.org/10.1017/S0962492917000034.
[8] C.F. Silva, K.J. Yong, L. Magri, Thermoacoustic modes of quasi-1D combustors in the region of marginal stability, in: Proceedings of the ASME 2018 Turbomachinery Technical Conference & Exposition, GT2018-76921, 2018, pp. 1–12.
[9] G. Mensah, G. Campa, J. Moeck, Efficient computation of thermoacoustic modes in industrial annular combustion chambers based on Bloch-wave theory, J. Eng. Gas Turbines Power 138 (2016) 081502 (7 pages).
[10] A.P. Seyranian, O.N. Kirillov, A.A. Mailybaev, Coupling of eigenvalues of complex matrices at diabolic and exceptional points, J. Phys. A Math. Gen. 38 (2005) 1723–1740.

Solution of Thermoacoustic Eigenvalue Problems with a Noniterative Method

Intrinsic thermoacoustic modes in an annular combustion chamber

Combustion and Flame 214 (2020) 251–262

Contents lists available at ScienceDirect

Combustion and Flame

journal homepage: www.elsevier.com/locate/combustflame

Intrinsic thermoacoustic modes in an annular combustion chamber

Philip E. Buschmann[a,*], Georg A. Mensah[b], Jonas P. Moeck[a]

[a] Department of Energy and Process Engineering, Norwegian University of Science and Technology, Trondheim, Norway
[b] CAPS Laboratory, Department of Mechanical and Process Engineering, ETH Zurich, Zurich, Switzerland

ARTICLE INFO

Article history:
Received 16 July 2019
Revised 7 November 2019
Accepted 7 November 2019
Available online 13 January 2020

Keywords:
Thermoacoustic instabilities
Combustion dynamics
Annular combustor
Intrinsic thermoacoustic modes

ABSTRACT

Thermoacoustic instabilities originate from the interaction of unsteady heat release rate associated with flames and the acoustic modes of a combustor. A feedback loop not involving the natural acoustic modes has been observed in single-flame configurations with anechoic terminations: an acoustic wave emitted by the flame travels upstream, and the associated velocity fluctuation again excites the flame. This feedback cycle gives rise to thermoacoustic modes intrinsic to the flame. An analytical model for an annular thermoacoustic system is formulated, and the existence of intrinsic modes of various azimuthal orders is demonstrated. The spectrum of an annular combustor is computed with a three-dimensional thermoacoustic Helmholtz solver. The configuration resembles those commonly found in gas turbines. In addition to the observations in previous studies, numerous intrinsic modes are found, with frequencies close to the lowest acoustic modes. All of the intrinsic modes can be grouped into clusters, at frequencies corresponding to multiples of the inverse flame response time delay. It is demonstrated that the newly observed intrinsic modes belong to the same mechanism that has recently been studied in single-sector/flame configurations. An analysis of the evanescent character of cut-off azimuthal modes explains the pattern in the spectrum. The underlying physical mechanism is generically present in any annular combustion chamber and a possible source of instability.

1. Introduction

Modern combustion systems with high power densities, such as rocket engines and gas turbines, are prone to an unstable coupling between acoustic waves and the fluctuating heat release rate generated by one or multiple flames. In particular, annular combustion chambers enable high power densities in a compact fashion [1]. This combination is especially advantageous in aerospace applications where weight reduction is essential, but it is also favored in many stationary applications since the small surfaces in the combustor require minimal cooling. A positive feedback loop between the fluctuating heat release rate and the acoustic waves causes a growth in amplitude of the pressure oscillation: a thermoacoustic instability (TAI) manifests in the system. Combustion instabilities resulting from thermoacoustic interaction cause significant mechanical wear and potentially result in catastrophic failure of the combustion system [2]. Avoiding this undesirable unsteady phenomenon is, thus, crucial for gas turbine operation.

Numerical modeling tools are essential in identifying designs that are susceptible to TAIs at an early stage. Modeling of TAIs can be conducted based on large-eddy simulations (LES) [3,4], linearized Navier–Stokes/Euler equations [5,6], thermoacoustic Helmholtz models [7] or low-order acoustic networks [8–10]. Solving the three-dimensional thermoacoustic Helmholtz equation has been successful in predicting TAIs in realistic configurations [11–13], with significantly smaller numerical cost than LES, but having fewer modeling assumptions than network-based approaches. Linear stability analysis of the thermoacoustic system solves for the thermoacoustic modes, the complex eigenfrequencies ω with associated mode shape (or eigenfunction) $\hat{p}$, and determines whether these are amplified or attenuated in time. In the present work, we refer to a pair $(\omega, \hat{p})$ as a *mode*. The design of the system is geared towards achieving thermoacoustic stability by ensuring that all modes are damped. Evidently, this requires computing all $\omega \in \mathbb{C}$ in a relevant frequency range.

1.1. Thermoacoustic feedback mechanisms

Fluctuations in the heat release rate of the flame in a combustor generate pressure waves. These are reflected at the boundaries and travel back to cause a new perturbation of the flame [14]. This feedback loop is usually related to the natural acoustic resonance frequencies of the combustion system. From a modeling perspective, the Helmholtz equation describing the purely

* Corresponding author.
E-mail address: philip.e.buschmann@ntnu.no (P.E. Buschmann).

https://doi.org/10.1016/j.combustflame.2019.11.006

acoustic system is extended with a feedback term accounting for the active flame effect. This feedback term is commonly expressed in terms of the flame transfer function and, thus, depends nonlinearly on the eigenfrequency, but linearly on the mode shape. The flame feedback causes a shift in frequency and amplification or attenuation of the resonant modes. If the flame feedback is considered as a perturbation of the purely acoustic system, the thermoacoustic modes of acoustic origin are expected to be in the vicinity of the purely acoustic resonance frequencies.

In recent experiments, Hoejimakers [15] introduced anechoic terminations to a single-flame setup and observed the manifestation of a TAI. These experimental results are surprising in the sense that an increased damping at the boundaries, due to the anechoic terminations, renders the system unstable – a situation that appears paradoxical. As Hoejimakers [15] interrupted any acoustic feedback via the boundaries, an independent mechanism must be responsible for the onset of the TAI. Analysis of network models by Hoeijmakers et al. [16], Bomberg et al. [17], and Emmert et al. [18] showed that another feedback loop exists that does not require acoustic wave reflection at the boundaries. Instead, this so-called intrinsic feedback loop rests on the velocity fluctuation associated with the flame-emitted acoustic wave traveling upstream. Thus, the mechanism does not require acoustic reflection at the boundaries, as demonstrated by [19] based on an explicit solution and is solely a property of the flame response to acoustic perturbations. Consequently, the thermoacoustic modes associated with this mechanism are termed *intrinsic* (to the flame). Courtine et al. [20] gave a physical explanation for the intrinsic thermoacoustic mechanism based on a DNS study. Courtine et al.'s study in time-domain clearly shows how the intrinsic feedback loop is confined locally to the domain of the burner mouth.

Previous work [15,16,18,19] showed that in a one-dimensional Rijke tube with anechoic terminations, thermoacoustic modes, which must be intrinsic for this kind of system, have the analytical solution[1]

$$\omega = \frac{\pi\,(2j+1)}{\tau} - \frac{\mathrm{i}}{\tau}\ln\left(\frac{\tilde{n}}{1+\xi}\right),\ j \in \mathbb{N}^+, \tag{1}$$

with $\xi = \frac{\rho_{\mathrm{cold}} c_{\mathrm{cold}}}{\rho_{\mathrm{hot}} c_{\mathrm{hot}}}$. τ is the time delay associated with the flame response to acoustic perturbations; $\tilde{n}$ is the interaction index describing the gain of the response; ρ and c are mean density and mean speed of sound, respectively. The analytical solution exhibits two properties. First, high attenuation for a weakly interacting flame:

$$\mathrm{Im}\,\omega \to \infty, \quad \text{as } n \to 0, \tag{2}$$

and, second, an equidistant frequency spacing Δf on the real line between adjacent modes (of orders $j+1$ and j), proportional to the inverse of the flame time delay:

$$\Delta f = \mathrm{Re}\left(\omega^{j+1} - \omega^{j}\right)/2\pi = 1/\tau\,. \tag{3}$$

Recently, Mukherjee et al. [19] revisited McManus et al.'s model of the Rijke tube with reflective boundary conditions [21]. In the limit of a vanishing interaction index ($n \to 0$) Mukherjee et al. showed that strongly damped intrinsic modes have solution Eq. (1), in spite of the fact that the model does not feature anechoic terminations.

It will be demonstrated in Section 3 and Section 5 that intrinsic modes of azimuthal type exist in annular combustion chambers with reflective boundary conditions. These modes interact with their respective cut-off frequencies. Strongly cut-off modes show an equidistant frequency spacing on the real line (Eq. (3)) even for non-vanishing n. This is a peculiarity of annular combustors since in the single-flame setup with reflective boundary conditions, Eq. (1) only holds for intrinsic modes if $n \to 0$, as shown by Mukherjee et al. [19]. Moreover, the acoustic resonance frequencies serve as no indicator for the intrinsic modes, and cut-on intrinsic modes are observed in close proximity to modes of acoustic origin. Orchini et al. [22] and Buschmann et al. [47] report intrinsic modes in annular chambers but do not explain their occurrence. To the best of the authors' knowledge, the connection of the intrinsic mechanism with azimuthal cut-off frequencies has not yet been investigated in annular combustion chambers.

Recent studies focused on the intrinsic mechanism in single-flame configurations, where it was established that intrinsic modes can be the cause of TAIs and need to be taken into account by numerical tools [23–25]. Our findings imply an equal importance for the computation of intrinsic modes in annular combustors.

1.2. Numerical solution of nonlinear eigenvalue problem using contour integration

Previous studies in similar settings of annular combustors [11,26–30] exclusively identified modes as belonging to the acoustic feedback mechanism. It is possible, though, that intrinsic modes were computed but not identified as such. In a recent review article [13] on thermoacoustic instabilities in annular combustion chambers, intrinsic modes were not mentioned as potential sources of instabilities; however, the general relevance of intrinsic modes to annular chambers is pointed out in the review article [1].

The eigenfrequencies ω are obtained as solutions to a nonlinear eigenvalue problem (NLEVP). In general, NLEVPs cannot be cast into a form that permits an explicit solution. In thermoacoustics, NLEVPs are usually solved by employing a locally convergent fixed-point strategy, initially proposed by [7] for Helmholtz solvers. This approach requires adequate initial values, such as acoustic resonance frequencies for the modes associated with the conventional feedback mechanism; however, suitable initial guesses for intrinsic modes are more difficult to provide. In the present work, a numerical solution strategy for the NLEVP was chosen that is fundamentally different from the commonly employed iterative techniques. This alternative method is based on contour integration and was suggested by Beyn [31]. It is a global strategy and determines *all* eigenfrequencies in a specified domain in the complex plane, inside a defined contour. In related work [47], the fixed-point method [7] and Beyn's method based on contour integration [31] are compared in detail with respect to their application to NLEVPs arising in thermoacoustics. A combination of Beyn's global solution algorithm and subsequent iterative local refinements[2] is used to solve all NLEVPs considered in this article. We emphasize that this strategy was essential in finding the intrinsic modes that are the main topic of the present work. Incidentally, it was the interest in Beyn's global algorithm for the solution of NLEVPs that led the present authors to the discovery of the patterns of intrinsic modes discussed in the remainder of this article.

1.3. Outline of this work

The thermoacoustic Helmholtz equation, which is the basis for an analytical study and the FEM formulation, is introduced in Section 2. In Section 3 an analytical model of an annular cavity with a flame is formulated. This elementary model exhibits intrinsic modes of various azimuthal mode orders, which form a distinct pattern. A model of the MICCA combustor is formulated in

[1] We use a Fourier transform such that a time derivative $\partial_t p'$ is mapped to $+\mathrm{i}\omega\hat{p}$ in frequency domain, see Section 2.

[2] For network models, this iterative local refinement is based on numerical solutions of the characteristic equation; for the FEM models, traditional fixed-point iteration is used for this purpose.

Section 4. A qualitatively similar pattern of intrinsic modes is observed in the numerical study of the MICCA combustor, Section 5. It is explained how the intrinsic modes in the MICCA combustor originate from the intrinsic mechanism observed in axial systems. In Section 6, implications of intrinsic modes for stability analysis in annular combustion chambers are discussed.

2. Thermoacoustic model

The transport equations for mass, momentum and entropy can be linearized and then recombined into a wave equation for the pressure fluctuation p', see [7]. Transforming the wave equation for the pressure fluctuations into frequency domain (with the convention $\partial_t p' \mapsto +\mathrm{i}\omega\hat{p}$ for the Fourier transform) yields the thermoacoustic Helmholtz equation [7]:

$$\nabla\cdot\left(c^2\nabla\hat{p}\right)+\omega^2\hat{p}=-\mathrm{i}\omega(\gamma-1)\hat{q}\,, \tag{4}$$

where c is the field of the speed of sound and γ the ratio of specific heats (which is assumed to be constant). The Fourier transforms of the pressure and the heat release rate fluctuations are denoted by $\hat{p}$ and $\hat{q}$, respectively. Stability of the thermoacoustic system is determined by the eigenfrequencies $\omega\in\mathbb{C}$, where the real part of ω corresponds to the angular oscillation frequency and the negative imaginary part to the growth rate of the mode. A mode is, hence, linearly stable if $\mathrm{Im}(\omega)>0$, and the perturbation associated with this mode experiences exponential decay in the long-time limit. Overall thermoacoustic stability requires all modes to be damped. Since modes corresponding to higher oscillation frequencies typically experience stronger damping due to visco-thermal effects, practical stability analysis is usually restricted to modes below a threshold frequency. A reasonable choice for a threshold is highly problem-specific and its selection remains at the engineer's discretion.

Equation (4) is closed by relating $\hat{q}$ linearly to a velocity fluctuation $\hat{\mathbf{u}}$ at an upstream reference position $\mathbf{x}_{\mathrm{ref}}$ via a flame transfer function (FTF) $\mathcal{F}(\omega)$:

$$\hat{q}=\frac{\bar{Q}}{u_\mathrm{b}V_\mathrm{f}}\mathcal{F}(\omega)\hat{\mathbf{u}}_{\mathrm{ref}}\cdot\mathbf{n}_{\mathrm{ref}}\,. \tag{5}$$

Here, $\bar{Q}$ denotes the mean global heat release rate and u_b the bulk velocity. In Section 3 the fraction $\bar{Q}/u_\mathrm{b}$ is expressed in terms of a volumetric flow rate and the flame-induced temperature jump, while in Section 4 values from a measurement of Laera et al. [29] are employed. In the discrete model, a domain of volume V_F is specified which represents the flame and where the FTF acts as a volume source. The linearized momentum balance permits to express $\hat{\mathbf{u}}$ in terms of $\hat{p}$:

$$-\mathrm{i}\omega\hat{\mathbf{u}}=\frac{1}{\rho_0}\nabla\hat{p}\,, \tag{6}$$

and, thus, Eq. (4) can be expressed in $\hat{p}$ alone, if $\mathcal{F}(\omega)$ is known (e.g. from measurements, large-eddy simulations or an analytical model).

In the present study, the n–τ model, initially proposed by [32], is employed:

$$\mathcal{F}(\omega)=ne^{-\mathrm{i}\omega\tau}\,, \tag{7}$$

where the interaction index n and time delay τ have to be specified. With suitable acoustic boundary conditions, Eqs. (4)–(7) form a closed problem that can be solved numerically; this is the subject of Section 4.

3. Theoretical analysis of an elementary model problem

In this section, we show that intrinsic modes of different azimuthal mode orders exist in an analytical model of an annular combustion chamber and, strikingly, exhibit a pattern which is encountered in the 3D model of Section 5. This elementary model indicates that intrinsic modes generally exist in annular combustion chambers.

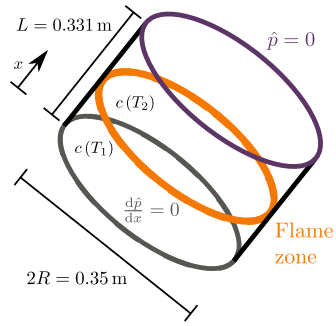

Fig. 1. Schematic depiction of the annular model. A flame zone at $x_\mathrm{F}=L/2$ spans the entire circumference and splits the domain into a cold and a hot zone: with c_1 and c_2. The reference position for the n–τ model is assumed to be in the cold zone $x_{\mathrm{ref}}<x_\mathrm{F}$.

A model for an annulus is formulated with a pressure node at the outlet and a pressure anti-node at the inlet, see Fig. 1. Network models for annular combustion chambers were studied by [8,33,34]; however, the present model is considerably simpler. An active flame that is distributed homogeneously around the circumference is placed at some axial position. For an azimuthal wavenumber $m=0$, by setting $x_{\mathrm{ref}}=L/2$ and by neglecting the effect of heat release on mean flow quantities, this model reduces to the well-known one-dimensional thermoacoustic resonator, the Rijke tube, studied in [19,21].

3.1. Analytical model for a thin annulus with circumferential flame zone

Consider an annulus of radius R and length L with a centrally positioned flame zone over the entire circumference that separates the annulus into a cold and a hot zone, see Fig. 1. The ideal gas law for the speed of sound $c=\sqrt{\gamma\bar{R}T}$ with $\gamma=1.4$ and $\bar{R}=288.68\,\mathrm{J\,kg^{-1}\,K^{-1}}$ is used in the hot and cold zones. The radial dimension is neglected, and the flame response is modelled by the n–τ model with the location of the reference position x_{ref} in the cold zone left arbitrary.

In both zones, the problem is governed by the purely acoustic Helmholtz equation:

$$\nabla^2\hat{p}+\left(\frac{\omega}{c}\right)^2\hat{p}=0\,, \tag{8}$$

which motivates a separation ansatz in each zone:

$$\hat{p}_1(x,\theta)=X_1(x)\Theta(\theta)\,,\ x\le L/2 \tag{9}$$

$$\hat{p}_2(x,\theta)=X_2(x)\Theta(\theta)\,,\ L/2<x\le L\,. \tag{10}$$

The azimuthal coordinate spans the right-open interval $\theta\in[0,2\pi R)$. It is assumed that the flame induces a jump in the axial acoustic velocity component alone and, thus, the azimuthal function $\Theta(\theta)$ is identical in $\hat{p}_1$ and $\hat{p}_2$. The matching conditions at the flame location x_F are the jump (denoted by square brackets) in acoustic velocity:

$$\left[c^2\frac{\mathrm{d}\hat{p}}{\mathrm{d}x}\right]\Bigg|_{L/2-}^{L/2+}=Q(\omega)\,, \tag{11}$$

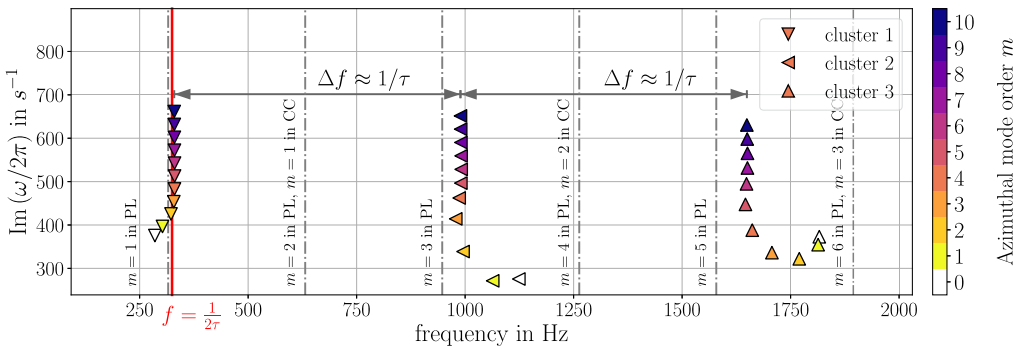

Fig. 2. Intrinsic modes in the stable half-plane for $x_{\mathrm{ref}} = L/2 - 0.05\,\mathrm{m}$ and $n = 0.05$ ($\bar{n} = 3n$). The intrinsic modes of different azimuthal mode orders fan out. For every azimuthal mode order, there exist also thermoacoustic modes of acoustic origin close to the real axis (not depicted here). The clusters are separated by a distance of $\Delta f \approx 1/\tau$, when the modes of highest azimuthal mode order are compared. Cluster 1 is 5 Hz off from the value $f = 1/2\tau$ for Eq. (1) for $j = 0$. Cut-off frequencies in plenum (PL) and combustion chamber (CC) are computed according to the analytic expression in [14] and drawn as vertical gray dash-dotted lines.

with the response given by the n–τ model:

$$Q(\omega) = \underbrace{\frac{\gamma p_0}{\rho_0}\left(\frac{T_2}{T_1} - 1\right)}_{\hat{Q}} n e^{-\mathrm{i}\omega\tau} \left.\frac{\mathrm{d}\hat{p}}{\mathrm{d}x}\right|_{x_{\mathrm{ref}}}, \tag{12}$$

and continuity in $\hat{p}$:

$$\hat{p}_1|_{\frac{L}{2}} = \hat{p}_2|_{\frac{L}{2}}. \tag{13}$$

Note that the interaction index here is defined differently compared to McManus et al. [21]:

$$\bar{n} = \left(\frac{T_2}{T_1} - 1\right) n, \tag{14}$$

where $\bar{n}$ corresponds to the interaction index "n" in McManus et al. [21], which has also been noted by [19]. The formulation in Eq. (12) is consistent with the definition in Eq. (7), which is employed in the FEM model later on.

Inserting Eq. (9) and Eq. (10) into Eq. (8) allows a separation of variables. The axial wavenumbers k_j and the azimuthal wavenumber k_θ are introduced to formulate the solvability condition as:

$$\left(\frac{\omega}{c_j}\right)^2 = k_j^2 + k_\theta^2,\ j = 1, 2. \tag{15}$$

The ansatz Eq. (9) and (10) for every half $j = 1, 2$ takes the form:

$$\hat{p}_j = \left(A_j e^{\mathrm{i}k_j x} + B_j e^{-\mathrm{i}k_j x}\right)\left(E e^{\mathrm{i}k_\theta \theta} + F e^{-\mathrm{i}k_\theta \theta}\right). \tag{16}$$

The constants A_1, B_1, A_2, B_2 and an expression for the azimuthal wavenumber k_θ are determined by evaluating the boundary and matching conditions. The constants E and F in the ansatz for the azimuthal component cannot be determined for eigenfrequencies of azimuthal type due to their degeneracy. The solution has to be $2\pi R$ periodic, hence:

$$k_\theta = \frac{m}{R},\ m \in \mathbb{Z}, \tag{17}$$

where m is the azimuthal wavenumber, which has to be specified. Equation (15) needs to be rearranged to obtain expressions for k_j as functions of ω and the parameter m. One of the two branches of the square root needs to be selected. The negative choice

$$k_j = -\mathrm{i}\,\mathrm{PV}\sqrt{\left(\frac{m}{R}\right)^2 - \left(\frac{\omega}{c_j}\right)^2},\ j = 1, 2, \tag{18}$$

guarantees that evanescent waves have $\mathrm{Im}(k_j) \leq 0$ and decay exponentially, which is the physical choice. The principle value (PV) of the complex square root is employed since the argument is complex-valued and therefore gives two solutions. The present choice yields the solution with positive real part, i.e. in the right half plane. For further details see [35].

With the chosen boundary conditions and the matching conditions, the homogeneous linear system of equations is defined through the matrix

$$\underbrace{\begin{pmatrix} 0 & e^{-\mathrm{i}k_2 L} & e^{\mathrm{i}k_2 L} \\ e^{-\mathrm{i}k_1 \frac{L}{2}} + e^{\mathrm{i}k_1 \frac{L}{2}} & -e^{-\mathrm{i}k_2 \frac{L}{2}} & -e^{\mathrm{i}k_2 \frac{L}{2}} \\ L_{31}(\omega, m) & -c_2^2(\mathrm{i}k_2)e^{-\mathrm{i}k_2 \frac{L}{2}} & c_2^2(\mathrm{i}k_2)e^{\mathrm{i}k_2 \frac{L}{2}} \end{pmatrix}}_{\mathbf{L}(\omega,m)}. \tag{19}$$

The element

$$\begin{aligned} L_{31}(\omega, m) = &-c_1^2\left[(-\mathrm{i}k_1)e^{-\mathrm{i}k_1 \frac{L}{2}} + (\mathrm{i}k_1)e^{\mathrm{i}k_1 \frac{L}{2}}\right] \\ &-\hat{Q} n e^{-\mathrm{i}\omega\tau}\left[(-\mathrm{i}k_1)e^{-\mathrm{i}k_1 x_{\mathrm{ref}}} + (\mathrm{i}k_1)e^{\mathrm{i}k_1 x_{\mathrm{ref}}}\right] \end{aligned} \tag{20}$$

contains the active flame effect. The linear system of equations for the coefficients B_1, A_2, and B_2 thus reads

$$\mathbf{L}(\omega, m)\begin{pmatrix} B_1 \\ B_2 \\ A_2 \end{pmatrix} = 0. \tag{21}$$

with $A_1 = B_1$ due to the pressure anti-node at the inlet. It is interesting to note that the matrix in Eq. (21) is identical to the 1D case [19]. The only difference is the relation between the eigenfrequency ω and the axial wavenumbers k_1 and k_2, which now involves the azimuthal wavenumber m. The 1D formulation is recovered for $m = 0$. For fixed m, Eq. (21) exhibits non-trivial solutions only for certain values of ω, the eigenvalues, which are computed numerically in the next section.

3.2. Numerical solution of the analytical model

Eigenvalues ω of the annular model are computed by solving the dispersion relation $\det \mathbf{L}(\omega, m) = 0$. The physical parameters are chosen similar to the numerical study of the MICCA combustor in Section 4, viz. $\tau = 1.54\,\mathrm{ms}$, $T_1 = 300\,\mathrm{K}$, $T_2 = 1200\,\mathrm{K}$; see Fig. 1 for the geometrical dimensions. The analytic model is not meant to represent the MICCA quantitatively.

Figure 2 shows eigenvalues of Eq. (21) for different azimuthal mode orders m in the complex plane. The mode order m can be selected arbitrarily high, but for the sake of presentation, only modes up to azimuthal order $m = 10$ are shown. The interaction index is set to $n = 0.05$ ($\bar{n} = 3n$), to remain close to the limit of

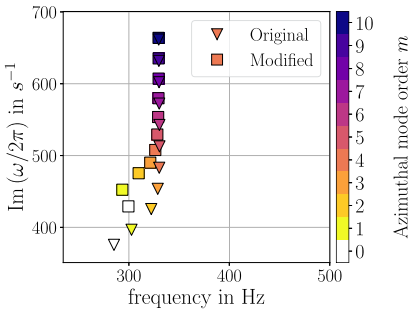

Fig. 3. Eigenvalues of cluster 1 depicted in Fig. 2 (triangles) and of a longer model (squares) of twice the length with the flame zone at 1/8 of the total length (instead of half). All other parameters are identical. The location of the flame zone and the length of the acoustic resonator have no effect on the intrinsic modes of higher azimuthal orders.

a weakly interacting flame. Only the part of the complex plane with high damping rates is depicted to focus on strongly damped modes. Later on it is demonstrated that these modes are of intrinsic origin and will, hence, be termed *intrinsic* even though non-anechoic boundary conditions are employed throughout this work. Any mode of a model with an active flame ($n > 0$) is generally referred to as *thermoacoustic*. This work classifies thermoacoustic modes by their behavior as $n \to 0$ into either *acoustic* ($\mathrm{Im}(\omega) \to 0$) or *intrinsic* ($\mathrm{Im}(\omega) \to +\infty$). This definition will be further explained in the next section. A precise definition of the terms *intrinsic, acoustic* and *thermoacoustic modes*, and the degree to which these overlap is outside the scope of this work (but see [36] and [22] for a more detailed discussion of these terms). Eigenvalues of acoustic origin are located close to the real axis due to the small interaction index.

A clear pattern is visible: modes of increasing azimuthal order line-up at certain real frequencies, forming *clusters*. These clusters are separated by approximately $\Delta f = 1/\tau$, consistent with Eq. (3). The exact value between clusters 1 and 2 (2 and 3) is $\tau_{12} = 1.510\,\mathrm{ms}$ ($\tau_{23} = 1.508\,\mathrm{ms}$), measured between modes of highest azimuthal order shown. The first cluster is at 329.70 Hz, which is close to the value of the first intrinsic mode $1/2\tau = 324.68\,\mathrm{Hz}$ according to Eq. (1). In addition, the lower the azimuthal mode order, the further away a mode is from the rests of its respective cluster.

Figure 3 shows a peculiarity between models with different geometries: modes of lower order differ between configurations, but modes of higher order are essentially identical. Thus, for an intrinsic mode the azimuthal order plays a role in the independence on the acoustic properties of the system. The discussion of the peculiarities of the eigenvalue pattern observed here are postponed until Section 5, where they are observed in the 3D MICCA combustor.

4. Numerical calculation of intrinsic modes in the MICCA annular combustor

The MICCA configuration, an annular model combustor at Laboratoire EM2C (CentraleSupélec), consists of 16 burners. It is now analyzed numerically for the presence of intrinsic modes.

4.1. Model of the MICCA combustor

The geometry and experimental data of Laera et al. [29] are used for the numerical model. Following Laera et al. [28], two geometric changes are made to the discrete model as compared to the actual experiment: an end-correction is added to the combustor outlet, and the burner is modeled in a simplified manner, as a stack of two cylinders. Figure 4 shows the geometry and indicates the speeds of sound, which are set as constant in their respective cavities. Table 1 lists cut-off frequencies for the azimuthal modes of first, second and third order in the combustion chamber.

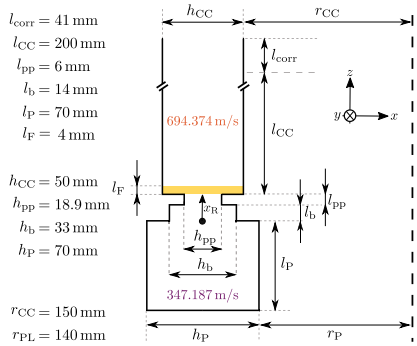

Fig. 4. Cut view of a single burner in the MICCA combustor, including all geometric dimensions. The dashed line is the symmetry axis. All boundaries are set as rigid walls, except for the outlet where a pressure node is prescribed. The subscripts refer to: combustion chamber (CC), end correction (corr), flame (F), perforated plate (pp), burner (b) and plenum (PL). Temperatures are set as constant in combustion chamber and plenum.

Table 1
The first three azimuthal cut-off frequencies f_m^c in the combustion chamber according to the analytic expression in [14, p. 138] for an annular geometry. In addition, the acoustic resonance frequencies of the MICCA combustor below 1700 Hz are given. The azimuthal mode orders m are given, and it is specified in which cavity the modes are dominant. The plenum-dominant modes are of Helmholtz type (approximately constant in axial direction), while the CC-dominant modes exhibit an axial quarter-wave structure. The ninth mode (not shown) exhibits a minor radial variation but is still of radial order zero.

Index	f in Hz	m	Dominant in
P1	332.09	0	Plenum
P2	471.35	1	Plenum
P3	730.70	2	Plenum
P4	816.64	0	CC
P5	1018.72	3	Plenum
P6	1028.00	1	CC
P7	1316.86	4	Plenum
P8	1499.78	2	CC
P9	1618.79	5	Plenum
$f_{m=1}^c$	633.60	1	CC
$f_{m=2}^c$	1266.78	2	CC
$f_{m=3}^c$	1899.04	3	CC

A pressure node $\hat{p} = 0$ is prescribed at the outlet; all other boundaries are set as rigid walls. The active flame parameters n and τ are taken from the experimental flame-describing function of [27]. From data for the lowest forcing amplitude ($u'/u_0 = 0.1$), the average gain is approximately $n = 0.9$. Linear regression of the phase gives $\tau = 1.54\,\mathrm{ms}$. The reference points for the n–τ model are positioned just at the inlet to the lower cylinder in the central axis of each respective burner. The flames are modeled as a flat zone spanning the floor of their individual segment with height $l_F = 4\,\mathrm{mm}$. An average heat release rate of $\bar{Q} = 1.44\,\mathrm{kW}$ per flame and a mean bulk flow velocity $u_b = 0.49\,\mathrm{m/s}$ are set according to [28]. To ensure that the discrete model inherits the discrete rotational symmetry of the actual combustor, the mesh of a half cell of a single combustor is first mirrored and then copied around the circumference. The mesh of the full discrete model has 38.7 k degrees of freedom.

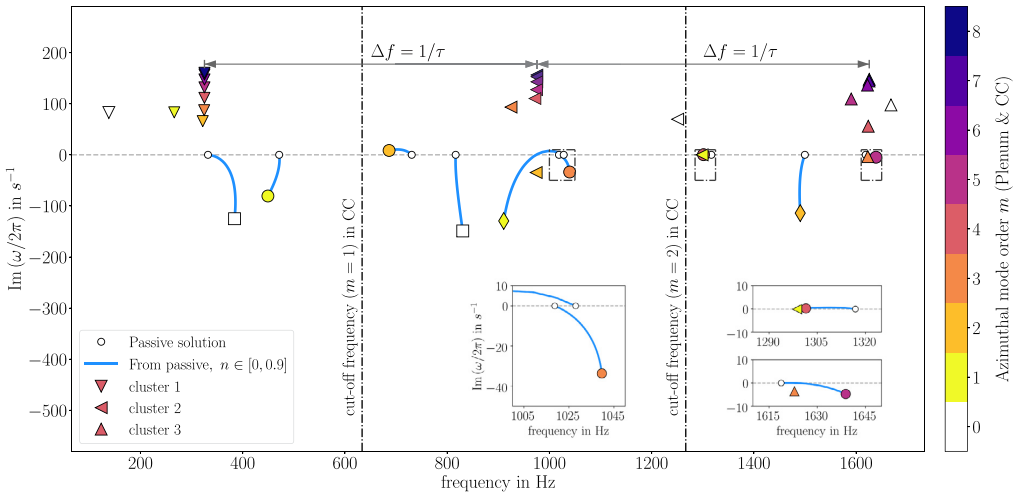

Fig. 5. Intrinsic and acoustic modes in the spectrum of the MICCA combustor below 1700 Hz. There are three types of acoustic modes: axial (white squares), azimuthal plenum-dominant (circles) and azimuthal CC-dominant (diamonds). Three clusters of intrinsic CC-dominant modes are observed: 1, 2 and 3 ($\triangledown$, $\triangleleft$ and $\triangle$). The color of the modes corresponds to the respective azimuthal mode order, starting with $m = 0$ (white, axial mode) then $m = 1$ (yellow) and up to $m = 8$ (darkest purple). The dash-dotted boxes mark the windows in the complex plane which are shown enlarged as insets. The paths of the intrinsic modes as functions of n are not depicted here but in Fig. 6. (For interpretation of the references to color in this figure legend, the reader is referred to the web version of this article.)

4.2. Nonlinear eigenvalue problem

The terms in Eq. (4), closed with Eq. (7) are discretized using linear finite elements in the solver PyHoltz [37], to yield a matrix-valued equation:

$$\mathbf{Kp} + \omega\mathbf{Cp} + \omega^2\mathbf{Mp} + ne^{-i\omega\tau}\mathbf{Qp} = 0\,, \qquad (22)$$
$$\mathbf{K}, \mathbf{C}, \mathbf{M}, \mathbf{Q} \in \mathbb{C}^{d\times d}\,, \mathbf{p} \in \mathbb{C}^{d\times 1}\,.$$

Matrices $\mathbf{K}$ and $\mathbf{M}$ are the stiffness and mass matrices, respectively, while $\mathbf{C}$ is related to the boundary impedance Z (here $Z = 0$ for the pressure node at the outlet; rigid walls enter the FEM formulation as natural boundary conditions) and $\mathbf{Q}$ is associated with the acoustically active flame. The complex-valued matrices have dimension d, the number of nodes in the mesh. Equation (22) contains the parameters, boundary conditions and flame response, which were listed in the previous section for the MICCA combustor.

The purely acoustic modes (or passive modes) are computed as solutions to Eq. (22) when $n = 0$, but there is still an increase in the mean temperature across the location of the flame. For the MICCA combustor, these modes are listed in Table 1. Solutions with $n > 0$ are referred to as active modes.

Equation (22) constitutes a nonlinear eigenvalue problem (NLEVP), which is commonly written as:

$$\mathbf{L}(\omega)\mathbf{p} = 0\,. \qquad (23)$$

The solutions are the eigenpairs $(\omega, \mathbf{p})$; at the eigenvalues ω, $\mathbf{L}(\omega)$ is not invertible. The set of all eigenvalues of $\mathbf{L}$ is referred to as the spectrum. Properties of and solution strategies for general NLEVPs arising in disciplines outside of thermoacoustics are reviewed in [38] and [39].

In the following, $\mathbf{L}(\omega)$ is also considered as a function of the parameter n, hence written as $\mathbf{L}(\omega; n)\mathbf{p} = 0$. Since $\mathbf{L}(\omega; n)$ depends continuously on n, see Eq. (22), the eigenvalues are also continuous functions of n, see [40]. This property facilitates a nearest-neighbour continuation of the eigenvalues as functions of n and a definition of the origin of a mode as acoustic or intrinsic, depending on whether the mode trajectory parameterized in n tends to an acoustic or and intrinsic mode when $n \to 0$.

5. Results and discussion

The MICCA combustor exhibits 9 distinct acoustic resonance frequencies below 1700 Hz, see Table 1. Since the boundary conditions are ideal (fully reflective) and no damping is included, for $n{=}0$ $\mathbf{L}(\omega)$ is self-adjoint, and all passive modes are purely real-valued. The ninth mode exhibits a minor radial variation (not shown) but is still of radial order zero. In addition, the first three azimuthal cut-off frequencies f_m^c in the combustion chamber are given according to the analytic expression in [14] for an annular geometry.

5.1. The complete spectrum below 1700 Hz

Figure 5 shows the spectrum below 1700 Hz, and Table 2 contains the full list of active modes. The active flame effect ($n > 0$) induces a shift in frequency and causes amplification/attenuation of the passive modes. Consequently, the eigenvalues depart from the real axis and enter the complex plane as active modes. This behavior is tracked by gradually increasing $n \in [0, 0.9]$ with a nearest-neighbour (NN) continuation and shows which modes are of acoustic origin for the final value $n = 0.9$. The stable and unstable half-planes are considered in the range $\mathrm{Im}(\omega/2\pi) = \pm 240\,\mathrm{s}^{-1}$. No modes immediately outside this range of growth/attenuation rates were observed. The numerical methods and employed parameters are detailed in Appendix A.

In total, 34 distinct modes (not counting multiplicity) are computed – a significantly higher mode density than previously reported in similar studies. Via NN-continuation, modes of acoustic origin are identified. In addition, a complementary set of intrinsic modes is observed. Azimuthal mode orders are counted from $m = 0$ to $m = 8$ in order to group the intrinsic modes into three clusters. As an additional criterion for grouping the modes, the interaction index n is decreased towards zero, and it is determined whether all modes originate from the same region in the stable

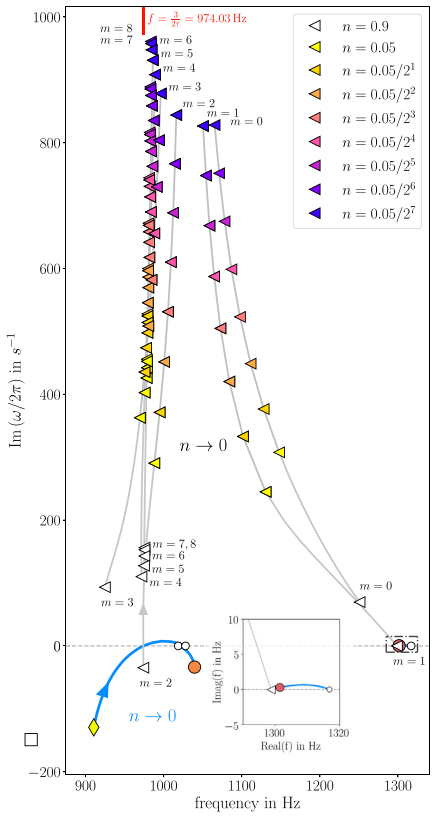

Fig. 6. Intrinsic modes of cluster 2 are tracked by decreasing n from 0.9 towards zero. Intrinsic modes are colored by their value of the interaction index n, while acoustic modes are colored by their azimuthal mode order as in Fig. 5. The solid gray lines represent the eigenvalue loci as functions of n. The dash-dotted box marks the window which is shown in the enlarged inset. The modes move to $\mathrm{Im}\, f \to +\infty$ for $n \to 0$. For decreasing n, the eigenvalues corresponding to different azimuthal mode orders move closer; in fact, as n tends to zero, all eigenvalues in a cluster merge. This is explained in Section 5.3. For comparison, the frequency for $j = 1$ in Table 3 is included as a small vertical red line. Cut-on intrinsic modes exhibit complex paths; for example, $m = 0, 1$ of cluster 2 span a wide range of oscillation frequencies as a function of n, while cut-off intrinsic modes only move to higher damping rates. The acoustic (yellow diamond) and intrinsic (left pointing white triangle labelled with $m = 2$) modes do not intersect for a certain n. Both modes pass the same point but for a different n. (For interpretation of the references to color in this figure legend, the reader is referred to the web version of this article.)

half-plane (not depicted here); for details, see Fig. 6. The latter criterion also serves as a test to exclude the possibility that a mode originates from an acoustic resonance frequency outside the considered frequency window.

At the chosen operating conditions, experiments by Durox et al. [41] showed that the MICCA combustor exhibits an unstable spinning mode at 457 Hz. The FEM result is consistent with this by predicting an unstable azimuthal mode at 449 Hz, see Fig. 5. For different operating conditions, a superposition of two unstable modes was observed by Bourgouin et al. [42] in the form of a slanted mode. The slanted mode originates from an interaction between the unstable azimuthal mode and the neighboring unstable axial mode [43]. The computation predicts additional unstable acoustic modes at higher frequencies, with slightly larger growth rates. These growth rates are likely overestimated since the model does not account for damping effects, which typically increase with frequency. A further potential source of discrepancy is the fitting of the original FDF of [27] to an n–τ model. Unstable intrinsic modes are predicted but these have comparatively low growth rates. The experimentally observed instability reported in [41] is, thus, due to the acoustic feedback mechanism.

The three clusters are separated by a real spacing of $\Delta f = 1/\tau$ (within almost 1 Hz for the modes of highest azimuthal order). This is precisely the real spacing predicted in Eq. (3), which is also observed in the model problem of Section 3. The surprisingly ordered pattern initially sparked the investigation into the origin of these modes. Modes of the first cluster line up in an orderly fashion. For the second cluster, this is only the case for the upper half of the modes, and for the third cluster, only the two modes of highest azimuthal order do so. If a mode is separated from its cluster, it also no longer adheres to the spacing $\Delta f = 1/\tau$ and consequently neither to the 1D result of Eq. (3). Next, it is explained how azimuthal cut-off frequencies affect the separation of intrinsic modes from their respective clusters.

5.2. Azimuthal intrinsic modes of evanescent type

In acoustic waveguides, such as ducts of circular or annular cross section, plane waves, whose amplitude is constant over the duct cross section, always propagate. However, transverse waves propagate along the duct only at frequencies above their respective cut-off frequency; otherwise, these waves experience exponential decay in the axial direction – they are evanescent. The cut-off frequency for a given transverse mode is a function of the cross-sectional geometry and the speed of sound [35]. For the combustion chamber in the MICCA configuration, the cut-off frequencies for the first and second azimuthal mode are given in Table 1 and plotted in Fig. 5 as vertical dash-dotted lines. Below 1700 Hz, only the two modes of lowest azimuthal mode order are cut-on in the combustion chamber. However, intrinsic modes of much higher mode orders are observed.

The modes of the first cluster depicted in Fig. 5 are all below their respective cut-off frequencies. These modes are confined to the immediate vicinity of the flame, as illustrated on the basis of the modes of azimuthal orders 3 and 8 in Fig. 7. A subsequent cut through the modes reveals their evanescent character, which increases with mode order, see Fig. 8.

The axial decay of an evanescent wave in the CC starts just downstream of the flame zone (l_F). Based on Eq. (18) and with the eigenvalues ω from Table 2, the axial amplitude distribution of an evanescent wave downstream of the flame takes the form

$$\hat{p}(z) \sim e^{-ik(z-l_F)}\,, \tag{24}$$

where k is given by Eq. (18). Figure 8 shows that the modes of high azimuthal order agree well with the evanescent result of Eq. (24). At a given clustering frequency, the higher the azimuthal order of a mode, the further away it is from its associated cut-off frequency and the stronger is the axial attenuation. This is visible in the mode shape as a strong exponential decay in longitudinal direction. If the longitudinal decay is sufficiently strong, the mode is unaffected by the outlet boundary condition, see the modes of high azimuthal order in Fig. 8. This is an environment somewhat similar to anechoic boundary conditions, which were shown to facilitate 'pure' intrinsic modes [16,18,19,44].

Table 3 lists the observed frequencies and the values predicted by Eq. (1). A strong similarity is evident, even though the cut-off modes experience very different boundary conditions. The stronger cut-off a mode is, the closer its frequency is to the one-dimensional result for anechoic terminations of Eq. (1). The difference in boundary conditions does not appear to affect the frequencies. However, amplification/attenuation rates do not agree:

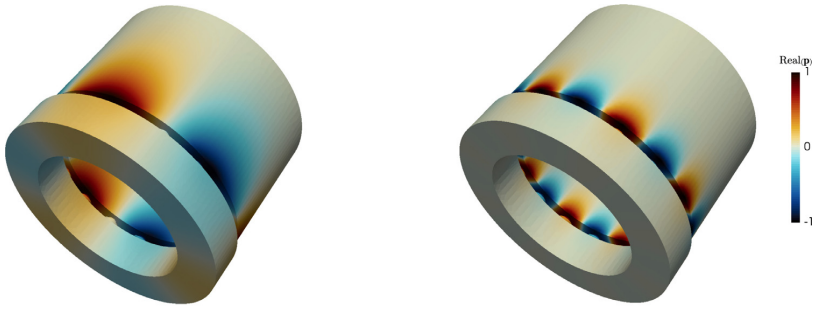

(a) Mode #4 ($\triangledown, m = 3$) (b) Mode #9 ($\triangledown, m = 8$)

Fig. 7. Real part of the azimuthal modes $m = 3, 8$ of cluster 1, see Fig. 5 and Table 2. Mode #4 is degenerate, but only one mode of the degenerate pair is depicted. The modes are dominant at the inlet to the combustion chamber. Mode #4, with lower azimuthal order, extends further into the CC than #9, which is of higher azimuthal order. This trend is confirmed for the remaining modes of cluster 1 ($m = 2, 4, 5, 6, 7$).

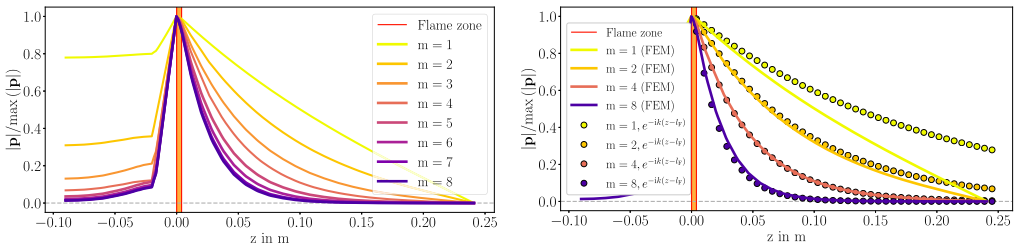

(a) (b)

Fig. 8. Cluster 1: normalized absolute value of the pressure **p** over the axial coordinate along a burner axis for azimuthal modes. The colors correspond to those in Fig. 5. Left: All modes are cut-off and a higher mode order corresponds to a stronger cut-off. The mode with $m = 1$ is just barely cut-off. Right: FEM results (solid line) and ansatz for evanescent waves Eq. (24) (dots). The ansatz matches well for strongly cut-off modes. Modes of lower azimuthal order are weakly cut-off and experience the pressure node boundary condition at the outlet: the mode shapes deviate from the purely evanescent character as Eq. (24) does not account for reflective boundary conditions.

Table 2
List of active modes depicted in Fig. 5, sorted by increasing oscillation frequency. Only azimuthal mode orders m are listed. Except for the $m = 8$ modes, all azimuthal modes ($m > 0$) are degenerate, with multiplicity two. Plenum modes are labeled with (PL), and all other modes are dominant in the CC. The two azimuthal CC modes of acoustic origin are highlighted **in boldface**. Intrinsic modes belong to one of the three clusters (symbols $\triangledown, \triangleleft$ and $\triangle$ in Fig. 5.). The azimuthal modes $m = 1, 2$ of cluster 3 are not in the considered frequency range. Between modes #9 and #21 (modes #21 and #32) a real spacing of $\Delta f = 650.37$ Hz (650.12 Hz) is observed, which is approximately $1/\tau = 649.35$ Hz.

No.	f in Hz	$\mathrm{Im}\left(\frac{\omega}{2\pi}\right)$ in s^{-1}	m	cluster	No.	f in Hz	$\mathrm{Im}\left(\frac{\omega}{2\pi}\right)$ in s^{-1}	m	cluster
1	138.15	+82.79	0	1	18	974.97	+127.47	5	2
2	266.07	+83.11	1	1	19	975.47	+142.86	6	2
3	321.80	+65.91	2	1	20	975.57	+152.81	7	2
4	324.62	+87.27	3	1	21	975.58	+156.23	8	2
5	325.08	+111.46	4	1	22	1039.63	−33.67	3 (PL)	acoustic
6	325.19	+131.94	5	1	23	1250.93	+69.63	0	2
7	325.21	+157.21	7	1	24	1298.73	−0.04	1	2
8	325.21	+147.46	6	1	25	1301.47	+0.29	4 (PL)	acoustic
9	325.21	+160.55	8	1	**26**	**1490.70**	**−114.07**	**2**	**acoustic**
10	384.05	−125.01	0 (PL)	Acoustic	27	1590.47	+109.23	5	3
11	449.32	−80.62	1 (PL)	Acoustic	28	1622.36	+136.42	6	3
12	686.37	+8.49	2 (PL)	Acoustic	29	1622.91	−3.59	3	3
13	830.47	−148.97	0	Acoustic	30	1623.78	+55.92	4	3
14	**910.64**	**−129.42**	**1**	**Acoustic**	31	1625.35	+144.46	7	3
15	924.93	+93.36	3	2	32	1625.70	+147.69	8	3
16	971.71	+110.15	4	2	33	1638.85	−4.72	5 (PL)	acoustic
17	974.11	−34.66	2	2	34	1668.24	+97.61	0	3

Eq. (1) gives $\mathrm{Im}(\omega/2\pi) = +10.89 s^{-1}$ while all clustered intrinsic modes in the MICCA combustor are damped much stronger.

Figure 5 shows that the mode of azimuthal order $m = 1$ is visibly separated from the first cluster of intrinsic modes. In the second cluster, modes $m = 1, 2, 3$ are separated and mode $m = 2$ is even cut-on. The relation between the degree of the cut-off and separation from a cluster can be explained by considering the cut through the mode shapes in Fig. 9. Modes $m = 2, 3$ are cut-off but the exponential decay is not strong enough: the modes still have to fulfill the outlet boundary condition. Modes of higher order than $m = 3$ have essentially decayed to zero upstream of the outlet. Even though a mode is cut-off, if its mode shape is affected

Table 3
Frequencies according to Eq. (1) for a 1D Rijke tube with anechoic terminations and the frequencies of the intrinsic modes in the MICCA combustor with the most strongly evanescent character (highest azimuthal mode order in their respective cluster) from Table 2.

	$j=0$	$j=1$	$j=2$
$\frac{\pi(2j+1)}{\tau}$	324.68 Hz	974.03 Hz	1623.38 Hz
	cluster 1	cluster 2	cluster 3
$m=8$	325.21 Hz	975.58 Hz	1625.70 Hz

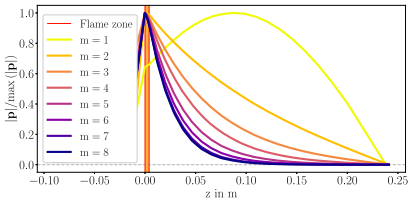

Fig. 9. Cluster 2: normalized absolute value of the pressure **p** over the axial coordinate along a burner axis for intrinsic modes of different azimuthal orders. Mode $m=1$ is cut-on and exhibits a quarter-wave shape. Modes $m=2,3$ are cut-off but the exponential decay is not sufficiently strong so that they are affected by the pressure node at the outlet. Both modes deviate from the purely evanescent character and are, consequently, separated from their cluster, see the spectrum in Fig. 5 and for more detail Fig. 6.

by the boundary condition, then so is its frequency. A shift in the frequency away from the cluster then occurs, and the eigenvalue expression from the one-dimensional case, Eq. (1), does no longer hold. The modes experience acoustic reflection at the outlet and are, thus, not purely intrinsic anymore. Most clearly, the cut-on mode $m=1$ of cluster 2 shows a distinct quarter-wave structure, very different from the evanescent modes of higher azimuthal order in its cluster. For the third cluster, more modes exhibit this behavior since even more modes are close, or even above, their respective cut-off frequencies.

The spectrum also contains three intrinsic modes of axial type. These are always cut-on and, hence, separated from their respective cluster.

The pattern in Fig. 6 for $n=0.05$ is qualitatively similar to the pattern observed in the results from the analytical model (Fig. 2). In the latter case, less separation of individual modes from their respective cluster is observed and grouping is straightforward.

5.3. The limiting case of an acoustically weak flame

As discussed in Section 1.1 on the basis of Eq. (1), the frequency spacing between two intrinsic modes in a Rijke tube with anechoic boundaries is $\Delta f = 1/\tau$. One can furthermore deduce from Eq. (1) that $\mathrm{Im}\,\omega \to +\infty$, as $n \to 0$. Figure 6 shows that all modes of non-acoustic origin exhibit increasingly higher damping rates as the interaction index tends to zero, consistent with the theoretical prediction. Consequently, every mode not originating from a passive acoustic mode is considered of intrinsic origin. Figure 6 also shows that intrinsic modes close to or above their respective cut-off frequency ($m=0,1,2$ in the figure) exhibit non-trivial trajectories as functions of n. Cut-off intrinsic modes remain close to one frequency for all values of n and only show a change in their imaginary part.

In each intrinsic cluster, only modes up to azimuthal order $m=8$ are observed. In contrast, in the analytical model, modes of arbitrarily high azimuthal order can be found. Modes of acoustic origin (or purely acoustic modes in systems without flame response) in an annular combustor can have much higher azimuthal orders than half the number of burners; in fact, the azimuthal order can be arbitrarily high. Bloch-wave theory ascertains that all modes can be represented with Bloch wave numbers up to ± 8. But the equivalence between Bloch wave number and azimuthal mode order holds only for small azimuthal mode orders (see Mensah et al. [12]). Modes of any azimuthal order can still be represented with Bloch wave numbers up to ± 8 because waves can form on the sub-unit-cell scale. For example, a mode of azimuthal order 9 can be represented as a Bloch wave with Bloch wave number 7; the part of the solution that is periodic on the unit cell then hosts one wave length on the cell.

The observed maximum mode order is explained by considering the limit $n \to 0$ for the intrinsic modes in one cluster. As we know from previous studies on intrinsic modes, and as also our results in the present work show, the growth rates of intrinsic modes tend to negative infinity as $n \to 0$, see Fig. 6. In this limit, the modes are infinitely confined to the immediate vicinity of the flame, as they are infinitely damped ($\mathrm{Im}\,\omega \to \infty$). But then the flames do not affect each other and become effectively uncoupled. This situation is conceptually similar to 16 identical but isolated combustors. Such a configuration must exhibit a 16-fold degeneracy because each combustor has the same eigenvalues (as they are identical and uncoupled). This degeneracy is semi-simple, i.e. it has a full eigenspace with finite eigenvalue sensitivity. It is easy to see that these eigenvalues are not defective; in fact, an obvious basis for the degenerate eigenspace is the set of the 16 individual flame modes. An alternative basis is given by a set of 16 Bloch waves that recombine the 16 individual flame modes by modulating them according to the 16 sixteen-point discrete Fourier modes. It is the latter basis into which the degenerate eigenspace unfolds when n is perturbed from zero. As soon as $n > 0$, the intrinsic modes exhibit only finite damping ($\mathrm{Im}\,\omega < \infty$) and the flames start communicating so that the system becomes fully coupled. The only degeneracy that remains is that generally associated with 16-fold discrete rotational symmetry, i.e. modes of azimuthal order 0 and multiples of 8 being simple and all others being two-fold degenerate. However, the sum of all algebraic multiplicities of all eigenvalues in one cluster must be conserved (i.e. it remains 16 for all values of n) because the eigenvalues are continuous functions of the parameter (here, the interaction index n), see [40]. Assuming that the lower-order azimuthal modes are populated first, the total algebraic multiplicity of 16, originating from the $n \to 0$ limit, is only sufficient to go up to azimuthal order $m=8$ (because modes with $m=1,\ldots,7$ are two-fold degenerate).

5.4. Closeness of intrinsic modes to acoustic modes

Figure 5 shows that intrinsic modes are located close to modes of acoustic origin. The two insets to the right in Fig. 5 depict the two cases with the modes being closest. Evidently, modes of intrinsic origin can appear not only at non-acoustic resonance frequencies, but also very close to the passive acoustic modes. As a consequence, the nature of a mode cannot be established solely by its frequency but requires analysis of the mode shape or its locus in the complex plane as a function of the interaction index n (or another suitable parameter).

5.5. Unstable intrinsic modes

Three intrinsic modes are unstable for $n=0.9$, see Table 2. Figure 10 shows the values of n for which all intrinsic modes depicted in Fig. 5 become unstable. Nearest-neighbor continuation is utilized to obtain the unstable n values, but the computation is not continued for modes that remain stable for $n < 10$. The majority of modes of intrinsic origin become unstable for sufficiently high

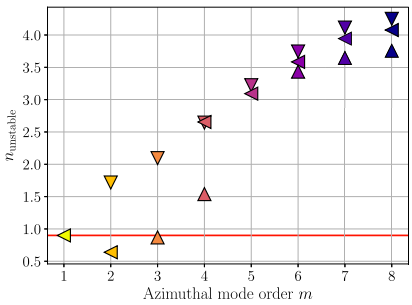

Fig. 10. The values of the interaction index, for which the intrinsic modes enter the unstable half-plane. Markers and colors chosen according to Fig. 5. The red line corresponds to the value $n = 0.9$. Modes #1 ($\triangledown, m = 1$), #14 ($\triangleleft, m = 3$) and #26 ($\triangle, m = 5$) did not become unstable for $n < 10$ and are, thus, not depicted. For these modes the computation was not continued further. Note that the modes of cluster 3 with $m = 1, 2$ are outside of the considered frequency range and not investigated here. The axial intrinsic modes (not depicted here) become unstable for $n = 2.613$ (mode #23) and $n = 3.140$ (mode #34); mode #1 did not become unstable for $n < 10$.

n. In addition, it can be observed that modes with higher frequencies, closer to or below their respective cut-off frequencies, become unstable for lower values of the interaction index than modes with lower frequencies.

Two unstable intrinsic modes of special interest can be seen in Fig. 6 for $n = 0.9$. Both modes originate from the same cluster. One mode ($m = 1$) is cut-on and marginally unstable, while the other one ($m = 2$) is unstable despite being cut-off. Somewhat unexpectedly, the mode of higher azimuthal mode order is encountered at a lower frequency and exhibits a larger growth rate.

6. Conclusion

The intrinsic feedback mechanism in annular thermoacoustic systems is illustrated on the basis of an annular laboratory model combustor. Modes originating from the intrinsic mechanism form clusters, with frequencies that correspond to those of intrinsic modes in a simple single-flame Rijke tube.

The clustering of the eigenvalues is related to the acoustic cut-off mechanism for non-planar modes. In fact, the evanescent character of cut-off azimuthal modes provides an environment similar to non-reflective boundary conditions, hence the concurrence with intrinsic modes in an anechoic single-flame setup. This environment allows intrinsic modes of different azimuthal orders to exist at very similar frequencies and, thus, to form clusters. However, not all intrinsic modes are clustered. Those that are too close to or even above their cut-off frequency are affected by the outlet boundary condition. This manifests as a marked separation from the intrinsic eigenvalue cluster.

The intrinsic mechanism scrutinized in this work is not new per se. It is of the same origin as in single-flame systems, where it has been studied in detail over the last 5 years. In the present work, it has been shown how the very same mechanism manifests itself in an annular geometry in the form of intrinsic azimuthal modes, and the crucial role of the cut-off mechanism has been highlighted. In the present configuration, the modes with the largest growth rates are not intrinsic and would not be observed in experiments. An increase of acoustic losses at the boundaries could dampen the acoustic modes to a point at which an intrinsic mode is the most unstable one; this would potentially facilitate observing a thermoacoustic mode of intrinsic origin experimentally.

For the first time, a systematic and complete description of the thermoacoustic spectrum of an annular combustor has been given. Previously, this has only been available for single-flame configurations. The intrinsic mechanism explored in this paper can be expected to be generically present in all annular acoustic configurations with flame response. We conjecture that earlier numerical studies of thermoacoustic modes in annular combustion chambers did not observe intrinsic mode clusters because they are challenging to find numerically with iterative methods. In the present work, the non-iterative method of Beyn [31] has been utilized for the solution of the nonlinear eigenvalue problem associated with the thermoacoustic Helmholtz equation. This was essential in order to determine all eigenvalues of acoustic and intrinsic origin.

Declaration of Competing Interest

The authors declare that they have no competing financial interests or personal relationships that could have appeared to influence the work reported in this paper.

Appendix A. Numerical solution of the nonlinear eigenvalue problem

The problem size of $\mathbf{L}(\omega)$ in Eq. (23) prohibits the application of root-finding algorithms to the determinant $\det \mathbf{L}(\omega)$. Two applicable solution strategies are briefly described in this appendix: a non-iterative strategy based on contour integration due to Beyn [31] and a Newton-based iterative algorithm.

Both methods are part of the NLEVP-solution routines of PyHoltz [37]. The parameters employed in both methods to obtain the results of Section 5.1 are listed in Table A.4.

A.1. Beyn's method based on contour integration

The original work of Beyn [31] extensively covers the technical details of his method. A concise and less technical description of the theoretical background and guidelines for the application to thermoacoustic problems are given in [47]. We refer to both papers for details and only summarize the main ideas of the technique here. Beyn's method returns all eigenvalues and corresponding eigenvectors inside a user-specified contour in the complex plane.

In short, two variants of the inverse $\mathbf{L}(z)^{-1}$ of Eq. (23) are numerically integrated along a closed contour Γ in the complex plane, specified by the user:

$$\oint_\Gamma z^p \mathbf{L}(z)^{-1}\hat{\mathbf{V}}\,\mathrm{d}z \approx \sum_{j=0}^{N-1} \alpha_j z_j^p \mathbf{L}\left(z_j\right)^{-1}\hat{\mathbf{V}} = \mathbf{A}_p,\ p \in \{0, 1\}\,. \tag{A.1}$$

Gauss–Legendre integration with N sampling points z_j and corresponding weights α_j is used for computing the moment matrices $\mathbf{A}_0$ and $\mathbf{A}_1$. The contour Γ is the domain of interest, spanning the oscillation frequencies and amplification/attenuation rates to be considered. The algorithm avoids complete inversion of $\mathbf{L}(z_j)$ to

Table A.4
Parameters employed in Beyn's method (see [31] and [47] for details) and Newton iterations. Beyn's method is performed with a series of overlapping circles of radius 160 Hz to obtain the results in Fig. 5. All eigenvalues presented in this paper have been converged in the Newton method using the listed parameters, with the values obtained by Beyn's method as initial guesses.

l	N	tol_σ
32	72	1.0×10^{-10}
$\mathrm{tol}_{\Delta\omega}$	$\mathrm{tol}_{\mathrm{residual}}$	Relaxation
1.0×10^{-4}	1.0×10^{-4}	0.5

reduce numerical cost by solving the linear system $\mathbf{L}(z_j)^{-1}\hat{\mathbf{V}}$ at every sampling point. The random matrix $\hat{\mathbf{V}} \in \mathbb{C}^{d\times l}$ is chosen s.t. the number of columns l is smaller than the expected sum of the geometric multiplicities of all eigenvalues inside Γ. The parameter l needs to be chosen with care to limit computational cost. A discussion of an adequate choice for thermoacoustic applications can be found in [47]. From the $\mathbf{A}_p$ matrices all eigenpairs inside the contour Γ are obtained following an advantageous decomposition, see [31].

Simple, semi-simple and even defective eigenvalues can be computed. This technique is, thus, suitable for systems with spatial symmetries and for the recently discussed exceptional points [45]. Beyn's method can be employed as a black box solver for arbitrary NLEVPs, but requires $\mathbf{L}(\omega)$ to depend analytically on ω, which is the case in the present formulation due to the n–τ model and the chosen boundary conditions.

A.2. Iterative method

In Beyn's method the matrices $\mathbf{A}_p$ have to be computed with an increase in the number of sampling points N (or l) to establish convergence, which is a costly step. Instead, it is less costly and quicker to perform Beyn's method once and use the result in a locally convergent iterative method. A Newton-type method that is known as generalized Rayleigh quotient iteration [46] is employed for this purpose. The method reformulates the problem as a linear eigenvalue problem

$$\mathbf{L}(\omega)\mathbf{p} = \lambda\mathbf{M}\mathbf{p} \tag{A.2}$$

in the auxiliary eigenvalue λ. The goal is to find an ω such that $\lambda = 0$ is an eigenvalue of the linear eigenvalue problem. First-order perturbation theory is used to compute the derivative $\frac{\mathrm{d}\lambda}{\mathrm{d}\omega}$ and, thus, to facilitate a Newton iteration to solve the problem. With good initial values, the Newton method converges in a few iterations.

To establish convergence, two criteria are checked: a tolerance on the residual following [31] (with $\mathbf{p}$ normalized in $\|\cdot\|_2$), and the relative change in the eigenvalue:

$$||\mathbf{L}(\omega)\mathbf{p}||_2 < \mathrm{tol}_{\mathrm{residual}}\,, \tag{A.3}$$

$$\frac{|\omega_{i+1} - \omega_i|}{|\omega_i|} < \mathrm{tol}_{\Delta\omega}\,. \tag{A.4}$$

Iterative algorithms require good initial values. The acoustic resonance frequencies are a suitable choice to compute the modes of acoustic origin. The results in this paper demonstrate that the intrinsic modes can appear seemingly anywhere in the complex plane. Therefore, a suitable initial value is hard to come up with for intrinsic modes. Here, Beyn's method is the ideal tool to compute these. As a check, eigenvalues from Beyn's method are entered into the Newton method because Beyn's method can return numerically spurious eigenvalues, see [47] for details and a discussion.

References

[1] T. Poinsot, Prediction and control of combustion instabilities in real engines, Proc. Combust. Inst. 36 (1) (2017) 1–28.
[2] T. C. Lieuwen, V. Yang (Eds.), Combustion Instabilities in Gas Turbine Engines, volume 210 of Prog. Astronaut. Aeronaut., AIAA, Inc., 2005.
[3] G. Staffelbach, L. Gicquel, T. Poinsot, Large eddy simulation of self-excited azimuthal modes in annular combustors, Proc. Combust. Inst. 32 (2) (2009) 2909–2916.
[4] P. Wolf, G. Staffelbach, L. Gicquel, D. Müller, T. Poinsot, Acoustic and large eddy simulation studies of azimuthal modes in annular combustion chambers, Combust. Flame 159 (2012) 3398–3413.
[5] J. Gikadi, Prediction of Acoustic Modes in Combustors Using Linearized Navier–Stokes Equations in Frequency Space, Technische Universität München, 2014 (Ph.D. thesis).
[6] M. Schulze, T. Hummel, N. Klarmann, F. Berger, B. Schuermans, T. Sattelmayer, Linearized Euler equations for the prediction of linear high-frequency stability in gas turbine combustors, J. Eng. Gas Turbines Power 139 (3) (2017) 031510.
[7] F. Nicoud, L. Benoit, C. Sensiau, T. Poinsot, Acoustic modes in combustors with complex impedances and multidimensional active flames, AIAA J. 45 (2) (2007) 426–441.
[8] S. Evesque, W. Polifke, Low-order acoustic modelling for annular combustors: Validation and inclusion of modal coupling, ASME turbo expo 2002: power for land, sea, and air, ASME paper GT-2002-30064 (2002), pp. 321–331.
[9] B. Schuermans, V. Bellucci, C.O. Paschereit, Thermoacoustic modeling and control of multi burner combustion systems, ASME Turbo Expo 2003, collocated with the 2003 International Joint Power Generation Conference, ASME paper 2003-GT-38688 (2003), pp. 509–519.
[10] T. Sattelmayer, W. Polifke, Assessment of methods for the computation of the linear stability of combustors, Combust. Sci. Technol. 175 (2003) 453–476.
[11] S.M. Camporeale, B. Fortunator, G. Campa, A finite element method for three-dimensional analysis of thermo-acoustic combustion instability, J. Eng. Gas Turbines Power 133 (1) (2011) 15506.
[12] G.A. Mensah, G. Campa, J.P. Moeck, Efficient computation of thermoacoustic modes in industrial annular combustion chambers based on Bloch wave theory, J. Eng. Gas Turbines Power 138 (8) (2016) 81502.
[13] M. Bauerheim, F. Nicoud, T. Poinsot, Progress in analytical methods to predict and control azimuthal combustion instability modes in annular chambers, Phys. Fluids 28 (2016) 021303.
[14] T.C. Lieuwen, Unsteady combustor physics, Cambridge University Press, 2012, p. 138.
[15] P. Hoeijmakers, Flame-acoustic coupling in combustion instabilities, Technische Universiteit Eindhoven, 2014 (Ph.D. thesis).
[16] M. Hoeijmakers, V. Kornilov, I.L. Arteaga, P. de Goey, H. Nijmeijer, Intrinsic instability of flame–acoustic coupling, Combust. Flame 161 (11) (2014) 2860–2867.
[17] S. Bomberg, T. Emmert, W. Polifke, Thermal versus acoustic response of velocity sensitive premixed flames, Proc. Combust. Inst. 35 (3) (2015) 3185–3192.
[18] T. Emmert, S. Bomberg, W. Polifke, Intrinsic thermoacoustic instability of premixed flames, Combust. Flame 162 (1) (2015) 75–85.
[19] N.K. Mukherjee, V. Shrira, Intrinsic flame instabilities in combustors: Analytic description of a 1-d resonator model, Combust. Flame 185 (2017) 188–209.
[20] E. Courtine, L. Selle, T. Poinsot, DNS of intrinsic thermoacoustic modes in laminar premixed flames, Combust. Flame 162 (11) (2015) 4331–4341.
[21] K.R. McManus, T. Poinsot, S. Candel, A review of active control of combustion instabilities, Prog. Energy Combust. Sci. 19 (1) (1993) 1–29.
[22] A. Orchini, C.F. Silva, G.A. Mensah, J.P. Moeck, Thermoacoustic modes of intrinsic and acoustic origin and their interplay with exceptional points, Combust. Flame 211 (2020) 83–95.
[23] E. Courtine, L. Selle, F. Nicoud, W. Polifke, C. Silva, M. Bauerheim, T. Poinsot, Causality and intrinsic thermoacoustic instability modes, Proceedings of the summer program, Center for Turbulence Research (2014), p. 169.
[24] C.F. Silva, M. Merk, T. Komarek, W. Polifke, The contribution of intrinsic thermoacoustic feedback to combustion noise and resonances of a confined turbulent premixed flame, Combust. Flame 182 (2017) 269–278.
[25] A. Ghani, T. Steinbacher, A. Albayrak, W. Polifke, Intrinsic thermoacoustic feedback loop in turbulent spray flames, Combust. Flame 205 (2019) 22–32.
[26] J.-F. Bourgouin, D. Durox, J. Moeck, T. Schuller, S. Candel, Self-sustained instabilities in an annular combustor coupled by azimuthal and longitudinal acoustic modes, ASME paper GT2013-95010, 2013.
[27] J.-F. Bourgouin, D. Durox, J. Moeck, T. Schuller, S. Candel, Characterization and modeling of a spinning thermoacoustic instability in an annular combustor equipped with multiple matrix injectors, J. Eng. Gas Turbines Power 137 (2) (2015) 021503.
[28] D. Laera, K. Prieur, D. Durox, T. Schuller, S. Camporeale, S. Candel, Flame describing function analysis of standing modes in an annular combustor and comparison with experiments, Thermoacoustic Instabilities in Gas Turbines and Rocket Engines: Industry meets Academia, Paper No: GTRE-044, Munich, Germany, 2016.
[29] D. Laera, K. Prieur, D. Durox, T. Schuller, S. Camporeale, S. Candel, Impact of heat release distribution on the spinning modes of an annular combustor with multiple matrix burners, J. Eng. Gas Turbines Power 139 (5) (2017a) 051505.
[30] D. Laera, G. Campa, S. Camporeale, A finite element method for a weakly nonlinear dynamic analysis and bifurcation tracking of thermo-acoustic instability in longitudinal and annular combustors, Appl. Energy 187 (2017b) 216–227.
[31] W.-J. Beyn, An integral method for solving nonlinear eigenvalue problems, Linear Algebra Appl. 436 (2012) 3839–3863.
[32] L. Crocco, S.-I. Cheng, Theory of combustion instability in liquid propellant rocket motors, AGARDograph No. 8, Butterworths Scientific Publications, 1956.
[33] W. Polifke, C.O. Paschereit, K. Döbbeling, Constructive and destructive interference of acoustic and entropy waves in a premixed combustor with a choked exit, Int. J. Acoust. Vib. 6 (3) (2001) 135–146.
[34] D. Yang, A.S. Morgans, Low-order network modeling for annular combustors exhibiting longitudinal and circumferential modes, ASME turbo expo 2018: turbomachinery technical conference and exposition, American Society of Mechanical Engineers, 2018. V04BT04A026–V04BT04A026
[35] S.W. Rienstra, A. Hirschberg, An Introduction to Acoustics, Report IWDE 92-06, Eindhoven University of Technology, 2018.

[36] C.F. Silva, K.J. Yong, L. Magri, Thermoacoustic modes of quasi-one-dimensional combustors in the region of marginal stability, J. Eng. Gas Turbines Power 141 (2) (2019) 021022.
[37] G.A. Mensah, P.E. Buschmann, A. Orchini, J.P. Moeck, Pyholtz, 2018, (https://bitbucket.org/pyholtzdevelopers/public.git).
[38] S. Güttel, F. Tisseur, The nonlinear eigenvalue problem, Acta Numer. 26 (2017) 1–94.
[39] V. Mehrmann, H. Voss, Nonlinear eigenvalue problems: a challenge for modern eigenvalue methods, GAMM-Mitteilungen 27 (2) (2014) 121–152.
[40] T. Kato, Perturbation theory for linear operators, 2nd, Springer, Berlin, Heidelberg, 1980.
[41] D. Durox, J.-F. Bourgouin, J.P. Moeck, M. Philip, T. Schuller, S. Candel, Nonlinear interactions in combustion instabilities coupled by azimuthal acoustic modes, International summer school and workshop on non-normal and nonlinear effects in aero- and thermoacoustics, Munich, 2013.
[42] J.-F. Bourgouin, D. Durox, J. Moeck, T. Schuller, S. Candel, A new pattern of instability observed in an annular combustor: the slanted mode, Proc. Combust. Inst. 35 (2015) 3237–3244.
[43] J.P. Moeck, D. Durox, T. Schuller, S. Candel, Nonlinear thermoacoustic mode synchronization in annular combustors, Proc. Combust. Inst. 37 (2019) 5343–5350.
[44] C.F. Silva, T. Emmert, S. Jaensch, W. Polifke, Numerical study on intrinsic thermoacoustic instability of a laminar premixed flame, Combust. Flame 162 (2015) 3370–3378.
[45] G.A. Mensah, L. Magri, C.F. Silva, P.E. Buschmann, J.P. Moeck, Exceptional points in the thermoacoustic spectrum, J. Sound Vib. 433 (2018) 124–128.
[46] P. Lancaster, A generalised Rayleigh quotient iteration for lambda-matrices, Arch. Ration. Mech. Anal. 8 (1) (1961) 309.
[47] P.E. Buschmann, G.A. Mensah, F. Nicoud, J.P. Moeck, Solution of Thermoacoustic Eigenvalue Problems with a Non-iterative Method, J. Eng. Gas Turbines Power (2019), doi:10.1115/1.4045076.

Iterative Solvers for the Thermoacoustic Nonlinear Eigenvalue Problem and Their Convergence Properties

Symposium on Thermoacoustics in Combustion: Industry meets Academia (SoTiC 2021)
Sept. 6 - Sept. 10, 2021
Munich, Germany
Paper No.: 8495

Iterative Solvers for the Thermoacoustic Nonlinear Eigenvalue Problem and Their Convergence Properties

Georg A. Mensah[1], Philip E. Buschmann[2] and Alessandro Orchini[1]

Abstract

The spectrum of the thermoacoustic operator is governed by a nonlinear eigenvalue problem. A few different strategies have been proposed by the thermoacoustic community to tackle it and identify the frequencies and growth rates of thermoacoustic eigenmodes. These strategies typically require the use of iterative algorithms, which need an initial guess and are not necessarily guaranteed to converge to an eigenvalue. A quantitative comparison between the convergence properties of these methods has however never been addressed. By using adjoint-based sensitivity, in this study we derive an explicit formula that can be used to quantify the behaviour of an iterative method in the vicinity of an eigenvalue. In particular, we employ Banach's fixed-point theorem to demonstrate that there exist thermoacoustic eigenvalues that cannot be identified by some of the iterative methods proposed in the literature, in particular fixed-point iterations, regardless of the accuracy of the initial guess provided. We then introduce a family of iterative methods known as Householder's methods, of which Newton's method is a special case. The coefficients needed to use these methods are explicitly derived by means of high-order adjoint-based perturbation theory. We demonstrate how these methods are always guaranteed to converge to the closest eigenvalue, provided that the initial guess is accurate enough. We also show numerically how the basin of attraction of the eigenvalues varies with the order of the employed Householder's method.

Keywords

Thermoacoustics, Nonlinear eigenvalue problem, ITA, Basin of attraction

Introduction

Thermoacoustic instabilities can be assessed by solving the inhomogeneous Helmholtz equation

$$\nabla \cdot \left(c^2 \nabla \hat{p}\right) + \omega^2 \hat{p} = (c_2^2 - c_1^2) n(\boldsymbol{x}) e^{-\mathrm{i}\omega\tau} \left.\nabla \hat{p}\right|_{\boldsymbol{x}_{\mathrm{ref}}} \quad (1)$$

on a prescribed geometry with appropriate boundary conditions (Dowling and Stow 2003). In Eq. (1) $\hat{p}$ indicates the complex-valued amplitude of the Fourier transform of the pressure fluctuations (the eigenfunction) and c the speed of sound, with the subscripts $_1$ and $_2$ indicating the regions upstream and downstream the flame, respectively. The interaction index n, which is non-zero only over an acoustically compact volume, and the time delay τ model the flame response (Crocco 1951; Nicoud et al. 2007).

Equation (1) defines a nonlinear eigenvalue problem (NLEVP) in the complex frequency ω. Once discretized, e.g. by means of finite elements, the NLEVP can be expressed in compact form as

$$\mathbf{L}(\omega)\boldsymbol{p} = \mathbf{0}, \quad (2)$$

where $\mathbf{L}$ is an $N \times N$ large, sparse matrix depending nonlinearly on ω. Although there exist efficient algorithms to solve generalized linear eigenvalue problems, for which $\mathbf{L}(\omega) = (\mathbf{X} - \omega\mathbf{Y})$, solving an eigenvalue problem that is nonlinear in the eigenvalue ω is intrinsically harder (Mehrmann and Voss 2004; Effenberger 2013; Güttel and Tisseur 2017). A typical approach is to transform the NLEVP into a (series of) associated eigenvalue problems linear in the eigenvalue. For example:

- NLEVPs that are polynomial in ω with order K can be recast into linear eigenvalue problems of dimension KN (Nicoud et al. 2007);
- Solutions of NLEVPs can be found by iteratively solving linear eigenvalue problems resulting from the expansion of $\mathbf{L}(\omega)$ (to any desired ordered) in the eigenvalue (Güttel and Tisseur 2017);
- Contour integration methods reduce the NLEVP to a linear eigenvalue problem possessing only the eigenvalues of $\mathbf{L}$ inside a given contour in the complex plane (Beyn 2012; Buschmann et al. 2020b).

These approaches exploit the fact that efficient and robust methods (e.g. Arnoldi) exist for large scale linear eigenvalue problems (Lehoucq et al. 1998; Saad 2011). A common feature of iterative methods is that they all require an initial guess ω_1 for the eigenvalue[1], which is updated at every iteration. Eigenvalues of the thermoacoustic operator are fixed points of the mapping defined by the chosen iterative algorithm.

[0][1]Institute of Fluid Dynamics and Technical Acoustics, TU Berlin, DE
[2]Department of Energy and Process Engineering, NTNU Trondheim, NO
[0]
Corresponding author:
a.orchini@tu-berlin.de

[1]Some methods require also an initial guess for the eigenvector. Contour methods instead do not require guesses for the eigenvalues, but a contour within which eigenvalues are sought.

According to Banach's fixed-point theorem (Ciarlet 2013, p. 152), for an iterative algorithm to be able to identify an eigenvalue, the mapping defined by the algorithm needs to be contracting in the vicinity of the eigenvalue. This means that, provided that the initial guess is sufficiently close to an eigenvalue, at each iteration the algorithm will move the guess closer to the eigenvalue, until a prescribed tolerance is reached. On the other hand, if the mapping is repelling in the vicinity of an eigenvalue, it will not be possible to identify this eigenvalue with the chosen algorithm, since a sufficiently close guess will be pushed further away from the solution. An overlooked eigenvalue can have serious consequences in thermoacoustics, as the reliable and accurate determination of all relevant[2] eigenvalues is of paramount importance to ensure the safe operability of an engine.

The fixed-point iteration method described in Nicoud et al. (2007) is a commonly used algorithm for identifying eigenvalues of the thermoacoustic Helmholtz operator – it is used in Sensiau et al. (2008), Sensiau et al. (2009), Wolf et al. (2012), Silva et al. (2013), Campa and Camporeale (2014), and Mensah et al. (2016) to name a few. However, with the exception of a short discussion in Sensiau et al. (2008), there is no reference in the literature investigating the convergence properties of this method in relation to the spectrum of the thermoacoustic operator. The aim of this work is to quantify the convergence properties of fixed-point iteration methods that are commonly used in thermoacoustics. It will be shown that some thermoacoustic eigenvalues cannot be found using a fixed-point algorithm, regardless of the chosen initial guess. We will then introduce an alternative adjoint-based iterative method that has more robust convergence properties and is thus better suited to tackle the thermoacoustic problem.

This study is organized as follows. First the thermoacoustic problem and the fixed-point iteration presented in Nicoud et al. (2007) are introduced. An explicit formula that quantifies the convergence properties of the fixed-point mapping is derived. The same procedure is conducted for a so-called Picard iteration, which is another form of fixed-point iteration. Both methods are applied to a generic thermoacoustic test case to demonstrate that some eigenvalues are repellors with respect to these mappings. We will then introduce a class of adjoint-based solution methods known as Householder, of which Newton's method is a special case. It will be discussed how all eigenvalues of the thermoacoustic operator are attractors with respect to these solution methods, and how the basins of attraction of each eigenvalue vary depending on the order of the Householder's method used.

The thermoacoustic nonlinear eigenvalue problem

The weak formulation and discretization of the thermoacoustic Helmholtz equation (1) results in an N-dimensional NLEVP that reads

$$\mathbf{L}(\omega)\boldsymbol{p} = \left(\mathbf{K} + \omega\mathbf{C} + \omega^2\mathbf{M} + \mathbf{Q}(\omega)\right)\boldsymbol{p} = \mathbf{0}. \tag{3}$$

The matrices in (3) arise from discretizing the operators in equation (1), viz. the stiffness operator $\nabla\cdot\left(c^2\nabla(\cdot)\right) \mapsto \mathbf{K}$, the mass operator $\omega^2(\cdot) \mapsto \omega^2\mathbf{M}$, and the flame operator $-(c_2^2 - c_1^2)n(\boldsymbol{x})e^{-\mathrm{i}\omega\tau}\ \nabla|_{\boldsymbol{x}_{\mathrm{ref}}}(\cdot) \mapsto \mathbf{Q}(\omega)$. The matrix $\mathbf{C}$ results from the discretization of the boundary conditions needed to close the problem. They can be expressed in terms of the acoustic impedance Z on all boundaries

$$\mathrm{i}\omega\hat{p} + \frac{1}{\rho}Z(\omega)\nabla\hat{p}\cdot\hat{\boldsymbol{n}} = 0, \tag{4}$$

where $\hat{\boldsymbol{n}}$ is a unit vector normal to the boundary.

Equation (3) represents a nonlinear eigenvalue problem. The challenge is to find all its eigenvalues ω – and their corresponding eigenvectors $\boldsymbol{p}$ – in a prescribed portion of the complex plane.

Rijke tube test-case

Throughout this study we will employ the classic Rijke tube configuration (McManus et al. 1993) to demonstrate our results. It consists of a straight duct in which a flame is located. Across the flame the temperature, and hence the speed of sound, rise abruptly. The axial flame location x_{f} is chosen to be in the middle of the tube. The parameters that determine the acoustic response of the system are chosen to be identical to those used in Nicoud et al. (2007). By non-dimensionalizing all quantities using the tube length L as a characteristic length and the speed of sound c_1 in the cold section of the duct as a characteristic velocity, the chosen Rijke tube's parameter are $x_{\mathrm{f}} = 0.5$, $c(x) = 1$ for $x \leq x_{\mathrm{f}}$ and $c(x) = 2$ otherwise. The boundary conditions are chosen to be acoustically closed ($\nabla\hat{p} = 0$) and opened ($\hat{p} = 0$) at the inlet ($x = 0$) and outlet ($x = 1$), respectively. The flame model parameters are chosen to be $n = 1/3$ and $\tau = 2$.

For the range of frequencies that we will consider all transverse modes are cut-off. The problem can therefore be considered as one-dimensional, and the flame to be a point source in the Helmholtz equation (1), $n(x) = n\delta(x - x_{\mathrm{f}})$. The eigenvalues of this problem can be calculated semi-analytically by using an acoustic network approach (McManus et al. 1993). By assuming one-dimensional acoustics, equation (1) can be expressed in terms of the Riemann invariants f and g. With suitable matching conditions at the flame zone and for the parameters introduced above, the acoustic-network eigenvalue problem reads (Orchini et al. 2015)

$$\mathbf{L}_{1\mathrm{D}}\begin{bmatrix} g_1 \\ f_2 \end{bmatrix} = \left(\mathbf{L}_{\mathrm{ac}} - \mathbf{L}_{\mathrm{fl}}\right)\begin{bmatrix} g_1 \\ f_2 \end{bmatrix} = \begin{bmatrix} 0 \\ 0 \end{bmatrix}, \tag{5}$$

where $\mathbf{L}_{\mathrm{ac}}$ is the acoustic response in the absence of an active flame

$$\mathbf{L}_{\mathrm{ac}} \equiv \begin{bmatrix} e^{-i\omega} + 1 & e^{-i\omega/2} - 1 \\ 1 - e^{-i\omega} & 2e^{-i\omega/2} + 2 \end{bmatrix}, \tag{6}$$

and $\mathbf{L}_{\mathrm{fl}}$ provides the feedback between heat release rate fluctuations and the acoustics

$$\mathbf{L}_{\mathrm{fl}} \equiv \begin{bmatrix} 0 & 0 \\ e^{-2i\omega}\left(e^{-i\omega} - 1\right) & 0 \end{bmatrix}. \tag{7}$$

[2]NLEVPs can have infinitely many eigenvalues. In thermoacoustics those with frequencies below a threshold – within which the heat release zone is acoustically compact – are of interest, since these are often observed in experiments and for these the thermoacoustic Helmholtz equation (1) is valid.

Table 1. Eigenvalues of the Rijke tube network model (5) in the considered portion of the complex plane together with the associated acoustic (no flame) and intrinsic (anechoic boundary conditions) eigenvalues from which they stem.

#	ω	ω_{ac}	ω_{ITA}
1	2.396-0.262i	2.462+0i	–
2	4.692 +0.304i	–	4.712+0i
3	6.283+0i	6.283+0i	–
4	7.874+0.304i	–	7.854+0i

By imposing $\det(\mathbf{L}_{1\mathrm{D}}) = 0$ the eigenvalues of the Rijke tube can be obtained by using standard root-finder methods. We shall focus our analysis on the properties of the four thermoacoustic eigenvalues found in the region $\mathcal{S}$ of the complex plane delimited by

$$\mathcal{S} = \{\, \omega \mid \Re(\omega) \in [0, 10] \wedge \Im(\omega) \in [-1, 1] \,\}, \tag{8}$$

which are reported in Table 1. Two of these eigenvalues can be linked to acoustic modes – whose eigenvalues ω_{ac} can be calculated by setting $n = 0$, which implies $\mathbf{L}_{\mathrm{fl}} = \mathbf{0}$ – while the other two can be linked to intrinsic thermoacoustic (ITA) modes – whose frequencies are given by (Emmert et al. 2015; Orchini et al. 2020)

$$\omega_{\mathrm{ITA}} = \frac{2k+1}{\tau}\pi - \mathrm{i}\frac{1}{\tau}\log\left[\left(\frac{c_2}{c_1} - 1\right) n\right]. \tag{9}$$

In the following, we will discretize by finite elements the thermoacoustic eigenproblem (3) and use various iterative solution techniques to identify its eigenvalues. The semi-analytical wave-based solutions presented in Table 1 will serve as benchmarks. The dimensions of the resulting matrix operator $\mathbf{L}$ do not allow for the use of determinant-based methods, and alternative iterative strategies are needed.

State-of-the-art iterative solution method

A fixed-point iteration to solve the NLEVP (3) was proposed in Nicoud et al. (2007). This algorithm exploits the fact that the problem is quadratic in ω, except for the heat release term[3]. The flame operator can therefore be thought of as a perturbation of the underlying purely acoustic problem, which is obtained with $\mathbf{Q} = \mathbf{0}$. This motivates the use of an iterative strategy, starting from the (known) purely acoustic solutions.

The key idea is to recast the problem into a linear eigenvalue problem of doubled dimension, and then to iteratively identify a thermoacoustic eigenvalue starting from an initial guess. We shall indicate this linear eigenvalue problem as $\mathbf{L}_{\mathrm{FP}}(\omega_n;\omega)\tilde{\boldsymbol{p}} = \mathbf{0}$. It reads

$$\underbrace{\begin{bmatrix} \mathbf{0} & -\mathbf{I} \\ \mathbf{K}+\mathbf{Q}(\omega_n) & \mathbf{C} \end{bmatrix}}_{\mathbf{X}_{\mathrm{FP}}} \begin{bmatrix} \boldsymbol{p} \\ \boldsymbol{p}_{\mathrm{I}} \end{bmatrix} = -\omega \underbrace{\begin{bmatrix} \mathbf{I} & \mathbf{0} \\ \mathbf{0} & \mathbf{M} \end{bmatrix}}_{\mathbf{Y}_{\mathrm{FP}}} \begin{bmatrix} \boldsymbol{p} \\ \boldsymbol{p}_{\mathrm{I}} \end{bmatrix}. \tag{10}$$

On the the left hand side, the nonlinear dependency of the problem on the eigenvalue has been removed by freezing the evaluation of the flame operator $\mathbf{Q}$, i.e, by evaluating at ω_n, the eigenvalue guess. This guess is updated by iteratively replacing ω_n with the closest eigenvalue ω of (10), which can be found by means of, e.g., the Arnoldi iteration method.

The eigenvector in (10) has been extended into

$$\tilde{\boldsymbol{p}} = [\boldsymbol{p}, \omega\boldsymbol{p}]\,. \tag{11}$$

This can be seen from the first matrix equation defined by (10), which reads $\boldsymbol{p}_{\mathrm{I}} = \omega\boldsymbol{p}$. By using this relation, the second matrix equation of (10) reduces to (3) when $\omega_n = \omega$. The algorithm terminates successfully if the difference between the results of two successive iterations is less than a prescribed tolerance tol_ω, or is aborted if a predefined maximum number of iterations is reached.

Algorithm 1 Nicoud's algorithm

function ITERATE($\omega_1, \boldsymbol{p}_1, \mathrm{tol}_\omega, \mathrm{maxiter}, \mathbf{K}, \mathbf{C}, \mathbf{M}, \mathbf{Q}$)
  $\omega_0 \leftarrow \infty$
  $n \leftarrow 1$
  $\tilde{\boldsymbol{p}}_1 \leftarrow \begin{bmatrix} \boldsymbol{p}_1 \\ \omega_1\boldsymbol{p}_1 \end{bmatrix}$
  $\mathbf{Y}_{\mathrm{FP}} \leftarrow \begin{bmatrix} \mathbf{I} & \mathbf{0} \\ \mathbf{0} & \mathbf{M} \end{bmatrix}$
  while $|\omega_n - \omega_{n-1}| > \mathrm{tol}_\omega$ **and** $n < \mathrm{maxiter}$ **do**
    $\mathbf{X}_{\mathrm{FP}} \leftarrow \begin{bmatrix} \mathbf{0} & -\mathbf{I} \\ \mathbf{K}+\mathbf{Q}(\omega_n) & \mathbf{C} \end{bmatrix}$
    $\boldsymbol{\omega}_{n+1}, \tilde{\boldsymbol{p}}_{n+1} \leftarrow \mathrm{EIGS}(-\mathbf{X}_{\mathrm{FP}}, \mathbf{Y}_{\mathrm{FP}}, \omega_n, \tilde{\boldsymbol{p}}_n)$
    $n \leftarrow n + 1$
  end while
  $\boldsymbol{p}_n \leftarrow \tilde{\boldsymbol{p}}_n[1:N]$
  return $\omega_n, \boldsymbol{p}_n, n$
end function

The pseudocode for the fixed-point iterative scheme is outlined in Alg. 1. We have denoted with $\mathrm{EIGS}(\mathbf{X}, \mathbf{Y}, \omega_1, \boldsymbol{p}_1)$ the Arnoldi method that identifies the eigenpair $\omega, \boldsymbol{p}$ of the linear eigenvalue problem $\mathbf{X}\boldsymbol{p} = \omega\mathbf{Y}\boldsymbol{p}$ closest to ω_1. An initial guess for the eigenvector $\boldsymbol{p}_1$, if known, may also be provided to the algorithm, in order to improve the convergence of the Arnoldi method. Also note that the matrix $\mathbf{M}$ is always positive-definite – as it defines a mass matrix – and hence is $\mathbf{Y}_{\mathrm{FP}}$. Thus, the eigenvalue problem $(\mathbf{X}_{\mathrm{FP}}(\omega_n) - \omega\mathbf{Y}_{\mathrm{FP}})\,\tilde{\boldsymbol{p}} = \mathbf{0}$ appearing at each iteration, can be solved efficiently.

Fixed-point iteration schemes in thermoacoustics

A single iteration of the procedure described in Alg. 1 defines a mapping $\omega_{n+1} = f(\omega_n)$ for which fixed-points ω are sought. This fixed-point map f can be explicitly expressed by rewriting the eigenvalue problem (10) as

$$\mathbf{L}_{\mathrm{FP}}(f;\omega_n)\tilde{\boldsymbol{p}} = (\mathbf{X}_{\mathrm{FP}}(\omega_n) + f\mathbf{Y}_{\mathrm{FP}})\,\tilde{\boldsymbol{p}} = \mathbf{0}. \tag{12}$$

A condition for the convergence of the mapping to an eigenvalue of the thermoacoustic operator is provided by Banach's fixed-point theorem, which we briefly recall. Consider a bounded domain $\Gamma \subset \mathbb{C}$ that contains the fixed-point ω. Banach's fixed-point theorem guarantees that f has

[3] There might also be ω dependent boundary conditions, as discussed in Nicoud et al. (2007). This would not alter the following discussion on the convergence properties of the method.

one (unique) fixed-point in Γ as long as f is a contraction everywhere in Γ.

For our purposes, we are only interested at the behaviour of the iterative map at the fixed-point. In particular, to know if an eigenvalue ω is an attractor of a given iterative method f it is sufficient to verify that

$$|f'(\omega)| < 1. \tag{13}$$

This in fact implies that the mapping f represents a contraction in the vicinity of ω. Provided that Eq. (13) is satisfied, the eigenvalue ω can be found if the initial guess lies sufficiently close to it.

Nicoud et al. (2007) recognized the importance of the contraction properties of f, but stated that "[...] *obtaining general results about the contracting properties of the operator f from physical arguments is out of reach of the current understanding of the thermoacoustic instabilities.*" Significant progress has been made in this direction by the thermoacoustic community in recent years, and tools are now available to quantify the behaviour of the mapping f from the thermoacoustic equations. In particular, the contraction properties of the mapping f can be quantified by exploiting adjoint-based sensitivity (Magri et al. 2016; Orchini and Juniper 2016). In the following, we use adjoint methods to derive an analytical expression that allows us to compute $|f'(\omega)|$ and thus make explicit use of Banach's theorem.

Contraction properties of the fixed-point iteration

The adjoint equation associated with the mapping (12) reads:

$$\mathbf{L}^{\dagger}_{\mathrm{FP}}(f;\omega)\tilde{\boldsymbol{p}}^{\dagger} = \left(\begin{bmatrix} \mathbf{0} & \mathbf{K}^{\mathrm{H}}+\mathbf{Q}^{\mathrm{H}}(\omega) \\ -\mathbf{I} & \mathbf{C}^{\mathrm{H}} \end{bmatrix} + f^{*}\begin{bmatrix} \mathbf{I} & \mathbf{0} \\ \mathbf{0} & \mathbf{M}^{\mathrm{H}} \end{bmatrix}\right)\begin{bmatrix} \boldsymbol{p}^{\dagger}_{\mathrm{I}} \\ \boldsymbol{p}^{\dagger} \end{bmatrix} = \mathbf{0}, \tag{14}$$

where f^{*} denotes the complex conjugate of f. Its fixed-points are found when $f^{*}=\omega^{*}$. The second matrix equation defined by (14) shows that $\boldsymbol{p}^{\dagger}_{\mathrm{I}} = \left(\mathbf{C}^{\mathrm{H}}+\omega^{*}\mathbf{M}^{\mathrm{H}}\right)\boldsymbol{p}^{\dagger}$, so that the extended adjoint eigenvector $\tilde{\boldsymbol{p}}^{\dagger}$ satisfies

$$\tilde{\boldsymbol{p}}^{\dagger} = \left[\left(\mathbf{C}^{\mathrm{H}}+\omega^{*}\mathbf{M}^{\mathrm{H}}\right)\boldsymbol{p}^{\dagger}, \boldsymbol{p}^{\dagger}\right]^{\mathrm{T}}. \tag{15}$$

The first matrix equation in (14) defines the adjoint eigenvalue problem $\mathbf{L}^{\dagger}(\omega)\boldsymbol{p}^{\dagger}=\mathbf{0}$.

From adjoint-based sensitivity analysis, the following formula is known for evaluating the derivative of f with respect to ω (Magri et al. 2016; Orchini and Juniper 2016):

$$f' = \frac{df}{d\omega} = -\frac{\left\langle \tilde{\boldsymbol{p}}^{\dagger}\middle|\dfrac{\partial \mathbf{L}_{\mathrm{FP}}}{\partial\omega}\tilde{\boldsymbol{p}}\right\rangle}{\left\langle \tilde{\boldsymbol{p}}^{\dagger}\middle|\dfrac{\partial \mathbf{L}_{\mathrm{FP}}}{\partial f}\tilde{\boldsymbol{p}}\right\rangle} \tag{16}$$

By combining the known information on the direct and adjoint eigenvectors – Eqs. (11) and (15), respectively – as well as on the functional shape of $\mathbf{L}_{\mathrm{FP}}$ – Eqs. (12) and (10) – we have

$$\left\langle \tilde{\boldsymbol{p}}^{\dagger}\middle|\frac{\partial \mathbf{L}_{\mathrm{FP}}}{\partial\omega}\tilde{\boldsymbol{p}}\right\rangle = \langle\tilde{\boldsymbol{p}}^{\dagger}|\mathbf{X}'_{\mathrm{FP}}\tilde{\boldsymbol{p}}\rangle = \boldsymbol{p}^{\dagger\mathrm{H}}\mathbf{Q}'(\omega)\boldsymbol{p} \tag{17a}$$

$$\left\langle \tilde{\boldsymbol{p}}^{\dagger}\middle|\frac{\partial \mathbf{L}_{\mathrm{FP}}}{\partial f}\tilde{\boldsymbol{p}}\right\rangle = \langle\tilde{\boldsymbol{p}}^{\dagger}|\mathbf{Y}_{\mathrm{FP}}\tilde{\boldsymbol{p}}\rangle = \boldsymbol{p}^{\dagger\mathrm{H}}\left(\mathbf{C}+2\omega\mathbf{M}\right)\boldsymbol{p} \tag{17b}$$

This yields a closed-form expression for the sensitivity of the mapping f as required to apply Banach's theorem:

$$|f'_{\mathrm{FP}}(\omega)| = \left|\frac{\boldsymbol{p}^{\dagger\mathrm{H}}\mathbf{Q}'(\omega)\boldsymbol{p}}{\boldsymbol{p}^{\dagger\mathrm{H}}\left(\mathbf{C}+2\omega\mathbf{M}\right)\boldsymbol{p}}\right|. \tag{18}$$

The mapping sensitivity (18) is generally expected to be non-zero. This implies that, if the fixed-point iteration converges, $|f'|<1$, then it possesses a linear convergence rate – see Eq. (21).

An alternative fixed-point iteration scheme

The choice of a fixed-point iteration method is not unique. One of the disadvantages of the solution method proposed in Nicoud et al. (2007) is that it casts the original problem in an eigenvalue problem having doubled dimensions, which is computationally more expensive to solve. Alternatively, one can perform an iteration in the ω^2 term of Eq. (3), while the remaining occurrences of the eigenvalues are fixed to ω_n. The square root of the eigenvalues of the resulting (linear) eigenvalue problem are then an approximation of the sought eigenvalues. This choice is convenient since the matrix $\mathbf{M}$ that appears on the r.h.s. of the resulting generalised eigenvalue problem is positive definite, allowing for the use of robust linear eigenvalue solvers. We shall refer to this solution scheme, described in Alg. 2, as Picard iteration (Ciarlet 2013, p. 154) .

Algorithm 2 Picard iteration

```
function ITERATE(ω_1, p_1, tol_ω, maxiter, K, C, M, Q)
    ω_0 ← ∞
    n ← 1
    while |ω_n − ω_{n−1}| > tol_ω and n < maxiter do
        X ← K + ω_n C + Q(ω_n)
        ω_{n+1}, p_{n+1} ← EIGS(−X, M, ω_n, p_n)
        ω_{n+1} ← sqrt(ω_{n+1})
        n ← n + 1
    end while
    return ω_n, p_n, n
end function
```

The Picard iteration defines the mapping f given by

$$\mathbf{L}_{\mathrm{PC}}(f;\omega_n)\boldsymbol{p} = \left(\underbrace{\mathbf{K}+\omega_n\mathbf{C}+\mathbf{Q}(\omega_n)}_{\mathbf{X}_{\mathrm{PC}}(\omega_n)}+f^{2}\mathbf{M}\right)\boldsymbol{p}=\mathbf{0}. \tag{19}$$

By invoking the associated adjoint eigenvalue problem, and by using the adjoint sensitivity Eq. (16), one can show that the sensitivity of the Picard iteration reads

$$|f'_{\mathrm{PC}}(\omega)| = \left|\frac{\boldsymbol{p}^{\dagger\mathrm{H}}(\mathbf{Q}'(\omega)+\mathbf{C})\boldsymbol{p}}{\boldsymbol{p}^{\dagger\mathrm{H}}2\omega\mathbf{M}\boldsymbol{p}}\right|. \tag{20}$$

Table 2. Eigenvalues identified by means of finite elements and values of the contracting operator $|f'|$. Only the eigenvalues for which $|f'| < 1$ can be identified, provided that an accurate initial guess is known.

#	ω	$\lvert f'_{\mathrm{FP}}\rvert$	$\lvert f'_{\mathrm{PC}}\rvert$
1	2.396-0.260i	0.519	0.519
2	4.696+0.297i	17.025	17.025
3	6.300-0.000i	0.022	0.022
4	7.880+0.316i	12.204	12.204

Notably, the only difference with respect to the sensitivity of the fixed-point iteration proposed by Nicoud et al. (2007), Eq. (17), is that the matrix $\mathbf{C}$ is moved to the numerator. However, for the simple boundary conditions considered in this study, one finds that the matrix $\mathbf{C}$ has non-zero elements only at the open-end boundary, where both $\boldsymbol{p}$ and $\boldsymbol{p}^\dagger$ vanish, so that the contribution of the term $\boldsymbol{p}^{\dagger\mathrm{H}}\mathbf{C}\boldsymbol{p}$ vanishes.

This is a general result. When considering non-trivial boundary conditions, the convergence properties of the two proposed fixed-point solution methods are going to differ, and one cannot draw general conclusions on which method will be able to identify more eigenvalues a priori. On the other hand, for trivial (open and/or closed) boundary conditions one can show that $\boldsymbol{p}^{\dagger\mathrm{H}}\mathbf{C}\boldsymbol{p} = 0$. Therefore, when considering geometries with simple open or closed boundary conditions, the Picard iteration method should be preferred as a fixed-point iteration scheme since (i) it is computationally cheaper and (ii) has the same contraction properties at the eigenvalues.

Convergence properties of fixed-point iterative methods

Table 2 highlights the contraction properties of the discussed fixed-point algorithm for the the four eigenvalues of interest that the problem has when discretized using an equidistant linear finite elements mesh with 127 degrees of freedom. These eigenvalues have been calculated using a higher-order iterative method, described in the next section. This is because, as we will now show, fixed-point methods fail in identifying some eigenvalues. The modeshapes associated with the four eigenvalues are shown in Figure 1.

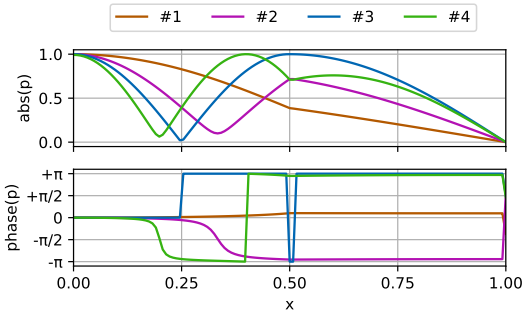

Figure 1. Modeshapes of the four eigenvalues in the considered portion of the complex plane. The colors orange, purple, blue and green indicate, respectively, the thermoacoustic modes number 1, 2, 3 and 4, as listed in Table 2. Modes 1 and 3 are of acoustic origin, 2 and 4 of ITA origin (see Table 1).

The sensitivity that the mapping f takes at these solutions in Table 2 are then evaluated according to Eq. (18). By comparison with Table 1 one finds that $|f'|$ is less than one for thermoacoustic modes of acoustic origin, whereas it is greater than one for modes of ITA origin. This implies that modes of ITA origin cannot be identified with this iterative scheme. Indeed, even if a good initial estimate is known for those, since $|f'| > 1$ the iterative algorithm will repel the initial guess from the actual solution. This fact might be partly responsible for the late discovery of modes of ITA origin in thermoacoustics, in particular for annular combustion chambers (Buschmann et al. 2020a; Orchini et al. 2020), for which larger nonlinear eigenvalue problems need to be solved.

Although a formal proof is not available, the difficulties that the fixed-point iterations have in converging towards ITA modes can be intuitively explained by the following argument. The matrix in the numerator of (18) is proportional to the flame delay, $\exp(-\mathrm{i}\omega\tau)$. Modes of ITA origin tend to have largely negative growth rates, $\Im[\omega] \gg 0$, implying that $|\exp(-\mathrm{i}\omega\tau)| \gg 1$. Additionally, the eigenvectors of modes of ITA origin (and their adjoint) have a strong magnitude at the flame – see Figure 1 – exactly the zone in which the flame response $\mathbf{Q}$ is large, due to a strong gradient in the pressure modeshapes at the reference position. In combination, these two effects yield a large value of the term $\boldsymbol{p}^{\dagger\mathrm{H}}\mathbf{Q}'(\omega)\boldsymbol{p}$, appearing in the numerator of (18). Thus, $|f'| \gg 1$ can be expected for ITA modes.

To demonstrate that the fixed-point iterations cannot identify modes for which $|f'| > 1$, we perform a large number of brute-force calculations in the complex plane. We initialize the fixed-point algorithm with initial guesses ω_1 in the region $\mathcal{S}$ defined in (8) sampled on a uniform 1001×201 grid. The eigenvectors for the Krylov-subspace methods were initialized with the $\boldsymbol{p}_1 = [1, 1, \ldots, 1]^{\mathrm{T}}$. We stop the algorithm when a tolerance $\mathrm{tol}_\omega \equiv |\omega_n - \omega_{n-1}| < 10^{-10}$ is reached – an eigenvalue has converged – or when a maximum number of 16 iterations is exceeded – the algorithm does not converge with this initial condition to the desired tolerance. The results are shown in Fig. 2. The axis indicate the value taken by the initial guess, and the color scheme indicates to which eigenvalue the initial guess has converged and how many steps it took. The actual solutions are highlighted with white markers.

Brute-force numerical calculations confirm that the modes of ITA origin, #2 and #4 in Table 1, cannot be found by using fixed-point iterative methods, even for guesses that start very close to the actual solutions. The modes of acoustic origin, instead, can be identified. The portions of the complex plane that, when used as an initial guess, converge to modes #1 and #3, are highlighted in orange and blue, respectively. Notably, convergence of mode #1 always requires a number of iterations much larger than those needed for mode #3 to converge. This is in line with the fact that the sensitivity of mode #1, although less than 1, is an order of magnitude larger than that of mode #3. More quantitatively, when $0 < |f'| < 1$, in the vicinity of a solution the number of steps N_s needed to improve the accuracy by an order of magnitude can

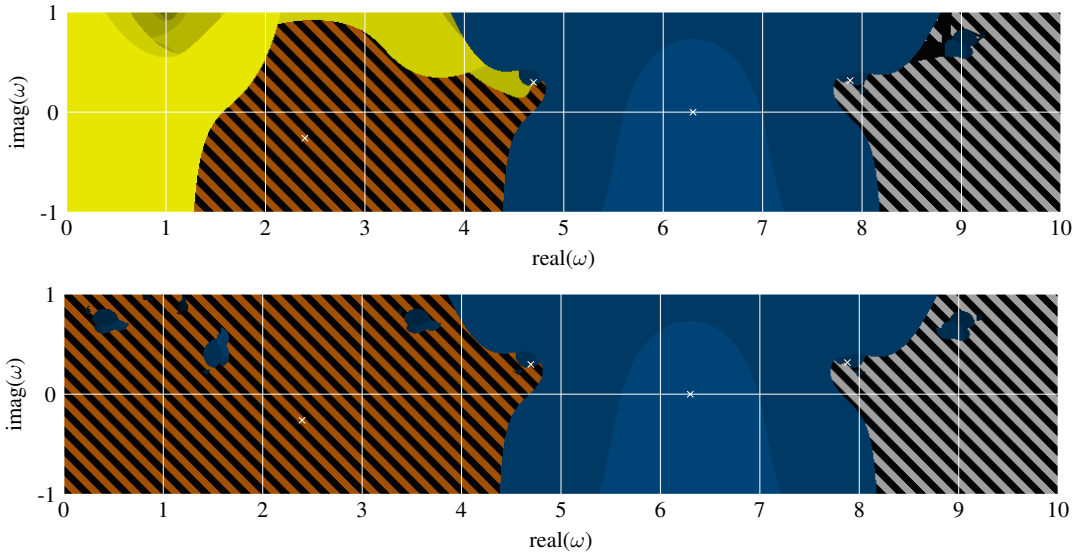

Figure 2. Convergence and basins of attractions for (top) the fixed-point iteration described in Nicoud et al. (2007) , Alg. 1, and (bottom) the Picard iteration described in this study, Alg. 2. The areas in orange and blue indicate, respectively, the basins of attraction of the thermoacoustic modes #1 and #3, as listed in Table 2. The basin of attraction of mode #1 is hatched with black because, although the algorithm is slowly converging, the convergence rate is very low, and it takes more than 16 iterations to identify the eigenvalue to the prescribed accuracy of 10^{-10}. Both methods are unable to identify modes number 2 and 4, of ITA origin. The lighter the color, the less steps are needed for convergence. Gray-black hatched surfaces indicate (slow) convergence towards an eigenvalue outside of the considered domain. Yellow indicates convergence to a (spurious) eigenvalue with $\omega = 0$.

be estimated by $N_s = \lceil 1/\log_{10}(1/|f'|)\rceil$. From the values reported in Table 2, this yields $N_s = 4$ for mode #1 and $N_s = 1$ for mode #3, i.e., the former requires approximately 4 times more iterations than the latter to converge to a predefined tolerance. Within the required 16 iterations limit, the eigenvalue #1 can be identified with a tolerance of 10^{-6}. A larger number of iterations is needed to converge to the prescribed tolerance $\mathrm{tol}_\omega = 10^{-10}$, emphasized by the presence of black stripes in Figure 2. Lastly, in yellow we have highlighted the portion of the complex plane that converges to the $\omega = 0$ eigenvalue. This is always a solution of the thermoacoustic weak form (3), but it represents a spurious solution that does not satisfy the boundary conditions, except when all boundaries are acoustically closed. This spurious solution arises from manipulation of the impedance boundary condition equations when deriving the weak form (3). The fixed-point algorithm proposed by Nicoud et al. (2007) and summarised in Alg. 1 strongly promotes convergence towards this spurious eigenvalue because it separates the action of the boundary matrix, $\mathbf{C}$, from that of the stiffness and flame matrices, $\mathbf{K}$ and $\mathbf{Q}$, as can be seen in Eq. (10).

Together with the higher dimensions of the linearized eigenvalue problem, the promotion of the convergence towards a spurious eigenvalue is another disadvantage of the method of Nicoud et al. (2007) in contrast to the Picard iteration (19). Nonetheless, the slow convergence of some modes and the non-convergence of other modes for both fixed-point iterations are inherently linked to their linear convergence rate. To overcome this limitations, we will now consider methods with a super-linear convergence rate.

Newton-like iteration methods

A sequence generated from an iterative algorithm is said to have a rate of convergence m if there exists a bound $G > 0$ such that

$$|\omega_{n+1} - \omega| \leq G|\omega_n - \omega|^m. \tag{21}$$

When the contraction condition (13) is satisfied, the iterative fixed-point algorithms described so far converge towards the closest eigenvalue at a linear rate, $m = 1$. However, when one has $|f'(\omega)| = 0$, the rate of convergence becomes super-linear, with $m > 1$. Importantly, $|f'(\omega)| = 0$ always satisfies Banach's condition (13), implying that super-linear converging algorithms are guaranteed to converge to all eigenvalues. Super-linear convergence is a feature of Newton's method, which is therefore more robust than fixed-point methods (0th order), since it uses gradient information (1st order). Gradient information may be included also in a fixed-point iteration by introducing a relaxation parameter (Ni 2017, Appenidx C.4). This procedure is however based on finite difference approximations and requires solving two eigenvalue problems at each iteration. A direct application of Newton's method is preferable.

Since the eigenvalues of (3) are found when the determinant of $\mathbf{L}$ vanishes, a direct application of Newton's method to $\det[\mathbf{L}(\omega)] = 0$ leads to

$$\omega_{n+1} = \omega_n - \left.\frac{\det\left[\mathbf{L}(\omega)\right]}{d(\det\left[\mathbf{L}(\omega)\right])/d\omega}\right|_{\omega=\omega_n}. \tag{22}$$

Evaluating the determinant is however a demanding and error-prone operation. A determinant-free Newton scheme

was suggested in Juniper (2018), which exploits Jacobi's formula

$$\frac{\det\left[\mathbf{L}(\omega)\right]}{d(\det\left[\mathbf{L}(\omega)\right])/d\omega} = \frac{1}{\operatorname{tr}\left[\mathbf{L}^{-1}(\omega)d\mathbf{L}(\omega)/d\omega\right]}. \tag{23}$$

Although this scheme is more robust than a direct evaluation of the determinant, the evaluation of the inverse of the matrix operator $\mathbf{L}$ becomes prohibitively expensive when $\mathbf{L}$ has hundreds of thousand of degrees of freedom, as is typical in real-world thermoacoustic calculations.

To bypass these issues, in the following section we will discuss how adjoint-based methods allow us to use Newton's method directly on the NLEVP equations. This will not require the evaluation of determinants nor matrix inverses, and provides more accurate information on the mapping sensitivity than finite difference approximations.

Adjoint-based Newton iteration

By introducing an auxiliary variable λ, the NLEVP (2) can be written as

$$\mathbf{L}(\omega)\boldsymbol{p} = \lambda\mathbf{Y}\boldsymbol{p}. \tag{24}$$

Equation (24) can be thought of as a generalized eigenvalue problem with eigenvalue λ depending on a parameter ω. From this viewpoint λ is an implicitly defined function of ω, i.e. $\lambda = \lambda(\omega)$. If the parameter ω is chosen such that the eigenvalue problem (24) has an eigenvalue $\lambda = 0$, then ω (and the corresponding eigenvector $\boldsymbol{p}$) is a solution of the NLEVP (2). Since the implicitly restarted Arnoldi algorithm is used to solve the sparse eigenvalue problem (24), linear in λ, choosing the matrix $\mathbf{Y}$ to be semi-positive definite has significant advantages. Possible choices are $\mathbf{Y} = \mathbf{I}$, the identity matrix, or $\mathbf{Y} = \mathbf{M}$, the mass matrix. In our analysis the latter will be used, since it naturally arises when discretizing the continuous thermoacoustic operator by means of finite elements. The following discussion on the convergence of the method is however independent from the specific form chosen for $\mathbf{Y}$.

To find values of ω for which (24) has a zero eigenvalue in λ, we seek the roots of the implicit relation $\lambda = \lambda(\omega)$. Newton's iteration on this relation reads

$$\omega_{n+1} = \omega_n - \lambda(\omega_n)/\lambda'(\omega_n) = f(\omega_n), \tag{25}$$

which requires the sensitivity of the eigenvalue with respect to the parameter, $\lambda' = d\lambda/d\omega$. This sensitivity can be obtained by means of adjoint methods. Starting from Eq. (24) it can be shown that the sensitivity of a linear eigenvalue problem is (Magri et al. 2016; Orchini and Juniper 2016)

$$\lambda'(\omega_n) = \frac{\boldsymbol{p}^{\dagger\mathrm{H}}\mathbf{L}'(\omega_n)\boldsymbol{p}}{\boldsymbol{p}^{\dagger\mathrm{H}}\mathbf{Y}\boldsymbol{p}}. \tag{26}$$

By using this expression, one can iteratively update the parameter ω in (25) until an eigenvalue $\lambda = 0$ is found.

The algorithm for the adjoint-based Newton iteration is given in Alg. 3. Note that this method requires solving both the direct and the adjoint problem, which requires a numerical implementation of the adjoint matrix $\mathbf{L}^\dagger$. This may cause difficulties in codes which are implemented in a matrix-free fashion, or in which the direct and adjoint discrete equations are derived independently from the continuous equations, and have different discretizations (Magri and Juniper 2013). In our implementation[4], the elements of the sparse matrix $\mathbf{L}$ are explicitly stored. Furthermore, since we employ a Bubnov-Galerkin finite elements discretization, the discretization of the continuous adjoint equation is equivalent to the adjoint of the discretized direct equation, and one can show that $\mathbf{L}^\dagger = \mathbf{L}^\mathrm{H}$ (Mensah 2018).

Algorithm 3 Newton adjoint-based method

function ITERATE($\omega_1, \boldsymbol{p}_1, \boldsymbol{p}_1^\dagger, \mathbf{L}, \mathrm{tol}_\omega, \mathrm{maxiter}$)
  $\omega_0 \leftarrow \infty$
  $n \leftarrow 1$
  while $|\omega_n - \omega_{n-1}| > \mathrm{tol}_\omega$ **and** $n < \mathrm{maxiter}$ **do**
    $\lambda_n, \boldsymbol{p}_{n+1} \leftarrow \mathrm{EIGS}(\mathbf{L}(\omega_n), \mathbf{M}, 0, \boldsymbol{p}_n)$
    ${\lambda_n}^*, \boldsymbol{p}_{n+1}^\dagger \leftarrow \mathrm{EIGS}(\mathbf{L}^\mathrm{H}(\omega_n), \mathbf{M}, 0, \boldsymbol{p}_n^\dagger)$
    $\lambda_n' \leftarrow -\frac{\boldsymbol{p}_{n+1}^{\dagger\mathrm{H}}\mathbf{L}'(\omega_n)\boldsymbol{p}_{n+1}}{\boldsymbol{p}_{n+1}^{\dagger\mathrm{H}}\mathbf{M}\boldsymbol{p}_{n+1}}$
    $\omega_{n+1} \leftarrow \omega_n - \frac{\lambda_n}{\lambda_n'}$
    $n \leftarrow n+1$
  end while
  $\lambda_n \leftarrow \mathrm{EIGS}(\mathbf{L}(\omega_n), \mathbf{M}, 0, \boldsymbol{p}_n)$ ▷ This line basically computes the residual for possible later use
  return $\omega_n, \boldsymbol{p}_n^\dagger, \boldsymbol{p}_n, \lambda_n n$
end function

As always for mappings obtained from Newton's method, the mapping defined by (25) has super-linear convergence, i.e. $f' = 0$. This guarantees that *all* thermoacosutic eigenvalues are attractors for this iteration method, and, provided sufficiently good guesses are provided, they can always be identified. This is formally shown in the Appendix.

Householder's methods

Newton's method can be generalized by considering higher-order expansions of the relation $\lambda = \lambda(\omega)$. The resulting class of iterative root-finding methods are known as Householder's methods (Householder 1970). At an arbitrary order $m > 0$ the iterative Householder step reads

$$\omega_{n+1} = \omega_n + m\frac{(1/\lambda)^{\{m-1\}}(\omega_n)}{(1/\lambda)^{\{m\}}(\omega_n)}. \tag{27}$$

At first order ($m = 1$), Eq. (27) corresponds to the Newton iteration (25). At second order ($m = 2$) one obtains

$$\omega_{n+1} = \omega_n - \frac{2\lambda(\omega_n)\lambda'(\omega_n)}{2\left(\lambda'(\omega_n)\right)^2 - \lambda(\omega_n)\lambda''(\omega_n)}, \tag{28}$$

which is also known as Halley's method (Halley 1694).

In order to apply higher-order Householder's methods, the evaluation of high-order eigenvalue sensitivities $\lambda^{\{m\}}$ is required. Once again, adjoint-based theory can be exploited in this regard. By using perturbation theory, explicit formulas

[4]The code is open-source and is implemented in the Julia package WavesAndEigenvalues (https://github.com/JulHoltzDevelopers/WavesAndEigenvalues.jl).

for the calculation of arbitrarily high-order sensitivity have been derived in Mensah et al. (2020), to which we refer the interested reader. For the purpose of this study, we shall assume that a function PERT that computes arbitrarily high-order sensitivities is available. With this at hand, the pseudocode for the Householder iterative method is given in Alg. 4, in which the function HOUSE computes the Householder update to ω_n at the desired order, according to Eq. (27).

Algorithm 4 Householder's method

function ITERATE($\omega_1, \mathbf{L}, \boldsymbol{p}_1, \boldsymbol{p}_1^\dagger, \mathrm{tol}_\omega, \mathrm{maxiter}, \mathrm{order}$)
  $\omega_0 \leftarrow \infty$
  $n \leftarrow 1$
  while $|\omega_n - \omega_{n-1}| > \mathrm{tol}_\omega$ **and** $n < \mathrm{maxiter}$ **do**
    $\lambda_n, \boldsymbol{p}_{n+1} \leftarrow \mathrm{EIGS}(\mathbf{L}(\omega_n), \mathbf{M}, 0, \boldsymbol{p}_n)$
    $\lambda_n^*, \boldsymbol{p}_{n+1}^\dagger \leftarrow \mathrm{EIGS}(\mathbf{L}^\mathrm{H}(\omega_n), \mathbf{M}, 0, \boldsymbol{p}_n^\dagger)$
    $\lambda_{\mathrm{derivs},n} \leftarrow \mathrm{PERT}(\mathbf{L}(\omega_n) - \lambda_n \mathbf{M}, \mathrm{order})$
    $\omega_{n+1} \leftarrow \omega_n + \mathrm{HOUSE}(\lambda_{\mathrm{derivs},n}, \mathrm{order})$
    $n \leftarrow n + 1$
  end while
  $\lambda_n \leftarrow \mathrm{EIG}(\mathbf{L}(\omega_n), \mathbf{M}, 0, \boldsymbol{p}_n)$
  return $\omega_n, \boldsymbol{p}^\dagger, \boldsymbol{p}, \lambda_n, n$
end function

Convergence properties of Householder's methods By construction, all Houselder's methods have $f' = 0$ at the fixed points, implying that all eigenvalues are attractors and have a non-empty basin of attraction. When considering simple roots, the mth order Householder's method has a convergence rate of $m + 1$, meaning that a lower number of iterations in generally required to identify a solution. Yet, these methods are generally not applied to scalar equations because the increase in function evaluations per iteration outweighs the improved convergence rate when the order is increased. This limitation however does not straightforwardly apply to large eigenvalue problems. This is because one needs to weight the computational effort needed for the solution of a linear eigenvalue problem at each step – ruled by the dimension of the problem only – against the one needed to perform all the matrix-vector products needed – which depends on the problem size, but also significantly increases at each perturbation order (Mensah et al. 2020). Thus, for adjoint-based perturbation theory applied on large matrices, computational optimality is ruled by a non-trivial trade-off between the number of iterations needed to converge and the cost of the perturbation method at the chosen order. Numerical experiments have shown (details not reported here) that the Householder's method of order 3 has, on average, optimal performances (minimum time and memory used) for eigenvalue problems that have a few thousands degrees of freedom.

Degenerate eigenvalues Special care needs to be taken if the eigenvalue searched for is a multiple root of the characteristic function of $\mathbf{L}$, i.e., if the eigenvalue is degenerate. For degenerate semi-simple eigenvalues perturbation theory can still be used to compute the necessary derivatives (Lancaster et al. 2003; Orchini et al. 2021). To retain the high convergence rate of Householder's methods, the scheme must be applied to the ath root of λ, where that a is the algebraic multiplicity of the eigenvalue. The mth order expansion reads

$$\omega_{n+1} = \omega_n + m \frac{\left(1/\lambda^{\frac{1}{a}}\right)^{\{m-1\}}(\omega_n)}{\left(1/\lambda^{\frac{1}{a}}\right)^{\{m\}}(\omega_n)}. \tag{29}$$

This however requires *a priori* knowledge on the multiplicity of an eigenvalue. In thermoacoustic applications, degeneracies with multiplicity 2 are typically induced by symmetries of the system (Moeck 2010) and can be often predicted with intuition and/or the use of symmetry breaking criteria (Mensah et al. 2019). In most cases, multiplicities can be removed from the problem by a proper symmetry reduction scheme, such as reduction to Bloch-periodic unit cells (Mensah et al. 2016).

Lastly, in case of defective eigenvalues, the adjoint-based schemes presented here cannot be applied, because defective eigenvalues are not analytic in their parameters. However, defective eigenvalues can only appear as isolated points in the parametrized spectrum of $\mathbf{L}$ (Kato 1980) and are, thus, not considered generic.

Convergence examples

Figure 3 shows the eigenvalue convergence maps when using Householder's methods from first order (top) to fifth order (bottom). The tolerance for convergence is set to $\mathrm{tol}_\omega = 10^{-10}$ for all cases. The convergence properties have significantly improved compared to those of the fixed-point methods shown in Figure 2. Indeed, for all considered orders of the Houselder's method, all the four thermoacoustic eigenvalues in the considered portion of the complex plane can be found. In fact, as predicted by Banach's theorem for this mapping each mode possesses a non-empty basin of attraction in its vicinity – recall that $f' = 0$. Furthermore, the higher the order of the considered Householder iteration, the fewer iteration steps are generally needed to converge to the desired accuracy, as can be seen from the fact that the higher is the perturbation order, the brighter is its figure. This does not necessarily mean a faster convergence time, but it demonstrates the increase in convergence rate, Eq. (21), with an increase in the order of the method m. Another notable feature of the Householder's methods is that the size of the basins of attraction of the ITA modes (purple and green) grows when the order of the method is increased. This implies that, when using a (say) fourth order Householder scheme (fourth row in Figure 3), a coarse grid of initial guesses is sufficient to identify all the eigenvalues of interest. On the other hand for the Newton method (top row in Figure 3), although the basins of attraction of modes of ITA origin are non-empty, they have a small size. A finer mesh of initial guesses is therefore required if the eigenvalues are randomly searched. Higher-order Householder's scheme suffer, however, from the existence of larger portions of the complex plane within which the method does not converge to any eigenvalues (in black). All these considerations suggest that a third order Householder scheme is on average the optimal choice, as it provides both faster computational times and possess good convergence properties.

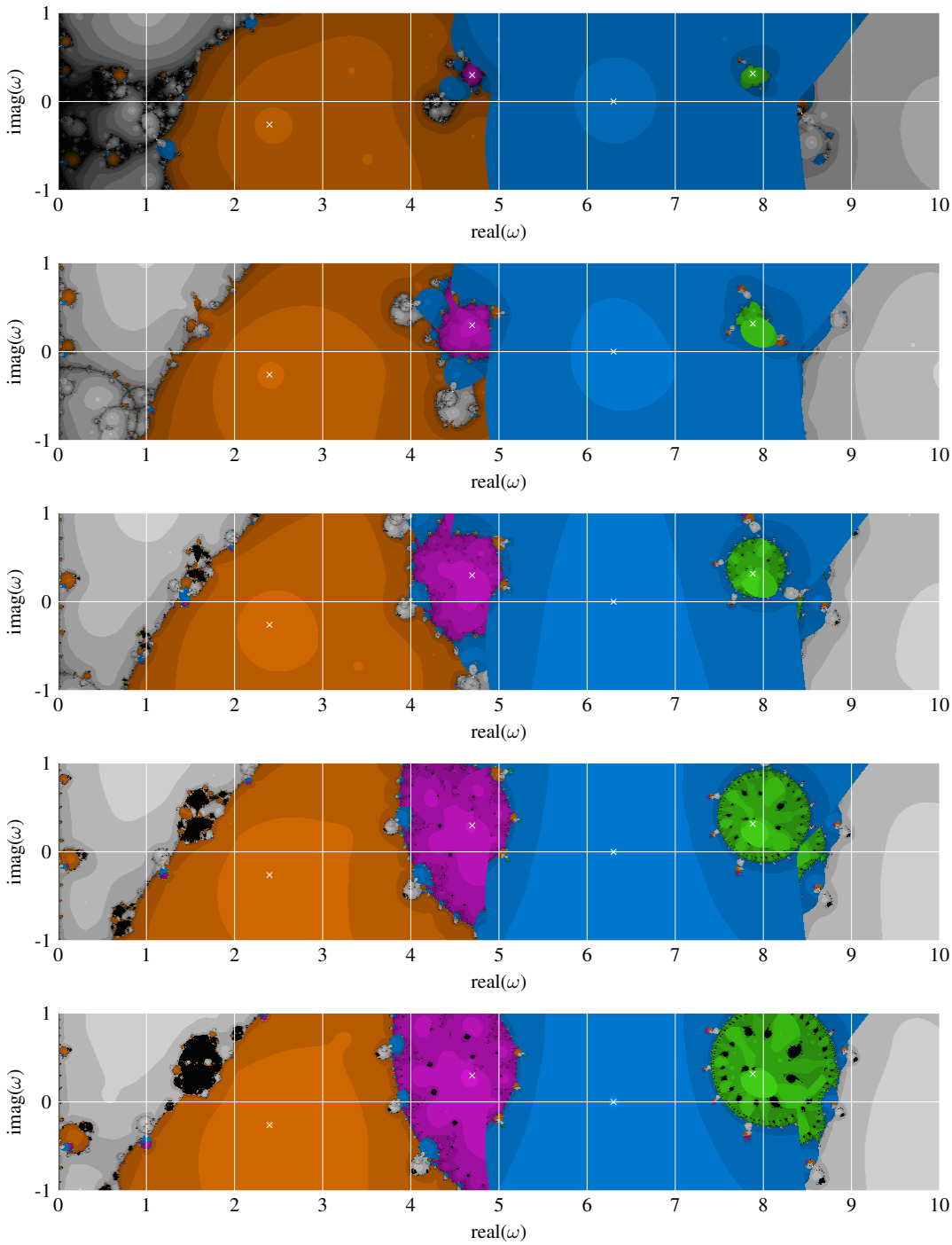

Figure 3. Convergence and basins of attractions for the Householder's methods from first order (top, also known as Newton's method) to fifth order (bottom). The areas in orange, purple, blue and green indicate, respectively, convergence to the thermoacoustic modes number 1, 2, 3 and 4, as listed in Table 2. Modes 1 and 3 are of acoustic origin, 2 and 4 of ITA origin. The lighter the color, the less steps are needed for convergence. Gray indicates convergence to an eigenvalue outside of the considered domain. Black indicates that the algorithm does not converge with these initial conditions.

To conclude, we remark that the convergence maps show fractal patterns at the boundaries between different basins of attraction. The fractal nature of the boundaries of attraction (sometimes referred to as Julia sets) is a known feature of Newton-like iteration maps already when applied to scalar equations (Devaney et al. 1994). However, we note how some of the boundaries in Figure 3 are non-fractal. This can be attributed to the fact that we apply Newton/Householder's methods to eigenvalue problems. Our adjoint-based algorithms require the identification of the smallest eigenvalue of a linear eigenvalues problem to the initial guess (see Alg. 3 and 4). This choice becomes ambiguous when the closest eigenvalue of the linear eigenvalue problem (24) becomes degenerate. This is what happens at non-fractal boundaries, and the clear-cut between convergence to two different eigenvalues when using very close guesses is explained by the fact that our solution method suddenly tracks a different eigenvalue branch of the linear eigenvalue problem.

Conclusions

In this study, we have investigated the convergence properties of the most common methods used to identify eigenvalues in thermoacoustic systems by means of iterative methods. By exploiting adjoint-based sensitivity, we have derived explicit equations that can be used to assess the contraction properties of various algorithms in the vicinity of eigenvalues. Thanks to Banach's fixed-point theorem, this information is sufficient to know if a given algorithm can or cannot converge to an eigenvalue.

For fixed-point iterations, which are commonly employed in thermoacoustics, we found that not all eigenvalues are attractors. In particular, numerical calculations on a Rijke tube system showed that thermoacoustic modes of ITA origin are repellors. This implies that these eigenvalues can never be identified by fixed-point algorithms, regardless on the accuracy of the initial guess. This may be linked to the late discovery of ITA modes by the thermoacoustic community.

We then discussed how Newton-like iterative methods should always be preferred to fixed-point iterations. This is because they are always guaranteed to converge to all eigenvalues, provided that sufficiently good initial guesses are provided. The most straightforward use of Newton's method to eigenvalue problems, however, is inefficient, as it requires the evaluation of matrix determinants or inverses, which becomes prohibitively expensive for large matrices. To overcome this issue, we have introduced a set of adjoint-based methods, known as Householder's methods, which make use of high-order perturbation expansions. We have discussed both the computational efficiency of the algorithms and the dimensions of the basins of attractions of the eigenvalues for these methods up to 5th order. By combining formal results and numerical evidence, we conclude that a third order Householder's method is, among the methods discussed in this study, the optimal choice for identifying eigenvalues of thermoacoustic systems.

Our results highlight the importance on the choice of the solution methods for thermoacoustic eigenvalue problems. In particular, fixed-point iterations should be always avoided since they do not guarantee the identification of all the eigenvalues, and failure in identifying potentially unstable thermoacoustic modes at the design stage can have very expensive side-effects.

Acknowledgement

The authors would like to thank Jonas P. Moeck and Luka Grubišić for helpful discussions on NLEVPs. A.O. acknowledges the support of the German Research Foundation (DFG), project nr. 422037803.

Appendix: Super-linear convergence of Newton method

By evaluating the sensitivity of the mapping f defined in Eq. (25) we can quantify the convergence properties of this method. We have

$$\frac{df}{d\omega} = 1 - \frac{(\lambda')^2 - \lambda''\lambda}{(\lambda')^2} = 1 - \frac{(\lambda')^2}{(\lambda')^2} = 0, \qquad (30)$$

where in the second step we have used the fact that, for any thermoacoustic solution, $\lambda = 0$. This proves that the Banach condition (13) is satisfied for *all* thermoacoustic eigenvalues. Thus, provided a sufficiently good guess, this method converges towards the closest eigenvalue at a super-linear rate, and is able to identify all eigenvalues in the spectrum of the thermoacoustic operator.

References

Beyn WJ (2012) An integral method for solving nonlinear eigenvalue problems. Linear Algebra and its Applications 436: 3839–3863. DOI:10.1016/j.laa.2011.03.030.

Buschmann PE, Mensah GA and Moeck JP (2020a) Intrinsic thermoacoustic modes in an annular combustion chamber. Combustion and Flame 214: 251–262.

Buschmann PE, Mensah GA, Nicoud F and Moeck JP (2020b) Solution of thermoacoustic eigenvalue problems with a noniterative method. Journal of Engineering for Gas Turbines and Power 142: 031022 (11 pages).

Campa G and Camporeale SM (2014) Prediction of the thermoacoustic combustion instabilities in practical annular combustors. Journal of Engineering for Gas Turbines and Power 136(9): 091504 (10 pages).

Ciarlet PG (2013) Linear and nonlinear functional analysis with applications, volume 130. Siam.

Crocco L (1951) Aspects of Combustion Stability in Liquid Propellant Rocket Motors. AIAA Journal 8: 163–178.

Devaney RL, Branner B, Keen L, Douady A, Blanchard P, Hubbard JH and Schleicher D (1994) Complex Dynamical Systems: The Mathematics Behind the Mandelbrot and Julia Sets. American Mathematical Society. DOI:10.1090/psapm/049.

Dowling AP and Stow SR (2003) Acoustic Analysis of Gas Turbine Combustors. Journal of Propulsion and Power 19(5): 751–764.

Effenberger C (2013) Robust solution methods for nonlinear eigenvalue problems. PhD Thesis, École polytechnique fédérale de Lausanne.

Emmert T, Bomberg S and Polifke W (2015) Intrinsic thermoacoustic instability of premixed flames. Combustion and Flame 162(1): 75 – 85. DOI:https://doi.org/10.1016/j.combustflame.2014.06.008.

Güttel S and Tisseur F (2017) The nonlinear eigenvalue problem. Acta Numerica 26: 1–94. DOI:10.1017/S0962492917000034.

Halley E (1694) Methodus nova accurata et facilis inveniendi radices aequationum quarumcumque generaliter, sine praevia reductione. Philosophical Transactions 18: 136–148. DOI: 10.1098/rstl.1694.0029.

Householder AS (1970) The numerical treatment of a single nonlinear equation. New York: McGraw-Hill.

Juniper MP (2018) Sensitivity analysis of thermoacoustic instability with adjoint Helmholtz solvers. Physical Review Fluids 3: 110509 (43 pages). DOI:10.1103/PhysRevFluids.3.110509.

Kato T (1980) Perturbation Theory for Linear Operators, Grundlehren der mathematischen Wissenchaften, volume 132. Springer-Verlag.

Lancaster P, Markus AS and Zhou F (2003) Perturbation theory for analytic matrix functions: The semisimple case. SIAM Journal on Matrix Analysis and Applications 25(3): 606–626. DOI: 10.1137/S0895479803423792.

Lehoucq RB, Sorensen DC and Yang C (1998) ARPACK users' guide: solution of large-scale eigenvalue problems with implicitly restarted Arnoldi methods. SIAM.

Magri L, Bauerheim M and Juniper MP (2016) Stability analysis of thermo-acoustic nonlinear eigenproblems in annular combustors. part I. sensitivity. J. Comput. Phys. DOI:10.1016/j.jcp.2016.07.032.

Magri L and Juniper MP (2013) Sensitivity analysis of a time-delayed thermo-acoustic system via an adjoint-based approach. Journal of Fluid Mechanics 719: 183–202. DOI:10.1017/jfm.2012.639.

McManus KR, Poinsot T and Candel S (1993) A review of active control of combustion instabilities. Progress in Energy and Combustion Science 19(1): 1–29.

Mehrmann V and Voss H (2004) Nonlinear eigenvalue problems: a challenge for modern eigenvalue methods. GAMM-Mitteilungen 27(2): 121–152. DOI: 10.1002/gamm.201490007.

Mensah GA (2018) Efficient Computation of Thermoacoustic Modes. PhD Thesis, TU Berlin.

Mensah GA, Campa G and Moeck JP (2016) Efficient computation of thermoacoustic modes in industrial annular combustion chambers based on bloch-wave theory. Journal of Engineering for Gas Turbines and Power 138(8): 081502 (7 pages). DOI: 10.1115/1.4032335.

Mensah GA, Magri L, Orchini A and Moeck JP (2019) Effects of Asymmetry on Thermoacoustic Modes in Annular Combustors: A Higher- Order Perturbation Study. Journal of Engineering for Gas Turbines and Power 141: 041030 (8 pages). DOI:10.1115/1.4041007.

Mensah GA, Orchini A and Moeck JP (2020) Perturbation theory of nonlinear, non-self-adjoint eigenvalue problems: Simple eigenvalues. Journal of Sound and Vibration 473: 115200. DOI:10.1016/j.jsv.2020.115200.

Moeck JP (2010) Analysis, modeling, and control of thermoacoustic instabilities. PhD Thesis, TU Berlin.

Ni F (2017) Accounting for complex flow-acoustic interactions in a 3D thermo-acoustic Helmholtz solver. PhD Thesis, Université de Toulouse.

Nicoud F, Benoit L, Sensiau C and Poinsot T (2007) Acoustic modes in combustors with complex impedances and multidimensional active flames. AIAA Journal 45(2): 426–441. DOI: 10.2514/1.24933.

Orchini A, Illingworth SJ and Juniper MP (2015) Frequency domain and time domain analysis of thermoacoustic oscillations with wave-based acoustics. Journal of Fluid Mechanics 775(submitted): 387–414.

Orchini A and Juniper MP (2016) Linear stability and adjoint sensitivity analysis of thermoacoustic networks with premixed flames. Combustion and Flame 165: 97–108. DOI:10.1016/j.combustflame.2015.10.011.

Orchini A, Mensah GA and Moeck JP (2021) Perturbation theory of nonlinear, non-self-adjoint eigenvalue problems: Semisimple eigenvalues. Journal of Sound and Vibration 507: 116150. DOI:https://doi.org/10.1016/j.jsv.2021.116150.

Orchini A, Silva C, Mensah G and Moeck J (2020) Thermoacoustic modes of intrinsic and acoustic origin and their interplay with exceptional points. Combustion and Flame 211. DOI:10.1016/j.combustflame.2019.09.018.

Saad Y (2011) Numerical methods for large eigenvalue problems: revised edition. SIAM.

Sensiau C, Nicoud F and Poinsot T (2009) A tool to study azimuthal standing and spinning modes in annular combustors. International Journal of Aeroacoustics 8: 57–67. DOI:10.1260/147547209786235037.

Sensiau C, Nicoud F, van Gijzen M and van Leeuwen JW (2008) A comparison of solvers for quadratic eigenvalue problems from combustion. International Journal for Numerical Methods in Fluids 56(8): 1481–1487. DOI:10.1002/fld.1691.

Silva CF, Nicoud F, Schuller T, Durox D and Candel S (2013) Combining a helmholtz solver with the flame describing function to assess combustion instability in a premixed swirled combustor. Combust. Flame 160(9): 1743–1754. DOI:10.1016/j.combustflame.2013.03.020.

Wolf P, Staffelbach G, Gicquel LY, Müller JD and Poinsot T (2012) Acoustic and large eddy simulation studies of azimuthal modes in annular combustion chambers. Combustion and Flame 159(11): 3398 – 3413. DOI:https://doi.org/10.1016/j.combustflame.2012.06.016.

Experimental study of thermoacoustic modes in a can-annular model combustor

Symposium on Thermoacoustics in Combustion: Industry meets Academia (SoTiC 2021)
Sept. 6 - Sept. 10, 2021
Munich, Germany
Paper No.: 8445

Experimental study of thermoacoustic modes in a can-annular model combustor

Philip E. Buschmann[1], Nicholas A. Worth[1] and Jonas P. Moeck[1]

Abstract

Can-annular combustors are an important type of design for gas turbines employed in stationary power generation. Such a combustor consists of a large number of nominally identical cans arranged around a circumference. A substantial amount of engineering can be conducted on a single can, which cuts development cost and time. However, all cans need to be merged at their downstream end into an annulus towards the turbine stage. This results in a small gap between adjacent cans. Engines in operation and subsequent theoretical studies have shown that the acoustic coupling via this so-called cross-talk affects thermoacoustic stability of the system. Unwanted pressure oscillations may then originate from a coupling between unsteady heat-release rate and pressure waves. Due to the weak coupling via the cross-talk area, can-annular combustors can exhibit multiple linearly unstable modes of different azimuthal mode orders within a narrow frequency band. The interaction between these unstable modes needs to be understood to design thermoacoustically stable combustors. The work in this paper presents the first results of a set of experiments on a new laboratory can-annular combustor with eight cans. The combustor permits an adjustment of the cross-talk strength and, in this way, facilitates detailed investigations on the resulting effect on mode selection. Besides varying the cross-talk strength, two configurations with and without plenum coupling are investigated. The absence of the plenum coupling results in modes clustered within narrow frequency bands. Moreover, the experiments confirm several predictions from theoretical studies and show interesting features in the form of multiple unstable modes.

Keywords

Can-annular combustion chamber, Thermoacoustic instabilities, Azimuthal modes, Mode switching

Introduction

Can-annular combustors are employed in many industrial gas turbines for stationary power generation. It is the predominant concept in the portfolios of major industrial manufactures. Air from the compressor stage is split into a number of nominally identical cans, arranged circumferentially, in which combustion takes place. Downstream of the flame, the circular cross section of every can smoothly transitions into an annular segment to match the annular inlet of the turbine. By the nature of this geometrical transition, a small gap between adjacent cans – the cross-talk (XT) area – remains. Properties associated only with the combustion process, such as the flame shape, static stability limits, pollutant emissions and thermal loads, can be characterised by considering a single can. This significantly reduces the costs and complexity of the development process but does not take into account the acoustic coupling between adjacent cans in the full can-annular arrangement.

In effect, the cans are nearly identical and therefore exhibit almost the same acoustic resonances, if considered individually. Since the cross-talk area is small, the thermoacoustic dynamics in these systems are similar to those associated with a set of weakly coupled identical oscillators. Clusters of eigenfrequencies are the result: within a narrow frequency band modes of different azimuthal mode orders m occur. Such a cluster in a can-annular combustor was first observed by Bethke et al. (2002) in computations with a thermoacoustic finite-element model.

Ghirardo et al. (2019) studied thermoacoustic modes in a generic can-annular combustor with a network model. By increasing the coupling strength between adjacent cans, it is shown how the modes of various azimuthal orders in a cluster originate from one axial mode of the isolated can. Therefore, in this paper a cluster of modes is defined as a group of modes with different azimuthal mode orders having the same axial order. The study also found that modes in a cluster are ordered by increasing frequency according to their azimuthal mode order m.

Ghirardo et al. (2019) also predict *mode localization*. This is a well known phenomenon in weakly coupled identical oscillators as the nominal symmetry of the entire system is slightly perturbed. In can-annular combustors this manifests as an instability where all cans oscillate at the same frequency but the amplitude shows a large variation over the circumference. Data from full-scale engines indicates that only a small number of cans oscillates at amplitudes far higher than the remaining ones.

[1]Department of Energy and Process Engineering
Norwegian University of Science and Technology
Trondheim, Norway

Corresponding author:
Philip E. Buschmann
Email: philip.e.buschmann@ntnu.no

Several modes in a cluster can be linearly unstable and this gives rise to two possible outcomes: Either a self-sustained oscillation with several modes manifests itself or competition between the modes suppresses all but one. In thermoacoustics, the former is rarely observed with the notable exception of a slanted mode as reported by Bourgouin et al. (2015), which is a superposition of an axial and an azimuthal mode. Instead, the latter case is the norm: after an initial transient one frequency dominates the system, see work on the annular MICCA (Laera et al. 2016) and Cambridge/NTNU (Worth and Dawson 2013) combustors. For can-annular combustors by using a time domain model, von Saldern et al. (2020) shed light onto the transient growth of multiple unstable modes and inter-modal competition: In a short transient multiple modes grow in amplitude but only the mode of highest azimuthal order reaches a steady limit cycle.

There is little experimental data published on can-annular combustors. So far only Moon et al. (2020a,b) report results on a laboratory-scale can-annular combustor. The model combustor they employed with $N = 4$ cans has two predecessors: A single $N = 1$ can (Kim 2016, 2017) and a twin $N = 2$ can setup (Jegal et al. 2019; Moon et al. 2019). The same weak coupling in the twin setup is employed in the can-annular layout. The authors report clustered modes of different azimuthal mode orders and localisation phenomena.

In the present paper, the first results of experiments on a can-annular combustor with $N = 8$ cans are presented. The combustor operates under atmospheric conditions with perfectly premixed flames. Major differences to the work of Moon et al. (2020a,b) are: eight cans, reactants are fed from a shared plenum, adjustable XT-strength and an outlet that is open to the atmosphere.

This work is organised as follows. First azimuthal mode orders of clustered modes in can-annular combustors are explained. Then the experimental setup, data analysis and numerical setup for a linear stability analysis are described. Afterwards, the results section follows, which is split into two parts since two major configurations are studied in both of which the XT strength is varied: one configuration with a connected plenum and one where the plenum is decoupled acoustically.

Azimuthal mode orders in can-annular combustors

To visualize the mode topology in a can-annular combustor, it is convenient to picture a set of N isolated, identical combustors arranged in a circular fashion. Each combustor exhibits modes of increasing axial orders. Any such mode exists N times for the entire system, since every can oscillates in a standalone fashion. Here, N is also the algebraic and geometric multiplicity of every mode. As the cans are taken out of isolation via coupling, every N-fold mode splits into distinct modes of varying azimuthal orders. Since the coupling via the XT is weak the post-split modes remain in a narrow frequency band. This is what is referred to as a mode *cluster* in the following. By definition, all modes in the same cluster have the same axial order. Later, when considering modes obtained from a linear stability analysis, the axial order is used to assign cluster numbers.

Ghirardo et al. (2019, 2020) and von Saldern et al. (2020) predicted the splitting of N-fold degenerate modes as the XT size is increased from zero. Both show that the $m = 0$ mode before and after the split stays in place and that higher order modes are further offset from $m = 0$. Unlike in these models, in experiments a XT has a finite volume and thus the mode $m = 0$ experiences a minor shift in frequency. Furthermore, in the aforementioned studies it is also show that clustered modes are ordered by increasing frequency according to their mode order and that modes of higher order are more sensitive to the coupling strength, i.e. more offset from $m = 0$. Experimentally, Moon et al. (2019, 2020b) give a first proof of these properties and report a variety of oscillation patterns.

Results from Ghirardo et al. (2020) show that modes in a cluster occupy the lowest azimuthal mode orders. Mathematically, a breakdown into higher mode orders is possible. For the first few clusters at low frequencies, which are of thermoacoustic relevance, this is not the case. As a consequence and in the limit of low frequencies, for the $N = 4$ combustor of Moon et al. (2020a,b), modes of orders $m = 0, 1, 2$ are obtained. The modes $m = 0, 2$ are simple while $m = 1$ is twofold degenerate. The combustor in the present paper with $N = 8$ exhibits $m = 0, 1, 2, 3, 4$ modes. Likewise, all modes are degenerate except for the $m = 0, 4$ modes.

In the present work, modes $m = 0$ are called *push-push* while those of highest order $m = 4$ are referred to as *push-pull*. The latter correspond to 'push-pull alternating' in Moon et al. For standing modes $m = 1, 2$, the nodal lines can be located inside opposite cans or between cans, i.e. in the XTs. This notation differs from the one in Moon et al. who refer to an $m = 1$ mode as 'push-pull pairwise' or 'push-pull 2-cans', depending on the location of the nodal line. Furthermore, degenerate modes $m = 1, 2, 3$ can be of spinning and mixed type.

Experimental setup and data analysis

The baseline configuration of the combustor is depicted in Fig. 1. It consists of eight cans that are fed with perfectly premixed mixture from a shared plenum. Up until the end of the injector section, the combustor is identical to the atmospheric annular combustor employed by Worth and Dawson (2013); Mazur et al. (2019); Indlekofer et al. (2021). However, in the work cited above, twelve or more injectors were employed.

For the cans, steel pipes with inner diameter $d_{\mathrm{can}} = 41.9\,\mathrm{mm}$ are used: hence, there is no optical access except via the outlets. Each can consists of a lower and upper piece with the XT in-between, see Fig. 1 b).

In Figure 1 c), the lower half of the XT-segment is depicted. Blocking elements of cuboidal shape with a central bore can be inserted into the annular groove to vary the strength of the acoustic coupling. Apart from inserting no element at all, blocking elements with five different bore sizes are available, see Tab. 1. In addition, loose sheet metal pieces are put on top of the outlets to reduce acoustic communication via the outlets, Fig. 2a. Hereafter, this configuration is referred to as BL (baseline). In this paper, the effects of an additional adjustment to the base

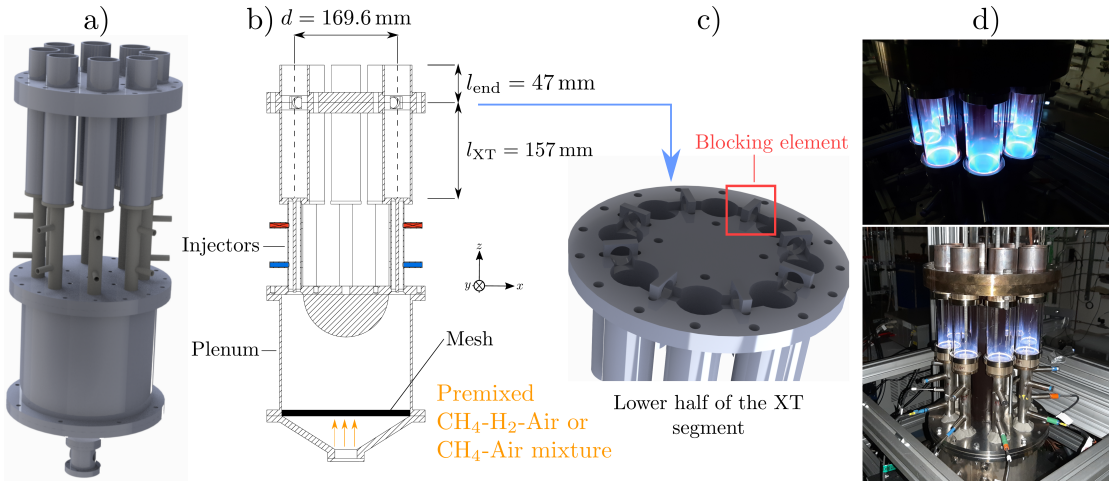

Figure 1. a) Rendering of the can-annular rig. From the plenum, injectors feed mixture into individual cans. Pressure transducers are mounted in the injectors. Each can consists of a lower and an upper part, with the two-part XT-ring sandwiched in between. b) Axial cut through the rig. Dimensions upstream of the base of the cans and of the bluff bodies can be found in Indlekofer et al. (2021). Pressure transducers are mounted in the lower ports (blue), while the upper ones (red) are blocked. Steel wool is inserted into the conical section at the inlet and closed with a mesh to suppress any large-scale asymmetries in the inflow. c) Lower half of the XT with the blocking stones mounted. An identical plate is mounted from above. The revolving groove is $10\,\mathrm{mm}$ deep (in each plate) and has outer and inner diameters $189.6\,\mathrm{mm}$ and $149.6\,\mathrm{mm}$, respectively. d) Photos of the rig during operation with quartz tubes instead of steel pipes for the combustion chambers. The setup with quartz tubes was employed during a later experimental campaign; all data discussed in the present work was acquired with steel tubes.

Table 1. Dimensions of the blocking elements.

Name	Tiny	Small	Medium	Large	Huge	Open
d_{XT}	9.4 mm	13.2 mm	16.2 mm	18.7 mm	20.0 mm	-
$A_{\mathrm{XT}}/A_{\mathrm{can}}$	0.05	0.10	0.15	0.20	0.23	0.29

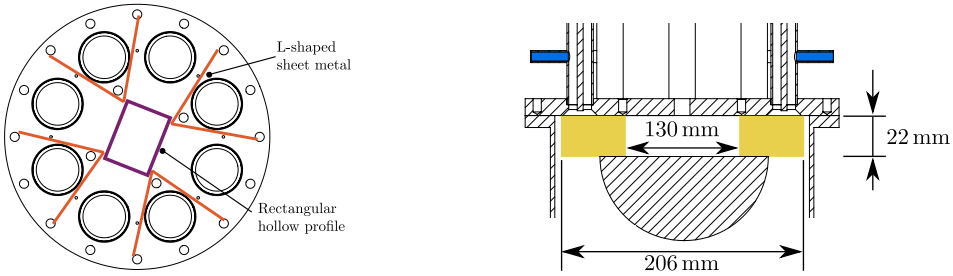

(a) **(b)**

Figure 2. a) Top view of the combustor with sheet metals placed loosely on top to suppress acoustic communication via the outlets. An end correction gives $0.61 d_{\mathrm{can}}/2 = 12.78\,\mathrm{mm}$ for the location of the pressure node downstream of each outlet. The length of the pipe segment is $45\,\mathrm{mm}$ to yield a total of $57.78\,\mathrm{mm}$, which is significantly shorter then the sheet metal of height $150\,\mathrm{mm}$. b) Detailed view of the plenum in Fig. 1 with the sintered plate (yellow) mounted upstream of the injectors. The sintered plate is of type SIKA-B200 with a porosity of 51% and pore size $124\,\mu\mathrm{m}$.

configuration is also investigated: in order to decouple acoustic communication via the plenum, a sintered plate is mounted upstream of the injectors, Fig. 2b. The plate has a high pressure drop and is highly acoustically reflective. This configuration is referred to as SP (sintered plate). Figure 3 depicts transfer functions for BL and SP obtained from forcing via the outlets and recording signals in all cans. There is significant communication via the plenum in the BL case and the addition of the sintered plate reduces this significantly in the entire range of frequencies but particularly between $750\,\mathrm{Hz}$ and $1000\,\mathrm{Hz}$.

Operation of the combustor

Perfectly premixed blends of methane, hydrogen and air are injected into the plenum. The precise mixture compositions are given in the respective result sections.

To monitor whether all flames are stabilised as intended on the bluff body flame holders rather than lifted, an overhead Photron SA1.1 CMOS camera is employed. In conjunction

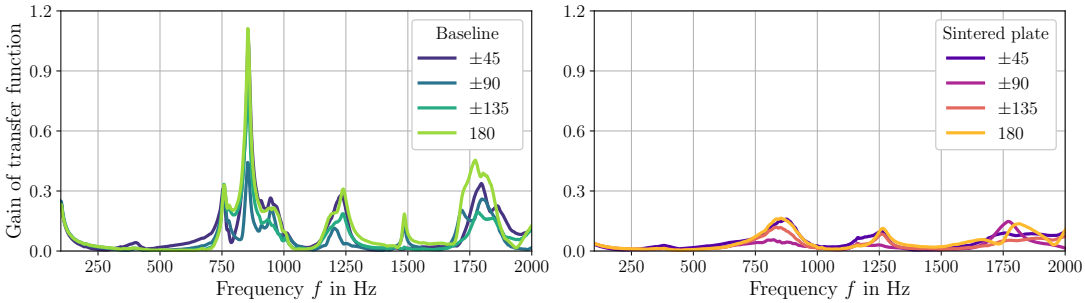

Figure 3. For cases BL and SP the XTs are closed and the cans are forced via the outlets with a loudspeaker in the range of 100 Hz to 2000 Hz. This yields seven transfer functions with respect to the microphones in the other cans. This is done for all eight cans and the average taken. Finally, transfer functions of cans at angles $+45°$ and $-45°$ are averaged (likewise for the other angles). The addition of the sintered plate significantly reduces communication via the plenum.

with a LaVision Intensified Relay Optics unit and a Cerco 2178 UV lens equipped with a D20-VG0035942 filter (centre wavelength 310 nm, full width half maximum 10 nm), the camera images the OH^* chemiluminescence in the heat release zone. Apart from the monitoring, the camera data is not used in this paper. On the OH^* images a lifted flame can be clearly distinguished from a flame stabilized at the flame holders. If a lifted flame is identified, an upstream propagation is triggered by briefly increasing the hydrogen content of the reactants or by repeating the ignition procedure. Measurements are taken for a duration of 60 s.

An Optris CTlaser 3MHCF4 pyrometer is aimed at the inside wall of the outlet of the can at an angle of 225° to record the temperature. A new experimental run is commenced once the outlet temperature has dropped to 350 °C.

Pressure data acquisition and spectral analysis

In every injector tube, one Kulite (XCS-093-05D) pressure transducer is mounted, see Fig. 1. The pressure transducers are located in the lower of the two ports with the upper one blocked. Ideally, at least two pressure transducers would be placed in every injector to reconstruct the fluctuations in the cans via the multi-microphone method. However, eight microphones was the maximum number available during the experiments. A 24-bit DAQ system (NI model 9174) is used for the signal recording. Signals are recorded at $f_s = 51.2$ kHz and amplified with a FE-579-TA Bridge Amplifier from FYLDE set to a gain of 300 and using a built-in low-pass filter with cut-off at 20 kHz.

During operation, short time Fourier transform (STFT) is employed to identify dominant frequencies over time. Hereby, the data is binned into segments of 400 ms with an overlap of 75%. Each segment is extended via zero padding to 4 times its length. The spectra are computed with Welch's method with the same FFT parameters as the STFT.

In the post-processing step signals are filtered in the band of 250 Hz to 1450 Hz by using the inverse Fourier transformation and setting all frequencies outside this band to zero. As will be evident in the result section, the spectra show multiple peaks. In order to determine the mode orders of these peaks, the signals are filtered tightly with the inverse Fourier transformation and then projected onto a modal basis (see next section). Filter limits are chosen on a case-by-case basis depending on the spectra and to account for drifts in frequencies due to heat up of the rig. All oscillation amplitudes discussed in the following are obtained as the RMS of the pressure signals p or of the modal coefficients a_m^s, a_m^c discussed next.

Projection onto modal bases and definition of spin ratio

In the following, it is assumed that all eight pressure signals have been narrowly band-pass filtered around a frequency of interest. The signals are cast into a matrix $\mathbf{p} \in \mathbb{R}^{N\times l}$, where $N = 8$ is the number of pressure transducers and l is the number of samples – contingent on the chosen window in time domain during operation. In order to determine azimuthal mode orders m of a limit cycle oscillation, the signals are projected onto a set of circumferential basis functions, following Moeck (2010).

A standing wave basis is constructed in the form of a transformation matrix $\mathbf{B}_N \in \mathbb{R}^{N\times N}$ with columns

$$\mathbf{b}_n = \begin{pmatrix} w_0 1 \\ w_1 \cos\phi_n \\ w_1 \sin\phi_n \\ \dots \\ w_{N/2} \cos\left(N/2\,\phi_n\right) \end{pmatrix} \tag{1}$$

where the azimuthal coordinate takes discrete value $\phi_n = 0, \dots, 2\pi\,(N-1)\,/N$, and weights are chosen as $w_0 = w_{N/2} = 1/\sqrt{N}$ and $w_1, \dots, w_{N/2-1} = 1/\sqrt{N/2}$ to make $\mathbf{B}$ unitary. The matrix of modal coefficients $\mathbf{p}_m \in \mathbb{R}^{N\times l}$ is obtained via projection

$$\mathbf{p}_m = \mathbf{B}_N \mathbf{p}\,. \tag{2}$$

Columns of $\mathbf{p}_m$ contain the modal coefficients, which are termed a_m^s and a_m^c for sine and cosine basis, respectively. To represent the physical oscillation amplitudes, the modal coefficients need to be normalized by $\sqrt{N/2}$ for $m = 1, \dots, N-1$ and $\sqrt{N}$ otherwise. Notice that for the $m = N/2$ mode (here $m = 4$) it cannot be determined whether the mode is of spinning or standing type due to aliasing.

A spin ratio is defined following Bourgouin et al. (2013) as

$$\Delta_{\mathrm{sp}} = \frac{|a_m^+| - |a_m^-|}{|a_m^+| + |a_m^-|} \in [-1, +1] \,, \tag{3}$$

where a_m^+ and a_m^- are spinning mode coefficients derived from the standing basis. Values $+1$ and -1 denote a spinning state in clockwise and counterclockwise directions, respectively. A spin ratio of zero corresponds to a standing mode.

Numerical model for linear stability analysis

Linear stability analysis of the combustor is conducted using the package WavesAndEigenvalues.jl (Mensah and Orchini 2021), which solves the 3D thermoacoustic Helmholtz equation (Nicoud et al. 2007). Meshes are created with GMSH (Geuzaine and Remacle 2009) and have approximately 24 k degrees of freedom on a Bloch cell (Mensah et al. 2016). The cans are extended via an end correction $L_{\mathrm{corr}} = 0.61 d_{\mathrm{can}}/2$ (Levine and Schwinger 1948) to account for the effective downstream location of the pressure node.

For the mixtures employed in this work, flame transfer functions (FTFs) have been recorded on a single sector setup identical to the one employed in Æsøy et al. (2020). The temperature in the flame zone is set to 80% of the adiabatic flame temperature, to account for unknown heat losses, and then decreases linearly to the outlet where it is matched with the value recorded by the pyrometer.

Modal dynamics in the baseline configuration

The baseline configuration of Fig. 1 with the L-shaped decoupling at the outlets (Fig. 2a) is operated exclusively with CH_4–air mixture at 4 kW per burner and equivalence ratio of $\phi = 0.8$. The combustor is unstable for this operating condition.

In Figure 4 a), b), d) the frequencies, amplitudes of the modal coefficients and the pressure amplitudes over the circumference are depicted for the final 30 s of each run. Sizes ‘Small’ and ‘Large’ were not recorded since this data set was part of an exploratory test at the end of the commissioning campaign to characterize the test rig. For all XT sizes several peaks in a relatively narrow frequency band (approx. 150 Hz) can be observed, indicating clustered modes. The dominant frequency for the three largest XT sizes are close at around 760 Hz, while ‘Tiny’ shows two active frequencies at 730 Hz and 765 Hz. The right peak of ‘Tiny’ belongs to a mode with different azimuthal order ($m = 4$) than the main peaks corresponding to ‘Open’, ‘Large’ and ‘Medium’ ($m = 2$).

All XT sizes show most activity in the $m = 2$ mode except for ‘Tiny’, which has an active $m = 4$ mode in addition, see Fig. 4 c). For ‘Open’ and ‘Huge’ the amplitudes of sine and cosine components are very similar. This property in combination with an almost identical pressure amplitude in all eight cans shows that the $m = 2$ modes oscillate pairwise for these two geometries. The spin ratios in Fig. 7 confirm this predominantly standing state. As the XT size is decreased to ‘Medium’, the amplitudes of the cosine component increases while the sine component decreases. The spin ratio for ‘Medium’ shows this in the form of a mixed mode with a preference for a counterclockwise rotation.

The amplitudes in Fig. 4 d) are constant over the circumference for ‘Open’, ‘Huge’ and ‘Tiny’. Only ‘Medium’ shows a spatially varying amplitude; however, this is not sufficient proof of mode localization. Figure 4 b) shows that the $m = 3$ component is strongest for ‘Medium’ and that there is very little activity in any other mode orders. Thus, the variation in amplitude over the circumference is due to the mixed state of the mode, see the spin ratio in Fig. 7 a).

Figure 4 e) shows the mean pressure amplitude of the two peaks for ‘Tiny’ and Figure 4 c) the amplitudes of the modal coefficients. The mode at 730 Hz shows mainly activity in the $m = 2$ components and as such the nodal lines are located in cans at angles $45°, 135°, 225°$ and $315°$. The non-vanishing value of the pressure amplitude in the nodes is again due to the mixed state of the mode, see Fig. 7 a). The mode at 765 Hz has an active $m = 4$ component, indicating a push-pull mode. In addition, there is activity in the $m = 3$ component. For this mode there is a significantly higher amplitude in the can at $225°$. This is the only sign of mode localization in this configuration.

In Figures 4 f) & g) the STFTs are shown for two pressure transducers. The pressure transducer at $135°$ is located in a pressure node of the $m = 2$ mode and the pressure transducer at $180°$ in an antinode. According to the STFTs, both modes are active simultaneously and it can be observed how the frequencies drift upwards during operation due to the heating of the rig during operation.

Figure 5 depicts the eigenvalues from the linear stability analysis in the complex plane. A group of modes is unstable. In that group, the $m = 2$ mode matches with the experimentally observed $m = 2$ mode. The side peaks in the pressure spectrum corresponding to ‘Open’ match well with the FEM but the noise content is so high that no modal order can be determined for these to further validate the numerical result. Table 2 lists the experimental and numerical results. The agreement for other XT sizes is similarly good, see Fig. 5 c). However, the agreement should be treated with caution. The linear stability analysis does not model finite-amplitude effects and interaction between multiple unstable modes. These nonlinear effects may play a role that results in a shift in frequency but it cannot be determined to what extent this is the case, since there is a second unknown in the form of the actual heat losses. Setting the temperature in the flame zone to 80% of the adiabatic flame temperature also has an effect on the frequencies. Thus, it cannot be determined if the temperature is chosen correctly and the nonlinear effects are insignificant or if the choice in temperature incidentally conceals the nonlinear effects.

The experimental results and the linear stability analysis agree that a decrease in XT size results in a lowering of the frequencies, as predicted by Ghirardo et al. (2019) and von Saldern et al. (2021). Also, frequencies of higher mode orders are more sensitive to the XT strength, see bottom of Fig. 5 b), which is consistent with the results of Ghirardo et al. (2019). The modes will not merge for XT$\to 0$ because of coupling through the plenum.

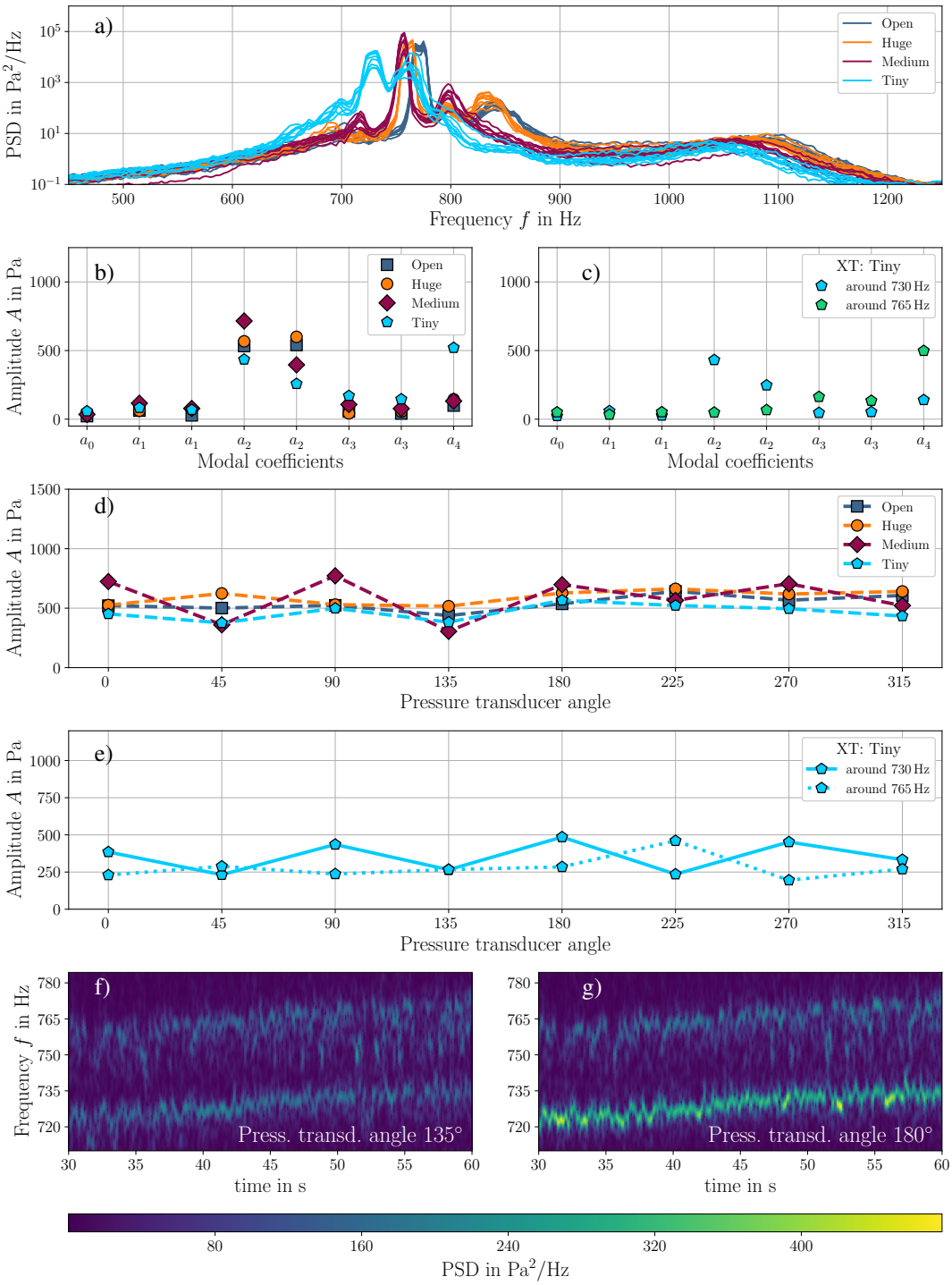

Figure 4. Baseline configuration with four different XT sizes. Pressure signals are taken from the last 30 s of an experimental run. a) Spectra for all eight pressure transducers and every XT size. b) Modal amplitudes for signals filtered in range $f \in [600, 900]$ Hz. c) Modal amplitudes for 'Tiny' filtered around the two peaks, i.e. in the range $f \in [710, 742]$ Hz and $f \in [742, 800]$ Hz, respectively. d) Mean pressure amplitude over the circumference. e) Mean pressure amplitudes over the circumference for 'Tiny' when the pressure signals are filtered narrowly around the two peaks in a). f) and g) STFT for 'Tiny' for the two pressure transducers at angles of $135°$ and $180°$.

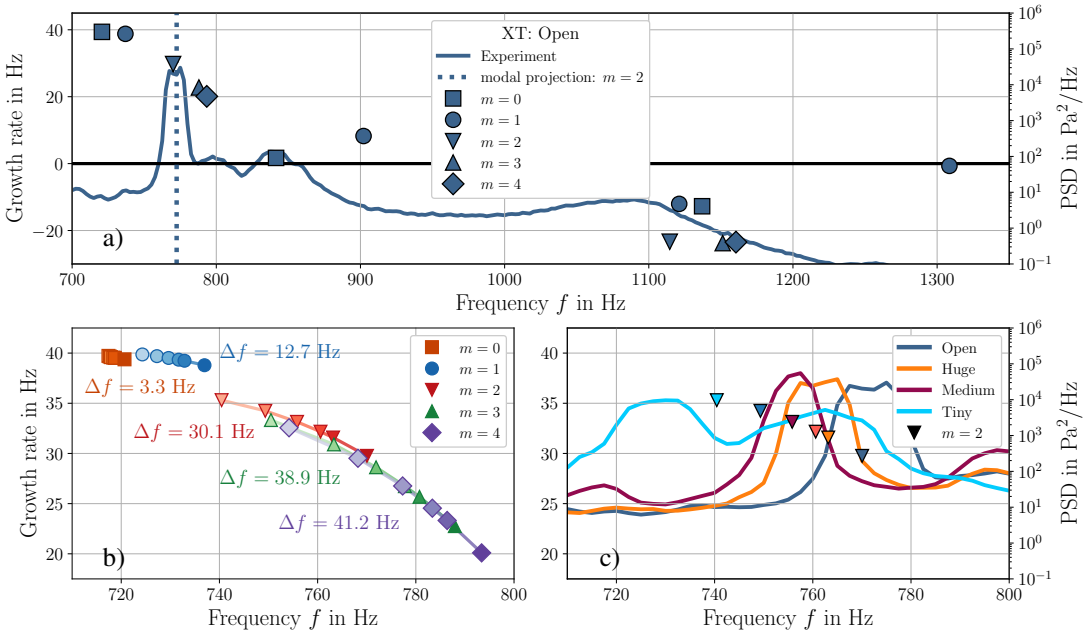

Figure 5. Baseline case. a) Eigenfrequencies computed with a linear stability analysis below 1400 Hz for 'Open' and the average spectrum from Fig. 4 a) for 'Open'. The spectra from all eight microphones are averaged. A stable plenum mode around 60 Hz is not depicted. A group of unstable modes is found in the vicinity of the experimentally observed $m = 2$ mode at 773 Hz. b) Clustered modes in range $f \in [700\,\text{Hz}, 800\,\text{Hz}]$ for all XT sizes. A darker shading signifies a larger XT. The higher the mode order, the larger the effect of the increase in XT strength: Difference in the complex plane between eigenvalues $\omega = 2\pi f$ of 'Tiny' vs. 'Open' is denoted as $|\Delta f|$. c) Average spectra of Fig. 4 a) and eigenvalues of $m = 2$ for all XT sizes. Numerical results and experiments match well except for the smallest XT size 'Tiny'.

According to the eigenvalues of Fig. 5 the two most unstable modes (with almost the same growth rates) are a push-push and an $m = 1$ mode. However, an $m = 2$ mode is observed experimentally. The linear stability analysis cannot explain this discrepancy and more sophisticated models for the flame dynamics (von Saldern et al. 2020) and the acoustic-flow coupling via the XT (Orchini et al. 2021) are needed.

Altogether, the preferred state of the BL case is an $m = 2$ mode. A reduction in XT size shifts the frequencies downwards and also effects the states of the $m = 2$ modes. Only for the smallest XT size is an additional push-pull mode observed.

Effect of decoupling the plenum with a sintered plate

In the BL case a group of modes within a frequency band of 150 Hz is observed. However, due to the plenum acoustic communication between cans – including non-adjacent ones – is not restricted to the XTs. In order to isolate the effect of coupling via XTs a sintered plate, as depicted in Fig. 2b, is installed upstream of the injectors. The goal of this modification is to tighten the grouping of closely spaced modes and change the overall topology of the spectrum such that more than one cluster of modes can be studied. Moreover, the linear stability analysis shows that the unstable group in Fig. 5 does not nominally form a cluster: The mode

Table 2. Active modes below 1400 Hz for BL with XT 'Open', computed numerically. The cluster label is determined from the axial order. Modes belonging to the first cluster are depicted with a gray background, and the experimentally observed mode with a darker gray background. The group in the range $f \in [721\,\text{Hz}, 793\,\text{Hz}]$ contains a mode from another cluster, since the plenum mode at 60 Hz is the first mode in the first cluster. More overlap between clustered modes can be observed for modes at higher frequencies.

f in Hz	Azi. ord.	Ax. ord.	Cluster
60	0	0	I.
721	0	1	II.
737	1	0	I.
770	2	0	I.
773	$m = 2$ in experiments, main peak		
788	3	0	I.
793	4	0	I.
797	Side peak in experiments		
840	Side peak in experiments		
841	0	2	III.
902	1	1	II.
1115	2	1	II.
1121	1	2	III.
1137	0	3	IV.
1151	3	1	II.
1160	4	1	II.
1309	1	3	IV.

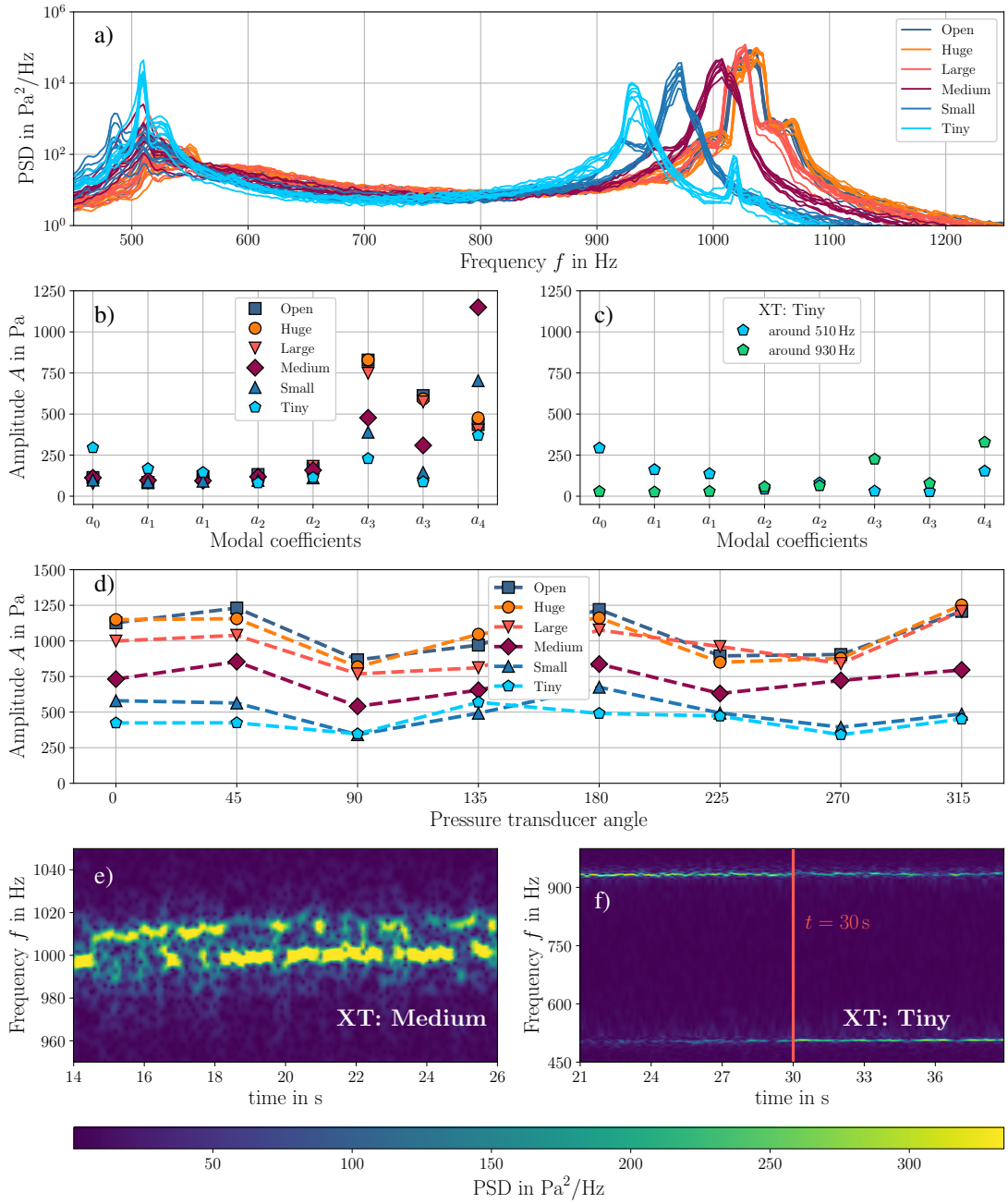

Figure 6. Sintered plate case. a) A lower cluster at $500\,\mathrm{Hz}$ and an upper cluster at ca. $900\,\mathrm{Hz}$ to $1100\,\mathrm{Hz}$ are observed, depending on XT size. The XT size strongly affects the dominant frequencies in the upper clusters. b) Sizes 'Large', 'Huge' and 'Open' can be grouped together: Frequencies and amplitudes are similar and the limit cycle oscillation is a mode of order $m = 3$. c) Amplitudes of modal coefficients for 'Tiny' when the peaks are filtered in the range $f \in [400, 550]$ Hz and $f \in [900, 960]$ Hz, respectively. d) Pressure amplitude decreases in all cans as the XT strength is decreased. e) & f) Spectrogram for pressure transducer at an angle of $180°$. e) For 'Medium' the combustor jumps between two modes. The mode at $1000\,\mathrm{Hz}$ is of order $m = 3$ and the mode at $1018\,\mathrm{Hz}$ of order $m = 4$. These are not identifiable as isolated peaks in a) since the spectrum contains the frequency content for the entire experimental run of $60\,\mathrm{s}$. During operation the rig heats up and causes a gradual shift in both frequencies, which results in the smooth peak shown in a). f) The smallest XT size, 'Tiny', shows activity in the $m = 4$ mode at $932\,\mathrm{Hz}$ which transitions over time into the $m = 0$ mode at $507\,\mathrm{Hz}$.

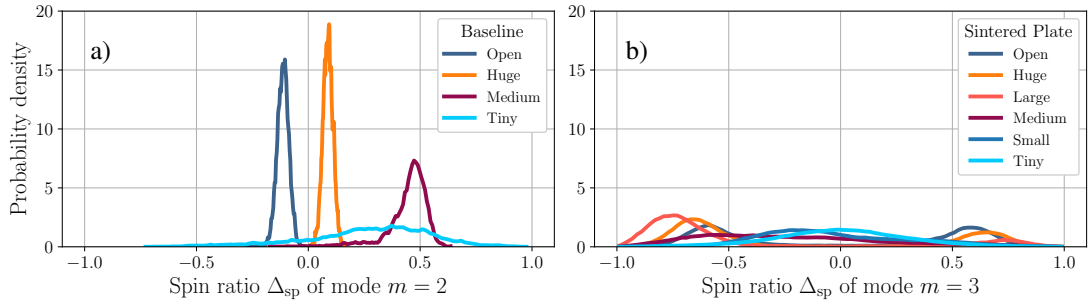

Figure 7. a) and b) Spin ratios for observed limit cycle oscillations. The time signal is filtered in a band of width 40 Hz centered at the respective frequencies. a) BL case. For 'Huge' and 'Open', a standing mode is observed. For 'Medium' the spin ratio stays close to 0.5 pointing to a mixed mode. The spin ratio for 'Tiny' is not conclusive. b) SP case. For the largest XT sizes spinning states are observed.

at 721 Hz has a higher axial order than the rest, see Tab. 2. This property seems to bear no consequence for treating the group as a cluster, as detailed in the previous section.

With the sintered plate the combustor is stable for a CH_4–air mixture and $\phi = 0.8$ – the operating condition in the previous section. However, for a CH_4–H_2–air mixture instabilities are observed. A hydrogen content of 8% by power (20.09% by volume) is chosen at a total power of 8.3 kW per burner. The combustor is stable for $\phi = 0.75$ and unstable for higher ϕ. All results presented in the following are for $\phi = 0.85$.

Figure 6 depicts the results for case SP. Comparison with the BL case in Fig. 4 shows that the spectra have decidedly fewer peaks: only two well-separated broad peaks are observed for all XT sizes. In fact, both peaks are formed by clustered modes. The analysis and its result are not depicted here, but for both clusters any available side-peaks are narrowly filtered in frequency domain and projected onto a modal basis. With this procedure it is observed that any identifiable peaks belong to modes of distinct azimuthal orders. Given that several modes are observed in a narrow band (50 Hz) the data suggests that clusters are present. However, per cluster and for all XT sizes at most three peaks are observed in parallel. Hence, some of the modes in the cluster are not unstable at any moment during an experimental run. Compared to the BL configuration the clusters are much more compact (50 Hz vs. 150 Hz).

The pressure spectra of the three largest XT sizes match almost identically. As the XT size is decreased, the dominant frequencies are strongly affected. For 'Tiny' the peak at 1040 Hz seems to be due to a higher harmonic of a mode from the lower cluster. Comparing Fig. 4 a) and Fig. 6 a) shows that the limit cycle frequencies are much more sensitive to a decrease in XT size for SP compared to BL.

All XT sizes show activities in the $m = 3$ and $m = 4$ modes but to varying degrees. For the three largest sizes, the $m = 3$ mode has larger amplitude than the $m = 4$ mode. At around 'Medium' the balance is shifted in favor of the $m = 4$ mode. Subsequent smaller sizes retain this slight preference. The lower left plot in Fig. 6 e) shows that the case 'Medium' jumps between modes of orders $m = 3$ and $m = 4$. No steady state is reached and unlike the case BL-Tiny in Fig. 4 f) and g) the two modes are not active simultaneously. During an experimental run with 'Tiny', the combustor starts in an $m = 4$ mode but slowly transitions into $m = 0$, see Fig. 6 f). The transition itself takes approximately 30 s.

The three largest XT sizes with a pronounced $m = 3$ mode show a spinning state, see Fig. 7. This preference is lost as the XT size is decreased. Due to the simultaneously high activity in modes of orders $m = 3$ and $m = 4$ for all XT sizes, a mode localization is visible in the form of a significant variation of the pressure amplitude over the circumference. This is more pronounced for larger XT sizes.

Overall, as the XT size is decreased the pressure amplitudes decrease strongly. However, case SP shows overall higher amplitudes than case BL and while case BL prefers standing or mixed modes, case SP shows a preference for a spinning state.

Conclusion

The first experimental results on a can-annular laboratory combustor with $N = 8$ cans are presented. The combustor facilitates studying the effect of varying cross-talk strength on modal dynamics and mode selection.

The spectrum of a baseline configuration shows a cluster of modes. Frequencies obtained from a linear stability analysis match well with the experimentally recorded ones and the numerical results predict that all clustered modes are unstable. By mounting a sintered plate upstream of the injectors, acoustic wave propagation via the plenum is suppressed. The consequent reduction in overall can-to-can coupling strongly affects the modes: two distinct clusters within narrow frequency bands emerge. The pressure amplitudes are consistently higher in the decoupled (SP) case when comparing XT sizes with the coupled (BL) case.

The experiments confirm several predictions of theoretical studies in the literature, namely: (1) clustered modes are ordered by increasing frequency, (2) a reduction in XT size lowers the frequency of the modes and (3) frequencies of higher order modes are more sensitive to the XT strength. In the BL case an $m = 2$ mode of standing/mixed type is mainly observed, while for the SP case it is an $m = 3$ mode of mixed/spinning type. Both cases show an increase of activity in a push-pull mode ($m = 4$) as the XT size is reduced. The probability density of the spin ratios is strongly

affected by the XT strength. Overall, the SP configuration is better suited to focus on the role of XT strength for thermoacoustic instabilities, since the clustered modes are more tightly grouped and several clusters are identifiable. Sensitivities of frequencies to changes in XT strength are also higher.

In conclusion, the presented dynamics show that thermoacoustic instabilities in a nominally symmetric can-annular combustor are strongly affected by the coupling strength. Small variation in the coupling strength leads to major shifts in the frequencies of the limit cycles. This has implications for the design of dampers of Helmholtz type for specific instability frequencies. Besides the limit cycle frequencies, amplitudes and modal coefficients also show strong variations as functions of the XT size.

The presence of multiple unstable modes makes it difficult to characterise and predict the steady states. For instance, for the BL case the most unstable mode ($m = 0$), according to a linear stability analysis, is not observed experimentally but another mode ($m = 2$) is. This shows that more sophisticated models are needed to capture the interaction and competition between the unstable modes. In the experiments, multiple unstable modes simultaneously, jumping between two modes and slow transitioning between two modes are all observed. These are interesting phenomena in their own right and show how diverse the steady states of thermoacoustic instabilities in can-annular combustors can be. In addition, mode localization in the form of simultaneously active modes of different azimuthal orders is observed for the case SP.

Acknowledgement

Philip E. Buschmann would like to thank Sam Wiseman for his guidance during the assembly of the can-annular experiment and the setup of the measurement devices. His help has been a great assistance in getting the experiment rapidly operational.

References

Æsøy E, Aguilar JG, Wiseman S, Bothien MR, Worth NA and Dawson JR (2020) Scaling and prediction of transfer functions in lean premixed H_2/CH_4-flames. *Combustion and Flame* 215: 269–282.

Bethke S, Krebs W, Flohr P and Prade B (2002) Thermoacoustic properties of can annular combustors. In: *8th AIAA/CEAS Aeroacoustics Conference & Exhibit*. p. 2570.

Bourgouin JF, Durox D, Moeck J, Schuller T and Candel S (2015) A new pattern of instability observed in an annular combustor: The slanted mode. *Proceedings of the Combustion Institute* 35(3): 3237–3244.

Bourgouin JF, Durox D, Moeck JP, Schuller T and Candel S (2013) Self-sustained instabilities in an annular combustor coupled by azimuthal and longitudinal acoustic modes. In: *Turbo Expo: Power for Land, Sea, and Air*, volume 55119. American Society of Mechanical Engineers, p. V01BT04A007.

Geuzaine C and Remacle JF (2009) Gmsh: A 3-D finite element mesh generator with built-in pre-and post-processing facilities. *International Journal for Numerical Methods in Engineering* 79(11): 1309–1331.

Ghirardo G, Di Giovine C, Moeck JP and Bothien MR (2019) Thermoacoustics of can-annular combustors. *Journal of Engineering for Gas Turbines and Power* 141(1): 011007.

Ghirardo G, Moeck J and Bothien MR (2020) Effect of noise and nonlinearities on thermoacoustics of can-annular combustors. *Journal of Engineering for Gas Turbines and Power* 142(4): 041005.

Indlekofer T, Faure-Beaulieu A, Noiray N and Dawson J (2021) The effect of dynamic operating conditions on the thermoacoustic response of hydrogen rich flames in an annular combustor. *Combustion and Flame* 223: 284–294.

Jegal H, Moon K, Gu J, Li LK and Kim KT (2019) Mutual synchronization of two lean-premixed gas turbine combustors: Phase locking and amplitude death. *Combustion and Flame* 206: 424–437.

Kim KT (2016) Combustion instability feedback mechanisms in a lean-premixed swirl-stabilized combustor. *Combustion and Flame* 171: 137–151.

Kim KT (2017) Nonlinear interactions between the fundamental and higher harmonics of self-excited combustion instabilities. *Combustion Science and Technology* 189(7): 1091–1106.

Laera D, Prieur K, Durox D, Schuller T, Camporeale S and Candel S (2016) Flame describing function analysis of standing modes in an annular combustor and comparison with experiments. In: *Thermoacoustic Instabilities in Gas Turbines and Rocket Engines: Industry meets Academia*, Paper No: GTRE-044. Munich, Germany.

Levine H and Schwinger J (1948) On the radiation of sound from an unflanged circular pipe. *Physical review* 73(4): 383.

Mazur M, Nygård HT, Dawson JR and Worth NA (2019) Characteristics of self-excited spinning azimuthal modes in an annular combustor with turbulent premixed bluff-body flames. *Proceedings of the Combustion Institute* 37(4): 5129–5136.

Mensah GA, Campa G and Moeck JP (2016) Efficient computation of thermoacoustic modes in industrial annular combustion chambers based on bloch-wave theory. *Journal of Engineering for Gas Turbines and Power* 138(8).

Mensah GA and Orchini A (2021) Wavesandeigenvalues. https://julholtzdevelopers.github.io/WavesAndEigenvalues.jl/dev/.

Moeck JP (2010) *Analysis, modeling, and control of thermoacoustic instabilities*. PhD Thesis, Technische Universität Berlin.

Moon K, Jegal H, Gu J and Kim KT (2019) Combustion-acoustic interactions through cross-talk area between adjacent model gas turbine combustors. *Combustion and Flame* 202: 405–416.

Moon K, Jegal H, Yoon C and Kim KT (2020a) Cross-talk-interaction-induced combustion instabilities in a can-annular lean-premixed combustor configuration. *Combustion and Flame* 220: 178–188.

Moon K, Yoon C and Kim KT (2020b) Influence of rotational asymmetry on thermoacoustic instabilities in a can-annular lean-premixed combustor. *Combustion and Flame* 223: 295–306.

Nicoud F, Benoit L, Sensiau C and Poinsot T (2007) Acoustic modes in combustors with complex impedances and multidimensional active flames. *AIAA Journal* 45(2): 426–441.

Orchini A, Pedergnana T, Buschmann PE, Worth NA, Moeck JP and Noiray N (2021) Reduced-order modelling ofthermoacoustic instabilities incan-annular combustors. In: *SoTiC 2021 - Symposium on Thermoacoustics in Combustion: Industry*

meets Academia.

von Saldern JG, Moeck JP and Orchini A (2020) Nonlinear interaction between clustered unstable thermoacoustic modes in can-annular combustors. *Proceedings of the Combustion Institute* 38(4): 6145–6153.

von Saldern JG, Orchini A and Moeck JP (2021) Analysis of thermoacoustic modes in can-annular combustors using effective Bloch-type boundary conditions. *Journal of Engineering for Gas Turbines and Power* 143(7): 071019.

Worth NA and Dawson JR (2013) Modal dynamics of self-excited azimuthal instabilities in an annular combustion chamber. *Combustion and Flame* 160(11): 2476–2489.

Reduced-order modelling of thermoacoustic instabilities in can-annular combustors

Reduced-order modelling of thermoacoustic instabilities in can-annular combustors

Alessandro Orchini[a], Tiemo Pedergnana[b], Philip E. Buschmann[c], Jonas P. Moeck[c,*], Nicolas Noiray[b]

[a]*Institute of Fluid Dynamics and Technical Acoustics, TU Berlin, Germany*
[b]*CAPS Laboratory, Department of Mechanical and Process Engineering, ETH Zürich, Switzerland*
[c]*Department of Mechanical and Process Engineering, NTNU Trondheim, Norway*

Abstract

Thermoacoustic instabilities in stationary gas turbines may cause high-amplitude limit cycles, leading to damaged components and costly down-time. To better understand the physical origin of such instabilities in a can-annular combustor configuration, we study the properties of the spectrum of a reduced-order can-annular thermoacoustic system. Increased focus is placed on representing the aeroacoustic interaction between the longitudinal eigenmodes of the individual cans with physically relevant models. To represent the acoustic pressure dynamics in the combustor, we combine an analytical, experimentally validated model for the can-to-can impedance with a frequency-dependent model of the flame response in the cans to acoustic perturbations. By using this approach, we perform a parametric study of the linear stability of an atmospheric can-annular thermoacoustic system, and emphasize general features of the structure and properties of the eigenvalues and the eigenvectors of can-annular combustors. Lastly, we emphasize the differences in the can-to-can coupling that arise when considering open-end boundary conditions – as in atmospheric set-ups – or closed-end boundary conditions – as in real gas turbine combustors.

Keywords: Can-annular, Sensitivity, Shear layer, V-flame

*Corresponding author: jonas.moeck@ntnu.no

Nomenclature

Latin symbols

A_r	Ratio between gap (A_g) and can (A_c) surface area
b	Bloch number
c_i	Speed of sound
f_i, g_i	Riemann invariants
G	Flame front level set (G=0)
K_R	Rayleigh conductivity
L_f	Flame length
l_g	Gap length
M_x	Mach number
N	Number of cans
p	Pressure
q	Heat release rate
r_can	Can radius
R_i	Reflection coefficient
s	Laplace variable
s_L	Flame speed
T	Temperature
u	Velocity
U_c	Convective velocity
Z_i	Impedance

Greek symbols

ω	Angular frequency
ρ	Density
σ	Growth rate
τ	Time delay
ζ	Can-to-can impedance

Other symbols

$\hat{\cdot}$	Laplace domain variable
$\bar{\cdot}$	Mean value
$\tilde{\cdot}$	Non-dimensional impedance (scaled with ρc)
FTF	Flame Transfer Function

1. Introduction

1.1. Thermoacoustic instabilities in can-annular combustors

Thermoacoustic instabilities can arise from the constructive interaction of a flame with the sound field in an enclosed volume, such as the combustion chamber of a gas turbine. This classic physical phenomenon was first studied in modern terms by [1]. Insufficiently damped instabilities lead to high-amplitude pressure oscillations in the chamber. These oscillations in turn induce high-cycle fatigue in the metal parts surrounding the enclosure, for instance the turbine vanes, which causes down-time and incurs fees and repair costs for the manufacturer. The modeling, prediction and suppression of thermoacoustic instabilities has come to renewed importance in the last 40 years due to strict emission limits and the resulting increased demand for lean-premixed combustion. In modern combustors for power generation, most of the air flow passes through the burner to ensure a lean mixture. The absence of dilution holes that are commonly found in aeroengines – and that

are highly efficient sound absorbers – leads to combustion instability problems similar to those encountered in rocket engines, with the difference that the life span of stationary gas turbines is expected to be in the order of tens of thousands of hours [2].

Much research has been devoted in the last decade to modeling and understanding thermoacoustics of single-can [3, 4, 5] and annular combustion chambers [6, 7]. In contrast, modern high-efficiency H-class gas turbines exclusively feature can-annular combustor architectures. In this design, combustion takes place in a number (typically 12 or 16) of cans. The annular turbine inlet is common to all cans and allows for acoustic cross-talk between neighboring elements. Upstream coupling via a plenum is also possible, but it will not be considered in this study. The increasing interest in the subject of thermoacoustic instabilities in can-annular combustor architectures is exemplified by numerical and experimental studies performed in academia and in industry, including Siemens [8, 9, 10, 11], General Electric [12, 13, 14], and Ansaldo Energia Switzerland [15, 16].

In the present work, we describe a general reduced-order model for predicting thermoacoustic instabilities in can-annular combustors (§2 and §3). This model is used to study a lab-scale can-annular combustor (§4), with the objective of understanding the influence that various physical parameters – viz., the mean flow speed and the magnitude of the heat release rate response – have on the frequency spectrum of the system. The physical counterpart of the modelled setup is located at NTNU, Norway [17]. This experimental setup is a modified version of the one described in [18], with the major difference that the annular combustion chamber has been replaced by a periodic set of weakly coupled ducts. This lab-scale combustor operates at atmospheric conditions, and the cans are (acoustically) open at the downstream end. This is in contrast to the acoustic boundary condition in real gas turbines, in which the cans are acoustically closed at their downstream end (choked turbine inlet). To address this key difference, in §5 we discuss the effect of the downstream boundary condition on the can-to-can coupling and the thermoacoustic spectrum.

1.2. Modelling of the aeroacoustic can-to-can coupling

In this work, special focus is placed on the effect that the can-to-can impedance has on the acoustic pressure dynamics in the chamber. The can-to-can impedance describes the aeroacoustic response at the openings connecting the ducts. It depends on the interaction between the acoustic

pressure fields in neighbouring cans and the aerodynamic modes of the turbulent wake in the openings connecting them. This acoustic–aerodynamic interaction plays an important role in self-sustained cavity oscillations, a classic physical phenomenon first described by [19]. The model we use is based on impedance measurements of a side-branch aperture presented in Fig. 6(a) of [20], which show a non-trivial behavior around a frequency corresponding to the least stable aerodynamic mode of the shear layer. For small enough acoustic pressure amplitudes, it was found that the aeroacoustic response of the aperture can be amplifying, which manifests itself in a reflection coefficient R exceeding 1. As the amplitude is increased, the response saturates, an effect that was recently studied numerically using large-eddy simulations (LES) by [21]. These measurements were used in [22] to calibrate an explicit, analytical model able to quantitatively predict the effect of the mean flow speed and the acoustic pressure amplitude on the acoustic impedance over the relevant frequency range.

2. Reduced-order thermoacoustic model

The reduced-order approach outlined in this study can be used to model a general can-annular combustor system. The generic configuration that highlights the can-to-can communication is shown in Figure 1. The reduced-order model will be applied to an atmospheric can-annular setup, whose details are outlined in [17], to study its thermoacoustic response and the sensitivity of its spectrum.

2.1. Can-acoustic network model

Analogous to [23], [15] and [24] we consider an array of N cans that communicate acoustically at the downstream end via small gaps. For the range of frequencies that will be considered in this study, transverse acoustic modes in a can are cut-off. It is thus appropriate to assume planar wave propagation in the axial direction for the acoustics. This is consistent with the results of [15], in which it was shown that non-axial acoustic propagation is relevant only in the vicinity of the connection gaps. To account for these near field effects, the acoustic transmission at the gaps will be modelled by means of an experimentally fitted impedance, presented in §3.

The one-dimensional acoustic field is described in terms of its Riemann invariants [25]. Considering the flame (and burner) as a scattering element,

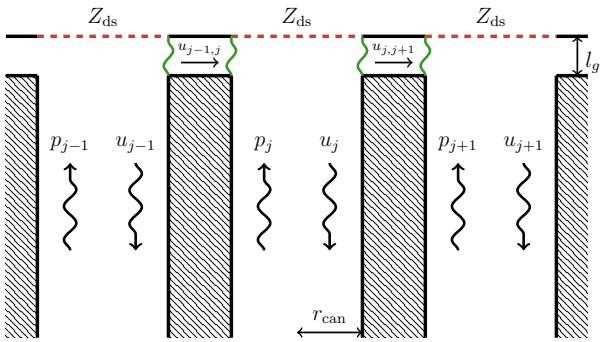

Figure 1: Sketch of the geometry considered. The cans are assumed to communicate only downstream through apertures having axial extension l_g. Acoustic waves at the downstream end of the cans are partly reflected back in the can by a downstream impedance Z_{ds} (dashed red lines) and partly transmitted to neighbouring cans, via transverse acoustic velocity fluctuations in the apertures. This coupling mechanism is driven by the dynamics of the shear layer that forms at the interface between the cans and the gaps (in green).

conservation of mass, momentum and energy yield [26, 27]

$$\begin{bmatrix} \hat{g}_1 \\ \hat{f}_2 \end{bmatrix} = \begin{bmatrix} S_{11} & S_{12} \\ S_{21} & S_{22} \end{bmatrix} \begin{bmatrix} \hat{f}_1 \\ \hat{g}_2 \end{bmatrix} + \begin{bmatrix} H_1 \\ H_2 \end{bmatrix} \hat{q}, \tag{1}$$

where $\hat{q}$ is the unsteady heat release rate, S_{ij} the elements of the scattering matrix, and H_j constant factors scaling the heat release response to acoustic fluctuations. Closure for the acoustics is provided by expressions for the reflection coefficients at the upstream (R_1) and downstream (R_2) boundaries

$$\hat{f}_1 = R_1 e^{-s\tau_1} \hat{g}_1, \quad \hat{g}_2 = R_2 e^{-s\tau_2} \hat{f}_2, \tag{2}$$

with $\tau_j \equiv 2l_j c_j/(c_j^2 - \overline{u}_j^2)$ and $s \equiv \sigma + \mathrm{i}\omega$. By substituting these expressions in the conservation laws (1) one obtains

$$\underbrace{\left(\mathcal{I} - \begin{bmatrix} S_{11}R_1 e^{-s\tau_1} & S_{12}R_2 e^{-s\tau_2} \\ S_{21}R_1 e^{-s\tau_1} & S_{22}R_2 e^{-s\tau_2} \end{bmatrix}\right)}_{\mathcal{M}_{\mathrm{ac}}} \begin{bmatrix} \hat{g}_1 \\ \hat{f}_2 \end{bmatrix} = \begin{bmatrix} H_1 \\ H_2 \end{bmatrix} \hat{q}, \tag{3}$$

where $\mathcal{I}$ is the identity matrix. In the absence of an unsteady heat release input, $\hat{q} = 0$, the eigenvalues s of the matrix $\mathcal{M}_{\mathrm{ac}}$ yield the acoustic eigenvalues.

To account for the effect of the flame on the thermoacoustic stability, the heat release rate term is modelled by means of a Flame Transfer Function (FTF)

$$\begin{aligned}\hat{q} &= \frac{\overline{Q}}{\overline{u}_1}\mathrm{FTF}(s)\hat{u}_1 = \frac{\overline{Q}}{\rho_1 c_1 \overline{u}_1}\mathrm{FTF}(s)\left(\hat{f}_1 - \hat{g}_1\right) = \\ &= \left[\frac{\overline{Q}}{\rho_1 c_1 \overline{u}_1}\mathrm{FTF}(s)\left(R_1 e^{-s\tau_1} - 1\right), 0\right]\begin{bmatrix}\hat{g}_1 \\ \hat{f}_2\end{bmatrix}.\end{aligned} \tag{4}$$

By defining the matrix

$$\mathcal{M}_{\mathrm{hr}} = \begin{bmatrix}H_1 \\ H_2\end{bmatrix}\left[\frac{\overline{Q}}{\rho_1 c_1 \overline{u}_1}\mathrm{FTF}(s)\left(R_1 e^{-s\tau_1} - 1\right), 0\right] \tag{5}$$

the thermoacoustic eigenvalue problem reads

$$\left(\mathcal{M}_{\mathrm{ac}}(s) - \mathcal{M}_{\mathrm{hr}}(s)\right)\begin{bmatrix}\hat{g}_1 \\ \hat{f}_2\end{bmatrix} = \begin{bmatrix}0 \\ 0\end{bmatrix}. \tag{6}$$

2.2. Bloch boundary conditions

Expressions for the boundary conditions are required to close the thermoacoustic equations. In particular, at the downstream boundary we wish to model the can-to-can acoustic interaction. To understand the effect that can-to-can communication has on the (thermo)acoustic response, it is convenient to make use of Bloch-wave theory. By assuming that all cans are identical, an effective expression for the Bloch-wavenumber-dependent reflection coefficient can be derived. From the results of [24] this effective can-to-can reflection coefficient R_b can be expressed as

$$R_b = \frac{Z_b - \overline{\rho}c}{Z_b + \overline{\rho}c} = 1 - 2\frac{4\frac{A_r}{\tilde{\zeta}}\sin^2\left(\frac{\pi b}{N}\right)}{1 + 4\frac{A_r}{\tilde{\zeta}}\sin^2\left(\frac{\pi b}{N}\right)}, \tag{7}$$

where $\overline{\rho}c$ is the characteristic specific acoustic impedance, N the number of cans, b the Bloch wavenumber, A_r the ratio between the cross section of the can-to-can aperture and the cross section of the can, and $\tilde{\zeta}$ the (non-dimensional) impedance that links the acoustic pressure difference between two adjacent cans and the acoustic velocity:

$$\tilde{\zeta} \equiv \frac{\zeta}{\overline{\rho}c} = \frac{1}{\overline{\rho}c}\frac{\hat{p}_j - \hat{p}_{j+1}}{\hat{u}_{j,j+1}}. \tag{8}$$

In [24] a simple purely reactive can-to-can impedance model was used. In this study we shall instead adopt a more realistic empirical model, fitted to experimental data, as discussed in §3.

Equation (7) has, however, been derived with some restrictions, specifically that (i) the Helmholtz number defined by $\mathrm{He} \equiv (sl_g)/c$, where l_g is the axial extension of the gap, is negligible; (ii) the cans are acoustically closed after the openings, thus having $Z_{\mathrm{ds}} = \infty$; (iii) the mean flow effects due to a non-zero Mach number grazing flow along the gap are negligible. Although assumption (i) holds in most practical cases, the same is not true for the others. It was in fact shown in [28] that the effect of the mean flow is non-negligible. Moreover, a downstream choked boundary condition does not represent the correct physics for atmospheric test-rigs, which normally have open ends. Assumptions (ii) and (iii) can be relaxed, and a more general expression for the effective reflection coefficient can be derived, which retains the Mach number effects and an arbitrary downstream impedance. It reads [29]

$$R_b = 1 - 2\frac{(1-\mathrm{M}_x^2) + 4A_r/\tilde{\zeta}(\mathrm{M}_x + \tilde{Z}_{\mathrm{ds}})\sin^2\left(\frac{\pi b}{N}\right)}{\left(\tilde{Z}_{\mathrm{ds}}+1\right)(1-\mathrm{M}_x^2) + 4A_r/\tilde{\zeta}(\mathrm{M}_x + \tilde{Z}_{\mathrm{ds}})\sin^2\left(\frac{\pi b}{N}\right)}, \tag{9}$$

where we have introduced the (axial) Mach number $\mathrm{M}_x = \overline{u}_2/c_2$. It can be verified that, in the zero Mach number and infinite downstream impedance case, Eq. (7) is retrieved.

At the downstream end of our reduced-order can model we shall therefore set $R_2 = R_b$, which makes the thermoacoustic problem (6) Bloch-number dependent.

2.3. Flame Transfer Function

The unsteady heat release rate response is chosen to be that of an axisymmetric, laminar V-flame. The flame dynamics is modelled via the kinematic G-equation, which tracks the flame front as the level set $G = 0$, and reads

$$\frac{\partial G}{\partial t} + \boldsymbol{u}\cdot\nabla G = s_L|\nabla G|. \tag{10}$$

The underlying velocity field is modelled as a uniform axial mean flow and an unsteady travelling wave moving along the axial direction at velocity $\overline{u}_c$ [30, 31]

$$\boldsymbol{u} = \left(\overline{u}_1 + \epsilon\sin\left[\omega\left(t - x/\overline{u}_c\right)\right]\right)\boldsymbol{x}. \tag{11}$$

For small fluctuations amplitudes ϵ, the flame front can be considered a single-valued function of the radial coordinate, see Figure 2. Within this limit, the G-equation can be linearised and solved, and the instantenous heat release rate can be quantified by

$$Q = 2\pi\rho s_L h_r \iint_V |\nabla G|\delta(G) r \,\mathrm{d}r \,\mathrm{d}x. \tag{12}$$

Following steps analogous to those of [32] and [33], it can be shown that the FTF for the V-flame configuration outlined in Figure 2 reads

$$\mathrm{FTF} = 2\frac{e^{-\eta \mathrm{St}_2}\left(\gamma + \eta \mathrm{St}_2\right) - \eta e^{-\mathrm{St}_2}\left(\gamma + \mathrm{St}_2\right) + \gamma(\eta - 1)}{\eta \mathrm{St}_2^2 (2-\gamma)(1-\eta)}. \tag{13}$$

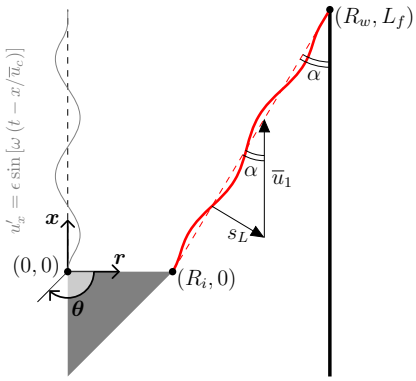

Figure 2: Geometry of the axisymmetric V-flame dynamics modelled with the G-equation. The steady flame (red dashed line) forms an angle α with the can wall, determined by the flame speed s_L and the axial mean flow velocity $\overline{u}_1$. An axially travelling perturbation, u'_x, induces oscillations in the flame front (thick red line), which in turn cause heat release rate fluctuations, quantified by the FTF (13).

In the latter, we have introduced the following non-dimensional variables:

$$\beta \equiv \frac{L_f}{R_w}, \qquad \gamma \equiv \frac{R_w - R_i}{R_w},$$
$$\sin\alpha = \frac{s_L}{\overline{u}_1} = \frac{R_w - R_i}{\sqrt{L_f^2 + (R_w - R_i)^2}} = \frac{\gamma}{\sqrt{\beta^2 + \gamma^2}}, \tag{14}$$
$$\mathrm{St}_2 \equiv \frac{sL_f}{\overline{u}_1 \cos^2\alpha}, \qquad \eta \equiv \frac{\overline{u}_1}{\overline{u}_c}\cos^2\alpha.$$

This FTF is a generalisation of that presented in Equation (28) of [32], in that the flame we consider is not (necessarily) anchored at the origin. The results of [32] are retrieved when setting $\gamma = 1$. The FTF that will be used in the rest of this study is shown in Figure 3.

We note that the FTF (13) depends on two time scales, $\tau_{f,1} \equiv \mathrm{St}_2/s$ and $\tau_{f,2} \equiv \eta\mathrm{St}_2/s$. The first is the characteristic time that perturbations take to travel along the unperturbed flame extension, $L_f/\cos\alpha$, when carried by the component of the mean velocity parallel to the unperturbed flame, $\overline{u}_1\cos\alpha$. This time scale was recognised as a characteristic time scale in both conical and V-flames in [34] and [35]. The second time scale is the characteristic time taken by velocity disturbances to travel along the axial extension of the flame L_f at the convective velocity $\overline{u}_c$. As discussed in [32], it is the constructive (destructive) interference between the waves propagating with these characteristic times that causes the presence of maxima (minima)

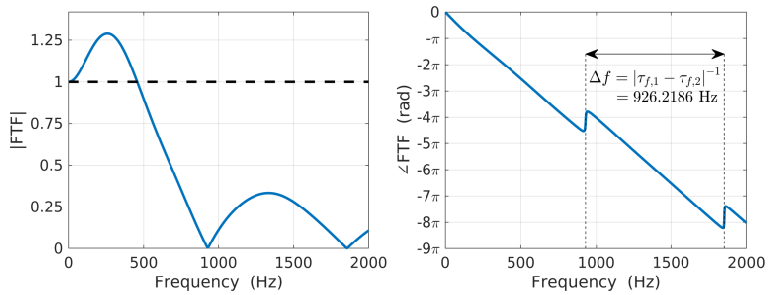

Figure 3: Gain and phase of the V-flame FTF that will be used in this study. The non-dimensional parameters used are $\beta = 0.955$, $\gamma = 0.690$, $\eta = 0.645$. They are are scaled by the cold mean flow velocity $\overline{u}_1 = 10$ m/s and the radial distance of the tip of the flame from the axis of symmetry, $R_w = 21$ mm.

in the amplitude of the FTF. This is shown in Fig. 3, where the distance between two zeros in the FTF response has been calculated analytically from knowledge on the characteristic time scales.

3. Effective can reflection coefficient with experimental can-to-can impedance model

The work of [22] has identified semi-empirical models that characterize the impedance of a side-branch aperture. These models were fitted against the experimental data of [20]. For the purpose of this manuscript, we shall adopt an impedance model based on the Rayleigh conductivity of an aperture with bias flow [36]

$$K_r(\Omega) = w\left[\frac{\pi}{2F(\Omega) + \log\frac{8w}{el_g}} + \gamma_1\right]. \tag{15}$$

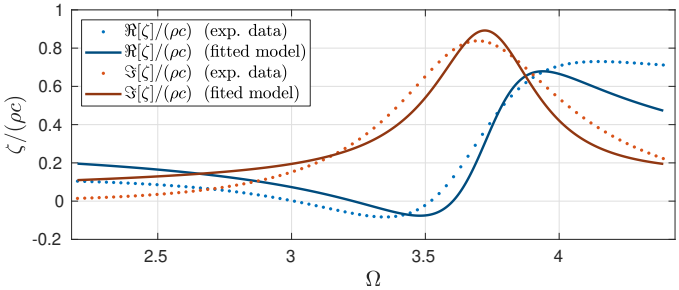

Figure 4: Fit of the impedance model (17) against the frequency response of the shear layer reported in [20] and [22]. The fitted coefficient values are $\kappa = 0.412$, $\gamma_1 = -0.196 + 0.162\mathrm{i}$ and $\gamma_2 = 0.154 + 0.079\mathrm{i}$.

The non-dimensional function F is defined by[1]

$$F(\Omega) = \frac{-J_0K - (J_0 + 2K)(J_0 + \mathrm{i}\Omega(J_0 - \mathrm{i}J_1))}{\Omega(J_0J_1 + \Omega(J_1^2 + (J_0 + 2\mathrm{i}J_1)^2))}, \tag{16}$$

[1]Eq. (16) is the complex conjugate of the expression reported in Eq. (3.3) of [36]. The complex conjugation is needed to compensate the different conventions used in the definition of the Laplace variable.

where w is the transverse dimension of the aperture, $K \equiv \mathrm{i}\Omega(J_0 + \mathrm{i}J_1)$, and $J_i = J_i(\Omega)$ are Bessel functions. The non-dimensional complex frequency used to evaluate the Rayleigh conductivity is $\Omega \equiv -\mathrm{i}sl_g/(2U_c)$, where $U_c \equiv \kappa\overline{U}$ is the characteristic convective velocity in the shear layer. From the definition of the Rayleigh conductivity, the impedance model for the aperture (8) is

$$\tilde{\zeta} = \frac{sA_g}{K_r(\Omega)c} + \gamma_2. \tag{17}$$

The non-dimensional coefficients γ_1 and γ_2 in Eqs. (15) and (17) are introduced to account for radiation losses and three dimensional effects. Together with κ, they are fitted against the experimental results of [20]. Figure 4 compares the measured and fitted resistance, $\Re[\zeta]$, and reactance, $\Im[\zeta]$, of the impedance at the connection cavities.

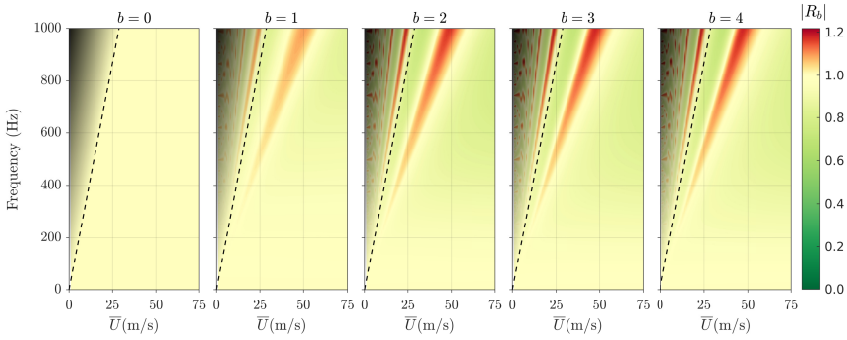

Figure 5: Effective reflection coefficient magnitude for a system with $N = 8$ cans, as a function of the mean flow and the frequency. The dashed lines indicate the upper limit of the data of [20] to which the aperture impedance model (17) has been fitted. Above this line (shaded regions), the higher the frequency the less reliable the fitted model.

To demonstrate how Eq. (9) can be used to understand the effect that the can-to-can coupling has on the effective reflection coefficient, we set up a generic system with $N = 8$ cans, and use the can-to-can impedance model (17) to represent the interaction of the cans. The can impedance downstream of the opening is chosen to be representative of the experimental configuration that will be considered in the following sections. It reads

$$\tilde{Z}_{\mathrm{ds}} \equiv \frac{Z_{\mathrm{ds}}}{\overline{\rho} c} = \frac{e^{s\tau_{\mathrm{end}}} - 1}{e^{s\tau_{\mathrm{end}}} + 1}, \quad \text{with} \quad \tau_{\mathrm{end}} = \frac{2 l_{\mathrm{end}} c}{c^2 - \overline{U}^2}, \tag{18}$$

which is the impedance of a tube of length l_{end} with mean flow and an open-end – when neglecting radiation and effective length corrections. Figure 5 shows the magnitude of the effective reflection coefficients for all positive values of the Bloch number b as a function of the mean flow and frequency. For $b = 0$, the can-to-can connection has no influence on the reflection coefficient. The (small) deviations from $R = 1$ are due to variations in the grazing flow Mach number. For $b > 0$, the effective reflection coefficient is strongly influenced by the flow properties and the forcing frequency. For any value of the convective mean flow u_c, we can identify a frequency at which the effective reflection coefficient for a specific Bloch number is minimized, and a frequency at which it is maximised. Notably, the effective reflection coefficient can exceed 1, due to the fact that, at its resonance frequency, the aerodynamic shear layer acts as an amplifier and enhances small impinging perturbations.

4. Thermoacoustic analysis of an atmospheric can-annular setup

The geometry we consider is an atmospheric can-annular setup, discussed in detail in [17]. It consists of 8 identical cans. Its geometrical details are reported in Figure 6. In the experiment, the cans are mounted on a large plenum upstream, which could couple the acoustics also on that side. To avoid this coupling, a reflective sintered plate is mounted at the connection between the plenum and the tubes. This plate was characterised experimentally by means of the multi-microphone method in [18]. From the scattering matrix coefficients shown in Fig. A2 of the latter study, one can infer that for frequencies below 1.5 kHz, the reflection coefficient of the plate is about 0.8 (it coincides with the S_{11} element of their scattering matrix). We therefore set $R_1 = 0.8$ in Eq. (6).

The downstream boundary condition of the modelled portion of the can is the Bloch-number dependent reflection coefficient downstream of the aperture, Eq. (9). This requires a model for the response of the shear layer at the gaps and the downstream boundary condition just after the gap in the scenario in which the gaps are closed. The former is given by Eq. (17), the latter by the impedance of an open-end tube of length $l_{\mathrm{end}} = 37$ mm, Eq. (18). All geometrical, flow and thermal parameters, listed in Figure 6, are chosen to be

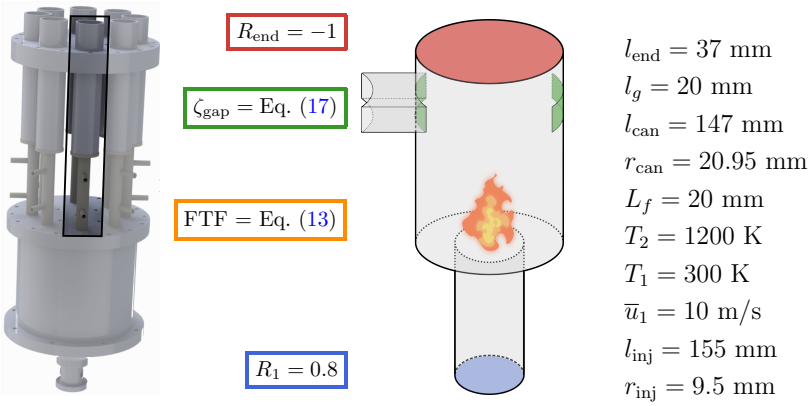

Figure 6: Left: rendering of the combustor considered in this study, with the Bloch-cell forming the highlighted can. Right: Sketch of the modelled can. The upstream boundary condition of the injectors (blue) is a reflective plate. A bluff-body stabilised flame is located at the intersection between the injector and the can. Close to the downstream end of the can, a small gap (green) allows for the aeroacoustic communication with the adjacent cans. The downstream end of the can (red) is open.

representative of the experiments described in [17]. The FTF is the only data that is not available. It is modelled by Eq. (13), using the geometrical/flow parameters of the experiment to determine the steady flame shape.

The spectrum of the semi-empirical can-annular combustor model described above (duct acoustics + FTF + Bloch boundary conditions + empirical can-to-can impedance) is shown in Figure 7. The eigenvalues are obtained by using the integral method described in [37] to solve the nonlinear eigenvalue problem (6) for each value of the Bloch wavenumber b. The circular contour is centered at 500 Hz and has radius 490 Hz. Only the eigenvalues with frequencies below 800 Hz are discussed: above this frequency, the range of validity of the empirical can-to-can impedance is exceeded, and spurious modes may be found. The spectrum shown in Figure 7 clearly exhibits the existence of clusters of eigenvalues. In particular, the clusters (a) and (b) can be related to frequencies which are close to the classic thermoacoustic frequencies of a single can. As will be further discussed in §4.1, cluster (a) is of acoustic origin whereas cluster (b) is of intrinsic origin [38, 39]. Each of these clusters (a and b) comprises a total of 8 eigenvalues (counting multiplicity).

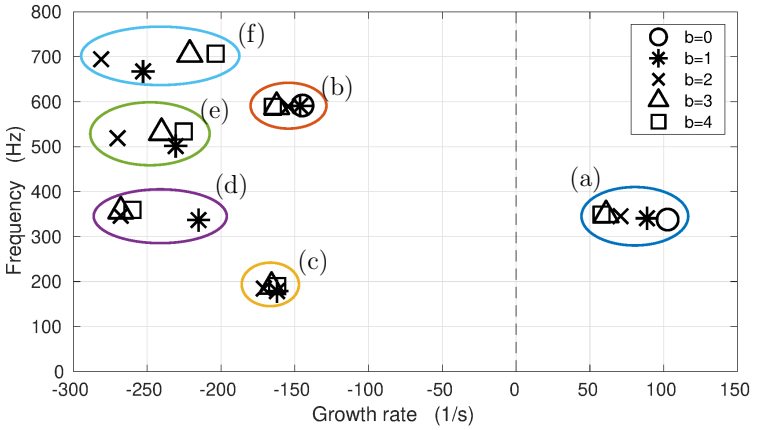

Figure 7: Clusters of eigenvalues in the can-annular configuration considered. The markers differentiate the modes by their azimuthal phase pattern. The modes in clusters (a) and (b) are associated to eigenvalues of thermoacoustic origin. The clusters (c)-(f), instead, originate from the aeroacoustic coupling with the response of the shear layer in the gaps between two cans. Notably, these clusters lack the $b = 0$ mode since no dynamics in the gaps can occur if the cans oscillate in phase.

In fact, due to the mirror symmetry of the Bloch cell, all eigenvalues found for Bloch numbers b in the range $0 < b < N/2$ are also eigenvalues of the system with Bloch number $-b$ [40]. For the $b = 0$ eigenvalues the effective reflection coefficient (9) reduces to the reflection coefficient of an open duct with mean flow. These eigenvalues are identical to those that one would find if the connection orifices would be closed, and the dynamics in each can would be independent of that in the others. The clusters of eigenvalues (c) to (f) in Figure 7, instead, are not originating from the can thermoacoustic response, but rather from the shear layer response in the openings, and its interaction with the can acoustics. In fact, the lowest frequency (cluster (c), approx. 180 Hz) can be linked to the reciprocal of the time that a perturbation takes to travel along the aperture at the convective velocity $\overline{u}_c$; higher frequencies are multiples of this fundamental frequency. Notably, these clusters lack the $b = 0$ mode. This is correct because for $b = 0$, the cans oscillate in phase, and there is, hence, no dynamics in the apertures connecting the cans. These clusters therefore comprise only 7 eigenvalues (counting multiplicity; 3 semi-simple degenerate pairs for $b = \{1, 2, 3\}$ and a simple one for

$b = 4$).

To gain further insight into the characteristics of the eigenvalues in the two types of clusters, Figure 8 shows the acoustic velocity of the $b = 1$ eigenvalues and pressure modeshapes of the $b = 2$ eigenvalues. The acoustic field in the section of the can downstream of the aperture is reconstructed using planar propagation of acoustic waves in a duct with a mean flow. All modeshapes satisfy the upstream boundary condition (close to be a velocity node) and the open-end boundary condition at the downstream end of the can (pressure node). The pressure modes in the cluster of acoustic origin, (a), have the typical quarter-wave shape; the acoustic velocity has a discontinuity at the combustor inlet due the area change. The modeshapes of the modes in the cluster of intrinsic origin, (b), has a strong response in the injectors, with a

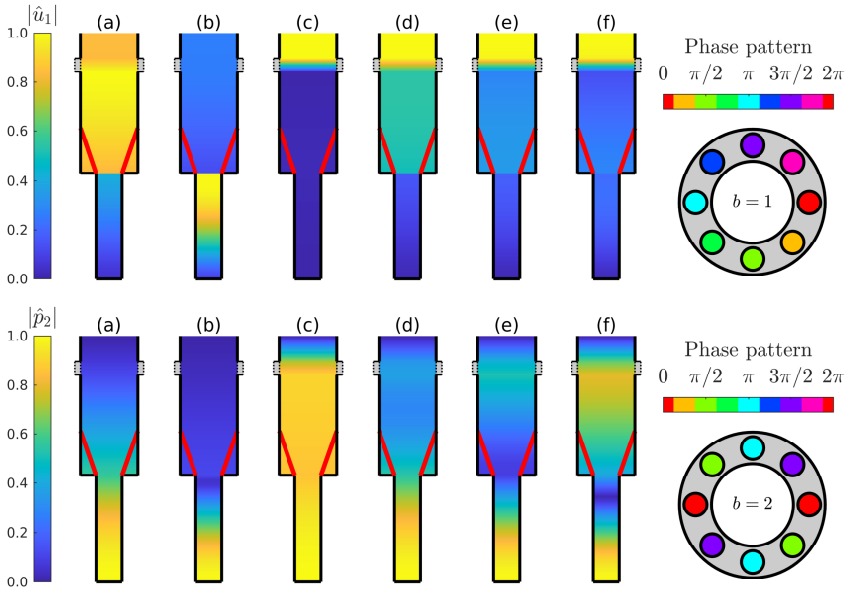

Figure 8: Top: Acoustic velocity modeshapes $\hat{u}_b$ for Bloch number $b = 1$. Bottom: Acoustic pressure modeshapes $\hat{p}_b$ for Bloch number $b = 2$. With reference to Figure 7, modeshapes (a) and (b) belong to clusters of thermoacoustic origin, whereas modeshapes (c) to (f) belong to clusters of aeroacoustic origin, in ascending frequency order. On the right end, a top view of the full annular combustor shows the phase oscillation patterns.

maximum at the flame, consistently with the typical modeshapes of intrinsic origin [41]. Lastly, the modeshapes of the eigenvalues associated with the aperture dynamics, (c) to (f), have less canonical shapes. In particular, all the acoustic velocity modeshapes have a low intensity in the whole section upstream of the aperture, followed by a strong gradient across the aperture and a maximum in the can's downstream ends.

4.1. Eigenvalue cluster sensitivity

The identified eigenvalue clusters can be related to three fundamentally different physical mechanisms: acoustic, intrinsic and shear layer dynamics. It is therefore reasonable to expect that their sensitivity to variations in the system parameters will be different, and depend on the influence that a specific parameter has on the dynamics of the underlying physical mechanisms. In this section, we will systematically vary (i) the flame heat release response magnitude and (ii) the shear layer convective velocity, to investigate how these two parameters influence the evolution of the eigenvalue clusters.

4.1.1. Sensitivity to FTF magnitude

To study the influence of the flame response strength on the eigenvalue clusters, we introduce a scaling parameter ξ in the definition of the FTF

$$\mathrm{FTF}_\xi(s) = \xi \mathrm{FTF}(s) \tag{19}$$

and we use this scaled Flame Transfer Function FTF_ξ in the definition of the heat release matrix response (5). When $\xi = 1$, the original FTF definition is unaffected, and the spectrum of the can-annular thermoacoustic system corresponds to that shown in Figure 7. When $\xi = 0$, instead, the flame response vanishes – i.e., $\mathcal{M}_{\mathrm{hr}} = \mathbf{0}$ in Eq. (5) – and only the aeroacoustic can-annular response in the absence of an active heat source is identified.

Figure 9 shows the evolution of the eigenvalues in all clusters when ξ is varied in the range [0,1]. The colors identify the clusters, in accordance to Fig. 7, and the markers indicate the Bloch-number associated with each eigenvalue and are located in the $\xi \to 0$ limit. The cluster of acoustic origin (a) moves into the stable half-plane ($\sigma < 0$) when the flame is switched off; indeed, in the absence of an active flame source, no thermoacoustic instability can occur. The cluster of intrinsic origin (b) is pushed towards growth rates tending to $-\infty$ as $\xi \to 0$. It was shown in [39, 42] that, in the vanishing flame limit, all the Bloch modes of this cluster tend towards the same

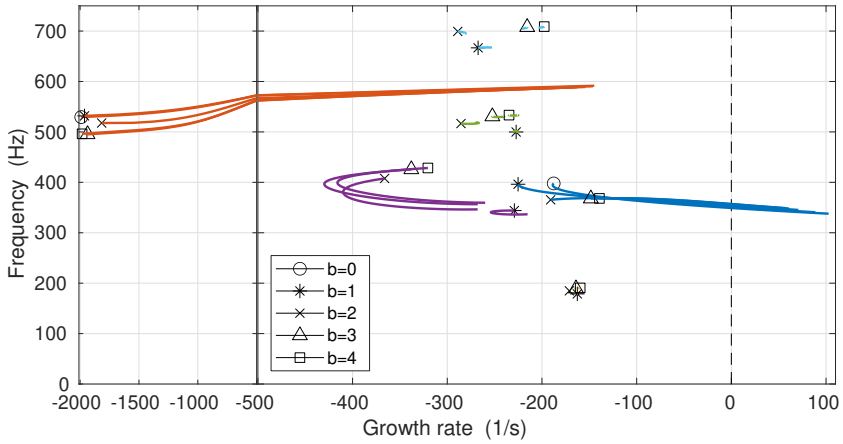

Figure 9: Eigenvalue trajectories when the flame gain is decreased. The markers indicate the eigenvalues (by their Bloch-number) in the passive flame case, i.e., in the limit $|\mathrm{FTF}_\xi| \to 0$. The color-scheme corresponds to that used in Figure 7 to emphasize the existence of clusters of eigenvalues.

frequency value, which can be predicted theoretically from the coefficients of the scattering matrix at the flame (see Appendix of [39]).

The remaining clusters, (c) to (f), are of shear layer dynamics origin. Their physical nature is not closely connected to the heat release dynamics, and it is reasonable to expect them to be almost independent of the flame response. This is true for clusters (c), (e) and (f), but not for cluster (d). The sensitivity of cluster (d) to the flame dynamics can be attributed to the fact that, when the flame dynamics is turned off ($\xi = 0$), its eigenvalues have both frequencies and growth rates close to those of cluster (a). This suggests that close-by in parameter space the eigenvalues coalesce, becoming degenerate. As discussed in [43], eigenvalues that are close to being degenerate exhibit a phenomenon known as mode veering. To avoid crossing, the eigenvalues steer away from each other. This can be observed in Fig. 9, which shows that the trajectories of the (a) and (d) clusters move in opposite directions for small values of ξ – close to the markers. To emphasize this further, Fig. 10 shows the dependence of the eigenvalues in cluster (d) on the parameter ξ. The sensitivity of the eigenvalues (slope of the curves) is non-uniform and high for small values of ξ, but tends to flatten as ξ becomes larger. When

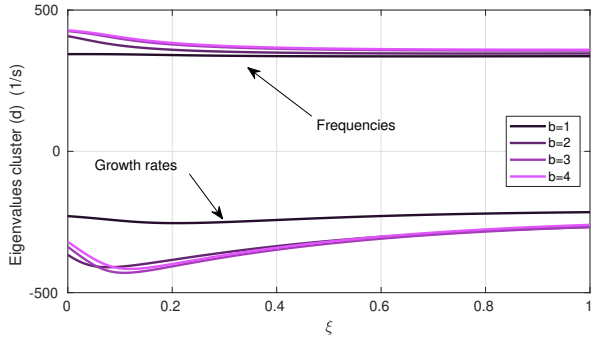

Figure 10: Evolution of the eigenvalues of cluster (d) when ξ is varied in Eq. (19).

the eigenvalues of clusters (d) are sufficiently far from those of cluster (a), the sensitivity of the eigenvalues of cluster (d) to the intensity of the flame becomes very small, similar to those of clusters (c), (e) and (f).

4.1.2. Sensitivity to aeroacoustic coupling

We shall now focus on the sensitivity that the the shear layer response has on the can-annular system's spectrum. In particular, we will investigate the effect of the convective speed in the shear layer, $U_c \equiv \kappa\overline{U}$, by varying the non-dimensional value κ in the range [0.2,0.62]. The mean flow velocities in the cold/hot regions of the can-annular system are unchanged. The trajectories of the eigenvalue clusters obtained while varying κ are shown in Figure 11. The thin (thick) markers identify the eigenvalues obtained for the minimum (maximum) values of κ considered.

First, we note that the $b = 0$ eigenvalues are not affected by κ. This is because only the can-to-can impedance (17) is affected by this parameter. For $b = 0$ the cans oscillate in phase, so that the pressure drop between neighbouring cans vanishes, and the can-to-can impedance does not play any role. The eigenvalues of the cluster of acoustic origin (a) are almost unaffected by this parameter, as emphasized in the bottom-right inset of Figure 11. Its eigenvalues with $b \neq 0$ exhibit loop patterns. This cyclic behavior is a manifestation of the phase induced by the convective time scale in the shear layer, which scales with l_g/U_c. It is analogous to the eigenvalue behaviour described in [44] when varying the time delay of the heat release response. Cluster (b), of intrinsic origin, has a non-trivial response to variations in

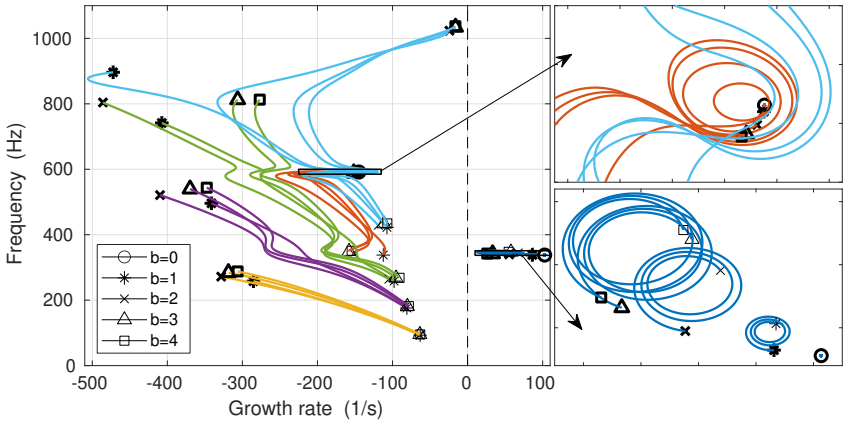

Figure 11: Eigenvalue trajectories when the convective speed in the aperture between cans is varied. Thick and thin markers indicate, respectively, the eigenvalues (by their Bloch-number) for the maximum (thick markers, $\kappa = 0.62$) and minimum (thin markers, $\kappa = 0.2$) convective speed considered. The color-scheme corresponds to that used in Figure 7 to emphasize the existence of clusters of eigenvalues. Right panels: magnification of the regions highlighted.

the convective velocity. For small values of κ, its frequency is particularly sensitive to variations in the shear layer convective speed. For larger values of κ, a cyclic behavior is again observed, emphasized in the top-right inset of Figure 11.

Clusters (c) to (f) are the most sensitive to a variations of κ, since they are directly related to the shear layer dynamics. Since the shear layer convection speed enters in the definition of the non-dimensional frequency Ω in the Rayleigh conductivity (15), increasing (decreasing) κ shifts the peak of the response of the can-to-can impedance (Figure 4) towards higher (lower) frequencies. The convection speed also has a significant effect on the growth rates of the eigenvalues of these clusters. For almost all the eigenvalues in these clusters, the larger the convection speed, the more stable are the eigenvalues. Additionally, for smaller values of κ the eigenvalue clusters are more dense, in the sense that a cluster is confined in a smaller portion of the complex frequency space.

5. Acoustically closed downstream end

A major difference between the experimental setup of [17] modelled in §4 and can-annular combustors in gas turbines is that in the former the cans are acoustically open at the downstream end, whereas in the latter the flow is nearly choked at the connection between the cans and the turbine inlet. Since the gaps that connect the cans are close to the downstream ends, they are located close to an acoustic pressure node when the cans are acoustically open. In this scenario, the coupling between the aerodynamics of the shear layer in the gaps and the thermoacoustics of the can is generally weaker, since it depends on the pressure difference between the cans [24, 29], which remains small close to a pressure node. This was already visible in Figure 9, in which almost all eigenvalues of aeroacoustic origin had very negative growth rates, corresponding to the (stable) dynamics of the decoupled aeroacoustic modes. On the contrary, for an acoustically closed boundary condition, the gaps are located in the vicinity of a pressure antinode. In this scenario, the pressure differences between neighbouring cans can be significantly higher, enhancing the can-to-can communication effects. In this last section, we will discuss how the spectrum and mode shapes of the can-annular system vary when the downstream boundary condition is acoustically closed.

An acoustically closed end of the cans, downstream of the gap, can be modelled by setting the downstream impedance to $Z_{\mathrm{ds}} = \infty$ in place of Eq. (18). In this limit, the effective downstream reflection coefficient (9) simplifies to

$$R_b = 1 - 2\frac{4A_r/\tilde{\zeta}\sin^2\left(\frac{\pi b}{N}\right)}{(1-\mathrm{M}_x^2) + 4A_r/\tilde{\zeta}\sin^2\left(\frac{\pi b}{N}\right)}. \tag{20}$$

Except for the downstream boundary condition, all the other parameters are kept to those presented in §4.

Figure 12 shows the spectrum of the can-annular system with a closed boundary condition. The existence of eigenvalue clusters has been emphasized, and the eigenvalues are distinguished by their Bloch-number, following the same color and marker conventions of Figure 7. Clusters (a) and (b) are clusters of classic thermoacoustic origin. We note how the frequencies and growth rates of cluster (a), which is of acoustic origin, have significantly changed compared to those of the open-end configuration, since acoustic modes are strongly affected by the boundary conditions. On the other hand, the frequencies of cluster (b) are very similar to those found for an open

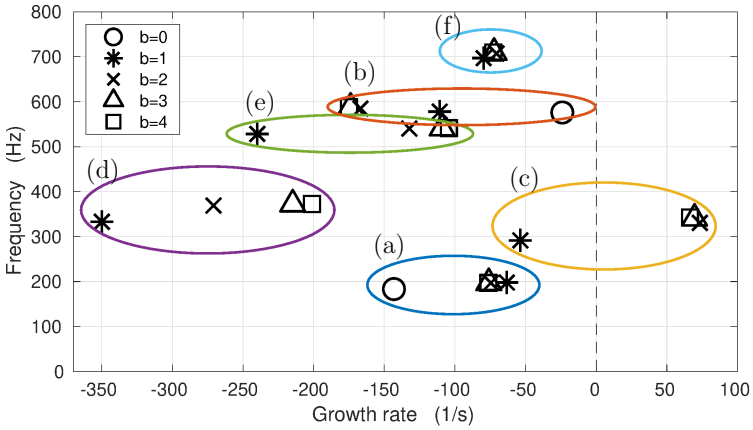

Figure 12: Clusters of eigenvalues in the can-annular configuration considered with a closed end. The markers differentiate the modes by their azimuthal phase pattern. The modes in clusters (a) and (b) are associated with eigenvalues of thermoacoustic origin. The clusters (c)–(f), that lack the $b = 0$ mode, originate from the aeroacoustic coupling with the response of the shear layer in the gaps between two cans. Notably, it is a cluster of aeroacoustic origin that becomes unstable.

end. This is consistent with the fact that this cluster was found to be associated with an intrinsic mode, and it is mostly ruled by the flame dynamics – unchanged with respect to the results shown in Figure 7 – and not by the acoustics. Clusters (c) to (f) of Figure 12 are associated with modes of aeroacoustic origin, as can be seen by the fact that they lack the $b = 0$ eigenvalues. The stronger coupling between the aeroacoustics of the gaps and the thermoacoustics of the cans in comparison to the open-end case can be seen by the fact that the growth rates of these eigenvalues are significantly different, and tend to have larger values. In particular, some of the eigenvalues of cluster (c) now have positive growth rates, implying that an instability in this configuration will mostly be driven by the aeroacoustics in the gaps.

The mode shapes associated with some of the eigenvalues of Figure 12 are shown in Figure 13. In comparison to Figure 8, the downstream open tube is missing since it has been replaced by a sound-hard end. Thus, the mode shapes exhibit qualitative differences as the acoustic pressure needs to now exhibit a pressure antinode at the downstream end rather than a node, and vice versa for the acoustic velocity. An exception to this observation

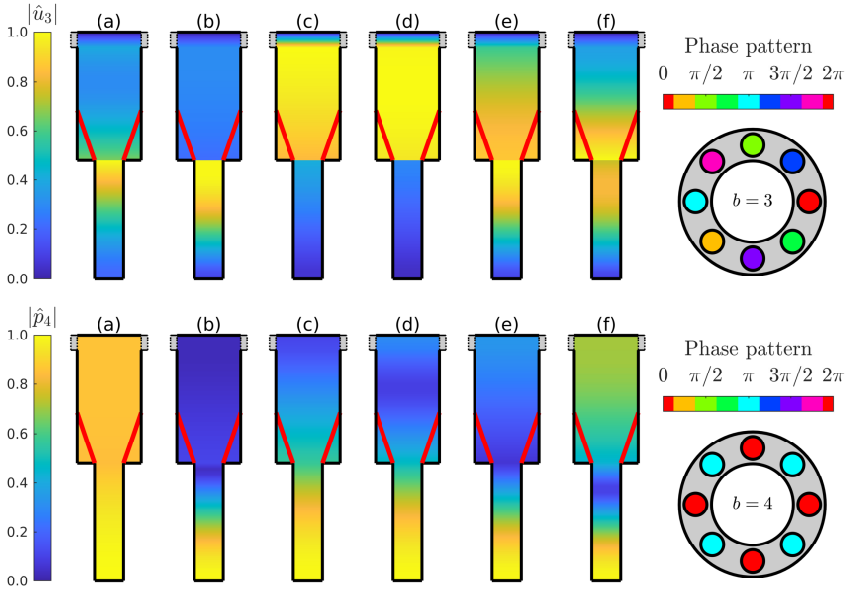

Figure 13: Modeshapes for the $Z_{\mathrm{ds}} = \infty$. Top: Acoustic velocity modeshapes $\hat{u}_b$ for Bloch number $b = 3$. Bottom: Acoustic pressure modeshapes $\hat{p}_b$ for Bloch number $b = 4$. With reference to Figure 7, modeshapes (a) and (b) belong to clusters of thermoacoustic origin, whereas modeshapes (c) to (f) belong to clusters of aeroacoustic origin, in ascending frequency order. On the right end, a top view of the full annular combustor shows the phase oscillation patterns.

occurs for cluster (b), the cluster associated with an intrinsic mode, which is therefore relatively insensitive to variations in the boundary conditions [39]. For this reason, both the pressure and acoustic mode shapes of cluster (b) are similar for open (Figure 8) or closed (Figure 13) boundary conditions. It is interesting to note how in clusters (c) to (f) the magnitude of the acoustic pressure field remains not very high close to the downstream end, despite having a local maximum close to the gaps, and has instead large pressure amplitudes upstream of the flame. By looking at the mode shapes only, it would therefore be difficult to determine the origin of these modes.

6. Conclusions

In this study, we have presented a general reduced-order model for investigating the thermoacoustic properties of can-annular combustors. Particular focus was placed on appropriately modelling the can-to-can communication, which was accomplished by embedding in the model semi-empirical impedance expressions fitted against experimental data. The modelling approach exploits Bloch-wave theory and reduces the analysis to a single can, equipped with an effective boundary condition that contains the aeroacoustic response of the apertures and the acoustic properties of the can downstream of the aperture.

The model was used to study the response of an existing atmospheric can-annular test-rig. Since the flame response data is not available, the flame dynamics has been approximated by that of a V-flame, modelled with the kinematic G-equation. The spectrum of the setup has been determined, highlighting the presence of clusters of eigenvalues. The origin of the clusters has been discussed, emphasizing how some clusters originate from the aeroacoustic response of the aperture, and not the acoustic response of the can. These clusters are peculiar in that they lack the presence of $b = 0$ (in-phase oscillation) modes. They, therefore, cannot be predicted if the can-to-can communication is ignored.

The properties of eigenvalues and eigenvectors having different physical origins – related to the acoustic, intrinsic and shear layer dynamics, respectively – have been discussed. In particular, a parametric analysis has been performed to demonstrate that the sensitivity of the eigenvalues with respect to specific parameters is strongly dependent on their physical origin. Lastly, the effect of the downstream boundary conditions has been analysed and discussed, emphasizing the differences between the can-to-can coupling in atmospheric experiments – which have acoustically open ends – and real gas turbine combustors – which have acoustically closed ends. Our discussion highlights how knowledge on the physical mechanisms that are responsible for the creation of a particular eigenvalue cluster is important for an assessment of the thermoacoustic spectrum, the eigenvalue sensitivities and their potential control. Future research on this topic will include the modelling of the nonlinear response of the apertures' dynamics, which, as recently shown by [20], may be non-negligible.

Acknowledgments

This work is the result of a D-A-CH international collaboration funded by the German Research Foundation (DFG project nr. 422037803) and the Swiss National Science Foundation (SNF project nr. 184617).

References

[1] J. W. S. Rayleigh, The explanation of certain acoustical phenomena, Nature 18 (1878) 319–321.

[2] J. Keller, Thermoacoustic oscillations in combustion chambers of gas turbines, AIAA J. 33 (1995) 2280–2287.

[3] L. Crocco, Aspects of combustion stability in liquid propellant rocket motors part i: fundamentals. low frequency instability with monopropellants, J. Am. Rocket Soc. 21 (1951) 163–178.

[4] J. Keller, W. Egli, J. Hellat, Thermally induced low-frequency oscillations, Z. Angew. Math. Phys. 36 (1985) 250–274.

[5] T. Schuller, T. Poinsot, S. Candel, Dynamics and control of premixed combustion systems based on flame transfer and describing functions, J. Fluid Mech. 894 (2020).

[6] N. Noiray, B. Schuermans, On the dynamic nature of azimuthal thermoacoustic modes in annular gas turbine combustion chambers, Proc. R. Soc. A 469 (2013).

[7] G. Ghirardo, M. Juniper, Azimuthal instabilities in annular combustors: Standing and spinning modes, Proc. R. Soc. A 469 (2013).

[8] S. Bethke, W. Krebs, P. Flohr, B. Prade, Thermoacoustic properties of can annular combustors, in: 8th AIAA/CEAS Aeroacoustics Conference and Exhibit, 2002, pp. 1–11.

[9] W. Krebs, S. Bethke, J. Lepers, P. Flohr, B. Prade, C. Johnson, S. Sattinger, Thermoacoustic Design Tools And Passive Control: Siemens Power Generation Approaches, AIAA, 2005, pp. 89–112.

[10] P. Kaufmann, W. Krebs, R. Valdes, U. Wever, 3D thermoacoustic properties of single can and multi can combustor configurations, in: Proceedings of the ASME Turbo Expo, volume 3A, 2008, pp. 527–538.

[11] F. Farisco, L. Panek, J. B. W. Kok, Thermo-acoustic cross-talk between cans in a can-annular combustor, Int. J. Spray Combust. 9 (2017) 452–469.

[12] K. Venkatesan, A. Cross, C. Yoon, F. Han, S. Bethke, Heavy duty gas turbine combustion dynamics study using a two-can combustion system, in: Proceedings of the ASME Turbo Expo, volume 4A, 2019, pp. 1–9.

[13] K. Moon, H. Jegal, C. Yoon, K. T. Kim, Cross-talk-interaction-induced combustion instabilities in a can-annular lean-premixed combustor configuration, Combust. Flame 220 (2020) 178–188.

[14] K. Moon, C. Yoon, K. T. Kim, Influence of rotational asymmetry on thermoacoustic instabilities in a can-annular lean-premixed combustor, Combust. Flame 223 (2021) 295–306.

[15] G. Ghirardo, C. D. Giovine, J. P. Moeck, M. R. Bothien, Thermoacoustics of Can-Annular Combustors, Journal of Engineering for Gas Turbines and Power 141 (2019) 011007 (10 pages). doi:10.1115/1.4040743.

[16] G. Ghirardo, J. P. Moeck, M. R. Bothien, Effect of noise and nonlinearities on thermoacoustics of can-annular combustors, J. Eng. Gas Turb. Power 142 (2020).

[17] P. E. Buschmann, N. A. Worth, J. P. Moeck, Experimental study of thermoacoustic modes in a can-annular model combustor, in: SoTiC 2021 - Symposium on Thermoacoustics in Combustion: Industry meets Academia, 2021.

[18] T. Indlekofer, B. Ahn, Y. H. Kwah, S. Wiseman, M. Mazur, J. R. Dawson, N. A. Worth, The effect of hydrogen addition on the amplitude and harmonic response of azimuthal instabilities in a pressurized annular combustor, Combustion and Flame 228 (2021) 375–387.

[19] C. Sondhauss, Ueber die beim ausströmen der luft entstehenden töne, Ann. Phys. (Leipzig) 167 (1854) 214–240.

[20] C. Bourquard, A. Faure-Beaulieu, N. Noiray, Whistling of deep cavities subject to turbulent grazing flow: intermittently unstable aeroacoustic feedback, Journal of Fluid Mechanics 909 (2021) A19.

[21] E. Boujo, M. Bauerheim, N. Noiray, Saturation of a turbulent mixing layer over a cavity: response to harmonic forcing around mean flows, J. Fluid Mech. 853 (2018) 386–418.

[22] T. Pedergnana, C. Bourquard, A. Faure-Beaulieu, N. Noiray, Modeling the nonlinear aeroacoustic response of a harmonically forced side branch aperture under turbulent grazing flow, Phys. Rev. Fluids 6 (2021) 023903. doi:10.1103/PhysRevFluids.6.023903.

[23] L. Panek, F. Farisco, M. Huth, Thermo-acoustic characterization of can–can interaction of a can-annular combustion system based on unsteady cfd les simulation, in: Global power and propulsion forum, 2017, pp. GPPF–81 (5 pages).

[24] J. von Saldern, A. Orchini, J. Moeck, Analysis of Thermoacoustic Modes in Can-Annular Combustors Using Effective Bloch-Type Boundary Conditions, Journal of Engineering for Gas Turbines and Power GTP-20-1439 (2020). doi:10.1115/1.4049162.

[25] S. W. Rienstra, A. Hirschberg, An Introduction to Acoustics, December, Eindhoven University of Technology, 2004.

[26] A. P. Dowling, Nonlinear self-excited oscillations of a ducted flame, Journal of Fluid Mechanics 346 (1997) 271–290.

[27] A. Orchini, S. J. Illingworth, M. P. Juniper, Frequency domain and time domain analysis of thermoacoustic oscillations with wave-based acoustics, Journal of Fluid Mechanics 775 (2015) 387–414. doi:10.1017/jfm.2015.139.

[28] J. G. R. von Saldern, A. Orchini, J. P. Moeck, A non-compact effective impedance model for can-to-can acoustic communication: analysis and optimization of damping mechanisms, in: ASME Turbo Expo, 2021, p. GT59321 (13 pages).

[29] A. Orchini, An effective impedance for modelling the aeroacoustic coupling of ducts connected via apertures, Journal of Sound and Vibrations (under consideration for publication) (2021).

[30] a. L. Birbaud, D. Durox, S. Candel, Upstream flow dynamics of a laminar premixed conical flame submitted to acoustic modulations, Combustion and Flame 146 (2006) 541–552. doi:10.1016/j.combustflame.2006.05.001.

[31] N. Karimi, M. J. Brear, S.-H. Jin, J. P. Monty, Linear and non-linear forced response of a conical, ducted, laminar premixed flame, Combustion and Flame 156 (2009) 2201–2212. doi:10.1016/j.combustflame.2009.06.027.

[32] Preetham, S. Hemchandra, T. Lieuwen, Dynamics of Laminar Premixed Flames Forced by Harmonic Velocity Disturbances, Journal of Propulsion and Power 24 (2008) 1390–1402. doi:10.2514/1.35432.

[33] A. Orchini, M. P. Juniper, Linear stability and adjoint sensitivity analysis of thermoacoustic networks with premixed flames, Combustion and Flame 165 (2016) 97–108. doi:10.1016/j.combustflame.2015.10.011.

[34] T. Schuller, D. Durox, S. Candel, A unified model for the prediction of laminar flame transfer functions: comparisons between conical and V-flames dynamics, Combustion and Flame 134 (2003) 21–34. doi:10.1016/S0010-2180(03)00042-7.

[35] R. S. Blumenthal, P. Subramanian, R. Sujith, W. Polifke, Novel perspectives on the dynamics of premixed flames, Combustion and Flame 160 (2013) 1215–1224. doi:10.1016/j.combustflame.2013.02.005.

[36] M. Howe, Influence of wall thickness on rayleigh conductivity and flow-induced aperture tones, Journal of Fluids and Structures 11 (1997) 351–366. doi:https://doi.org/10.1006/jfls.1997.0087.

[37] P. E. Buschmann, G. A. Mensah, F. Nicoud, J. Moeck, Solution of Thermoacoustic Eigenvalue Problems with a Non-iterative Method, Journal of Engineering for Gas Turbines and Power (2019) GTP–19–1413. doi:10.1115/1.4045076.

[38] T. Emmert, S. Bomberg, W. Polifke, Intrinsic thermoacoustic instability of premixed flames, Combustion and Flame 162 (2015) 75–85. doi:10.1016/j.combustflame.2014.06.008.

[39] A. Orchini, C. F. Silva, G. A. Mensah, J. P. Moeck, Thermoacoustic modes of intrinsic and acoustic origin and their interplay with exceptional points, Combustion and Flame 211 (2020) 83–95.

[40] G. A. Mensah, L. Magri, A. Orchini, J. P. Moeck, Effects of Asymmetry on Thermoacoustic Modes in Annular Combustors: A Higher- Order Perturbation Study, Journal of Engineering for Gas Turbines and Power 141 (2019) 041030 (8 pages). doi:10.1115/1.4041007.

[41] E. Courtine, L. Selle, T. Poinsot, DNS of intrinsic thermoacoustic modes in laminar premixed flames, Combustion and Flame 162 (2015) 4331–4341.

[42] P. E. Buschmann, G. A. Mensah, J. P. Moeck, Intrinsic thermoacoustic modes in an annular combustion chamber, Combustion and Flame 214 (2020) 251–262.

[43] A. Orchini, L. Magri, C. Silva, G. Mensah, J. Moeck, Degenerate perturbation theory in thermoacoustics: High-order sensitivities and exceptional points, Journal of Fluid Mechanics 903 (2020) A37 (30 pages).

[44] C. F. Silva, W. Polifke, Non-dimensional groups for similarity analysis of thermoacoustic instabilities, Proceedings of the Combustion Institute 37 (2019) 5289–5297.

A subspace-accelerated method for solving nonlinear thermoacoustic eigenvalue problems

Journal of Sound and Vibration 520 (2022) 116553

Contents lists available at ScienceDirect

Journal of Sound and Vibration

journal homepage: www.elsevier.com/locate/jsvi

Rapid communications

A subspace-accelerated method for solving nonlinear thermoacoustic eigenvalue problems

Georg A. Mensah [a], Alessandro Orchini [b], Philip E. Buschmann [c,*], Luka Grubišić [d]

[a] Dive Solutions, Bismarckstraße 10-12, 10625 Berlin, Germany
[b] TU Berlin, Institute of Fluid Dynamics and Technical Acoustics, Müller-Breslau Straße 8, 10623 Berlin, Germany
[c] Norwegian University of Science and Technology, Department of Energy and Process Engineering, Kolbjørn Hejesvei 2, 7491 Trondheim, Norway
[d] University of Zagreb, Faculty of Science, Department of Mathematics, Bijenička cesta 30, 10000 Zagreb, Croatia

ARTICLE INFO

Keywords:
Thermoacoustics
Subspace method
Reduced order model
Nonlinear eigenvalue problem

ABSTRACT

We propose a method to accelerate the solution of 3D FEM-discretized nonlinear eigenvalue problems by drastically reducing the problem dimension. Our method yields a reduced order model (ROM) via a projection onto a suitable subspace, with eigenpairs identical to the full problem in a region of the complex plane. The subspace is automatically constructed by solving the full problem at a few random points inside the region of interest. The method requires minimal user input and, although exemplified for with a thermoacoustic application, readily generalizes to applications dealing with other vibrational problems.

1. Introduction

Self-excited oscillations are detrimental in many technical systems. Stability of a design is often determined by solving large-scale, potentially nonlinear eigenvalue problems that arise from the discretization of the PDEs describing the underlying physics. For instance, in combustion chambers of gas turbines and aircraft engines thermoacoustic stability is sought. A combination of adjoint-based perturbation theory [1] and optimization methods has made significant advances in automatizing the process of designing a thermoacoustically stable combustor [2]. However, these strategies incur a substantial numerical cost by repeatedly solving large-scale eigenvalue problems as they iterate through the parameter space. A natural reduction technique for thermoacoustics requires a linearization of the nonlinear eigenvalue dependency [3]. However, the employed iterative reduction techniques can be unstable. This letter proposes a projection method that significantly reduces the dimension of the thermoacoustic eigenvalue problem in a region of the complex plane, while retaining the nonlinear dependency on the eigenvalue.

Thermoacoustic instabilities may arise in combustion chambers due to a constructive feedback between acoustics and heat release rate oscillations. The feedback mechanism can be modelled with equations derived from the reactive Navier–Stokes equations, or fitted on experimental data. In gas turbine engineering, one popular choice of the thermoacoustic eigenvalue problem reads [4]

$$\nabla \cdot c^2 \nabla \hat{p} + \omega^2 \hat{p} = n \exp(-\mathrm{i}\omega\tau) \nabla \hat{p}|_{\mathbf{x}_{\mathrm{ref}}}, \tag{1}$$

where c is the speed of sound, and n and τ an interaction index and time delay, respectively, quantifying the coupling between the acoustics and the heat release rate fluctuations. The flame response model $n\exp(-\mathrm{i}\omega\tau)$ is chosen for simplicity, but the proposed projection method is valid for any flame response model. By closing Eq. (1) with suitable boundary conditions, the aim is that of

* Corresponding author.
E-mail address: philip.e.buschmann@ntnu.no (P.E. Buschmann).

https://doi.org/10.1016/j.jsv.2021.116553
Received 4 August 2021; Received in revised form 14 October 2021; Accepted 15 October 2021
Available online 30 October 2021

efficiently identifying eigenpairs $(\omega, \hat{p})$ in a region of the complex plane. In engineering practise, only eigenvalues with frequencies below a cut-off threshold are sought, since for these values the flame is acoustically compact and correctly modelled by Eq. (1).

Discretization of Eq. (1) by the finite element method yields [4]

$$\underbrace{\left[\mathbf{K} + \omega \sum_i f_i(\omega)\,\mathbf{C}_i + \omega^2 \mathbf{M} + n\,\exp(-\mathrm{i}\omega\tau)\,\mathbf{F}\right]}_{\equiv \mathbf{L}(\omega)} \boldsymbol{p} = \mathbf{0}. \tag{2}$$

The matrices $\mathbf{C}_i$ are associated with the boundaries of the domain, labelled by index i, where ω-dependent boundary conditions f_i (related to acoustic impedances) are prescribed. All matrices in Eq. (2) have size N (ca. 10^3–10^6) corresponding to the degrees of freedom of the chosen discretization.

Eq. (2) is an eigenvalue problem nonlinear in the eigenvalue ω. We recall that linear eigenvalue problems can be written as

$$(\mathbf{A} - \omega\mathbf{B})\boldsymbol{p} = \mathbf{0}, \quad \mathbf{A}, \mathbf{B} \in \mathbb{C}^{N\times N}, \tag{3}$$

where $\mathbf{A}$ and $\mathbf{B}$ are constant matrices and $(\omega, \boldsymbol{p})$ are the desired eigenpairs. Fast solution algorithms for Eq. (3) are well-established [5]. In contrast, nonlinear eigenvalue problems (NLEVPs) cannot be expressed in the special form Eq. (3), but only more generally as [6]

$$\mathbf{L}(\omega)\boldsymbol{p} = \mathbf{0}, \quad \mathbf{L} \in \mathbb{C}^{N\times N}. \tag{4}$$

The nonlinearities in ω are typically associated with the presence of frequency-dependent boundary conditions, time delays, and higher-order time derivatives. All these sources of nonlinearity are present in the thermoacoustic equation (2), respectively via the boundary matrices $\omega f_i(\omega)\,\mathbf{C}_i$, the delayed heat release response $\exp(-\mathrm{i}\omega\tau)\,\mathbf{F}$, and the mass term $\omega^2\mathbf{M}$. One can always approximate a nonlinear eigenvalue problem in the special form Eq. (3) by linearizing the nonlinear dependency via a state–space formulation [7]. However, such a linearization increases the dimension of the eigenvalue problem and can introduce additional eigenvalues that are not solutions of the NLEVP — see Sec. 6 in [6]. By retaining the nonlinear dependence in ω these drawbacks are avoided.

Because $\mathbf{L}$ can take many forms depending on the underlying physics, many different solution strategies for NLEVPs tailored to specific problems have been developed [5,6]. These methods either require the iterative solution of $lN \times lN$ linearized eigenvalue problems [4] – where l is a positive integer that depends on the chosen linearization – or the repeated solution of large linear systems of the form [8,9]

$$\mathbf{L}(z)\,\mathbf{X} = \mathbf{Y}, \quad \mathbf{X}, \mathbf{Y} \in \mathbb{C}^{N\times R}, \quad R \ll N, \tag{5}$$

where z takes values in $\mathbb{C}$. Both strategies are numerically costly when N is very large. An efficiency development was suggested by Jorkowski et al. [10], who improved on a contour-integration solution method devised by Beyn [8] by using ideas from model order reduction. Their method uses a projection matrix to generate a low-rank subspace approximation of the linear Eqs. (5) – which appear in Beyn's method – along a contour in the complex plane. The subspace is automatically enlarged when a residual criterion is violated. The method achieves significant speed-up, but is deeply intertwined with the structure of Beyn's method.

In this letter, a reduced order method (ROM) is proposed to separate the subspace generation from the solution strategy by projecting the large operator $\mathbf{L}$ in Eq. (4) onto a precomputed subspace. The subspace can be adaptively enlarged should an *a posteriori* analysis based on residuals indicate that its quality is insufficient. The subspace is constructed by randomly exploring a region of the complex space within a contour Γ. After the projection, a reduced nonlinear eigenvalue problem of much smaller size M (ca. $10^1 - 10^2$) is obtained

$$\widetilde{\mathbf{L}}(\omega)\widetilde{\boldsymbol{p}} = \mathbf{0}, \quad \widetilde{\mathbf{L}} \in \mathbb{C}^{M\times M}, \quad M \ll N, \tag{6}$$

which, in a region of the complex plane, well-approximates the spectrum of the original problem (4). The reduced NLEVP can then be tackled by a variety of solution methods, not only contour-integration based ones.

2. Reduced order model method

We denote by $\{\boldsymbol{q}_1, \ldots, \boldsymbol{q}_M\}$ the orthonormal basis of the subspace we project the problem onto. Then, the orthogonal matrix $\mathbf{Q} \equiv \left[\boldsymbol{q}_1 \ldots \boldsymbol{q}_M\right] \in \mathbb{C}^{N\times M}$ is used to construct the ROM operator $\widetilde{\mathbf{L}}(z)$ via

$$\widetilde{\mathbf{L}}(z) \equiv \mathbf{Q}^{\mathrm{H}}\mathbf{L}(z)\mathbf{Q}. \tag{7}$$

If range($\mathbf{Q}$) well-approximates (some of) the eigenvectors of $\mathbf{L}(z)$, then $\widetilde{\mathbf{L}}(z)$ will feature the corresponding eigenvalues ω as its own eigenvalues, as per Eq. (6), and the eigenvectors are obtained from $\boldsymbol{p} = \mathbf{Q}\widetilde{\boldsymbol{p}}$. The challenge is to efficiently construct $\mathbf{Q}$ without explicitly calculating the eigenmodes. The method we propose improves on that first proposed in [10], by modifying the spectral parameter sampling strategy in the ROM construction. Namely, a set of sampling points z_i inside and on a contour Γ in the complex plane is chosen, where Γ is a region of the complex plane of interest. It reads:

1. Initialize the matrix $\mathbf{Y}$ that appears on the r.h.s. of Eq. (5) with a small set of random, normalized vectors. Initialize the projection matrix $\mathbf{Q}$ as $\mathbf{Q} = \mathbf{Y}$;

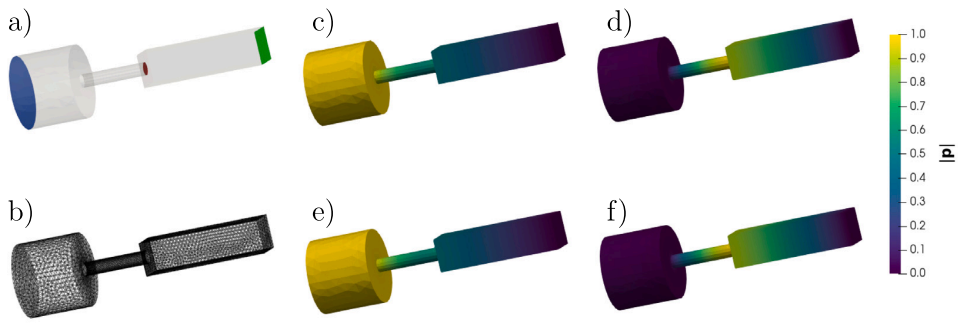

Fig. 1. (a) Geometry of the BRS combustor highlighting the flame domain (red), and the inlet (blue) and outlet (green) surface; b) FE mesh with 12200 points; (b) (c–d) lowest and highest frequency pressure eigenmodes identified by the ROM; (e–f) lowest and highest frequency pressure eigenmodes identified by the full model. (For interpretation of the references to colour in this figure legend, the reader is referred to the web version of this article.)

2. For a set of sampling points z_i solve the linear system of equations

$$\widetilde{\mathbf{L}}(z_i)\widetilde{\mathbf{X}}_i = \mathbf{Q}^H\mathbf{Y}, \tag{8}$$

in the current subspace of the ROM;
3. Map the ROM solution back in the original space via,[1] $\hat{\mathbf{X}}_i = \mathbf{Q}\widetilde{\mathbf{X}}_i$;
4. If the residual $\|\mathbf{L}(z_i)\hat{\mathbf{X}}_i - \mathbf{Y}\|_2$ is below a given tolerance, then the ROM well-approximates the behaviour of the original operator at z_i; otherwise the dimension of the subspace model has to be increased. This is accomplished by (i) calculating the exact solution $\mathbf{X}_i$ of the (large) original problem

$$\mathbf{L}(z_i)\mathbf{X}_i = \mathbf{Y}, \tag{9}$$

(ii) appending it to the compression matrix $\mathbf{Q}$, and (iii) orthonormalizing the columns of $\mathbf{Q}$.

The computational savings of the outlined algorithm arise from the fact that most calculations are performed in the ROM subspace, and only a handful of operations – needed to enlarge the subspace on-the-fly – are done on the full-sized problem. We emphasize that the update to the orthogonal basis $\mathbf{Q}$ can be efficiently implemented in an incremental fashion by exploiting Householder transformations or Givens rotations. We also note that the reduced order problem (7) may feature eigenpairs that do not correspond to eigenpairs of the original problem. Therefore, testing the residual of the approximate solution in the original space is required as an additional step [6].

In [10], the ROM is constructed to well-approximate $\mathbf{L}(z)\mathbf{X} = \mathbf{Y}$ on a contour Γ only, i.e., the sampling points z_i are all chosen to lie on Γ. This allows one to use Beyn's contour-integration method on the ROM to identify the eigenvalues of $\widetilde{\mathbf{L}}$ – which well-approximate those of $\mathbf{L}$ – inside the contour. The method proposed here, instead, constructs the compression matrix by sampling the complex plane not only *on* a contour, but also *inside* a contour Γ. As outlined in [10], the resolution of the contour ensures that the eigenvalues of the ROM operator approximate those of the original operator to a given threshold in a region of the complex plane. Resolving also the space inside the contour may result in a somewhat larger ROM, but it allows us to leverage any solution technique (not only contour-integrals) on the NLEVP resulting from the ROM [6].

The presented algorithm has been implemented in the open-source package *WavesAndEigenvalues.jl*.[2] The package provides all essential tools for discretizing a PDE-based NLEVP with FE, identifying a ROM of the full operator, and solving the NLEVP with contour-integral or iterative methods.

3. Model reduction of a Finite Element thermoacoustic NLEVP

As an application example, we consider the NLEVP resulting from the finite element discretization of the thermoacoustic Helmholtz equation (2). The geometry we model is that of the so-called BRS combustor, which has been thoroughly studied both experimentally and numerically in [11,12], to which we refer for all the geometrical and thermodynamic details. The boundary conditions are set to be sound hard ($\nabla\hat{p}\cdot\vec{n} = 0$) at all boundaries except the outlet, where an acoustically open-end ($\hat{p} = 0$) is imposed. The speed of sound jumps from 343 m/s to 801 m/s across the flame base, and the flame parameters are chosen to be $n = 1$ and $\tau = 7.45$ ms. By using a fine mesh, the resulting finite element discretized operator $\mathbf{L}$ has $N = 12200$ degrees of freedom. The geometry defining the problem and the mesh on which it has been discretized are shown in Fig. 1(a–b) .

[1] This is a cheap operation because both $\mathbf{Q}$ and $\widetilde{\mathbf{X}}_i$ are known, and, contrary to Eq. (5) no inversions nor least square solution methods are needed.
[2] https://github.com/JulHoltzDevelopers/WavesAndEigenvalues.jl.

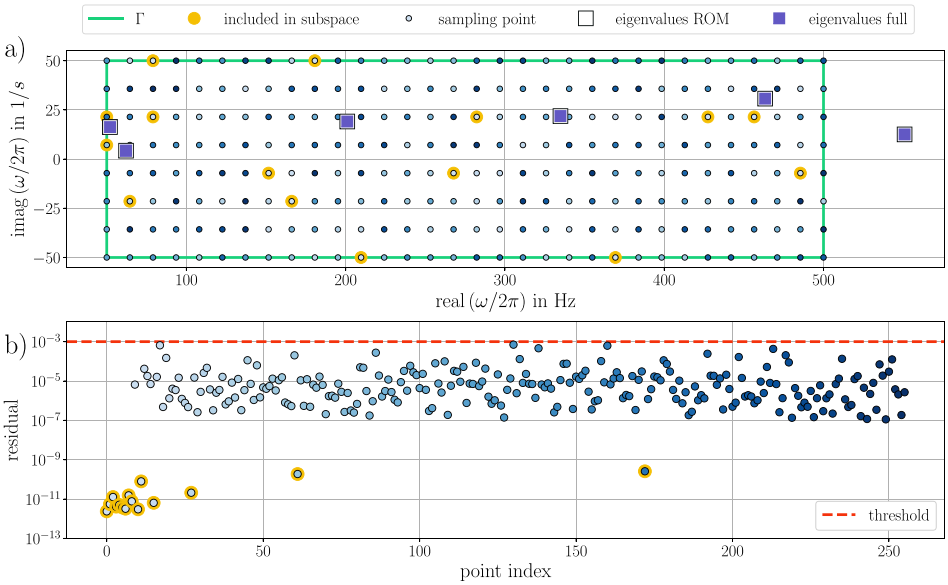

Fig. 2. (a) : Region of the complex plane considered and sampled at the circles. Eigenvalues computed with the ROM and full model show perfect agreement. (b): Residuals of the calculations in the ROM (corresponding points feature an identical unique shade of blue). The points that are highlighted in yellow did not pass the threshold test in the ROM subspace. (For interpretation of the references to colour in this figure legend, the reader is referred to the web version of this article.)

Eigenmodes are sought in the region Γ of the complex plane having frequencies between 50 and 500 Hz and growth rates between ± 50 s^{-1}. 256 sample points are uniformly distributed in Γ and used to generate the subspace — see Fig. 2(a). A single normalized vector $\boldsymbol{y}_1$ was chosen at random, to both define the matrix $\mathbf{Y}$ on the r.h.s. of Eq. (8) and initialize the projection matrix $\mathbf{Q}$. The threshold for the residual was set to 10^{-3} — dashed line in Fig. 2(b).

The sample points were tested in a random order to construct the subspace. The procedure led to the inclusion of 15 vectors in the subspace, which are drawn in yellow in Fig. 2. For these points an exact solution $\mathbf{X}_i$ in the full space – Eq. (9) – has been evaluated, and the results included in the subspace. The depicted residuals are computed after expanding the subspace for these points. Together with the randomly initialized vector, the ROM has $M = 16$ degrees of freedom. Note that the majority of the vectors used to construct the subspace belong to the first points tested by the algorithm — the first 9 points are all included, while of the remaining 247 only 6 are. This is because the first few samples show new, linearly independent features. The points added at a late stage often lie in the vicinity of an eigenvalue, although this is not a necessary condition.

Both the 16-dimensional reduced order model and the 10^4-dimensional full model were solved using Beyn's algorithm and the method of successive linear problems (MSLP) [5]. Both the eigenvalues (Fig. 2) and the eigenvectors (Fig. 1c–f) calculated with the ROM show excellent agreement with those from the full problem. Referring to Fig. 2, five eigenmodes are identified in the considered contour. The modeshapes of the lowest and highest modes in the contour are shown in Fig. 1. For some initial guesses, the MSLP also converges to eigenvalues that lie outside the contour. Jorkowski's method [10] relies on Beyn's method and, thus, the ROM obtained with it is restricted to the eigenvalues inside Γ. The method in this letter is guaranteed to approximate the eigenvalues inside Γ, but the sampling proves more robust and can even approximates eigenvalues outside Γ.

We conclude with some remarks on the numerical efficiency of the algorithm. Including the time needed to construct the subspace, the identification of the eigenvalues in the ROM subspace was about 15 times faster than in the full-problem space when using Beyn's method. A similar comparison has been made for a coarser and a finer grid resolution, yielding a speed-up factor of 8 for $N = 1800$ and of 30 for $N = 87000$. In general, the larger is N the greater is the computational gain, because the dimension of the ROM, M, relates to the number of eigenvalues in the portion of the complex plane investigated. When using the MSLP, a quantitative comparison depends on the number of initial guesses chosen. For the considered problem, it was found that the analysis in the ROM is already more efficient when the number of sampling point was larger than 8. Thus, unless good guesses for all the eigenvalues are known, the analysis in the ROM space should be preferred. When compared to the method of [10], the method proposed here has an analogous computational cost, but is more powerful since (i) it allows for the use of multiple solution algorithms and (ii) it is less dependent on the specific choice of the contour Γ, since it can identify also eigenvalues which lie outside of the considered domain.

4. Conclusions

We have presented a method that actively identifies a small dimensional subspace within which the eigenvalues and eigenvectors of a large matrix operator $\mathbf{L}$, resulting from the discretization of a vibrational problem, are well-approximated in a region of the complex plane. In contrast to existing models in the literature, the generated subspace retains the nonlinear dependency on the eigenvalues, and well-approximates the action of $\mathbf{L}$ not only along a contour, but also inside it. This allows us to leverage not only contour-based methods, but any solution technique on the reduced nonlinear eigenvalue problem. An application example to a thermoacoustic eigenvalue problem has been presented. It was shown how the method is able to cut down the dimension of the problem from $\mathcal{O}\left(10^4\right)$ for the full finite element model to $\mathcal{O}\left(10^1\right)$ after projection onto the subspace, without any significant loss in the accuracy of the calculated eigenvalues and eigenvectors. This results in a ROM able to accurately identify eigenpairs in a finite region of the complex plane with a much lower computational effort. It has also been shown how the constructed ROM is able to identify eigenvalues which lay outside of the considered region of the complex plane. How far these eigenvalues can be from the sampled domain is an open question currently under investigation.

CRediT authorship contribution statement

Georg A. Mensah: Conceptualization, Methodology, Software, Validation, Visualization, Writing – original draft, Writing – review & editing. **Alessandro Orchini:** Methodology, Software, Validation, Visualization, Writing – original draft, Writing – review & editing. **Philip E. Buschmann:** Methodology, Software, Data curation, Visualization, Writing – original draft, Writing – review & editing. **Luka Grubišić:** Conceptualization, Methodology, Formal analysis, Supervision, Writing – review & editing.

Declaration of competing interest

The authors declare that they have no known competing financial interests or personal relationships that could have appeared to influence the work reported in this paper.

Acknowledgements

The work of L.G. has been supported by the Croatian Science Foundation under the grant IP-2019-04-6268. A.O. acknowledges the support of the German Research Foundation (DFG), project nr. 422037803.

References

[1] G.A. Mensah, A. Orchini, J.P. Moeck, Perturbation theory of nonlinear, non-self-adjoint eigenvalue problems: Simple eigenvalues, J. Sound Vib. 473 (2020) 115200, http://dx.doi.org/10.1016/j.jsv.2020.115200.
[2] J.G. Aguilar, M.P. Juniper, Thermoacoustic stabilization of a longitudinal combustor using adjoint methods, Phys. Rev. Fluids 5 (8) (2020) 083902.
[3] N. Purwar, M. Meindl, W. Polifke, Comparison of model order reduction methods in thermoacoustic stability analysis, in: Turbo Expo: Power for Land, Sea, and Air, Vol. 84959, American Society of Mechanical Engineers, 2021, V03BT04A021.
[4] F. Nicoud, L. Benoit, C. Sensiau, T. Poinsot, Acoustic modes in combustors with complex impedances and multidimensional active flames, AIAA J. 45 (2) (2007) 426–441, http://dx.doi.org/10.2514/1.24933.
[5] Y. Saad, Numerical Methods for Large Eigenvalue Problems: Revised Edition, SIAM, 2011, http://dx.doi.org/10.1137/1.9781611970739.
[6] S. Güttel, F. Tisseur, The nonlinear eigenvalue problem, Acta Numer. 26 (2017) 1–94, http://dx.doi.org/10.1017/S0962492917000034.
[7] B. Schuermans, V. Bellucci, C. Paschereit, Thermoacoustic Modeling and Control of Multi Burner Combustion Systems, in: Turbo Expo: Power for Land, Sea, and Air, vol. 2, 2003, pp. 509–519, http://dx.doi.org/10.1115/GT2003-38688.
[8] W.-J. Beyn, An integral method for solving nonlinear eigenvalue problems, Linear Algebra Appl. 436 (10) (2012) 3839–3863, http://dx.doi.org/10.1016/j.laa.2011.03.030.
[9] P.E. Buschmann, G.A. Mensah, F. Nicoud, J.P. Moeck, Solution of thermoacoustic eigenvalue problems with a noniterative method, J. Eng. Gas Turb. Power 142 (3) (2020) http://dx.doi.org/10.1115/1.4045076, 031022.
[10] P. Jorkowski, R. Schuhmann, Solving nonlinear eigenvalue problems for waveguide-coupled cavities using an integral solver with subspace projection, IEEE Trans. Magn. 56 (1) (2020) 1–4, http://dx.doi.org/10.1109/TMAG.2019.2950513.
[11] L. Tay-Wo-Chong, S. Bomberg, A. Ulhaq, T. Komarek, W. Polifke, Comparative validation study on identification of premixed flame transfer function, J. Eng. Gas Turb. Power 134 (021502) (2012) 8, http://dx.doi.org/10.1115/1.4004183.
[12] A. Orchini, C.F. Silva, G.A. Mensah, J.P. Moeck, Thermoacoustic modes of intrinsic and acoustic origin and their interplay with exceptional points, Combust. Flame 211 (2020) 83–95, http://dx.doi.org/10.1016/j.combustflame.2019.09.018.

Symmetry groups in thermoacoustics

Symmetry groups in thermoacoustics

Philip E. Buschmann[a,*], Jonas P. Moeck[a]

[a] *Department of Energy and Process Engineering*
Norwegian University of Science and Technology
Trondheim, Norway

Contents

*Corresponding author
Email address: philip.e.buschmann@ntnu.no (Philip E. Buschmann)

1. Introduction

Thermoacoustic instabilities are a dangerous type of self-excited pressure oscillations in the combustion chambers of high-powered systems such as gas turbines and rocket engines. A considerable amount of research has been invested in predicting and mitigating these unwanted oscillations that can cause significant damage [1].

Two designs of major industrial importance are can-annular [2] and annular combustion chambers [3]. Both designs employ a large number of burners arranged around a circumference. Annular designs permit a high power density and are, thus, mainly employed in helicopter and aircraft engines. Can-annular designs, in which individual burners are isolated and only connected via a small gap at the downstream end, are favored in stationary power generation. The isolation of individual burners reduces development cost since flow properties and thermal loads can be characterised on a single burner.

To ensure that a combustion system is stable, an effective strategy consists in performing a linear stability analysis by solving the thermoacoustic Helmholtz equation [4, 5]. In shortened notation, the mathematical problem reads

$$\mathcal{L}(\omega)\,\hat{p} = 0\,, \tag{1}$$

where $\mathcal{L}$ is an operator representing the governing partial differential equation as well as boundary conditions. $\mathcal{L}$ is (generally) a nonlinear function of the complex eigenfrequency ω but depends linearly on the eigenvector $\hat{p}$. A combustion chamber is stable[1] when $\mathrm{Im}(\omega) > 0$ for all ω. Thus, Equation (1) constitutes a nonlinear eigenvalue problem (NLEVP) for the eigenpairs $(\omega, \hat{p})$.

In physics it is well known that if in an eigenvalue problem of type $\mathcal{L}$ exhibits an underlying symmetry, a number of properties of the solutions $(\omega, \hat{p})$ can be inferred *without* solving the problem. In fact, the annular and can-annular combustors encountered in thermoacoustics exhibit a discrete rotational symmetry. Here, 'symmetry' refers to the fact that for a can-annular or annular design consisting of N burners any multiple of a rotation by $2\pi/N$ leaves the geometry invariant. However, this is only one class of possible symmetry operations. The two most important groups for annular and can-annular combustors are C_N and C_{Nv}, where N is the number of burners (usually denoted as n in the literature).

Loosely speaking, all possible symmetry operations together form a *symmetry group*[2]. Symmetry groups themselves are invariant objects – molecules, geometric objects and equations can have the same symmetry group [6, Chap. 1]. Their properties are tabulated and these can be used once the symmetry group of an object, here a combustion chamber, has been identified.

The subject of this paper is to express thermoacoustics in the language of symmetry groups and use its powerful machinery to address a number of questions and re-interpret existing results. In particular, we will answer the following questions: What is the connection between symmetry and eigenvalue degeneracy? Why can only a combustor with C_{Nv} symmetry have degenerate modes? What is the relationship between azimuthal mode orders and Bloch wave numbers? Under which conditions can Bloch waves be used to reduce computational costs? Is there a maximal azimuthal mode order? How do degenerate thermoacoustic modes split under symmetry perturbations?

[1] The Fourier transformation follows the convention $\partial_t p' \to +\mathrm{i}\omega\hat{p}$.
[2] Care needs to be taken in not counting operations twice.

The machinery of symmetry groups is a powerful tool to draw upon when solving eigenvalue problems with underlying symmetries in engineering. However, symmetry group theory is most often encountered in quantum mechanics. Hence, there is a high barrier to transfer knowledge to more classical engineering applications, unless a solid background in quantum mechanics exists. This paper aims at removing this barrier.

Proofs for elementary properties of symmetry groups are largely omitted. Instead, examples are used to confirm stated properties. However, detailed references to proofs are given. The main reference for this work is the book by Inui, Tanabe and Onodera *Group Theory and Its Applications in Physics* [6].

1.1. Thermoacoustic model and basic assumptions

Following Nicoud et al. [4] the thermoacoustic Helmholtz equation is written as

$$\nabla \cdot \left(c^2 \, \nabla \hat{p}\right) + \omega^2 \hat{p} = -\mathrm{i}\omega \left(\gamma - 1\right) \hat{q} \,, \tag{2}$$

where $\hat{q}$ is the frequency response of the fluctuating heat-release rate(s). It is assumed that suitable boundary conditions have been prescribed. In order to close the equation, $\hat{q}$ needs to be expressed as a function of $\hat{p}$. One possible choice relates $\hat{q}$ linearly to an upstream velocity fluctuation at a reference location $\hat{u}|_{\mathrm{ref}}$ via a flame transfer function (FTF) $\mathcal{F}\left(\omega\right)$

$$\hat{q} = \frac{Q_0}{u_0 V_{\mathrm{F}}} \mathcal{F}\left(\omega\right) \hat{u}|_{\mathrm{ref}} \,. \tag{3}$$

Here Q_0 is the mean global heat release, u_0 the mean flow at the reference position and V_{F} the volume of the flame. FTFs can be obtained via measurements [7], large-eddy simulations [8] or from analytic considerations [9, 10]. In order to close the problem, the velocity fluctuation $\hat{u}|_{\mathrm{ref}}$ in Eq. (3) can be expressed via the linearized momentum balance as

$$-\mathrm{i}\omega\hat{u} = \frac{1}{\rho_0} \nabla \hat{p} \,. \tag{4}$$

By closing Eq. (2) with Eqs. (3) and (4) the eigenvalue problem is expressed only in the unknown eigenpairs $(\omega, \hat{p})$

$$\nabla \cdot \left(c^2 \, \nabla \hat{p}\right) + \omega^2 \hat{p} = \underbrace{\left(\gamma - 1\right) \frac{Q_0}{\rho_0 u_0 V_{\mathrm{F}}}}_{n_{\mathrm{loc}}} \mathcal{F}\left(\omega\right) \nabla \hat{p}|_{\mathrm{ref}} \,, \tag{5}$$

and abbreviated to

$$\mathcal{L}\left(\omega\right) \hat{p} = 0 \,. \tag{6}$$

For visualization purposes concrete tests cases of annular and can-annular combustors are solved numerically to visualize eigenpairs $(\omega, \hat{p})$. Using the packages [11] and [12] the thermoacoustic Helmholtz equation is discretized with the finite-element method (FEM) and a matrix-valued equation is obtained [13], written in abbreviated form as

$$\mathbf{L}\left(\omega\right) \mathbf{p} = 0 \,, \quad \mathbf{L} \in \mathbb{C}^{d \times d} \,, \tag{7}$$

where d is the number of degrees of freedom in the discrete mesh. Care is taken that the discretization that leads from Eq. (6) to Eq. (7) conserves the underlying symmetries. Solutions to the discrete NLEVP Eq. (7) are obtained using the methods described in [13] and [14]. Occasionally, it is convenient to trigger the effect of the flame term in Eq. (5) by a switch $s \in [0, 1]$

$$\nabla \cdot \left(c^2 \, \nabla \hat{p}\right) + \omega^2 \hat{p} = s \, n_{\mathrm{loc}} \, \mathcal{F}\left(\omega\right) \nabla \hat{p}|_{\mathrm{ref}} \,, \tag{8}$$

whereby $s = 0$ corresponds to a purely acoustic problem. The eigenvalues are then considered as functions of the switching parameter $\omega = \omega\left(s\right)$ and can be traced in the complex plane.

1.2. Literature review of previous studies of symmetry groups in thermoacoustics

The importance of symmetry groups has been recognized in thermoacoustics. Moeck et al. [15] study the splitting of twofold degenerate modes in an annular combustor due to a reduction of symmetry. In [15] as well as the subsequent dissertation by Moeck [16] the symmetry groups are identified as C_N. However, for the geometries featured in both publications [15, 16] the correct names are C_{Nv} – the group C_N cannot have degenerate modes associated with symmetry. The mistake is simply a miss-labelling: Moeck uses the properties of C_{Nv} to characterise the systems at hand and to deduce their degeneracy properties. A later publication by Ghirardo, Juniper and Moeck [17] identifies C_{Nv} correctly.

Mensah et al. [18] employed so-called Bloch waves successfully to significantly reduce the computational cost required to solve the eigenvalue problem Eq. (6). The reduction amounts to solving the eigenvalue problem on a unit cell with special boundary conditions, yet the eigenvalues of the full geometry are obtained. The Bloch-based approach has since been adopted in thermoacoustic research [19, 2, 20]. Bloch waves exploit the translational group C_N. Since C_N is a subgroup of C_{Nv} it can also be employed for the latter.

Bauerheim et al. in two papers [21, 22] discuss the splitting of degenerate eigenvalues from a quantitative perspective using a network model of an annular combustor.

1.3. Outline of this paper

Section 2 focuses on the simple case of a single combustor that only exhibits a mirror symmetry. By exploring this example, the language of symmetry groups is introduced. Section 2.4 covers the central derivation that links physics to symmetry groups.

In Section 3 the group of a (can)-annular combustor is studied in which a single combustor does not have a mirror symmetry. Here, the Bloch wave theory as employed by Mensah et al. [18] is cast into the formal language of symmetry groups. For this type of combustor thermoacoustic modes are often labelled by azimuthal mode orders m. However, care needs to be taken when relating m and Bloch wave numbers b. This is also subject of Sec. 3. In addition, the existence of special degenerate modes due to *time-reversal* symmetry is explained.

Section 4 extends the work of the previous section by treating (can)-annular combustors with a mirror symmetry. The group of the combustor is derived in its entirety from a geometrical analysis. In particular, it is explored why a theory similar to Mensah et al. [18] is not possible to further reduce computational cost.

Section 5, explains how perturbations affect eigenvalue degeneracy and how these can be predicted by knowing the symmetry groups before and after the perturbation.

2. Single combustor cell with parity symmetry

Consider the annular combustor in Fig. 1a and cut out one of the 16 identical combustors, Fig. 1b. This *unit cell* exhibits a mirror symmetry along the xz-plane, denoted by the symbol σ_v. Hence, the operation σ_v (with the σ_v for the first letter of the German word for mirroring 'Spiegelung', [6, p. 2]) brings the unit cell into coincidence with itself and is an element of the symmetry group G of the single cell. Unfortunately, it is the only non-trivial operation. Together with the identity operation E, a set is formed

$$\mathrm{G} = \{E, \sigma_v\} \ . \tag{9}$$

To make G into a group a group multiplication "$*$" between elements needs to be defined. Later, $*$ is dropped for better readability. Using a geometric understanding, i.e. using the mirror operation twice yields the identity operation $\sigma_v * \sigma_v = E$, the *multiplication table* 1 is obtained.

In the following, symmetry groups are denoted as G and their elements as g_i with $i = 1, \ldots, |\mathrm{G}|$. The number of elements, or *order*, of the group is denoted by the finite number $|\mathrm{G}|$. The more elements in a symmetry group the higher its symmetry. In the next section it is proven that G is a group.

In this work only finite groups, i.e. $|\mathrm{G}| < \infty$ are considered. Their properties (which are the so-called character tables, which are introduced later) are tabulated in books [6, 23] or online resources [24]. Groups with infinite order are called *continuous* groups. An example is an annular combustor with a continuous

Table 1: Multiplication table for C_S. The group multiplication is denoted as "$*$". A multiplication table contains all possible combinations between elements. By convention the first element is always the identity element. The table itself is only symmetric if group elements commute.

	E	σ_v
E	$E * E = E$	$E * \sigma_v = \sigma_v$
σ_v	$\sigma_v * E = \sigma_v$	$\sigma_v * \sigma_v = E$

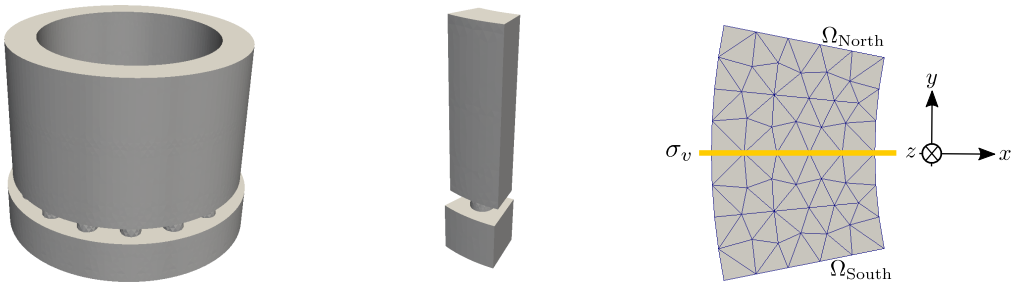

(a) (b) (c)

Figure 1: Left: Annular combustion chamber with 16 identical combustors. Middle: One of the sixteen combustors, a unit cell. In contrast to a *half-cell*, i.e. the top half of the single cell. Right: Top view of the single cell with the mirroring plane highlighted. The mirroring operation (not the plane itself) is denoted by σ_v. The Northern and Southern half cells form the unit cell $\Omega_{\text{Single cell}} = \Omega_{\text{North}} \cup \Omega_{\text{South}}$. Throughout the unit cell, the mesh is symmetric with respect to the mirroring plane $\partial\Omega_{xz} = \Omega_{\text{North}} \cap \Omega_{\text{South}}$.

heat-release zone over the circumference, see [25]. The combustor is invariant with respect to a rotation by an arbitrary angle, which is the group C_∞ and discussed in [16, p. 137]. Continuous groups, like the special orthogonal group $\mathrm{SO}(3)$, are important for field theories [6, p. 115] but not for thermoacoustic stability analysis.

The group in Eq. (9) is known as the group C_S (or C_{1v}) in *Schönfliess*[3] notation, a *crystallographic point group* of order $|\mathrm{G}| = 2$. The term crystallographic stems from the original application: Chemical molecules have precisely these symmetries. For instance, the methanol molecule $\mathrm{CH_3OH}$ has C_S symmetry while the methane molecule $\mathrm{CH_4}$ has T_d, which includes rotations around different axes and several reflections. A point group is a group that leaves at least one point invariant, for the single cell these are all the points on the yellow line in Fig. 1c. The property C_S is also known as *parity* symmetry. Due to molecular restrictions, only 32 point groups are relevant for quantum physics. Consequently, the literature in physics usually only tabulates these. Mathematically there is no constraint but it can become difficult to obtain character tables and representations for groups of high order. There are automatic tools available [26].

Now, consider a group $\bar{\mathrm{G}} = \{1, -1\}$ with "$*$" taken as ordinary multiplication. Evidently, the multiplication tables of $\bar{\mathrm{G}}$ and C_S are identical. Hence, a one-to-one correspondence between group elements of the two groups can be established. The two groups are said to be *isomorphic*

$$\mathrm{C}_S \cong \bar{\mathrm{G}}\,. \tag{10}$$

The isomorphism property signifies that symmetry groups themselves are unique objects: $\bar{\mathrm{G}}$ and C_S describe the same object yet originate from different applications.

2.1. Group properties of C_S

C_S is a group, and not just a set, because it fulfills the four group axioms G1–G4 [6, p. 7]. According to the multiplication table 1, the group is closed under multiplication (axiom G1), there exists an identity

[3] This is the convention employed in this work. Other conventions exist, see [6, p. 172].

element E (axiom G3) and the inverse element of every group element is contained in the group (axiom G4). Here, both E and σ_v are their own inverses.

The second axiom G2 is associativity. In order to show this, consider the geometric effect of the operations E and σ_v. For an arbitrary point $\mathbf{r} \in \mathbb{R}^3$ in the combustor, the identity operation E can be represented by the identity matrix and the mirroring operation along xz by the reflection matrix. In a Cartesian basis these are

$$E \doteq D(E) = \begin{pmatrix} 1 & 0 & 0 \\ 0 & 1 & 0 \\ 0 & 0 & 1 \end{pmatrix} \quad \text{and} \quad \sigma_v \doteq D(\sigma_v) = \text{Refl}_{xz} = \begin{pmatrix} 1 & 0 & 0 \\ 0 & -1 & 0 \\ 0 & 0 & 1 \end{pmatrix}. \tag{11}$$

In the following representation matrices are denoted as D. Since matrix multiplication is associative, it can be concluded that this property traces back to C_S. The symbol $\doteq$ denotes 'represented by'. Notice that the two elements E and σ_v commute, i.e. $E * \sigma_v = \sigma_v * E$. The symmetric multiplication table in Tab. 1 also signifies this. Such a group is called *Abelian* or *commutative*. Importantly, only non-Abelian groups lead to degenerate modes.

2.2. Representations and characters of C_S

In the previous section the abstract elements E and σ_v were represented by matrices and the group multiplication "$*$" was taken as the standard matrix multiplication. In fact, if every element g_i of a group is associated with a square matrix D and it holds

$$D(g_i)\, D(g_j) = D(g_k)\,, \tag{12}$$

for the group relations

$$g_i * g_j = g_k\,, \tag{13}$$

the set of matrices $D(g_1), \ldots, D\left(g_{|G|}\right)$ is called a *representation*. The representations are not unique: For C_S the element E can be represented by the number 1 and so can the element σ_v

$$D_1(E) = 1\,, \quad \text{and} \quad D_1(\sigma_v) = 1\,. \tag{14}$$

Together with ordinary multiplication for "$*$" Eq. (12) holds. This is the *identity representation*, which is an *unfaithful* representation in contrast to the matrices in Eq. (11) which form a faithful representation. The matrices Eq. (12) are 'too big' in the sense that it suffices to represent the elements of C_S by

$$D_2(E) = 1\,, \quad \text{and} \quad D_2(\sigma_v) = -1\,. \tag{15}$$

The representations in Eq. (14) and Eq. (15) are *irreducible* representations (irreps.) of the group C_S. It can be observed that the matrices in Eq. (12) are formed by combining the irreps. as

$$\hat{D}(g_i) = \begin{pmatrix} D_1(g_i) & 0 & 0 \\ 0 & D_2(g_i) & 0 \\ 0 & 0 & D_1(g_i) \end{pmatrix}. \tag{16}$$

The block-diagonal structure of Eq. (16) signifies that it is a reducible representation. Conversely, a representation that cannot be block-diagonalized is irreducible. For a more comprehensive introduction to representations see [6, Chapter 4].

Groups can be characterised completely by their *character* tables. A character χ is simply the trace of a representation matrix

$$\chi(g_i) = \operatorname{Tr} D(g_i)\,, \quad \text{for} \quad i = 1, \ldots, |\mathrm{G}|\,. \tag{17}$$

Table 2: Character table for C_S. All irreps. Γ_i are one-dimensional, so the characters χ_i are identical to the irreps. If the character tables of two groups are 1:1, the groups are isomorphic.

C_S	E	σ_v
$\Gamma_1 = \chi_1$	1	1
$\Gamma_2 = \chi_2$	1	-1

For C_S the character table is given in Tab. 2, which is trivial since all irreps are one-dimensional. The first column of the character table necessarily gives the dimension of the irrep. For now, it is sufficient that character tables and irreps. for all finite groups can be found online and need not be generated by hand.

Character tables are governed by orthogonality properties in column- and row-wise direction. Plus, the total number of irreps. of a group is identical to the number of classes. For details see Sec. 4 where the character table for a group of an annular combustor with mirror symmetry is derived in its entirety using these properties.

In the next two sections important theory is developed, s.t. if the governing symmetry group is known it can be exploited by means of its character table to: (1) Draw conclusions about degeneracy of modes and (2) potentially reduce computational cost.

2.3. Operators applied to vectors and functions

Consider a function $\psi : \mathbb{R}^3 \to \mathbb{C}$ which could describe the shape of a thermoacoustic mode in a given combustor geometry – for the following theory the function does not have to be an eigenfunction. For an example see Fig. 2. Here, $\psi(\mathbf{r})$ could describe the level of the acoustic pressure at a given location. Notice that $\psi(\mathbf{r})$ is not yet mirror symmetric – that comes later. If the figure is mirrored along the xz-plane, the new position vector $\mathbf{r}'$ is given by

$$\mathbf{r}' = \begin{pmatrix} x' \\ y' \\ z' \end{pmatrix} = \mathrm{Refl}_{xz} \begin{pmatrix} x \\ y \\ z \end{pmatrix} = R\,\mathbf{r}\,, \tag{18}$$

where Refl_{xz} is the previously introduced reflection matrix. Or for an arbitrary symmetry operation

$$\mathbf{r}' = R\mathbf{r}\,. \tag{19}$$

This relation can be inverted to yield $\mathbf{r} = R^{-1}\mathbf{r}'$. Next, consider a function ψ' which describes the mirrored mode shape

$$\psi'(\mathbf{r}') = P_R\psi(\mathbf{r}')\ . \tag{20}$$

In this work we discern in our notation between operations R acting on coordinates $\mathbf{r}$ and operations P_R acting on functions ψ. Both, R and P_R implement the same geometric operation, but it is technically more elegant to discern between them: A mirroring matrix R acting on a scalar function is mathematically inaccurate. In the literature this is often neglected, but in this work the distinction is made for readability. In addition, a general group element is denoted as g and a matrix that represents its geometric operation as R_g. The value of ψ' at $\mathbf{r}'$ should be equal to the value before the mirroring $\psi(\mathbf{r})$, see Fig. 2

$$\psi'(\mathbf{r}') = \psi(\mathbf{r})\ , \tag{21}$$

which is written with Eq. (20) as

$$P_R\psi(\mathbf{r}') = \psi(\mathbf{r})\ , \tag{22}$$

and

$$P_R\psi(\mathbf{r}') = \psi\left(R^{-1}\mathbf{r}'\right)\ . \tag{23}$$

Since $\mathbf{r}$ and $\mathbf{r}'$ are chosen arbitrarily, the primes are dropped and one obtains

$$P_R\psi(\mathbf{r}) = \psi\left(R^{-1}\mathbf{r}\right)\ , \tag{24}$$

which expresses that the value of the transformed function $P_R\psi(\mathbf{r})$ is equal to the value of ψ at $R^{-1}\mathbf{r}$.

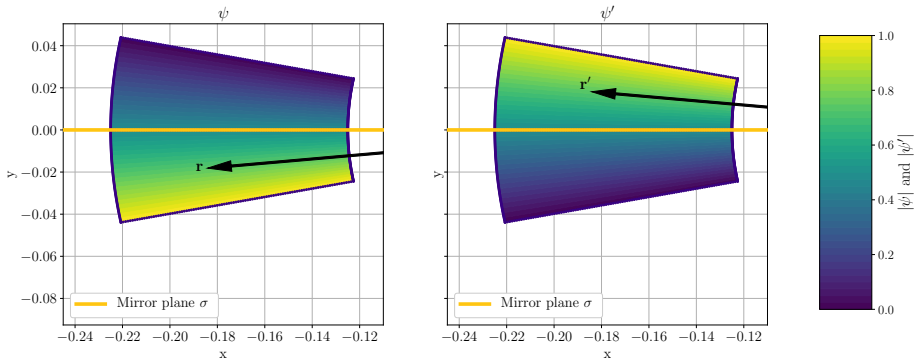

Figure 2: Top view of the single cell combustor in Fig. 1c with mode shape ψ and its mirrored version ψ'.

2.4. Transformation of $\mathcal{L}$ by elements of a symmetry group

The relation $P_R\psi(\mathbf{r}) = \psi\left(R^{-1}\mathbf{r}\right)$ expresses that P_R acts on a function ψ. Hence, P_R is an operator in the same way as $\mathcal{L}$, the linear operator describing thermoacoustic stability in an annular combustion chamber, is. Operators P_R are unitary[4] and leave the inner product invariant

$$(P_R\phi, P_R\psi) = (\phi, \psi)\ . \tag{25}$$

Then it can be written

$$(\phi, \mathcal{L}\psi) = (P_R\phi, P_R\mathcal{L}\psi) = \left(P_R\phi, P_R\mathcal{L}P_R^{-1}P_R\psi\right)\ . \tag{26}$$

Next, define $P_R\psi = \psi'$ and $P_R\phi = \phi'$ to obtain

$$(\phi, \mathcal{L}\psi) = \left(\phi', P_R\mathcal{L}P_R^{-1}\psi'\right) = (\phi', \mathcal{L}'\psi')\ , \tag{27}$$

which gives the definition of the transformed operator

$$\mathcal{L}' = P_R\mathcal{L}P_R^{-1}\,. \tag{28}$$

In this work, the subject is *symmetry operations*, that leave the operator invariant[5], therefore

$$\mathcal{L} = \mathcal{L}'\,, \tag{29}$$

and by definition

$$\mathcal{L} = P_R\mathcal{L}P_R^{-1}\,, \tag{30}$$

Acting with P_R from the right

$$\mathcal{L}P_R = P_R\mathcal{L}P_R^{-1}P_R\,, \tag{31}$$

yields

$$\mathcal{L}P_R = P_R\mathcal{L}\,, \tag{32}$$

which shows that $\mathcal{L}$ *commutes* with P_R. This is usually denoted as $[\mathcal{L}, P_R] = 0$ in quantum mechanics. In order to return to the subject of symmetry groups: The operator $\mathcal{L}$ is invariant under a set of symmetry transformations $P_R \in sym\,(\mathcal{L})$ which form a group. For the single-cell, the symmetry group of the operator is (isomorphic to) the symmetry group studied previously $sym\,(\mathcal{L}) \cong \mathrm{C}_S$ and which is properly characterised by its character table.

[4] An exception is the time-reversal operator in Section 3.6.

[5] The formulations in Eqs. (25)-(28) and Sec. 2.3 are more general and not restricted to symmetry operations. In quantum mechanics P_R can be an operator of interest which does not leave $\mathcal{L}$ invariant.

2.5. Basis of a representation

This section is taken from [6, Chap. 4.1.1.]. Consider d independent elements $\psi_1, \psi_2, \ldots, \psi_d$ in a vector space $\mathbb{C}^d$. The operators P_R, which are elements of the finite group $sym\,(\mathcal{L})$, operate on the ψ_n vectors. The set $\{\psi_1, \psi_2, \ldots, \psi_d\}$ is a basis for a representation of $sym\,(\mathcal{L})$ if it holds that

$$P_R \psi_n = \sum_{m=1}^{n} \psi_m D_{mn}\,(R)\ , \forall R \in sym\,(\mathcal{L})\ , \tag{33}$$

i.e. that the basis is large enough that P_R maps elements of $\mathbb{C}^d$ to itself. The Γ_{mn} are expansion coefficients with D being a coefficient matrix. One can show that the coefficient matrices Γ form a representation [6, 4.1.1.].

2.6. A first result: Dimensions of representations imply degeneracy

The crux from the previous section is that the operator $\mathcal{L}$ is invariant under actions $P_R \in sym\,(\mathcal{L})$ and thus $P_R \mathcal{L} = \mathcal{L} P_R$. Consider the thermoacoustic eigenvalue problem for a specific eigenpair $(\omega_n, \hat{p}_n)$

$$\mathcal{L}\,(\omega_n)\,\hat{p}_n = 0\,, \tag{34}$$

and act from the left with P_R

$$P_R \mathcal{L}\,(\omega_n)\,\hat{p}_n = P_R \cdot 0\,. \tag{35}$$

Due to the commutation

$$\mathcal{L}\,(\omega_n)\,(P_R\,\hat{p}_n) = 0\,. \tag{36}$$

Consequently $\hat{p}_n$ and $P_R\,\hat{p}_n$ belong to the same eigenvalue ω_n and represent the same state. Moreover, a formula for $P_R\,\hat{p}_n$ has been obtained in Sec. 2.5

$$P_R\,\hat{p}_n = \sum_{m=1}^{d} \hat{p}_n D_{mn}\,(R)\ , \tag{37}$$

where Γ_{mn} are the representation matrices for a representation of $sym\,(\mathcal{L})$. The dimension d is then the dimension of the irrep. of $sym\,(\mathcal{L})$ and, thus, equal to the degeneracy of the eigenvalue.

For the single cell, there are two sets of modes: $\hat{p}_1$ and $\hat{p}_2$, belonging to Γ_1 and Γ_2, respectively. These modes are simple since their irreps. are one-dimensional. However, for a two-dimensional irrep. – as encountered in the annular combustor – the associated eigenvalue will be twofold degenerate. As a consequence, we can restrict our studies to the symmetry group G in order to analyse the system described by $\mathcal{L}$.

In general it can be expected that eigenfunctions belonging to different irreps. have different eigenvalues. It is possible, that due to some non-symmetry related property two eigenvalues coincide. This is referred to as an *accidental* degeneracy: Picture an annular combustor, where the dimensions of the plenum and the combustion chamber are adjusted s.t. the eigenvalues of the first plenum mode and the first axial mode coincide.

2.7. A second result: Reduction in computational cost

For a single cell that exhibits a mirror symmetry, the operator $\mathcal{L}\,(\cdot)$ commutes with the mirror symmetry operation. Thus, application of the mirror operation P_{σ_v} to an eigenfunction yields

$$P_{\sigma_v} \hat{p}\,(\mathbf{r}) = \hat{p}\left(R_{\sigma_v}^{-1}\mathbf{r}\right)\ . \tag{38}$$

The left-hand side can be re-written in terms of the irreps. as

$$P_{\sigma_v} \hat{p}_i\,(\mathbf{r}) = \Gamma_i\,(\sigma_v)\,\hat{p}_i\,(\mathbf{r}) = \chi_i\,(\sigma_v)\,\hat{p}_i\,(\mathbf{r})\ , \tag{39}$$

where $i = 1, 2$ are the values of the characters as given in Tab. 2. Equation (38) is written as

$$\chi_i(\sigma_v)\,\hat{p}_i(\mathbf{r}) = \hat{p}_i\left(R_{\sigma_v}^{-1}\mathbf{r}\right)\,. \tag{40}$$

Next, the set of points is restricted to the xz plane and clearly $\mathbf{r} = R_{\sigma_v}^{-1}\mathbf{r}$, since these points are mapped to themselves. Two different cases need to be distinguished, first the *symmetric* (or *even*) one with $i = 1$

$$1 \cdot \hat{p}_1(\mathbf{r})|_{xz} = \hat{p}_1(\mathbf{r})|_{xz}\,, \tag{41}$$

and second the *anti-symmetric* (or *odd*) one with $i = 2$

$$-1 \cdot \hat{p}_2(\mathbf{r})|_{xz} = \hat{p}_2(\mathbf{r})|_{xz}\,. \tag{42}$$

These two conditions reveal properties of the associated eigenfunctions: All anti-symmetric eigenfunctions $\hat{p}_2$ have a node at the mirror plane, otherwise Eq. (42) cannot be fulfilled, hence the name. A Taylor expansion of Eq. (41) yields that all symmetric functions $\hat{p}_1$ have a pressure anti-node at the mirror plane.

Importantly, the set of all eigenfunctions is split into two types of functions and a label can be assigned to them depending on the irrep. they belong to. For the single cell combustor there are only two types, while for the full annular chamber the irreps. will lead to labeling by Bloch numbers b or azimuthal mode orders m.

Since any eigenfunction must belong to one of the irreps. the computational cost can be reduced by solving two separate eigenvalue problems on the northern half cell to the same eigenvalue. The problem that yields all symmetric eigenpairs is given as

$$\begin{aligned} \mathcal{L}(\omega_1)\,\hat{p}_1 &= 0\,, \quad \text{in} \quad \Omega_{1/2}\,, \\ \frac{\partial \hat{p}_1}{\partial \mathbf{n}} &= 0\,, \quad \text{on} \quad \partial\Omega_{xz}\,, \end{aligned} \tag{43}$$

and the problem that yields all anti-symmetric eigenpairs is

$$\begin{aligned} \mathcal{L}(\omega_2)\,\hat{p}_2 &= 0\,, \quad \text{in} \quad \Omega_{1/2}\,, \\ \hat{p}_2 &= 0\,, \quad \text{on} \quad \partial\Omega_{xz}\,. \end{aligned} \tag{44}$$

For a result where Eqs. (44) and (43) are solved, see Fig. 3. The result is compared with the solution on a full cell. In conclusion, half the computational effort is required in terms of degrees of freedom (DOF).

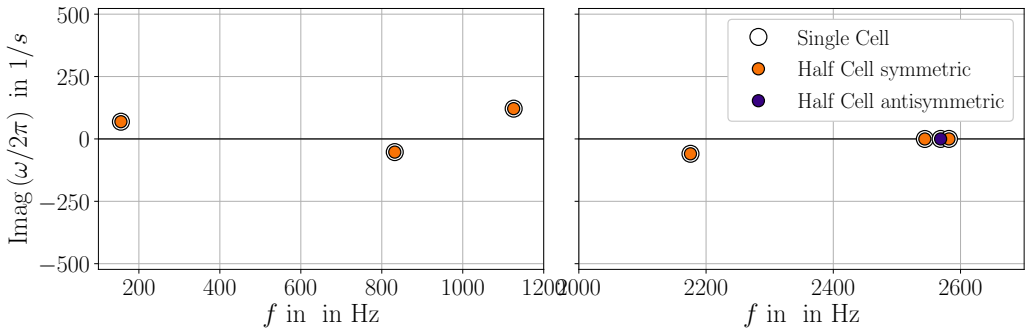

Figure 3: Acoustic resonance frequencies of a single cell below 2300 Hz. Solution computed on the full cell is identical to the solution computed on the half cell with adjusted boundary conditions. There are no frequencies outside the depicted range below 2600 Hz.

2.8. On the scope of validity of the theory presented in this paper

In this paper, it is always assumed that the geometric symmetry group of a combustor is the same as the symmetry group of $\mathcal{L}$. This is not the case, say, for a symmetric can-annular combustor with an asymmetric equivalence ratio distribution. In this case, the lower symmetry associated with the equivalence ratio would dictate the properties.

Due to manufacturing tolerances no real combustor is perfectly symmetric. However, the imperfections are usually small enough to consider the combustor as symmetric.

Notice that a can-annular and an annular combustor with the same number of burners N can have the same associated symmetry group. For this to hold, the symmetry groups of the unit elements – the cans or annular segments – must be identical. As an example: A can-annular combustor with 4 burners with swirl has the same symmetry group as an annular combustor with 4 burners with swirl. The swirl removes any mirror symmetry. Hence, both combustors are identical from the perspective of studying them via their symmetry groups. Therefore, the term 'annular' can be interchanges with 'can-annular' in this document.

In order to apply symmetry group theory $\mathcal{L}$ needs to commute with elements of a symmetry group, as detailed in Sec. 2.4. This is the case as long as $\mathcal{L}$ depends linearly on $\hat{p}$. In contrast, a nonlinear dependence on $\hat{p}$ due to a flame describing function [27] violates the commutation property – except under special conditions [19]. This case is not considered except in a short note in Sec. 3.7.

The theory presented in this paper is not limited to linear stability analysis by the thermoacoustic Helmholtz equation. A stability analysis of annular or can-annular combustion chambers by means of linearized Euler [28] or linearized Navier-Stokes equations [29] lends itself to the same analysis. However, the correct symmetry groups need to be identified. Unlike Eq. (2), these formulations contain mean flow fields, which can reduce the symmetry easily up to the point of leaving none left.

In quantum mechanics the Hamiltonian $\mathcal{H}$ takes the role of $\mathcal{L}$ and is Hermitian[6] – unlike in thermoacoustics, see discussions in [31] and [32]. The absence of the hermicity property increases difficulty, i.e. certain theorems that are exploited in quantum mechanics cannot be applied to thermoacoustic problems. In Section 3.6 a special case is considered where $\mathcal{L}$ is Hermitian.

An analysis of symmetry groups yields qualitative properties, i.e it predicts if degenerate modes exist and if they split under perturbations but not the quantitative values before and after the split. This is a subject extensively covered in Kato's book [33] and applied to thermoacoustic problems in [34] and [35].

3. Point group of an annular combustion chamber lacking mirror symmetry

In this section the point group of an annular combustor *without* mirror symmetry is derived: The cyclic group C_N (with N burners). From the irreps. of C_N it is shown that degenerate modes do not exist – unless the operator $\mathcal{L}$ has an additional $\mathcal{T}$-symmetry. Mensah et al. [18] reduced computational cost by exploiting the cyclic symmetry: Eigenmodes $(\omega, \hat{p})$ of the full annulus are obtained by solving smaller problem on a unit cell. In this work, Mensah et al.'s theory is formulated in the syntax of symmetry groups. This serves as an important preparation for the next section, where it is demonstrated that such a reduction in computational cost is not feasible for the annular combustor *with* mirror symmetry.

3.1. The unit cell as a generating element

In Figure 4 an annular combustion chamber with $N = 16$ burners is depicted. The highlighted single cell serves as the so-called unit cell: The complete annulus is obtained by repeated rotation of the unit cell by an angle $2\pi/16$. Such a rotation is written as C_{16}. An n-fold rotation can be written as

$$\underbrace{C_{16} * C_{16} * \ldots * C_{16}}_{n \text{ times}} = C_{16}^n \,. \tag{45}$$

[6] Neglecting non-Hermitian quantum mechanics [30].

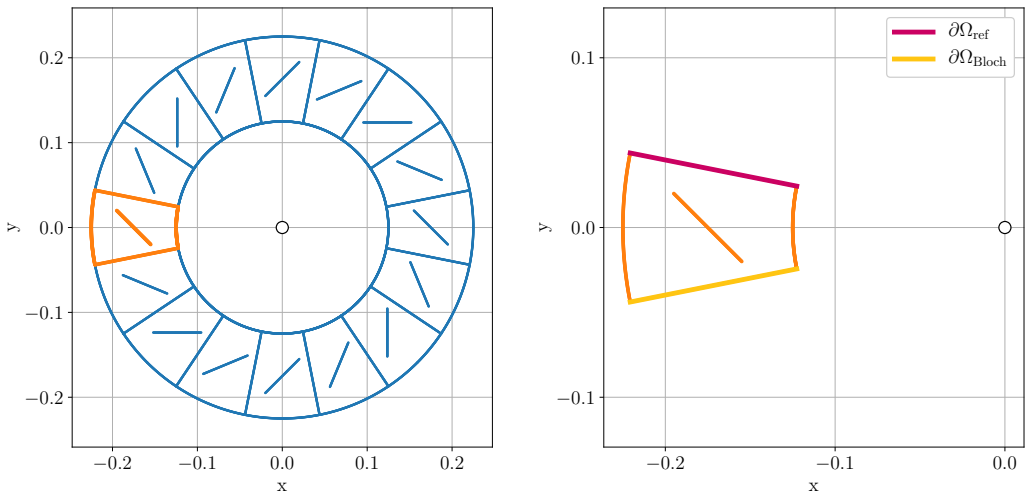

Figure 4: Left: Schematic depiction of an annular combustor that only exhibits a rotational symmetry in the form of the group C_{16}. Repeated rotation of the unit cell (orange) by an angle $2\pi/16$ yields the full annulus. Sixteen such rotations are unique. The diagonal bar in each cell signifies the absence of a mirror symmetry. Right: The unit cell with the Bloch boundary conditions.

Moreover, a periodic boundary condition exists

$$C_{16}^{N} = E\,, \tag{46}$$

with $N = 16$ in this case. The set of all rotations C_{16}^{n}

$$\mathrm{C}_{16} = \left\{E = C_{16}^{0}, C_{16}, C_{16}^{2}, \ldots, C_{16}^{N-1}\right\}\,, \tag{47}$$

forms the group C_{16} of order 16. The group axioms can be checked straightforwardly. Notice that the group operations C_{16}^{n} are written in italic while the group C_{16} itself is written non-italic. The two properties Eq. (45) and Eq. (46) make C_{16} a cyclic group, with the generating element C_{16}. Clearly, all elements of C_{16} commute with each other, which makes the group Abelian.

For now, the index n is restricted to the range $0, \ldots, N-1$. An index $n = -1$ refers to the same symmetry operation as the index $n = 17$ and, hence, different choices are possible. All the properties easily generalize to a combustor of arbitrary discrete rotational symmetry $N < \infty$.

3.2. Construction of the character table for C_N

In an Abelian Group every element is in a class of its own, [6, Chap. 2.8.]. From this it can be shown that all irreducible matrix representations are one-dimensional and, thus, identical to their characters

$$D\left(C_N^n\right) = \chi\left(C_N^n\right)\,. \tag{48}$$

There are N elements in C_N and, thus, N classes. This is a standard result for discrete groups, see [6, Chap. 4.6]. Therefore, the character table for C_N has N rows and columns. This gives the layout of the empty character table in Tab. 3 where only the trivial irrep. (first row) and the dimensions (first column) are filled in. The rest will be filled in step by step in the following.

In one irrep., the characters satisfy the homomorphism property [6, Chap. 2.5.2] which states for any two elements g_i and g_j of a group that

$$\chi\left(g_i * g_j\right) = \chi\left(g_i\right)\chi\left(g_j\right) . \tag{49}$$

For any of the N irreps. the homomorphism property gives

$$\left[\chi\left(C_N\right)\right]^N = \chi\left(E\right) = 1 . \tag{50}$$

Thus, the character of C_N takes values as the N-th roots of unity

$$\chi_b\left(C_N\right) = e^{2\pi \mathrm{i}\frac{b}{N}} \quad , \quad b = 0, \ldots, N-1 . \tag{51}$$

Consequently, the integer b can be used as a label for the irreps. With the abbreviation $\xi = e^{2\pi\mathrm{i}/N}$ the second column is filled in Tab. 4. Equation (49) can be applied to the second column of the table. This yields the character of C_{16}^2 for all irreps.

$$\chi_b\left(C_N^2\right) = \chi_b\left(C_N\right)\chi_b\left(C_N\right) = \xi^2 . \tag{52}$$

In this way, the character table can be completed, see Tab. 5. The character table can be extended with redundant rows, see Tab. 6 due to the complex root

$$e^{2\pi \mathrm{i}\frac{b}{N}} = e^{2\pi\mathrm{i}\left(\frac{N}{N}+\frac{b-N}{N}\right)} = e^{2\pi\mathrm{i}\frac{b-N}{N}} . \tag{53}$$

Hence, for two integers k and b, the characters are identical

$$\chi^{k\,N+b} = \chi^b . \tag{54}$$

Thus, the integer b does not have to be chosen in the range $0, \ldots, N-1$ but instead it is more convenient to use $-\left(N/2-1\right), \ldots N/2$. The proof for odd N is skipped, but it can be chosen as $-\left(N-1\right)/2, \ldots, N-1/2$. This labelling has certain advantages. A general element in the Tab. 6 is written as

$$\chi_b\left(C_N^n\right) = e^{\mathrm{i}\left(2\pi\frac{b}{N}n\right)} \tag{55}$$

and, thus, characterised by the integer b (defines to which irrep. it belongs) and n (defines for which group element it is).

3.3. Bloch's theorem and basis functions for C_N

An action by an element of C_N on a function $\psi\left(\mathbf{r}\right)$ – which is not yet an eigenfunction $\hat{p}$ – defined in the annulus is written as

$$P_{C_N^n}\psi\left(\mathbf{r}\right) = \psi\left(\mathbf{r}'\right) = \psi\left(R_{C_N^n}^{-1}\mathbf{r}\right) , \tag{56}$$

according to Eq. (24). As a visualization aid, a rotated function is depicted in Fig. 5. If the points $\mathbf{r}$ form the unit cell, the rotated points $\mathbf{r}'$ constitute the n-th cell in the annulus – a translation of sorts. In polar coordinates with $\mathbf{r} = \phi\,\mathbf{e}_\phi$, this can be written as

$$R_{C_N^n}^{-1}\mathbf{r} = \left(\phi - \frac{2\pi}{N}n\right)\mathbf{e}_\phi . \tag{57}$$

Elements of C_N also leave the linear operator $\mathcal{L}$ invariant and, thus, commute with it. As in Sec. 2.7 the commutation and Eq. (56) are the two key properties. All representations are one-dimensional and the basis function $\hat{p}_b\left(\mathbf{r}\right)$ of the irrep. (labelled by) b satisfies

$$P_{C_N^n}\hat{p}_b\left(\mathbf{r}\right) = \chi_b\left(C_N^n\right)\hat{p}_b\left(\mathbf{r}\right) = e^{\mathrm{i}\left(2\pi\frac{b}{N}n\right)}\hat{p}_b\left(\mathbf{r}\right) . \tag{58}$$

Table 3: Empty character table for the cyclic group C_N. The group has N classes and must of have N irreps. The trivial irrep. is written in the first row. The first column is given, since the group is Abelian and all irreps. are one-dimensional.

	$C_N^0 = E$	C_N^1	C_N^2	$\dots$	C_N^{N-1}
$\Gamma_0 = \chi_0$	1	1	1	$\dots$	1
χ_1	1				
χ_2	1				
$\vdots$	$\vdots$				
χ_{N-1}	1				

Table 4: Character table for the cyclic subgroup C_N with the characters for C_N^1 filled in.

	$C_N^0 = E$	C_N^1	C_N^2	$\dots$	C_N^{N-1}
χ_0	1	1	1	$\dots$	1
χ_1	1	ξ^1			
χ_2	1	ξ^2			
$\vdots$	$\vdots$	$\vdots$			
χ_{N-1}	1	ξ^{N-1}			

Table 5: Character table for the cyclic subgroup C_N with the remaining entries filled in.

	$C_N^0 = E$	C_N^1	C_N^2	$\dots$	C_N^{N-1}
χ_0	1	1	1	$\dots$	1
χ_1	1	ξ^1	ξ^2	$\dots$	ξ^{N-1}
χ_2	1	ξ^2	ξ^4	$\dots$	$\xi^{2(N-1)}$
$\vdots$	$\vdots$	$\vdots$	$\vdots$	$\vdots$	$\vdots$
χ_{N-1}	1	ξ^{N-1}	$\xi^{2(N-1)}$	$\dots$	$\xi^{(N-1)^2}$

Table 6: Character table for the cyclic subgroup C_N extended with redundant rows above and below the dashed line.

	$C_N^0 = E$	C_N^1	C_N^2	$\dots$	C_N^{N-1}
$\vdots$	$\vdots$	$\vdots$	$\vdots$	$\vdots$	$\vdots$
χ_{-2}	ξ^{-2}	ξ^{-4}	ξ^{-6}	$\dots$	$\xi^{-2(N-1)}$
χ_{-1}	ξ^{-1}	ξ^{-2}	$\xi-3$	$\dots$	$\xi^{-(N-1)}$
χ_0	1	1	1	$\dots$	1
χ_1	1	ξ^1	ξ^2	$\dots$	ξ^{N-1}
χ_2	1	ξ^2	ξ^4	$\dots$	$\xi^{2(N-1)}$
$\vdots$	$\vdots$	$\vdots$	$\vdots$	$\vdots$	$\vdots$
χ_{N-1}	1	ξ^{N-1}	$\xi^{2(N-1)}$	$\dots$	$\xi^{(N-1)^2}$
χ_N	1	1	1	$\dots$	1
χ_{N+1}	1	ξ^1	ξ^2	$\dots$	ξ^{N-1}
$\vdots$	$\vdots$	$\vdots$	$\vdots$	$\vdots$	$\vdots$

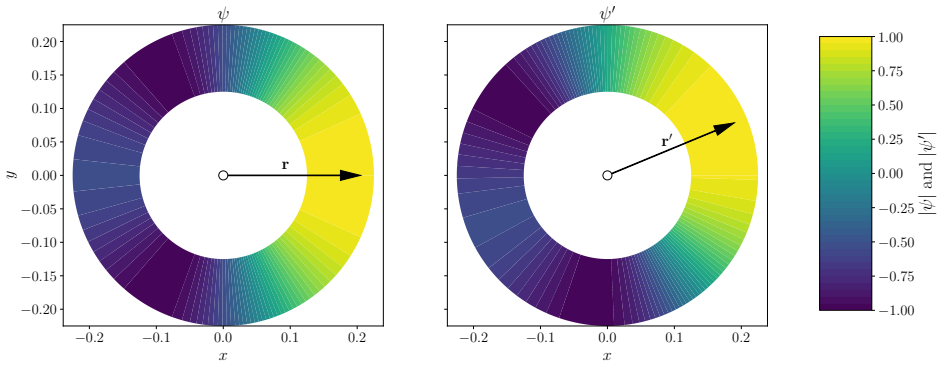

Figure 5: An arbitrary function ψ in an annular combustion chamber and its rotated version ψ'. This example is motivated from Inui et al. [6, Sec. 4.3] where a plot of the contour lines of Mount Fuji is considered.

By Equations (56) and (58) *Bloch's Theorem* is obtained

$$\hat{p}_b\left(R_{C_N^n}^{-1}\mathbf{r}\right) = e^{\mathrm{i}\left(2\pi\frac{b}{N}n\right)}\hat{p}_b\left(\mathbf{r}\right) . \tag{59}$$

The functions $\hat{p}_b\left(\mathbf{r}\right)$ are called *Bloch functions* and the origin of the phase factor $e^{\mathrm{i}\left(2\pi\frac{b}{N}n\right)}$ becomes evident: The irreps. is labelled by b, the *Bloch number*. Equation (58) shows that the phase factor $e^{\mathrm{i}\left(2\pi\frac{b}{N}n\right)}$ is the eigenvalue of the operator $P_{C_N^n}$ and the Bloch functions $\hat{p}_b\left(\mathbf{r}\right)$ are the basis functions for C_N. With the azimuthal coordinate ϕ another function can be defined as

$$\hat{p}_b\left(\mathbf{r}\right) = e^{-\mathrm{i}b\phi}u_b\left(\mathbf{r}\right) \tag{60}$$

and substitute into Bloch's Theorem (59) to obtain for the left-hand side

$$\hat{p}_b\left(R_{C_N^n}^{-1}\mathbf{r}\right) = e^{-\mathrm{i}b\left(\phi-\frac{2\pi}{N}n\right)}u_b\left(R_{C_N^n}^{-1}\mathbf{r}\right) = e^{-\mathrm{i}b\phi}e^{\mathrm{i}\left(2\pi\frac{b}{N}n\right)}u_b\left(R_{C_N^n}^{-1}\mathbf{r}\right) , \tag{61}$$

and for the right-hand side

$$e^{\mathrm{i}\left(2\pi\frac{b}{N}n\right)}\hat{p}_b\left(\mathbf{r}\right) = e^{\mathrm{i}\left(2\pi\frac{b}{N}n\right)}e^{-\mathrm{i}b\phi}u_b\left(\mathbf{r}\right) , \tag{62}$$

to yield

$$u_b\left(R_{C_N^n}^{-1}\mathbf{r}\right) = u_b\left(\mathbf{r}\right) . \tag{63}$$

Thus, $u_b\left(\mathbf{r}\right)$ is periodic on a unit cell. In this section Bloch's theorem was motivated with the point group C_N. In the literature, the theorem is part of space group theory, see [6, Chap. 11]. In short, the rotation by a set angle can be considered a translation around the circumference and $P_{C_N^n}$ is then a translation operator. This has applications in periodic crystals that exhibit translation-invariance in more than one dimension. The Bloch numbers b are considered continuous, not discrete, since the number N is large as it corresponds to the number of atoms in a crystal. Space group theory has its own syntax that is more convenient to express the extremely high symmetries associated with crystals. Usually, every atom (for us: a single combustor) alone exhibits a point group with high symmetry (for us: at most C_S) on top of the translational invariance in three dimension.

3.4. Unit cell computation and extrapolation to the full annulus using Bloch waves

Bloch's theorem from the previous section is the central equation from Mensah et al.'s work [18], repeated here

$$\hat{p}_b\left(R_{C_N^n}^{-1}\mathbf{r}\right) = e^{\mathrm{i}\left(2\pi\frac{b}{N}n\right)}\hat{p}_b\left(\mathbf{r}\right) . \tag{64}$$

Hence, if the mode shape is known for a unit cell $\hat{p}_b\left(\mathbf{r}\right)$, an extrapolation to any other cell $\hat{p}_b\left(R_{C_N^n}^{-1}\mathbf{r}\right)$ is straightforward by multiplication with the phase factor. In order to solve the problem on a unit cell a *Bloch boundary condition* has to be prescribed. Set $n = 1$ in Eq. (64) to obtain

$$\hat{p}_b\left(R_{C_N}^{-1}\mathbf{r}\right) = e^{\mathrm{i}b\left(\frac{2\pi}{N}\right)}\hat{p}_b\left(\mathbf{r}\right) . \tag{65}$$

This relation between values of $\hat{p}_b$ at different points $\mathbf{r}$ is valid for all points $\mathbf{r}$. For a unit cell computation of explicit interest are the points on the face $\partial\Omega_{\mathrm{ref}}$, which are partnered with a boundary at the next unit cell $\partial\Omega_{\mathrm{ref+1}}$. Yet the boundary $\partial\Omega_{\mathrm{ref+1}}$ still belongs to the original unit cell and is, hence, defined as $\partial\Omega_{\mathrm{Bloch}}$

$$e^{\mathrm{i}b\left(\frac{2\pi}{N}\right)}\,\hat{p}_b\left(\mathbf{r}\right)|_{\partial\Omega_{\mathrm{ref}}} = \hat{p}_b\left(\mathbf{r}\right)|_{\partial\Omega_{\mathrm{ref+1}}} \equiv \hat{p}_b\left(\mathbf{r}\right)|_{\partial\Omega_{\mathrm{Bloch}}} . \tag{66}$$

Consequently, the boundary $\partial\Omega_{\mathrm{Bloch}}$ is equipped with a modified boundary condition. See Figure 4 for a depiction. The value on the Bloch boundary is simply the value on the reference boundary times the phase factor. Consequently, for every b the eigenvalue problem is solved on the unit cell with the Bloch boundary conditions. Eigenfunctions of the full annulus are obtained by extrapolation from the unit cell using Eq. (64). An ordinary periodic boundary condition is obtained for $b = 0$.

3.5. Azimuthal wave number and Bloch number: Labelling modes by symmetry

Bloch numbers b label the irreps. and are the only correct labelling for eigenpairs $(\omega, \hat{p})$. How does a label by azimuthal mode order m relate to b? Consider a solution to the linear thermoacoustic eigenvalue problem $\hat{p}_b\left(\mathbf{r}\right)$ of order $m = 2$. This function is π-periodic and a rotation by $C_N^{N/2}$ turns this function into itself. Formally, this can be written as

$$P_{C_N^{N/2}}\hat{p}_b\left(\mathbf{r}\right) \overset{!}{=} \hat{p}_b\left(\mathbf{r}\right) , \tag{67}$$

and using the phase factor with $n = N/2$

$$e^{\mathrm{i}b\left(n\frac{2\pi}{N}\right)}\hat{p}_b\left(\mathbf{r}\right) = \hat{p}_b\left(\mathbf{r}\right) , \tag{68}$$

$$e^{\mathrm{i}b\left(n\frac{2\pi}{N}\right)} = 1 , \tag{69}$$

$$e^{\mathrm{i}b\left(\frac{N}{2}\frac{2\pi}{N}\right)} = 1 , \tag{70}$$

$$e^{\mathrm{i}b\pi} = 1 . \tag{71}$$

Excluding the trivial case $b = 0$ it holds that $b = 2 = m$, and the Bloch number and azimuthal mode number are identical. Generalizing Eq. (67) for arbitrary m, one obtains for the phase factor

$$e^{2\pi\mathrm{i}\frac{b}{m}} = 1 . \tag{72}$$

This result expresses that for azimuthal wave numbers with

$$m \leq \max\left(b\right) = N/2 , \tag{73}$$

Bloch numbers corresponds to the azimuthal wave number. As noted in Mensah et al. [18]: $N/2$ is sufficiently high in practical applications to use them interchangeably. What about higher mode orders? For $N = 4$ and $m = 3$ the relation yields

$$P_{C_4^{4/3}}\hat{p}_b\left(\mathbf{r}\right) = \hat{p}_b\left(\mathbf{r}\right) , \tag{74}$$

but clearly $C_4^{4/3}$ is not a symmetry operation of C_4. Using the cyclic property

$$\left(C_4^{4/3}\right)^3 = C_4^4 = C_4^{4/1}\,, \tag{75}$$

and Eq. (72) gives

$$e^{2\pi \mathrm{i} b} = 1\,, \tag{76}$$

which yields $b = -1, 1$. Likewise for $m = 4$

$$P_{C_4^1}\hat{p}_b\left(\mathbf{r}\right) = \hat{p}_b\left(\mathbf{r}\right)\,, \tag{77}$$

one obtains

$$e^{2\pi \mathrm{i} \frac{b}{4}} = 1\,, \tag{78}$$

and $b = 0$. Mode $m = 5$ yields $b = -1, 1$ again, while $m = 6$ with $P_{C_4^{4/6}}$ gives $C_4^{4/6} = C_4^{2/3}$ such that

$$\left(C_4^{2/3}\right)^3 = C_4^2\,, \tag{79}$$

and one obtains $b = 2$. Consequently azimuthal modes $m \geq N/2$ are not forbidden but alias in lower Bloch numbers. For C_4 the result is

$$\begin{array}{c|ccccccccc} m & 0 & 1 & 2 & 3 & 4 & 5 & 6 & 7 & 8 \\ b & 0 & -1,1 & 2 & -1,1 & 0 & -1,1 & 2 & -1,1 & 0 \end{array}\,. \tag{80}$$

3.6. Degenerate modes in the annulus due to time-reversal symmetry

The Abelian nature of C_N prohibits degenerate eigenvalues, since these require at least one 2D irrep. However, there is an exception when the linear operator is self-adjoint (or Hermitian). In the following, it is shown how the Hermitian property is a consequence of an additional symmetry of $\mathcal{L}\left(\cdot\right)$ that is not part of the geometric symmetry: Time-reversal $\mathcal{T}$, which pairs two 1D irreps. of C_N into one 2D irrep., resulting in two-fold degenerate modes. The group is then denoted as $\bar{\mathrm{C}}_N$.

Time-reversal symmetry is only encountered in special cases in thermoacoustics. For instance in a combustor with purely homogeneous boundary conditions, no viscous damping term(s) and a "switched-off" flame (also referred to as a passive flame in the literature), i.e. no damping or amplification. Under these conditions, Eq. (2) simplifies in time domain to

$$\frac{\partial^2 p'\left(t, \mathbf{r}\right)}{\partial t^2} - \nabla \cdot \left(c^2 \nabla p'\left(t, \mathbf{r}\right)\right) = 0\,. \tag{81}$$

This equation is symmetric with respect to time-reversal: t can be replaced with $-t$ and no signs of the operators change. Moreover, under complex-conjugation $\left(\cdot\right)^\dagger$ both operators are invariant

$$\left[\frac{\partial^2 \, p'^{\,\dagger}\left(t, \mathbf{r}\right)}{\partial t^2}\right] - \left[\nabla \cdot \left(c^2 \nabla \, p'^{\,\dagger}\left(t, \mathbf{r}\right)\right)\right] = 0\,, \tag{82}$$

and $p'^{\,\dagger}$ solves the same equation as p'. Hence, $p' = p'^{\,\dagger}$ and p' must be real. Fourier transformation of the equation for the time-reversed function $p'\left(-t\right)$ yields

$$\nabla \cdot \left(c^2 \, \nabla \, \hat{p}^{\,\dagger}\left(\mathbf{r}\right)\right) + \left(\omega\right)^2 \hat{p}^{\,\dagger}\left(\mathbf{r}\right) = 0\,, \tag{83}$$

since the Fourier transformation of a real, time-reversed function is the complex-conjugate of the original function. Taking the complex-conjugate of Eq. (81) in frequency domain yields

$$\nabla \cdot \left(c^2 \, \nabla \hat{p}^\dagger \left(\mathbf{r}\right)\right) + \left(\omega^\dagger\right)^2 \hat{p}^\dagger \left(\mathbf{r}\right) = 0 \, . \tag{84}$$

For Equations (83) and (84) to hold simultaneously ω must be real, and since the elliptic operator $\nabla \cdot \left(c^2 \, \nabla\right)$ is real, $\mathcal{L}$ is self-adjoint

$$\mathcal{L}^\dagger \left(\omega\right) = \mathcal{L} \left(\omega\right) \, . \tag{85}$$

This analysis shows that symmetry under time-reversal implies symmetry under complex-conjugation in frequency domain. Therefore, the time-reversal operator $P_\mathcal{T}$ is realized by complex-conjugation $(\cdot)^\dagger$.

A difficulty arises: Complex-conjugation is an *anti-unitary* operation and the addition of $\mathcal{T}$ to C_N leads to the theory of non-unitary groups, see [6, Chap. 13] for a thorough treatment. The non-unitary group with added $\mathcal{T}$-symmetry has a left coset decomposition

$$\bar{\mathrm{G}} = \mathrm{G} + \mathcal{T}\mathrm{G} \, , \tag{86}$$

where G is a normal subgroup. In this work it suffices that $\mathcal{T}$ does not add another symmetry label (in the form of another irrep.), but pairs two irreps. with each other. As in Sec. 2.7 an eigenfunction belonging to a 1D irrep. j transforms under a symmetry operation R as

$$P_g \hat{p}_j = D_j \left(g\right) \hat{p}_j \, . \tag{87}$$

Applying the time-reversal operator $P_\mathcal{T}$ yields

$$P_\mathcal{T} \, D_j \left(g\right) \hat{p}_j = D_j^\dagger \left(g\right) \hat{p}_j^\dagger \, . \tag{88}$$

As an example, consider C_4 in Tab. 7 and its four irreps. $j = 1, 2, 3, 4$. For $j = 1, 2$ the representation matrices are real, and the time-reversal has no effect

$$D_j^\dagger \left(g\right) = D_j \left(g\right) \, , \forall g \in \mathrm{C}_4 \, , \tag{89}$$

For $j = 3$ the situation is different

$$D_3^\dagger \left(g\right) = D_4 \left(g\right) \, , \forall g \in \mathrm{C}_4 \, , \tag{90}$$

as the matrices belonging to $j = 3$ are complex-conjugate to matrices in $j = 4$. Both of them form a *time reversal symmetry pair* according to [23, p. 408]. Consequently, there are two irreps. belonging to the same eigenvalue and the eigenvalue is two-fold degenerate.

As an example consider the case depicted in Figure 6. This case employs the same parameters as [13] but a field of the speed of sound and flame zones are chosen, such that every unit cell does not exhibit a mirror symmetry, akin to the schematic in Fig. 4. Consequently, the symmetry group is C_{16}. At first the problem is self-adjoint and a degenerate mode is found on the real line. As the flames are 'switched' on, the hermicity is lost and the degenerate modes split Fig. 6c. In quantum mechanics this is known as *Kramer degeneracy* [6, p. 294] and the equivalent to adding an active flame is the imposition of a magnetic field.

3.7. Nonlinearity in the eigenvector

Equation (67) can be valid even for a wave function $\hat{p}\left(\mathbf{r}\right)$ describing the mode shape in a limit cycle oscillation, e.g. a standing wave of order $m = 2$. However, such a function is a solution to a *nonlinear eigenvector* problem $\mathcal{N}\left(\omega, \hat{p}\right) = 0$. To the best of the authors' knowledge, a symmetry operator P_R does not necessarily commute with $\mathcal{N}\left(\cdot, \cdot\right)$ – a necessary condition in Sec. 2.4. Thus, even if $\mathcal{N}\left(\cdot, \cdot\right)$ is invariant under a symmetry operation $R \in \mathrm{sym}\left(\mathcal{N}\right)$, this does not imply that the eigenfunction $\hat{p}\left(\mathbf{r}\right)$ can be written in terms of irreps of R. In [19] Mensah et al. exploit Bloch wave theory for a spinning limit cycle oscillation, for which $[P_R, \mathcal{N}] = 0$.

Table 7: Character table for the cyclic group C_4 as encountered in the literature [23, App. A]. All classes have one element; all irreps. are 1D and equal to their characters. If the system exhibits $\mathcal{T}$-symmetry, the irreps. Γ_3 and Γ_4 are paired via complex-conjugation. In quantum mechanics $\mathcal{T}$-symmetry is encountered so frequently, that in the character tables of groups curly brackets indicate time reversal symmetry pairs, here via the letter E.

	C_4	E	C_4	C_4^2	C_4^3
	Γ_1	1	1	1	1
	Γ_2	1	−1	1	−1
E	Γ_3	1	−i	−1	i
E	Γ_4	1	i	−1	−i

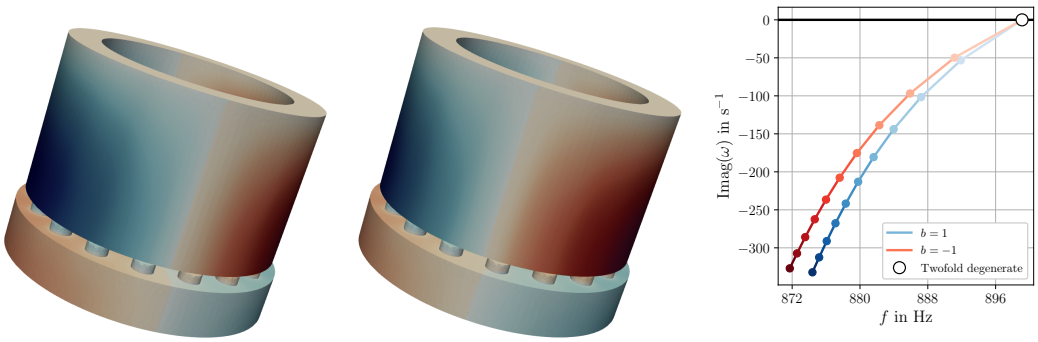

(a) (b) (c)

Figure 6: a) and b): Degenerate mode pair in the Micca combustor as featured in [13]. The normalized real part is depicted. The mode is of azimuthal order $m = 1$ and dominant in the combustion chamber. c): The $\mathcal{T}$-symmetric system exhibits a degenerate mode. As the active flame is activated the system loses $\mathcal{T}$-symmetry and the degenerate eigenvalue splits. The color of the line corresponds to the value of $s \in [0, 1]$. The split is very weak with $\Delta f = 2.67\,\mathrm{Hz}$ at $n = 1$. Both eigenvalues can individually be obtained via Bloch computations with $b = +1, -1$.

4. Point group of an annular combustion chamber exhibiting mirror symmetry

Consider the collection of points $\mathbf{r}^0 \in \mathbb{R}^2$, which form a half cell for an annulus with $N = 16$ burners, see Fig. 7. There are $M = 2\,N$ identical half cells which form the full annular combustor. In the following, the symmetry group of this combustor is derived in a systematic way by defining a set of lattice operations which, applied to $\mathbf{r}^0$, yield the full lattice. Then it is proven that the set forms a group, its character table is derived and its name in Schönfliess notation given.

In counter-clockwise direction, the second cell can be obtained by performing a mirror operation of the half cell in the vertical $x-z$ plane, denoted as σ_v, see Fig. 7. Denote as C_M a rotation that shifts the original half-cell onto the subsequent one. It is not a covering operation. A third cell is obtained by performing the rotation twice C_M^2 but no mirroring. For the fourth cell, mirroring σ_v is followed by C_M^2. The pattern that emerges is summarised in Tab. 8. Notice that the mirroring plane σ_v is fixed, as depicted in Fig. 7. Successive application of the symmetry operations yields the full annular combustion chamber.

Are these all symmetry operations? Yes. Due to the systematic approach every half cell has a distinct label going from 'zero' to $M - 1$ counterclockwise. The order of these has to be retained by any symmetry operation, i.e. 'zero' has neighbors 'one' (counterclockwise) and $M - 1$ (clockwise) and so forth. In total, there are only M distinct ways of orienting this chain of numbers. The set of all M operations in Tab. 8 is called L_M ('Lattice group') for now. This is a non-standard name and the correct group name, C_{Nv} in Schönfliess notation, is identified later. This derivation also shows that symmetry groups are the groups of all permutations of a finite set.

Table 8: Symmetry operations for the half cell. The index k labels the half cells in counter-clockwise direction.

$k = 0$	E
$k = 1$	σ_v
$k = 2$	C_M^2
$k = 3$	$C_M^2\,\sigma_v$
$k = 4$	C_M^4
$k = 5$	$C_M^4\sigma_v$
$k = 6$	C_M^6
$\vdots$	$\vdots$
$k = M-1$	$C_M^k\sigma_v$
$k = M$	$C_M^k = E$

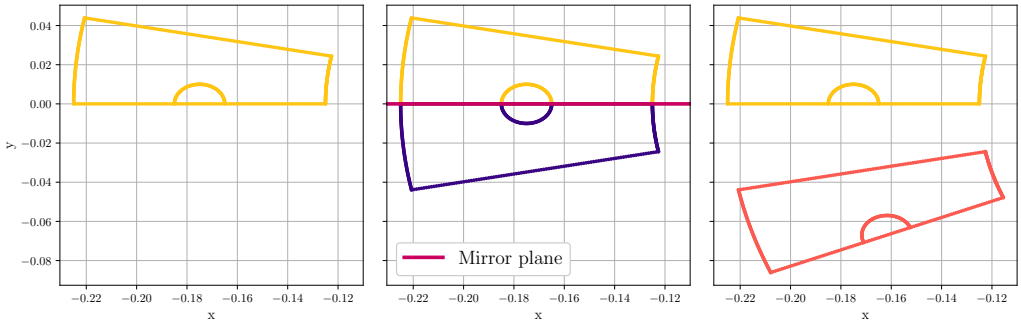

Figure 7: Left: One out of the $M = 2\,N$ half cells in a combustor with N burners. Middle: Mirroring operation σ_v to obtain the second cell. Right: Rotation (or also translation) operation C_{16}^2 to obtain the third cell.

4.1. A group L_8 *for an annular combustor with four burners*

To make the algebraic derivations simpler and an example of L_M with $N = 4$ is considered, see Fig. 8a. The set is written as

$$\mathrm{L}_8 = \left\{E, \sigma_v, C^2, C^2\sigma_v, C^4, C^4\sigma_v, C^6, C^6\sigma_v\right\}\,, \tag{91}$$

where the subscript for the rotational operations C_M (here C_8) is dropped for brevity. The multiplication table is given in Tab. 9. Every element only appears once in every column and row. Therefore, the rearrangement theorem [6, Chap. 2.4] holds and closure, existence of identity and existence of inverse are given. The mirroring and rotation operations can be represented by matrices. Since matrix multiplication is associative, L_8 is a group by extension. However, the multiplication table is not symmetric and thus elements of L_8 do not commute, e.g. $\sigma_v C^2 = C^6\sigma_v \neq C^2\sigma_v$. Thus, L_8 is not an Abelian group.

4.2. Group structure of L_8

Which properties does L_8 have and what is the structure of L_8? First, the class structure is derived. Two elements a and b are conjugate to each other if there exists and element g such that

$$b = g\,a\,g^{-1}\,. \tag{92}$$

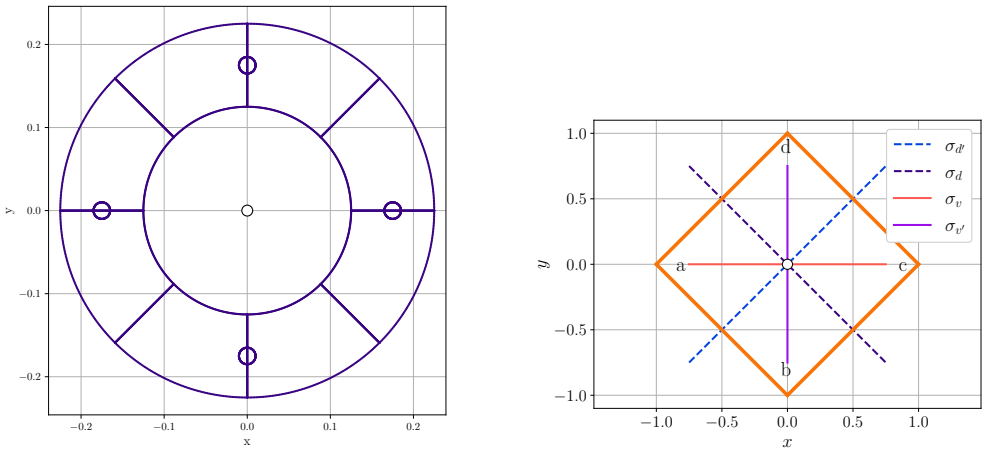

(a) (b)

Figure 8: Left: Top view of a combustor with $N = 4$ burners, which themselves exhibit a mirror symmetry. Right: The square and its covering operations leading to the symmetry group D_4 in 2D. The four mirror planes are specified. In addition, rotations by π (and multiples thereof) are possible.

Table 9: Multiplication table for the group L_8 with $N = 4$ burners and eight unit cells.

	E	σ_v	C^2	$C^2\sigma_v$	C^4	$C^4\sigma_v$	C^6	$C^6\sigma_v$
E	E	σ_v	C^2	$C^2\sigma_v$	C^4	$C^4\sigma_v$	C^6	$C^6\sigma_v$
σ_v	σ_v	E	$C^6\sigma_v$	C^6	$C^4\sigma_v$	C^4	$C^2\sigma_v$	C^2
C^2	C^2	$C^2\sigma_v$	C^4	$C^4\sigma_v$	C^6	$C^6\sigma_v$	E	σ_v
$C^2\sigma_v$	$C^2\sigma_v$	C^2	σ_v	E	$C^6\sigma_v$	C^6	$C^4\sigma_v$	C^4
C^4	C^4	$C^4\sigma_v$	C^6	$C^6\sigma_v$	E	σ_v	C^2	$C^2\sigma_v$
$C^4\sigma_v$	$C^4\sigma_v$	C^4	$C^2\sigma_v$	C^2	σ_v	E	$C^6\sigma_v$	C^6
C^6	C^6	$C^6\sigma_v$	E	σ_v	C^2	$C^2\sigma_v$	C^4	$C^4\sigma_v$
$C^6\sigma_v$	$C^6\sigma_v$	C^6	$C^4\sigma_v$	C^4	$C^2\sigma_v$	C^2	σ_v	E

Elements a and b are said to be in the same conjugacy class. The relation Eq. (92) is evaluated by looping over all elements in L_8 as a and then looping over all elements as g. The result is depicted in Tab. 11. After the trivial first row, the second row is obtained via

$$\sigma_v\,\sigma_v\,(\sigma_v)^{-1} = \sigma_v \tag{93}$$

$$C^2\,\sigma_v\,\left(C^2\right)^{-1} = C^4\sigma_v \tag{94}$$

$$\vdots = \vdots \tag{95}$$

The five (conjugate) classes are then the sets of unique elements in every respective row of Tab. 11 and

Table 10: Inverse elements summarized, as specified in Tab. 9.

g	E	σ_v	C^2	$C^2\sigma_v$	C^4	$C^4\sigma_v$	C^6	$C^6\sigma_v$
g^{-1}	E	σ_v	C^6	$C^2\sigma_v$	C^4	$C^4\sigma_v$	C^2	$C^6\sigma_v$

Table 11: Calculation of the conjugate classes for L_8. Notice that the bottom three rows are redundant, after the first five have been specified.

	E	σ_v	C^2	$C^2\sigma_v$	C^4	$C^4\sigma_v$	C^6	$C^6\sigma_v$
E	E	E	E	E	E	E	E	E
σ_v	σ_v	σ_v	$C^4\sigma_v$	$C^4\sigma_v$	σ_v	σ_v	$C^4\sigma_v$	$C^4\sigma_v$
C^2	C^2	C^6	C^2	C^6	C^2	C^6	C^2	C^6
$C^2\sigma_v$	$C^2\sigma_v$	$C^6\sigma_v$	$C^6\sigma_v$	$C^2\sigma_v$	$C^2\sigma_v$	$C^6\sigma_v$	$C^6\sigma_v$	$C^2\sigma_v$
C^4	C^4	C^4	C^4	C^4	C^4	C^4	C^4	C^4
$C^4\sigma_v$	$C^4\sigma_v$	$C^4\sigma_v$	σ_v	σ_v	$C^4\sigma_v$	$C^4\sigma_v$	σ_v	σ_v
C^6	C^6	C^2	C^6	C^2	C^6	C^2	C^6	C^2
$C^6\sigma_v$	$C^6\sigma_v$	$C^2\sigma_v$	$C^2\sigma_v$	$C^6\sigma_v$	$C^6\sigma_v$	$C^2\sigma_v$	$C^2\sigma_v$	$C^6\sigma_v$

given as

$$\mathcal{C}_1 = \{E\} \,, \tag{96}$$
$$\mathcal{C}_2 = \left\{\sigma_v, C^4\sigma_v\right\} \,, \tag{97}$$
$$\mathcal{C}_3 = \left\{C^2, C^6\right\} \,, \tag{98}$$
$$\mathcal{C}_4 = \left\{C^2\sigma_v, C^6\sigma_v\right\} \,, \tag{99}$$
$$\mathcal{C}_5 = \left\{C^4\right\} \,. \tag{100}$$
$$\tag{101}$$

Evidently, classes have no elements in common. By Lagrange's theorem [36, Chap. 1.4.3] the order of a subgroup must be an divisor of the order of a group. Here, $|\mathrm{L}_8| = 8$, thus possible divisors are $1, 2, 4$ and 8. Unless the group is Abelian, the number of subgroups cannot be determined from the order of the group alone and needs to be computed. The two trivial subgroups are

$$\mathrm{H}_1 = \{E\} \tag{102}$$
$$\mathrm{H}_2 = \mathrm{L}_8 \,. \tag{103}$$

By observation, a subgroup of order two is

$$\mathrm{H}_3 = \{E, C_4\} \,, \tag{104}$$

where the knowledge that C^4 is its own inverse is used to conveniently fulfill all group axioms. Other subgroups of order two are $\{E, \sigma_v\}, \left\{E, C^2\sigma_v\right\}, \left\{E, C^4\sigma_v\right\}$ and $\left\{E, C^6\sigma_v\right\}$ but only H_3 consists of complete conjugacy classes and is, hence, *normal* or *invariant* [6, Chap. 2.10]. Evidently, $\{E, \sigma_v\}$ has been encountered previously as the mirror group C_S in Sec. 2. It is also trivial to see that a subgroup of order four is

$$\mathrm{H}_4 = \left\{E, C^2, C^4, C^6\right\} \,. \tag{105}$$

The right coset decomposition of L_8 with respect to H_4 is

$$\mathrm{L}_8 = \mathrm{H}_4 + \mathrm{H}_4\sigma_v \,, \tag{106}$$

and for the left coset decomposition

$$\mathrm{L}_8 = \mathrm{H}_4 + \sigma_v \mathrm{H}_4 \,, \tag{107}$$

which shows that the left and right cosets are identical for a normal subgroup. H_4 is evidently a cyclic group C_N of order four as detailed in the previous Section 3. More normal subgroups of order 4 can be obtained, for instance

$$\mathrm{H}_5 = \left\{E, \sigma_v, C^4, C^4\sigma_v\right\} \,, \tag{108}$$

$$\mathrm{H}_6 = \left\{E, C^2\sigma_v, C^4, C^6\sigma_v\right\} \,, \tag{109}$$

and H_3 together with any of the subgroups of order two also forms a normal subgroup of order 4. Only the normal subgroup C_4 is relevant in the following. Since C_4 is a normal subgroup a *factor* (or *quotient*) group [6, Chap. 2.11] can be defined

$$\mathrm{L}_8/\mathrm{C}_4 = \{E, \sigma_v\} \,, \tag{110}$$

whose elements are the cosets. The elements of the factor group are formed by the cosets themselves

$$\mathrm{L}_8/\mathrm{C}_4 = \{\mathrm{C}_4, \mathrm{C}_4\sigma_v\} \,, \tag{111}$$

and a quick computation yields the Multiplication table 12. However, the existence of the factor group does not imply that L_8 can be formed as a *direct product* [6, Chap. 2.12] of C_4 and C_S

$$\mathrm{L}_8 \neq \mathrm{C}_4 \times \mathrm{C}_S \,, \tag{112}$$

because the elements of the two groups do not commute.

Table 12: Multiplication table of factor group $\mathrm{L}_8/\mathrm{C}_4$.

	C_4	$\mathrm{C}_4\sigma_v$
C_4	C_4	$\mathrm{C}_4\sigma_v$
$\mathrm{C}_4\sigma_v$	$\mathrm{C}_4\sigma_v$	C_4

4.3. Irreducible representation for L_8

The operations C and σ_v are conventional rotations and reflections, respectively. Hence, these can be represented by matrices in a Cartesian basis as

$$C \doteq \mathrm{Rot}\,(\Delta\phi) = \begin{pmatrix} \cos(\Delta\phi) & -\sin(\Delta\phi) \\ \sin(\Delta\phi) & \cos(\Delta\phi) \end{pmatrix} \,, \tag{113}$$

and

$$\sigma_v \doteq \mathrm{Refl}_{xz} = \begin{pmatrix} 1 & 0 \\ 0 & -1 \end{pmatrix} \,, \tag{114}$$

with a fixed $\Delta\phi = 2\pi/M$. The rotation operation is always employed at least in squared fashion and so

$$C^2 \doteq \mathrm{Rot}^2\,(\Delta\phi) = \begin{pmatrix} \cos(2\Delta\phi) & -\sin(2\Delta\phi) \\ \sin(2\Delta\phi) & \cos(2\Delta\phi) \end{pmatrix} = \mathrm{Rot}\,(2\Delta\phi) \,. \tag{115}$$

The representation matrices for all group elements of L_8 are then written as

$$E \doteq \begin{pmatrix} 1 & 0 \\ 0 & 1 \end{pmatrix} \tag{116}$$

$$\sigma_v \doteq \begin{pmatrix} 1 & 0 \\ 0 & -1 \end{pmatrix} \tag{117}$$

$$C^2 \doteq \mathrm{Rot}\,(2\Delta\phi) \tag{118}$$

$$C^2\sigma_v \doteq \mathrm{Rot}\,(2\Delta\phi)\,\mathrm{Refl}_{xz} \tag{119}$$

$$C^4 \doteq \mathrm{Rot}\,(4\Delta\phi) \tag{120}$$

$$C^4\sigma_v \doteq \mathrm{Rot}\,(4\Delta\phi)\,\mathrm{Refl}_{xz} \tag{121}$$

$$C^6 \doteq \mathrm{Rot}\,(6\Delta\phi) \tag{122}$$

$$C^6\sigma_v \doteq \mathrm{Rot}\,(6\Delta\phi)\,\mathrm{Refl}_{xz} \tag{123}$$

Is this representation reducible? This can be answered by computing the characters of the representation, see Tab. 13. Choose two irreps. i and j and sum over all classes

Table 13: Characters for the representations Eqs. (116)-(123).

	E	σ_v	C^2	$C^2\sigma_v$	C^4	$C^4\sigma_v$	C^6	$C^6\sigma_v$
$\mathrm{Tr}\,(\cdot)$	2	0	$2\cos(\pi/2)$	0	$2\cos(\pi)$	0	$2\cos(3\pi/2)$	0

$$\sum_c^{n_\mathrm{C}} e_c \chi_i\,(g_c)\;{\chi_j}^\dagger\,(g_c) = |\mathrm{G}|\delta_{ij}\,, \tag{124}$$

a property that is called *first orthogonality* of characters [6, p. 62]. g_c is any one element in a class and e_c the number of elements in that class. This is a row-wise orthogonality in a character table. This relation expresses that for $i = j$ the squared sum of all traces must be equal to the order of the group. For the chosen representation one obtains

$$2^2 + 0 + (-2)^2 + 0 = 8 = |\mathrm{L}_8|\,. \tag{125}$$

Hence, the chosen representation is in fact irreducible. Otherwise, the sum on the left hand side would be not equal to $|\mathrm{L}_8|$. Consequently, one irrep. of L_8 has been obtained, which is even two-dimensional. Modes associated with this irrep. are twofold degenerate.

4.4. Character table for L_8

The group L_8 has five classes. Thus, the number of in-equivalent irreducible representations is five as well, see [6, Chap. 4.6.1]. Elements belonging to the same class have the same characters [6, Chap. 4.6]. A *second orthogonality* of characters [6, p. 62] holds for a sum over all irreps. n_IR. Hereby choose an element g_c from one class and an element $g_{c'}$ from another class

$$\sum_{i=1}^{n_\mathrm{IR}} \chi_i\,(g_c)\;{\chi_i}^\dagger\,(g_{c'}) = \delta_{cc'}\frac{|\mathrm{G}|}{e_c}\,. \tag{126}$$

This is a column-wise orthogonality in a character table. For the first class, the identity element E with $e_c = 1$, one obtains

$$\sum_{i=1}^{n_\mathrm{IR}} d_i^2 = |\mathrm{G}|\,. \tag{127}$$

Table 14: Character table for the lattice group L_8.

	E	$\{\sigma_v, C^4\sigma_v\}$	$\{C^2, C^6\}$	$\{C^2\sigma_v, C^6\sigma_v\}$	$\{C^4\}$
χ_1	1	1	1	1	1
χ_2	1	1	-1	-1	1
χ_3	1	-1	1	-1	1
χ_4	1	-1	-1	1	1
χ_5	2	0	0	0	-2

This yields with the known trivial irrep. $d_0 = 1$

$$7 = d_1^2 + d_2^2 + d_3^2 + d_4^2 \,. \tag{128}$$

The only way to satisfy this is by choosing $d_1 = 1, d_2 = 1, d_3 = 1, d_4 = 2$. The choice itself is arbitrary, but by convention the highest dimension is chosen as the final row. This yields together with the trivial first row all black-colored digits in Tab. 14. In addition the characters for the fifth irrep. can be filled in from the result of the previous section.

Consider the three unknown 1D irreps. All elements $g \in \{E, \sigma_v, C^2\sigma_v, C^4, C^4\sigma_v, C^6\sigma_v\}$ are their own inverses and thus by the homomorphism theorem Eq. (49)

$$\chi_j\left(g^2\right) = \chi_j\left(E\right) = \chi_j\left(g\right)\chi_j\left(g\right) = \chi_j^2\left(g\right) \,, \tag{129}$$

and hence

$$1 = \chi_j^2\left(g\right) \,. \tag{130}$$

The multiplication table gives

$$\sigma_c C^4 \sigma_v = C^4 \,, \tag{131}$$

and by the homomorphism theorem

$$\chi\left(\sigma_v\right)\chi\left(C^4\sigma_v\right) = \chi\left(C^4\right) \,. \tag{132}$$

Both elements in the left hand side belong to the same class and must have the same character. Even though this could be $+1$ or -1 it still holds

$$1 = \chi_j\left(C^4\right) \,, \tag{133}$$

which is valid for all 1D irreps. and gives the blue digits in Tab. 14. With this result, row orthogonality between the first $i = 1$ and any of the other three rows $j = 2, 3, 4$ gives

$$-1 = \chi_j\left(\sigma_v\right) + \chi_j\left(C^2\right) + \chi_j\left(C^2\sigma_v\right) \,. \tag{134}$$

In order to fulfill this equation, two characters have to be $+1$ and one character -1 and thus the red digits in Tab. 14 are obtained. If the characters of $j = 5$ were unknown they could be computed by using column orthogonality and choosing $c = E$ while looping over all other classes.

4.5. Is L_8 isomorphic to C_{4v} or D_4?

The character Table 14 is known and is, in fact, the character table of the *dihedral* group D_4 (in Schönflies notation), a 2D point group. Dihedral groups in 2D are also known as the group of symmetries of regular n-polygons. See Figure 8b for the depiction of a square that exhibits the same symmetries as a 2D annular combustion chamber with $N = 4$ burners.

The situation is a little nebulous when point group notations and definitions are employed. In the derivation so far, symmetry properties in 2D have been studied exclusively – the third dimension was

Table 15: Character table for C_{4v} as commonly encountered in the literature. Every symmetry element represents a class and the given number specifies the number of elements in said class, i.e. 2 for C_4 (which includes rotation C_4^3). The labelling of the irreps. is not consistent in the literature. In this work Γ_j is used but sometimes letters A, B, E, F etc. are chosen. A and B for one-dimensional irreps. while E is for two-dimensional irreps. and so on, see [37, Chap. 4].

C_{4v}		E	$2\,C_4$	C_4^2	$2\,\sigma_v$	$2\,\sigma_d$
A_1	Γ_1	1	1	1	1	1
A_2	Γ_2	1	1	1	−1	−1
B_1	Γ_3	1	−1	1	1	−1
B_2	Γ_4	1	−1	1	−1	1
E	Γ_5	2	0	−2	0	0

neglected since annular combustion chambers do not exhibit a symmetry in this direction. In 2D the constructed lattice group L_8 is isomorphic to the abstract group D_4. However, once the combustor is considered in 3D – even if this does not add any symmetry – the resulting point group is denoted as C_{4v} and *not* D_4. The examples in the wikipedia article on 3D point groups clarify the difference between D_n and C_{Nv}.

This is purely an issue of naming convention. In our application the distinction is important because character tables and irreps. for abstract groups are tabulated in textbooks or generated automatically by online tools. Hence, the tables for the symmetry group of an annular combustor with N burners, C_{Nv} can be looked up/generated. Depending on the source, the term 'point group' alone can imply 3D. This is due to the fact that most of the applications of point groups are of 3D-type in quantum mechanics and quantum chemistry. Consequently, online tools that generate character tables for point groups of arbitrary order will (likely) focus on 3D. The 2D point groups are also known as 'Rosette groups´.

Comparison between the derived character table 14 and the one from literature 15 shows that symmetry operations have a naming convention themselves. The operation C^2 (C_8^2 with subscript) is denoted as C_4. Operation $C^4\sigma_v$ is another vertical mirroring operation going through the center off an annular combustor segment and denoted as $\sigma_{v'}$.The operations $C^2\sigma_v, C^6\sigma_v$ are vertical mirroring operations as well – but off-burner, i.e. planes between annular segments and denoted as $\sigma_d, \sigma_{d'}$. Figure 8b makes the distinction between σ_v and σ_d clear.

4.6. Irreps. of C_{4v} and associated azimuthal mode orders m

C_{4v} has five irreps. $j = 1, 2, 3, 4, 5$ including a two-dimensional one. These are the correct labels for eigenpairs $(\omega, \hat{p})$. How does the notion of an azimuthal mode order tie in here? Can an irrep. label be replaced by a specific m? These questions can be answered by considering how a function is transformed by irreps. In addition, the labelling as customary for can-annular combustors is given, since the can-annular combustor of Moon et al. [38, 39] exhibits this group – if swirlers are neglected. The characters of irrep. Γ_1 are all one

	E	$2C_4$	C_2	$2\sigma_v$	$2\sigma_d$
Γ_1	1	1	1	1	1

(135)

Consider an eigenfunction $\hat{p}$ belonging to Γ_1 (with no prior assumption on its shape) and its value at $\phi = 0$ denoted as $+1 \cdot \hat{p}$, see Fig. 9. According to the characters, a transformation by any symmetry operation leads to the same value around the circumference. Connecting the dots yields the example mode shape: A purely axial mode $m = 0$ or *push-push* mode.

Irrep. Γ_2 is more challenging due to the characters for the mirroring operations, see Fig. 8b for a depiction of the mirroring planes, and one obtains

	E	$2C_4$	C_2	$2\sigma_v$	$2\sigma_d$
Γ_2	1	1	1	−1	−1

(136)

Nominally, the rotations C_4, C_4^3 and C_2 would result in values of $+1 \cdot \hat{p}$ at the locations $\phi = \pi/2, \pi, 3\pi/2$. However, this contradicts with the mirroring operations, e.g. σ_v enforces $-1 \cdot \hat{p}$ at $\phi = \pi$. Taking this

Table 16: Labelling irreps. of C_{4v} with azimuthal mode orders m and Bloch numbers b.

C_{4v}	Γ_1	Γ_2	Γ_3	Γ_4	Γ_5
m	0	4	2	2	1
b	0	0	2	2	$-1, 1$

argumentation to its logical conclusion, only $\hat{p} = 0$ is possible at those locations. However, the mode is not the trivial one, as the mode shape in Fig. 9 depicts. In fact a mode $m = 4$ fulfills the symmetry required by the characters. There are no such conflicts for Γ_3

$$\begin{array}{c|ccccc} & E & 2C_4 & C_2 & 2\sigma_v & 2\sigma_d \\ \Gamma_3 & 1 & -1 & 1 & 1 & -1 \end{array} \tag{137}$$

and the mode is quickly identified to be a cosine function of order $m = 2$. In contrast for Γ_4

$$\begin{array}{c|ccccc} & E & 2C_4 & C_2 & 2\sigma_v & 2\sigma_d \\ \Gamma_4 & 1 & -1 & 1 & -1 & 1 \end{array} \tag{138}$$

the characters enforce $\hat{p} = 0$ at $\phi = 0, \pi/2, \pi$ and $3\pi/2$. Hence, the mode shape is a sine function of order $m = 2$. Both modes are called *push-pull* modes. In a can-annular context a standing mode belonging to Γ_4 would have nodal lines in cans and anti-nodal lines in the cross talks. The remaining irrep. is two-dimensional and yields a degenerate eigenvalue. Hence, the eigenspace is formed by two functions $\hat{p}_1(\phi)$ and $\hat{p}_2(\phi)$. As before, apply irreps. for instance for

$$\sigma_v: \quad \begin{pmatrix} 1 & 0 \\ 0 & -1 \end{pmatrix} \begin{pmatrix} \hat{p}_1 \\ \hat{p}_2 \end{pmatrix} = \begin{pmatrix} \hat{p}_1 \\ -\hat{p}_2 \end{pmatrix} \tag{139}$$

to the functions. Is this fashion a number of constraints are obtained and it can be concluded that functions $\hat{p}_1 = \cos(\phi)$ and $\hat{p}_2 = \sin(\phi)$ fulfill these – modes of order $m = 1$. In Section 4.2 it was derived that C_S and C_4 are subgroups of C_{4v}. Consequently, the Bloch numbers b can also be used to label irreps. of C_{4v}, albeit at a loss of information. Preempting a result from Sec. 5.4, the labelling is given in Tab. 16. In order to determine to which irrep. higher order modes $m > N/2$ belong, it is best to follow the procedure of Sec. 3.5 and to derive Bloch number. From b it is straightforward to obtain the irrep. number. If a mode m belongs to two Bloch numbers it is degenerate. It now becomes evident that a label m, as customary in thermoacoustics, is problematic from the perspective of symmetry groups which employs irreps.: Both labels cannot be mapped bijectively onto each other.

4.7. Higher order degeneracies and generalization to arbitrary N

Except for a specifically designed experiment, a degeneracy of higher order than two is not relevant for practical thermoacoustic systems. A threefold degeneracy would require a symmetry group with at least one 3D irrep. The group of lowest order with this property is the tetrahedral point group T associated with an equilateral tetrahedron – an impractical burner arrangement. Since combustion systems have a dedicated main flow direction this alone excludes symmetries in that direction.

Can a C_{Nv} of arbitrary order exhibit a 3D (or higher) irrep.? No. The answer touches upon bound estimates for the number of classes in finite groups of arbitrary order [40]. Here it suffices that Ito [41] published a result that can be applied. Any C_{Nv} has an Abelian normal subgroup C_N of order N (the maximal Abelian subgroup). The number of left and right cosets is called the *index* and given as

$$[C_{Nv} : C_N] = \frac{|C_{Nv}|}{|C_N|} = 2\,. \tag{140}$$

According to Ito [41] the dimension (called *degree*) of C_{Nv} must be a divisor of the index. Thus, only 1D and 2D irreps. are possible.

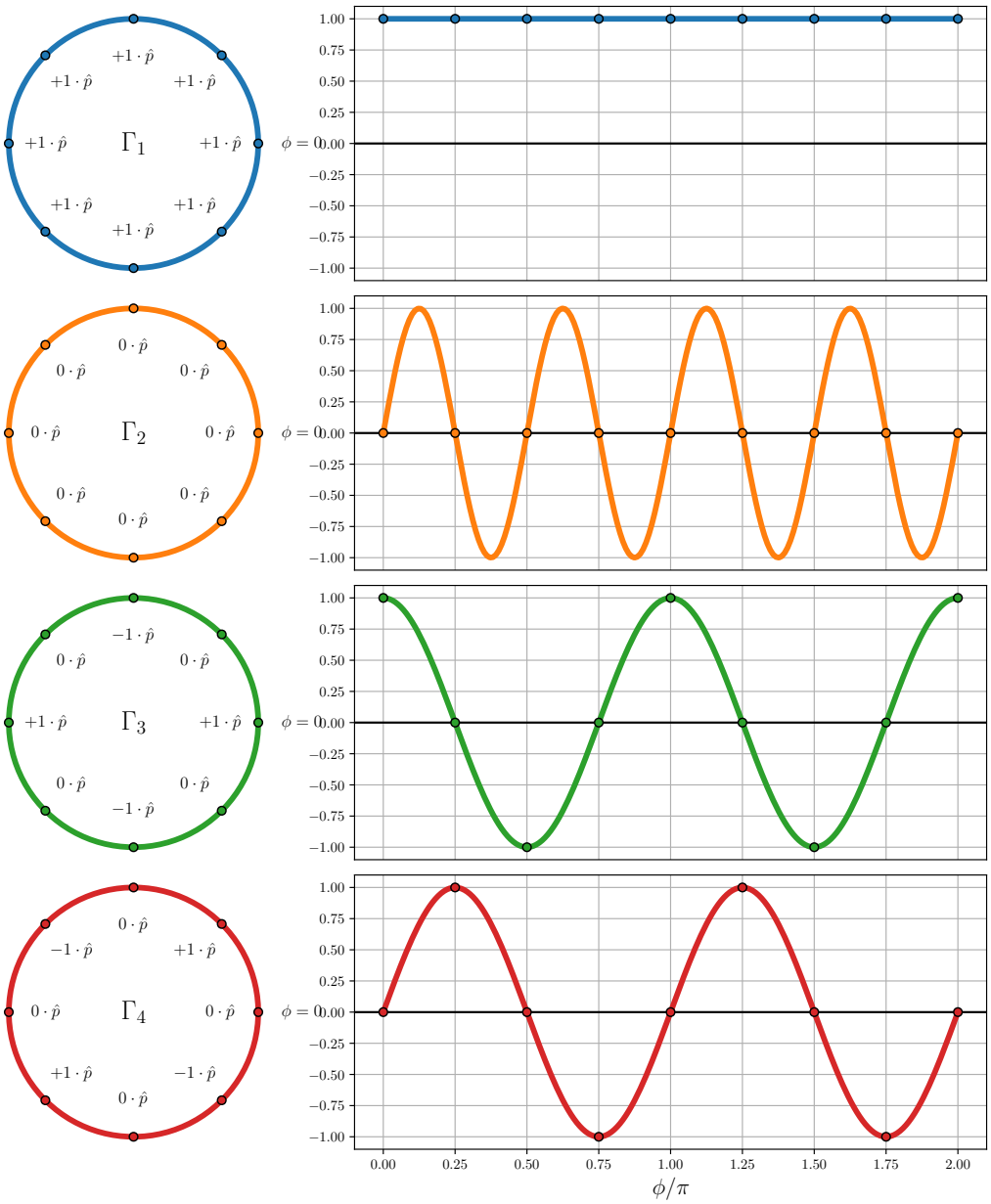

Figure 9: From top until bottom: Irreps. $\Gamma_1, \Gamma_2, \Gamma_3$ and Γ_4 (left) and their characters. Example mode shapes (right) over azimuthal coordinate ϕ.

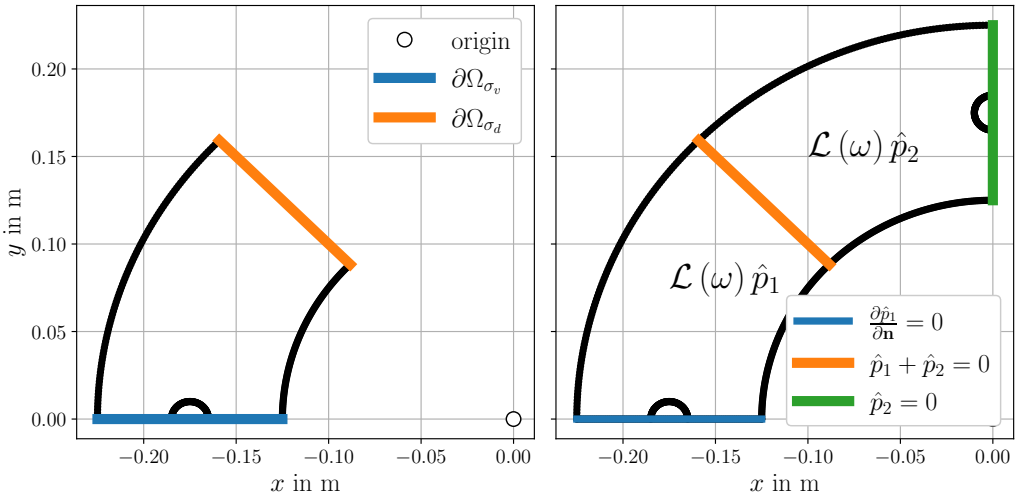

Figure 10: Left: Boundaries for the half cell. Right: The coupled problem to compute both eigenvectors $\hat{p}_1, \hat{p}_2$ of the degenerate pair.

Can $\mathcal{T}$-symmetry couple two irreps. of C_{Nv} into a 3D or 4D irrep.? Also No. Because Wang et al. [42] proved that boundedness of the index by two implies that all irreps. are real-valued and, hence, cannot form complex-conjugate pairs. Notice that the index for C_{16} with a subgroup C_8 is also two. Ito's bound does not prohibit a 2D irrep. but the Abelian property does.

4.8. Exploiting the mirror symmetry to reduce computational cost?

Following Mensah's success [18] in exploiting C_N to reduce computational cost with Bloch waves, it is natural to ask: Can C_{Nv} be exploited even further? The answer in short is: Yes, but not for degenerate modes. Bossavit's papers [43, 44][7] give a machinery to formulate suitable boundary conditions in order to exploit underlying symmetry groups and it is a lone exception that treats the non-Abelian case. In this section his machinery 'Step 1. until Step 5.' [43, p. 209] is carried out for a combustor with C_{4v} symmetry. Step 1. requires listing all irreps. Γ_i of C_{4v}. According to the character table 15 all but the Γ_5 irrep. are 1D and, hence identical to their characters. The 2D irreps. of Γ_5 are readily written as

$$\Gamma_5: \quad D_5(\sigma_v) = \begin{pmatrix} 1 & 0 \\ 0 & -1 \end{pmatrix}, \quad D_5(\sigma_d) = \begin{pmatrix} 0 & -1 \\ -1 & 0 \end{pmatrix}. \tag{141}$$

In Step 2. a symmetric cell is chosen, which is the half-cell depicted in Fig. 10. Step 3. is not applicable to eigenvalues problems, since it treats the load vector, i.e. the inhomogeneous term of boundary value problems.

Step 4. is the main part. Parts of the boundaries, that are mapped onto themselves by elements g of C_{4v}, are identified according to

$$\partial\Omega_g = \left\{ \mathbf{r} \in \partial\Omega \middle| \; R_g^{-1}\mathbf{r} \in \partial\Omega \right\}. \tag{142}$$

Figure 10 shows that there are only $\partial\Omega_{\sigma_v}$ and $\partial\Omega_{\sigma_d}$. Bossavit employs a variational restriction theorem to restrict the eigenfunction $\hat{p}$ defined on the entire domain to boundaries $\partial\Omega_g$ for an irrep Γ_j. The trace

[7] The earlier paper contains a number of errors in the equations, so the later one is recommended.

operator[8] γ_j that realizes this restriction is written as

$$\gamma_j \hat{p}\left(\mathbf{r}\right) = \left\{ \hat{p}_i\left(\mathbf{r}\right) - \sum_k D_j^{ik}\left(g\right) \hat{p}_k\left(R_g^{-1}\mathbf{r}\right) \mid \;\; i = 1, \ldots, d_j \right\} , \tag{143}$$

and it holds only for eigenvalue problems that

$$\gamma_j \hat{p}\left(\mathbf{r}\right) = 0 , \tag{144}$$

which expresses that eigenvalue problems must have homogeneous boundary conditions. Here $D_j\left(g\right)$ is the irrep. matrix for a symmetry element belonging to an irrep Γ_j of dimension d_j. Notice that Eq. (143) expresses that a set of functions forms $\hat{p}$ on the respective boundary – foreboding a 2D eigenspace for a 2D irrep. with a degenerate eigenvalue. Consequently, $\gamma_j \hat{p}$ is a tuple for $d_j > 1$.

4.8.1. Boundary conditions for the 1D irreps.

For the four 1D irreps. of $\mathrm{C_{4v}}$ Eq. (143) reduces on $\partial\Omega_g$ to

$$\gamma_j \hat{p}\left(\mathbf{r}\right) = \hat{p}\left(\mathbf{r}\right) - D_j\left(g\right) \hat{p}\left(R_g^{-1}\mathbf{r}\right) = 0 , \tag{145}$$

where the superscript $i = 1$ is dropped. Starting with the identity irrep. Γ_1 on $\partial\Omega_{\sigma_v}$ one obtains

$$0 = \hat{p}\left(\mathbf{r}\right) - D_1\left(\sigma_v\right) \hat{p}\left(R_{\sigma_v}^{-1}\mathbf{r}\right) , \tag{146}$$

and re-arranging

$$\hat{p}\left(\mathbf{r}\right) = 1 \cdot \hat{p}\left(R_{\sigma_v}^{-1}\mathbf{r}\right) . \tag{147}$$

Just like in Sec. 2.7 a Taylor expansion yields a homogeneous Neumann boundary condition. The same applies to $\partial\Omega_{\sigma_d}$. In summary the conditions are given as all possible permutations of homogeneous Neumann and Dirichlet boundary conditions

$$\begin{aligned}
\Gamma_1: \quad & \hat{p}\left(\mathbf{r}\right) = +1 \cdot \hat{p}\left(R_{\sigma_v}^{-1}\mathbf{r}\right) && \rightarrow \tfrac{\partial \hat{p}}{\partial \mathbf{n}} = 0 && \text{on } \partial\Omega_{\sigma_\mathrm{v}} \\
& \hat{p}\left(\mathbf{r}\right) = +1 \cdot \hat{p}\left(R_{\sigma_d}^{-1}\mathbf{r}\right) && \rightarrow \tfrac{\partial \hat{p}}{\partial \mathbf{n}} = 0 && \text{on } \partial\Omega_{\sigma_\mathrm{d}} \\
\Gamma_2: \quad & \hat{p}\left(\mathbf{r}\right) = -1 \cdot \hat{p}\left(R_{\sigma_v}^{-1}\mathbf{r}\right) && \rightarrow \hat{p} = 0 && \text{on } \partial\Omega_{\sigma_\mathrm{v}} \\
& \hat{p}\left(\mathbf{r}\right) = -1 \cdot \hat{p}\left(R_{\sigma_d}^{-1}\mathbf{r}\right) && \rightarrow \hat{p} = 0 && \text{on } \partial\Omega_{\sigma_\mathrm{d}} \\
\Gamma_3: \quad & \hat{p}\left(\mathbf{r}\right) = +1 \cdot \hat{p}\left(R_{\sigma_v}^{-1}\mathbf{r}\right) && \rightarrow \tfrac{\partial \hat{p}}{\partial \mathbf{n}} = 0 && \text{on } \partial\Omega_{\sigma_\mathrm{v}} \\
& \hat{p}\left(\mathbf{r}\right) = -1 \cdot \hat{p}\left(R_{\sigma_d}^{-1}\mathbf{r}\right) && \rightarrow \hat{p} = 0 && \text{on } \partial\Omega_{\sigma_\mathrm{d}} \\
\Gamma_4: \quad & \hat{p}\left(\mathbf{r}\right) = -1 \cdot \hat{p}\left(R_{\sigma_v}^{-1}\mathbf{r}\right) && \rightarrow \hat{p} = 0 && \text{on } \partial\Omega_{\sigma_\mathrm{v}} \\
& \hat{p}\left(\mathbf{r}\right) = +1 \cdot \hat{p}\left(R_{\sigma_d}^{-1}\mathbf{r}\right) && \rightarrow \tfrac{\partial \hat{p}}{\partial \mathbf{n}} = 0 && \text{on } \partial\Omega_{\sigma_\mathrm{d}}
\end{aligned} \tag{148}$$

In Figure 11 the result of an eigenvalue computation of the annular combustor is depicted. Solving the PDE on the half-cell with boundary conditions Eq. (148) yields all simple eigenvalues.

4.8.2. Boundary conditions for the 2D irrep.

For the 2D irrep. Γ_5 Equation (143) is written as

$$\mathbf{0} = \left\{ \hat{p}_1\left(\mathbf{r}\right) - \sum_k D_5^{1k}\left(g\right) \hat{p}_k\left(R_g^{-1}\mathbf{r}\right), \hat{p}_2\left(\mathbf{r}\right) - \sum_k D_5^{2k}\left(g\right) \hat{p}_k\left(R_g^{-1}\mathbf{r}\right) \right\} . \tag{149}$$

[8] For a definition for Sobolev space see [45, Chap. 6.6].

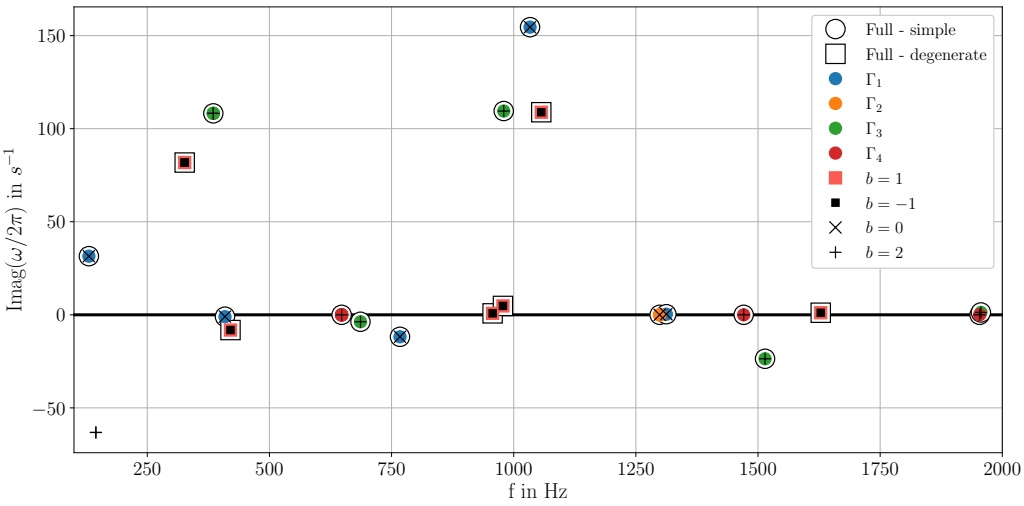

Figure 11: Eigenvalues for the full, half-cell and unit-cell computation. Solving the half-cell with boundary conditions (148) yields all simple eigenvalues. Bloch computation on the unit-cell returns the degenerate eigenvalues but does not classify them as such. Knowing that $b = 1$ and $b = -1$ return the same eigenvalue is enough to identify it as degenerate. All eigenvalues are labelled by irreps. including eigenvalues of intrinsic origin.

and clearly Eq. (149) can be written as

$$\begin{pmatrix} \hat{p}_1 \\ \hat{p}_2 \end{pmatrix} = D_5\left(g\right) \begin{pmatrix} \hat{p}_1 \\ \hat{p}_2 \end{pmatrix} . \tag{150}$$

For $\partial\Omega_{\sigma_v}$ one obtains

$$\begin{pmatrix} \hat{p}_1 \\ \hat{p}_2 \end{pmatrix} = D_5\left(\sigma_v\right) \begin{pmatrix} \hat{p}_1 \\ \hat{p}_2 \end{pmatrix} = \begin{pmatrix} \hat{p}_1 \\ -\hat{p}_2 \end{pmatrix} , \tag{151}$$

which yields homogeneous boundary conditions again

$$\begin{aligned} \hat{p}_1\left(\mathbf{r}\right) &= +1 \cdot \hat{p}_1\left(R^1_{\sigma_v}\mathbf{r}\right) \rightarrow \frac{\partial \hat{p}_1}{\partial \mathbf{n}} = 0 \\ \hat{p}_2\left(\mathbf{r}\right) &= -1 \cdot \hat{p}_2\left(R^{-1}_{\sigma_v}\mathbf{r}\right) \rightarrow \hat{p}_2 \quad = 0 \end{aligned} \tag{152}$$

However, the problem is different for $\partial\Omega_{\sigma_d}$

$$\begin{pmatrix} \hat{p}_1 \\ \hat{p}_2 \end{pmatrix} = D_5\left(\sigma_d\right) \begin{pmatrix} \hat{p}_1 \\ \hat{p}_2 \end{pmatrix} = \begin{pmatrix} -\hat{p}_2 \\ -\hat{p}_1 \end{pmatrix} , \tag{153}$$

where the problems become coupled via the boundaries

$$\hat{p}_1\left(\mathbf{r}\right) = -\hat{p}_2\left(R^{-1}_{\sigma_d}\mathbf{r}\right) , \tag{154}$$

$$\hat{p}_2\left(\mathbf{r}\right) = -\hat{p}_1\left(R^{-1}_{\sigma_d}\mathbf{r}\right) , \tag{155}$$

which yields

$$\hat{p}_1 + \hat{p}_2 = 0 \quad \text{on} \quad \partial\Omega_{\sigma_d} . \tag{156}$$

How to use this? One *could* formulate numerically two identical domains – one for $\hat{p}_1$ and one for $\hat{p}_2$ – connected at $\partial\Omega_{\sigma_d}$ and enforce Eq. (156) there. The sub problems would have boundary conditions Eq. (152) on their respective domains, see Fig. 10. Bossavit also notes in [44, p. 1368]: "Solving a *coupled* problem is the only way to do this." (emphasis his). Choosing a different representation instead of Eq. (141) leads to different boundary conditions but does not remove the coupling. Such a procedure could make sense for boundary value problems, which can have non-homogeneous boundary conditions.

However, there is little purpose in implementing such a constraint numerically in a thermoacoustic context, when a computation can be conducted on the unit cell using Bloch boundary conditions instead. It is expected that the constraint Eq. (156) requires an iterative procedure to be enforced. Degenerate modes belonging to Γ_5 also have the Bloch numbers $b = 1, -1$ and can, thus, be computed on a unit cell, see Fig. 11 which also gives the eigenvectors.

4.9. Parity property connects Bloch numbers: Kramer's Theorem

This section gives a formal proof that modes belonging to Bloch numbers $-b$ and $+b$ have the same eigenvalue for groups C_{Nv}. Mensah et al. [18] give a short proof but use the property $u_b(-\mathbf{r}) = u_{-b}(\mathbf{r})$, which is a consequence of the proof and should not be presupposed. Applying the parity operator P_{σ_v} to the eigenvalue problem and using commutation yields

$$P_{\sigma_v}\mathcal{L}(\omega_b)\hat{p}_b(\mathbf{r}) = \mathcal{L}(\omega_b)P_{\sigma_v}\hat{p}_b(\mathbf{r}) = 0\,. \tag{157}$$

Since $\mathcal{L}(\omega_b)\hat{p}_b(\mathbf{r}) = 0$ by definition, it must also hold that

$$\mathcal{L}(\omega_b)P_{\sigma_v}\hat{p}_b(\mathbf{r}) = 0\,, \tag{158}$$

and $P_{\sigma_v}\hat{p}_b(\mathbf{r})$ is an eigenvector to eigenvalue ω_b. If $P_{\sigma_v}\hat{p}_b(\mathbf{r})$ and $\hat{p}_b(\mathbf{r})$ are linearly independet, the eigenvalue is degenerate. Next, apply the rotation operator (here translation is a better word) to the newly created vector and using the definition of a Bloch function Eq. (60) plus the character of the rotation operator Eq. (58)

$$P_{C_N^n}P_{\sigma_v}\hat{p}_b(\mathbf{r}) = P_{C_N^n}\hat{p}_b(-\mathbf{r}) = P_{C_N^n}e^{+\mathrm{i}b\phi}u_b(-\mathbf{r}) = e^{\mathrm{i}b\left(\phi-\frac{2\pi}{N}n\right)}u_b\left(-\left(\mathbf{r}-2\pi/N\mathbf{e}_\phi\right)\right)\,. \tag{159}$$

The function $u_b(\mathbf{r})$ is periodic on the unit cell and thus

$$P_{C_N^n}P_{\sigma_v}\hat{p}_b(\mathbf{r}) = e^{-\mathrm{i}\left(2\pi\frac{b}{N}n\right)}e^{\mathrm{i}b\phi}u_b(-\mathbf{r})\,, \tag{160}$$

$$= e^{-\mathrm{i}\left(2\pi\frac{b}{N}n\right)}\hat{p}_b(-\mathbf{r})\,, \tag{161}$$

$$= e^{-\mathrm{i}\left(2\pi\frac{b}{N}n\right)}P_{\sigma_v}\hat{p}_b(\mathbf{r})\,. \tag{162}$$

However, for a function belonging to an irrep. $-b$ it holds

$$P_{C_N^n}\hat{p}_{-b}(\mathbf{r}) = e^{-\mathrm{i}\left(2\pi\frac{b}{N}n\right)}\hat{p}_{-b}(\mathbf{r})\,. \tag{163}$$

Thus, $P_{\sigma_v}\hat{p}_b(\mathbf{r})$ and $\hat{p}_{-b}(\mathbf{r})$ are both eigenfunction of $P_{C_N^n}$ with the phase factor $e^{-\mathrm{i}\left(2\pi\frac{b}{N}n\right)}$ as the eigenvalue. All irreps. of $P_{C_N^n}$ are 1D and, hence, the two cannot form a degenerate pair[9] for the operator $P_{\sigma_v}\hat{p}_b(\mathbf{r})$. Therefore

$$P_{\sigma_v}\hat{p}_b(\mathbf{r}) = \hat{p}_{-b}(\mathbf{r})\,, \tag{164}$$

so that the parity property for the eigenfunctions is obtained

$$\hat{p}_b(-\mathbf{r}) = \hat{p}_{-b}(\mathbf{r})\,. \tag{165}$$

[9] The two still form a degenerate pair for $\mathcal{L}$.

Since $P_{\sigma_v}\hat{p}_b(\mathbf{r})$ is an eigenfunction to ω_b according to Eq. (158), then so must be $\hat{p}_{-b}(\mathbf{r})$. However, the latter is evidently an eigenfunction to ω_{-b} and *Kramer's Theorem* [46, p. 117] is obtained

$$\omega_b = \omega_{-b}\,. \tag{166}$$

Using the definition, parity also holds for Bloch functions

$$u_b(-\mathbf{r}) = u_{-b}(\mathbf{r})\ . \tag{167}$$

4.10. $\mathrm{C}_{Nv} = \mathrm{C}_N \times \mathcal{P}$*?*

In Figure 4 the combustor with C_N symmetry is depicted. It can be seen that from the depicted angle the combustor seems to exhibit a parity (or inversion) symmetry, i.e. a point symmetry through the origin in the xy-plane. The abstract operation is denoted as $C_{i_{xy}}$ and the matrix that implements the operation as I_{xy}, which realizes

$$I_{xy}\mathbf{r} = I_{xy}\begin{pmatrix}x\\y\\z\end{pmatrix} = \begin{pmatrix}-x\\-y\\z\end{pmatrix}\ . \tag{168}$$

However, this is not a symmetry operation that has possibly been overlooked, like the $\mathcal{T}$-symmetry in Sec. 3.6, which would introduce degeneracy by connecting irreps. Because I_{xy} has the same effect as rotating the combustor by π/N. Hence,

$$C_{i_{xy}} = C_{N/2}\,, \tag{169}$$

the operation has been accounted for. One could construct a hypothetical – and *unphysical* – situation in which a combustor would exhibit an additional mirroring symmetry in z-direction, denoted as σ_h, then the group would be C_{Nh} instead of C_N. This groups contains full inversion symmetry C_i (also in z direction) for even N with

$$I_{xyz}\mathbf{r} = -\mathbf{r}\,, \tag{170}$$

and hence, can be decomposed into

$$\mathrm{C}_{Nh} = \mathrm{C}_N \times \mathcal{P}\,,\quad N \text{ even}\ . \tag{171}$$

The parity $\mathcal{P}$ (or inversion) group only has the elements

$$\mathcal{P} = \{E, C_i\}\ , \tag{172}$$

and often appears as a subgroup of bigger groups. In essence, a combination of rotations and inversions realizes a mirroring. More details can be found in [6][Chap. 8]. To conclude this section, it holds

$$\mathrm{C}_{Nv} \neq \mathrm{C}_N \times \mathcal{P}\,. \tag{173}$$

5. Symmetry breaking due to perturbations

Symmetry groups provide a dedicated machinery to analyse the splitting of degenerate eigenvalues due to a reduction in symmetry caused by a perturbation. Assume that the original problem $\mathcal{L}_0$ is perturbed by $\mathcal{L}_1$

$$\mathcal{L} = \mathcal{L}_0 + \mathcal{L}_1\,, \tag{174}$$

such that $\mathcal{L}_1$ has lower symmetry than $\mathcal{L}_0$. 'Lower' refers to the fact that group $sym(\mathcal{L}) = \mathrm{G_p}$ must be a subgroup[10] of $sym(\mathcal{L}_0) = \mathrm{G}$. A two-fold degenerate mode belonging to an irrep. Γ_j of $\mathcal{L}_0$ can consequently split into two simple eigenvalues. The split – and if it happens or the mode stays degenerate – can be predicted merely by the knowledge of the symmetry groups before and after the perturbation. The splitting of degenerate modes in Section 3.6 is an example: Loss of $\mathcal{T}$-symmetry causes degenerate modes to split.

[10] 4.2 shows how to determine if a group is a subgroup. But these are usually listed online as well.

5.1. Recipe to predict eigenvalue splitting

In the literature the study of eigenvalue splitting is termed *(energy) level splitting* and a treatment can be found in [37, Chap. 5.6] and [23, Chap. 5.3]. An irrep. Γ_j of the unperturbed group is decomposed into irreps. Γ_α of the group with lower symmetry $sym\,(\mathcal{L}) = \mathrm{G_p}$ as

$$\Gamma_j^{\mathrm{G}} = \bigoplus_\alpha a_\alpha \Gamma_\alpha^{\mathrm{G_p}}\,, \tag{175}$$

with the coefficients given by

$$a_\alpha = \frac{1}{|\mathrm{G_p}|} \sum_{g \in \mathrm{G_p}} \chi_\alpha^\dagger\,(g)\,\chi_j\,(g)\ . \tag{176}$$

Importantly, the sum goes over all group elements. Since elements in the same class have the same character, summation can also be conducted over classes

$$a_\alpha = \frac{1}{|\mathrm{G_p}|} \sum_{c \in \mathrm{Class(G_p)}} e_c\,\chi_\alpha^\dagger\,(g_c)\,\chi_j\,(g_c)\ . \tag{177}$$

and g_c is the number of elements in the class and g_c is one (any) operation from the class. To employ these formulas character tables of G and $\mathrm{G_p}$ are needed, e.g. from [24] or [6, App. B]. Care needs to be taken in identifying elements g of the perturbed group with their counterparts in the unperturbed group, e.g. a rotation by $2\pi/4$ (or C_4) is easy to identify but for mirror operations this can be more intricate due to labelling conventions – see a later case. A derivation of Eq. (177) can be found in [23, Chap. 3.4.] or [6, Chap. 5.1.].

5.2. Loss of mirror symmetry in annular combustor

Consider the degenerate eigenvalue of the group C_{4v} belonging to irrep. $j = 5$ as the mirror symmetry is lost. As discussed previously, the resulting system only exhibits a discrete rotational symmetry $sym\,(\mathcal{L}) = \mathrm{C}_4$, which has exclusively one-dimensional irreps as listed in Tab. 7. Applying Eq. (176) yields

$$a_1 = \frac{1}{4}\left[\chi_1^\dagger\,(E)\,\chi_5\,(E) + \chi_1^\dagger\,(C_4)\,\chi_5\,(C_4) + \chi_1^\dagger\left(C_4^2\right)\chi_5\left(C_4^2\right) + \chi_1^\dagger\left(C_4^3\right)\chi_5\left(C_4^3\right)\right]\,, \tag{178}$$

$$a_1 = \frac{1}{4}\left[1\cdot 2 + 1\cdot 0 + 1\cdot(-2) + 1\cdot 0\right] = 0\,. \tag{179}$$

For the other three coefficients

$$a_2 = \frac{1}{4}\left[1\cdot 2 - 1\cdot 0 + 1\cdot(-2) - 1\cdot 0\right] = 0\,, \tag{180}$$

$$a_3 = \frac{1}{4}\left[1\cdot 2 + \mathrm{i}\cdot 0 - 1\cdot(-2) + \mathrm{i}\cdot 0\right] \ = 1\,, \tag{181}$$

$$a_4 = \frac{1}{4}\left[1\cdot 2 - \mathrm{i}\cdot 0 - 1\cdot(-2) - \mathrm{i}\cdot 0\right] \ = 1\,, \tag{182}$$

and the irrep. is decomposed into

$$\Gamma_5^{\mathrm{C}_{4v}} = \Gamma_3^{\mathrm{C}_4} \oplus \Gamma_4^{\mathrm{C}_4}\,. \tag{183}$$

Hence, the degenerate eigenvalue of azimuthal order $m = 1$ splits into two simple eigenvalues belonging to irreps. three and four, respectively. This case also corresponds to the presence of a mean-swirl in the annulus that removes the mirror symmetry. A representation of an irrep. Γ_j by irreps. of $\mathrm{G_p}$ is denoted as $\Gamma_j \downarrow \mathrm{G_p}$.

Equation (183) expresses that $\Gamma_5^{\mathrm{C}_{4v}}$ is a representation of $\mathrm{G_p}$ and is 'too big', i.e. it permits a decomposition into irreps. of $\mathrm{G_p}$. This is the origin of Eq. (176): It is a recipe to decompose representations into irreps. In Algorithm 1 instructions are given how to use a tool available online to compute the decomposition instead of using Eq. (176).

Table 17: Decomposition of the irreps. from higher to lower symmetry. Degenerate modes of C_{16v} that retain their degeneracy are highlighted in gray.

	simple				degenerate						
C_{16v}	Γ_1	Γ_2	Γ_3	Γ_4	Γ_5	Γ_6	Γ_7	Γ_8	Γ_9	Γ_{10}	Γ_{11}
C_{4v}	Γ_1	Γ_2	Γ_1	Γ_2	Γ_5	$\Gamma_3 \oplus \Gamma_4$	Γ_5	$\Gamma_1 \oplus \Gamma_2$	Γ_5	$\Gamma_3 \oplus \Gamma_4$	Γ_5

5.3. Patterns considered in the thermoacoustic literature

In Figure 12 patterns considered by Mensah et al. in [47] are depicted. The unperturbed group is C_{16v} with four one-dimensional ($j = 1, 2, 3, 4$) and seven two-dimensional irreps. ($j = 5, \dots 11$) which can be studied for splitting. The character table can be found in [48]. For Mensah et al.'s Pattern C the perturbed group only consists of the identity element and, hence, it is not studied since all degeneracies are lost.

For Pattern A the perturbed group is C_S. Like in the single sector of Sec. 2 all modes bust be either symmetric or anti-symmetric. Consequently, every degenerate mode splits into one even and one odd mode. Equation (176) shows this, by considering all $j = 5, \dots, 11$ labelling the two-dimensional irreps.

$$a_1 = \frac{1}{2}\left[\chi_1^\dagger(E)\,\chi_j(E) + \chi_1^\dagger(\sigma_v)\,\chi_j(\sigma_v)\right], \tag{184}$$

$$a_2 = \frac{1}{2}\left[\chi_2^\dagger(E)\,\chi^j(E) + \chi_2\dagger(\sigma_v)\,\chi_j(\sigma_v)\right]. \tag{185}$$

Firstly, the characters $\chi_\alpha^\dagger(E)$ are one and the characters $\chi_j(E)$ are two. Secondly, characters $\chi_j(\sigma_v)$ are all zero, see [48]. Hence, the decomposition is always $a_1 = a_2 = 1$ and

$$\Gamma_j = \Gamma_1 \oplus \Gamma_2\,, \quad j = 5, \dots 11\,. \tag{186}$$

Pattern B has more interesting implications since the perturbed group, C_{4v}, exhibits degenerate modes as well. Therefore some degeneracies are conserved under the perturbation.

In this case it is more tricky to identify elements between the two groups. In Fig. 12 (right) the symmetry planes of C_{4v} are depicted. By convention σ_v specifies vertical mirror planes. Here, these are mirror planes going through two burners (two orange ones). Diagonal mirror planes σ_d are off-burner. Clearly, what is a plane σ_d for C_{4v} is a plane σ_v for C_{16v}, since the plane is no longer off-burner. The practical consequence is that in the character table of C_{16v} the column for σ_v is used exclusively – the column with σ_d is discarded since those operations are not present in C_{4v}. Even though C_{4v} has a column labelled σ_d, but these operations are found under σ_v for C_{16v}.

In Table 17 the decomposition is depicted. The result is consistent with Mensah et al. [47]: The mode of first order belonging to Γ_5 (mode#1 in [47]) does not split under the perturbation while the mode of second order belonging to Γ_6 (mode#2 ibidem.) splits.

Algorithm 1 Using an online tool of [24] to compute the eigenvalue splitting

1: Go to Jacobs University Tool Symmetry Groups.
2: Open tabs for higher symmetry (e.g. C_{4v}) and lower symmetry (e.g. C_4.)
3: Identify classes with each other. Care needs to be taken: See Fig. 12 (right).
4: **for** all irreps. Γ_i **do**
5: Take characters from higher group (e.g. $\chi(E) = 2, \chi(2C_4) = 0, \chi(C_2) = -2$ for C_{4v})
6: Insert into reduction formula for lower group (e.g. $2, 0, -2, 0$, taking the value of $2C_4$ for C_4 and C_4^3)
7: Hit *Submit* button
8: Obtain $\Gamma_j \downarrow G_p$
9: **end for**

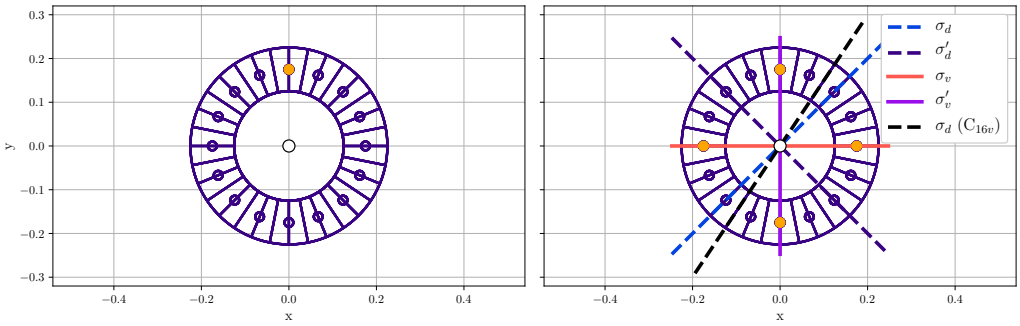

Figure 12: Perturbation patterns considered in [47] for an annular combustor with 16 burners. Left: Pattern A with C_S symmetry. Right: Pattern B with C_{4v}. All vertical mirror planes of C_{4v} are depicted. The planes σ_d and σ'_d are of type σ_v for C_{16v}. One of the eight σ_d planes of C_{16v} is shown, which does not exist for C_{4v}.

Table 18: Reduction of C_{4v} to C_4. The Bloch numbers for C_4 are given in addition.

C_{4v}	Γ_1	Γ_2	Γ_3	Γ_4	Γ_5
m	0	4	2	2	$1,3$
C_4	Γ_1	Γ_1	Γ_2	Γ_2	$\Gamma_3 \otimes \Gamma_4$
b	0	0	2	2	$1,-1$

5.4. Perturbation of C_{4v}

Consider a can-annular combustor with $N = 4$ cans operated with bluff-bodies and add swirlers. This perturbs C_{4v} into the lower symmetry C_4. With Equation (177) or the online tool [24], the splitting is obtained as depicted in Tab. 18

A reduction from C_4 to C_S is not possible, since the latter is not a subgroup of the former. This is obvious, since C_4 simply lacks any type of mirror operation – the formulas Eq. (176) cannot be applied. It is only possible to go from C_{4v} to C_S. Without a rotational symmetry only an off-burner plane σ_d remains. From the perspective of C_S, the character table of C_{4v} is

C_{4v}	E	σ_d
Γ_1	1	1
Γ_2	1	-1
Γ_3	1	-1
Γ_4	1	1
Γ_5	2	0

(187)

and it is obvious that modes belonging to Γ_1 and Γ_4 need to end up in the same irrep. of C_S (just like Γ_2 and Γ_3). One obtains

C_{4v}	Γ_1	Γ_2	Γ_3	Γ_4	Γ_5
C_S	Γ_1	Γ_2	Γ_2	Γ_1	$\Gamma_1 \otimes \Gamma_2$

(188)

Modes belonging to $\Gamma_5^{C_{4v}}$ are degenerate and of orders $m = 1, 3, \ldots$. These split into a symmetric and an anti-symmetric one. Modes of order $m = 2$ (cosine) and $m = 4$ become odd, while modes $m = 2$ (sine) and $m = 0$ become even.

In Figure 13 the reduction of symmetry is depicted for the computational case of Fig. 11. The result gives a perspective on the importance of the highest symmetry group C_{4v}. Even in the configurations without any symmetry, the eigenvalues are very close to those of C_{4v}. Thus, its presence is felt and explains the location

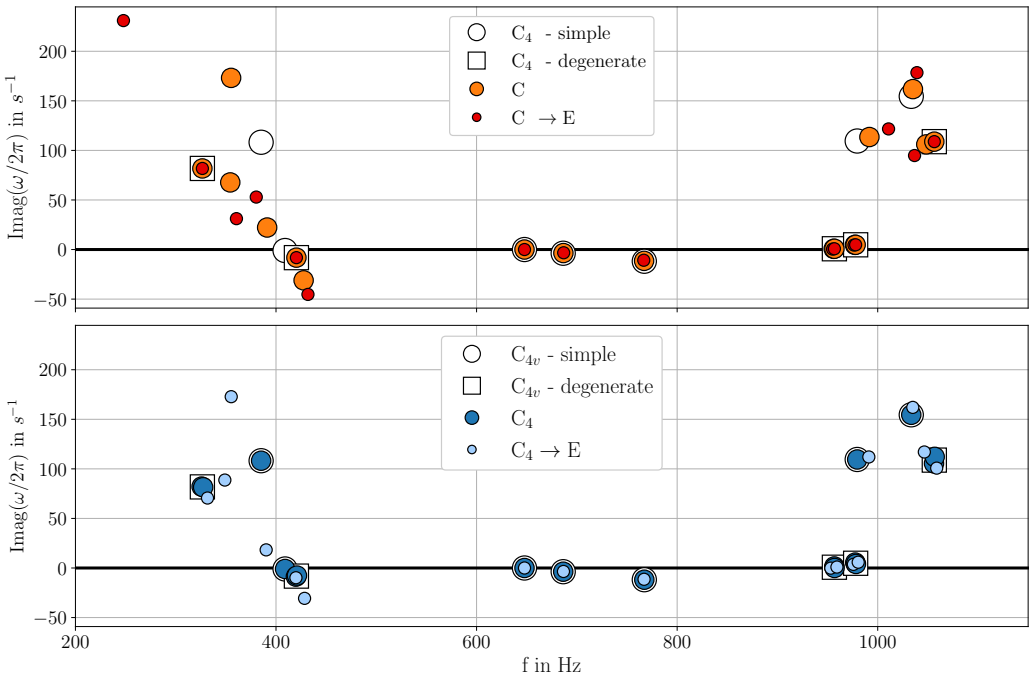

Figure 13: Splitting of modes as the symmetry is lowered. To introduce the perturbations the strength of the response of the four flames is adjusted but the global strength is conserved. For C_S the flame at $\phi = 0$ is increased by factor 1.5 and at $\phi = \pi$ reduced to 0.5. For $C_S \to E$ the individual flames are split into two domains (one per half cell) and factors are $\{(1.8, 0), (0.5, 0.5), (0.1, 0.1), (0.5, 0.5)\}$. Similarly for C_4 it is set to $\{(2.0, 0), (2.0, 0.0), (2.0, 0.0), (2.0, 0.0)\}$ and for $C_4 \to E$ the values are $\{(0.5 + 3/3, 0), (0.5 + 2/3, 0.0), (0.5 + 1/3, 0.0), (0.5, 0.0)\}$.

of the modes. The formerly degenerate modes are least affected by the reduction in symmetry. Modes that are completely unaffected are plenum modes.

6. Conclusion

This work has derived and discussed the groups C_S, C_N and C_{Nv} that are of major importance to thermoacoustic applications. A comprehensive introduction to the formal language of symmetry groups is given. Physical implications of the groups for thermoacoustic modes are discussed and visualised with computational results.

References

[1] T. C. Lieuwen, V. Yang (Eds.), Combustion Instabilities in Gas Turbine Engines, Vol. 210 of Prog. Astronaut. Aeronaut., AIAA, Inc., 2005.

[2] G. Ghirardo, C. Di Giovine, J. P. Moeck, M. R. Bothien, Thermoacoustics of can-annular combustors, Journal of Engineering for Gas Turbines and Power 141 (1) (2019).

[3] M. Bauerheim, F. Nicoud, T. Poinsot, Progress in analytical methods to predict and control azimuthal combustion instability modes in annular chambers, Physics of Fluids 28 (2) (2016) 021303.

[4] F. Nicoud, L. Benoit, C. Sensiau, T. Poinsot, Acoustic modes in combustors with complex impedances and multidimensional active flames, AIAA Journal 45 (2) (2007) 426–441. doi:10.2514/1.24933.

[5] S. M. Camporeale, B. Fortunator, G. Campa, A finite element method for three-dimensional analysis of thermo-acoustic combustion instability, J. Eng. Gas Turbines Power 133 (2011) 015506 (13 pages).
[6] T. Inui, Y. Tanabe, Y. Onodera, Group theory and its applications in physics, Vol. 78, Springer Science & Business Media, 2012.
[7] D. Durox, T. Schuller, N. Noiray, S. Candel, Experimental analysis of nonlinear flame transfer functions for different flame geometries, Proceedings of the Combustion Institute 32 (1) (2009) 1391–1398.
[8] A. Ghani, T. Poinsot, L. Gicquel, J.-D. Müller, Les study of transverse acoustic instabilities in a swirled kerosene/air combustion chamber, Flow, Turbulence and Combustion 96 (1) (2016) 207–226.
[9] S. Ducruix, D. Durox, S. Candel, Theoretical and experimental determinations of the transfer function of a laminar premixed flame, Proceedings of the combustion institute 28 (1) (2000) 765–773.
[10] T. Schuller, D. Durox, S. Candel, A unified model for the prediction of laminar flame transfer functions: comparisons between conical and v-flame dynamics, Combustion and Flame 134 (1-2) (2003) 21–34.
[11] G. A. Mensah, P. E. Buschmann, A. Orchini, J. P. Moeck, Pyholtz, https://bitbucket.org/pyholtzdevelopers/public.git (2018).
[12] G. A. Mensah, A. Orchini, Wavesandeigenvalues, https://julholtzdevelopers.github.io/WavesAndEigenvalues.jl/dev/ (2021).
[13] P. E. Buschmann, G. A. Mensah, F. Nicoud, J. P. Moeck, Solution of thermoacoustic eigenvalue problems with a non-iterative method, in: ASME Turbo Expo 2019: Turbomachinery Technical Conference and Exposition, American Society of Mechanical Engineers Digital Collection, 2019.
[14] G. A. Mensah, P. E. Buschmann, A. Orchini, Iterative solvers for the thermoacoustic nonlinear eigenvalue problem and their convergence properties, in: SoTiC 2021 - Symposium on Thermoacoustics in Combustion: Industry meets Academia, 2021.
[15] J. P. Moeck, M. Paul, C. O. Paschereit, Thermoacoustic instabilities in an annular rijke tube, in: Turbo Expo: Power for Land, Sea, and Air, Vol. 43970, 2010, pp. 1219–1232.
[16] J. P. Moeck, Analysis, modeling, and control of thermoacoustic instabilities, Ph.D. thesis, Technische Universität Berlin (2010).
[17] G. Ghirardo, M. Juniper, J. P. Moeck, Weakly nonlinear analysis of thermoacoustic instabilities in annular combustors (2016).
[18] G. A. Mensah, J. P. Moeck, Efficient computation of thermoacoustic modes in annular combustion chambers based on bloch-wave theory, in: ASME Turbo Expo 2015: Turbine Technical Conference and Exposition, American Society of Mechanical Engineers Digital Collection, 2015.
[19] G. A. Mensah, J. P. Moeck, Limit cycles of spinning thermoacoustic modes in annular combustors: A bloch-wave and adjoint-perturbation approach, in: ASME Turbo Expo 2017: Turbomachinery Technical Conference and Exposition, American Society of Mechanical Engineers Digital Collection, 2017.
[20] M. Haeringer, W. Polifke, Time-domain bloch boundary conditions for efficient simulation of thermoacoustic limit cycles in (can-) annular combustors, Journal of Engineering for Gas Turbines and Power 141 (12) (2019).
[21] M. Bauerheim, P. Salas, F. Nicoud, T. Poinsot, Symmetry breaking of azimuthal thermo-acoustic modes in annular cavities: a theoretical study, Journal of fluid mechanics 760 (2014) 431–465.
[22] M. Bauerheim, A. Ndiaye, P. Constantine, S. Moreau, F. Nicoud, Symmetry breaking of azimuthal thermoacoustic modes: the uq perspective, Journal of Fluid Mechanics 789 (2016) 534–566.
[23] M. S. Dresselhaus, G. Dresselhaus, A. Jorio, Group theory: application to the physics of condensed matter, Springer Science & Business Media, 2007.
[24] J. University, Character tables for chemically important point groups (2019).
URL http://symmetry.jacobs-university.de/
[25] P. E. Buschmann, G. A. Mensah, J. P. Moeck, Intrinsic thermoacoustic modes in an annular combustion chamber, Combustion and Flame 214 (2020) 251–262.
[26] The GAP Group, GAP – Groups, Algorithms, and Programming, Version 4.11.1 (2021).
URL https://www.gap-system.org
[27] N. Noiray, D. Durox, T. Schuller, S. Candel, A unified framework for nonlinear combustion instability analysis based on the flame describing function, Journal of Fluid Mechanics 615 (2008) 139.
[28] M. Schulze, T. Hummel, N. Klarmann, F. Berger, B. Schuermans, T. Sattelmayer, Linearized Euler equations for the prediction of linear high-frequency stability in gas turbine combustors, J. Eng. Gas Turbines Power 139 (10 2016).
[29] J. Gikadi, Prediction of acoustic modes in combustors using linearized Navier-Stokes equations in frequency space, Ph.D. thesis, Technische Universität München (2014).
[30] N. Moiseyev, Non-Hermitian quantum mechanics, Cambridge University Press, 2011.
[31] L. Magri, Adjoint methods as design tools in thermoacoustics, Applied Mechanics Reviews 71 (2) (2019).
[32] G. A. Mensah, Efficient computation of thermoacoustic modes, Ph.D. thesis, Technische Universität Berlin (2019).
[33] T. Kato, Perturbation theory for linear operators, Vol. 132, Springer Science & Business Media, 2013.
[34] G. A. Mensah, A. Orchini, J. P. Moeck, Perturbation theory of nonlinear, non-self-adjoint eigenvalue problems: simple eigenvalues, Journal of Sound and Vibration 473 (2020) 115200.
[35] A. Orchini, G. A. Mensah, J. P. Moeck, Perturbation theory of nonlinear, non-self-adjoint eigenvalue problems: semisimple eigenvalues, Journal of Sound and Vibration (2021) 116150.
[36] A. W. Joshi, Elements of group theory for physicists, New Age International, 1997.
[37] M. Hamermesh, Group theory and its application to physical problems, Courier Corporation, 2012.
[38] K. Moon, H. Jegal, J. Gu, K. T. Kim, Combustion-acoustic interactions through cross-talk area between adjacent model

gas turbine combustors, Combustion and Flame 202 (2019) 405–416.
[39] K. Moon, C. Yoon, K. T. Kim, Influence of rotational asymmetry on thermoacoustic instabilities in a can-annular lean-premixed combustor, Combustion and Flame 223 295–306.
[40] P. X. Gallagher, The number of conjugacy classes in a finite group, Mathematische Zeitschrift 118 (3) (1970) 175–179.
[41] N. Itô, On the degrees of irreducible representations of a finite group, Nagoya Mathematical Journal 3 (1951) 5–6.
[42] K. Wang, L. Grove, Realizability of representations of finite groups, Journal of Pure and Applied Algebra 54 (2-3) (1988) 299–310.
[43] A. Bossavit, Symmetry, groups, and boundary value problems. a progressive introduction to noncommutative harmonic analysis of partial differential equations in domains with geometrical symmetry, Computer Methods in Applied Mechanics and Engineering 56 (2) (1986) 167–215.
[44] A. Bossavit, Boundary value problems with symmetry and their approximation by finite elements, SIAM Journal on Applied Mathematics 53 (5) (1993) 1352–1380.
[45] P. G. Ciarlet, Linear and nonlinear functional analysis with applications, Vol. 130, Siam, 2013.
[46] G. Czycholl, Theoretische Festkörperphysik Band 1, Springer, 2016.
[47] G. A. Mensah, L. Magri, A. Orchini, J. P. Moeck, Effects of asymmetry on thermoacoustic modes in annular combustors: a higher-order perturbation study, Journal of Engineering for Gas Turbines and Power 141 (4) (2019).
[48] J. University, Character tablefor point group C_{16v} (2019).
URL http://symmetry.jacobs-university.de/cgi-bin/group.cgi?group=4&rot=16&option=0

Symmetry perturbations in a can-annular model combustor

This paper is awaiting publication and is therefore not included.

Appendix A

Technical drawings of the can-annular laboratory combustor

Table A.1: List of the technical drawings in the appendix with page numbers.

No.	Technical drawing	Quantity	Page
1.	Baseplate mounted on top of the plenum	1	p. 256
2.	Lower XT plate	1	p. 257
3.	Upper XT plate	1	p. 258
4.	Blocking element Blind	9	p. 259
5.	Blocking element Tiny	9	p. 260
6.	Blocking element Small	9	p. 261
7.	Blocking element Medium	9	p. 262
8.	Blocking element Large	9	p. 263
9.	Blocking element Huge	9	p. 264
10.	Can holder	9	p. 265
11.	Adapter for quartz tubes	9	p. 266

Table A.2: Steel pipes and quartz tubes used for the can combustors.

Component	Technical description	Quant./Vol.
Steel pipe	EN1.4404 - 1904074 48, $3 \times 3,2$ mm	6 m
Quartz tube	EN07 $\varnothing 50 \pm 1,5 \times 2,5 \pm 0,25 \times 100 \pm 1$ mm	10

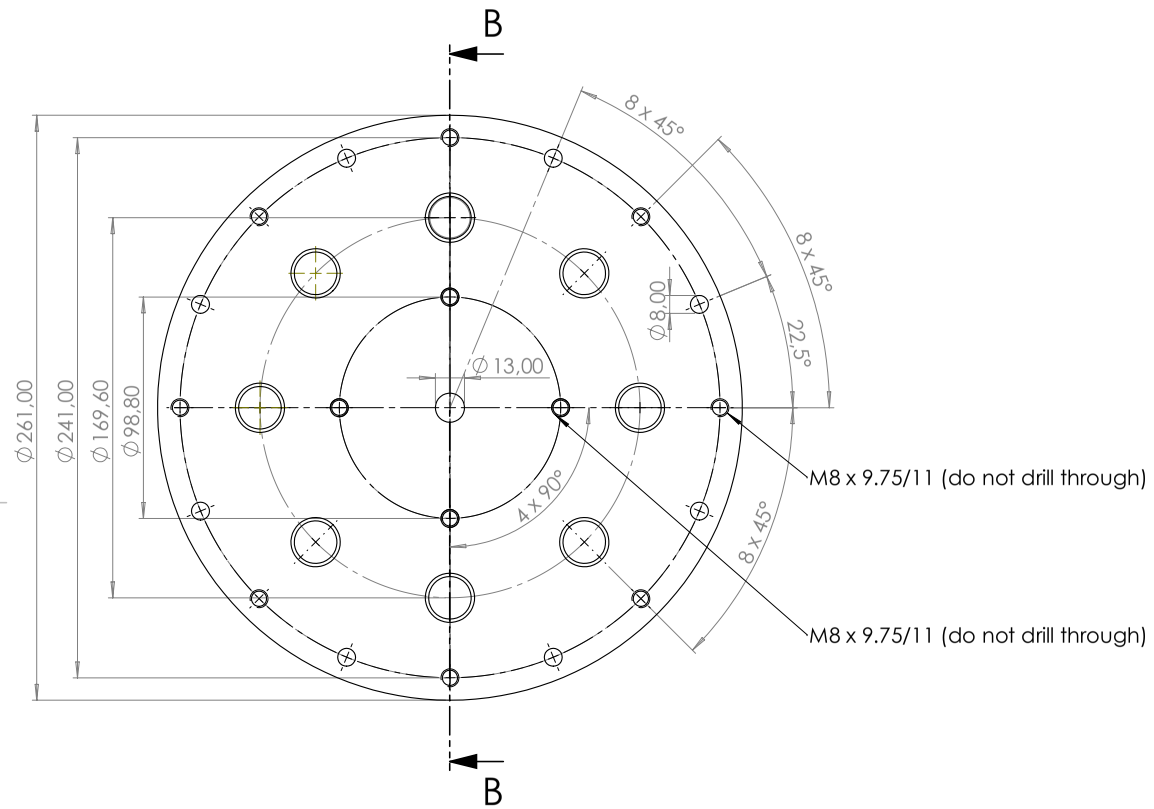

SECTION B-B

SCALE 1 : 2

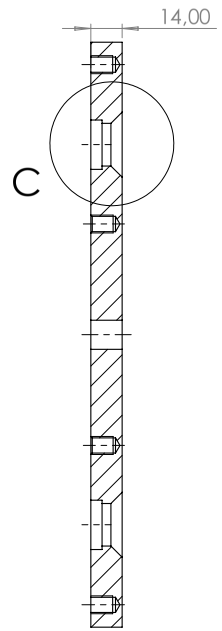

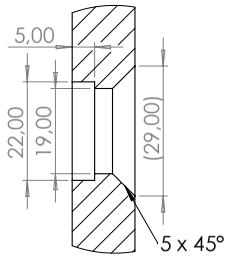

DETAIL C

SCALE 1 : 1

UNLESS OTHERWISE SPECIFIED: DIMENSIONS ARE IN MILLIMETERS SURFACE FINISH: TOLERANCES: DIN ISO 2768-1 middle LINEAR: ANGULAR:			FINISH:			DEBURR AND BREAK SHARP EDGES	DO NOT SCALE DRAWING / REVISION
							philip.e.buschmann@ntnu.no
	NAME	SIGNATURE	DATE				TITLE: Baseplate plenum
DRAWN	Buschmann						
CHK'D	Brandåstrø						
APPV'D	Moeck						
MFG							
Q.A				MATERIAL: 316 stainless steel			DWG NO. A3
				WEIGHT:			SCALE:1:2 / SHEET 1 OF 1

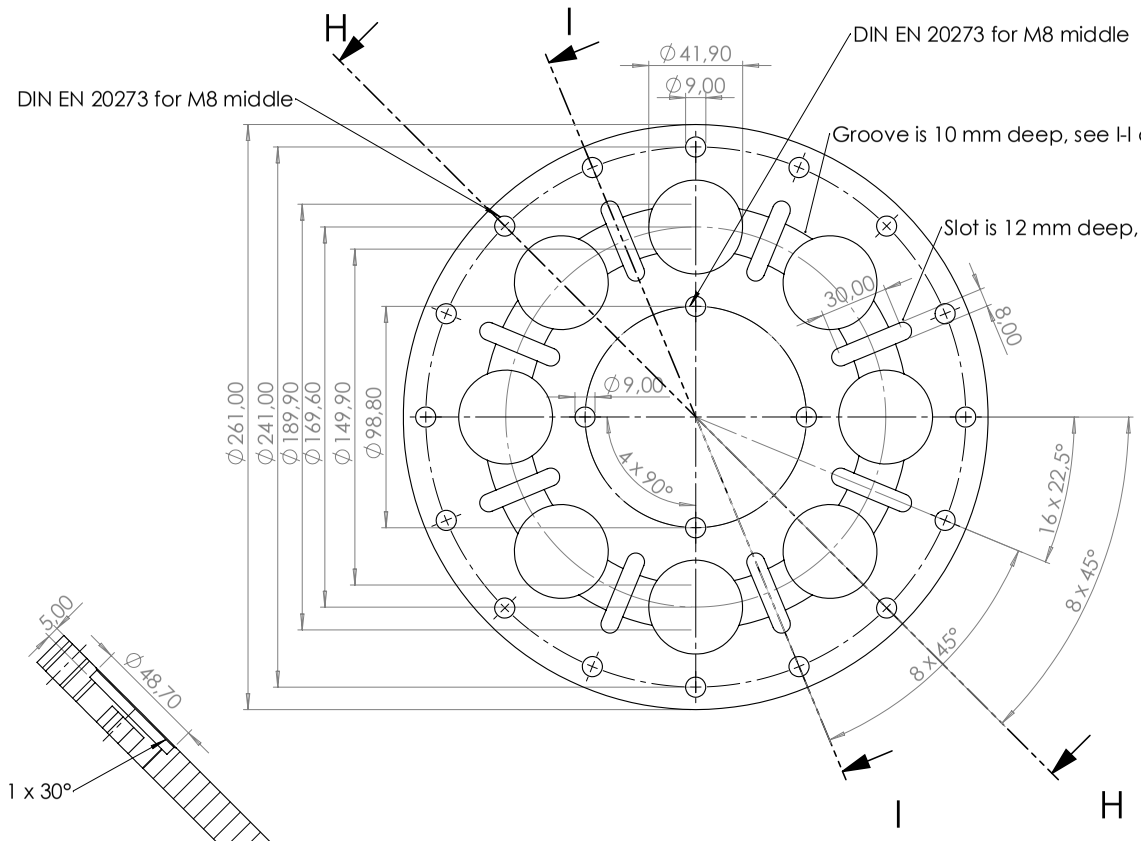

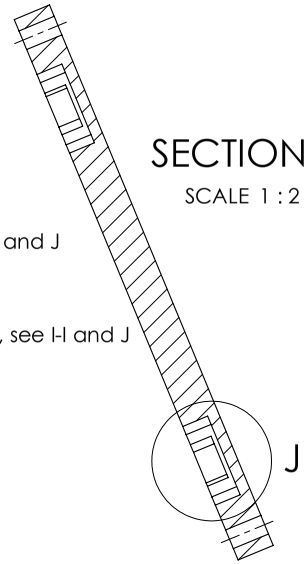

SECTION I-I
SCALE 1 : 2

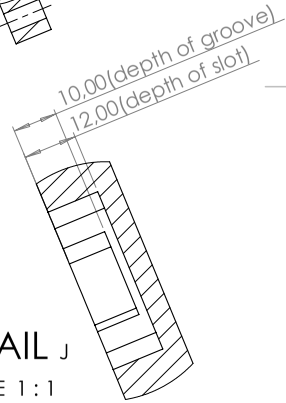

DETAIL J
SCALE 1 : 1

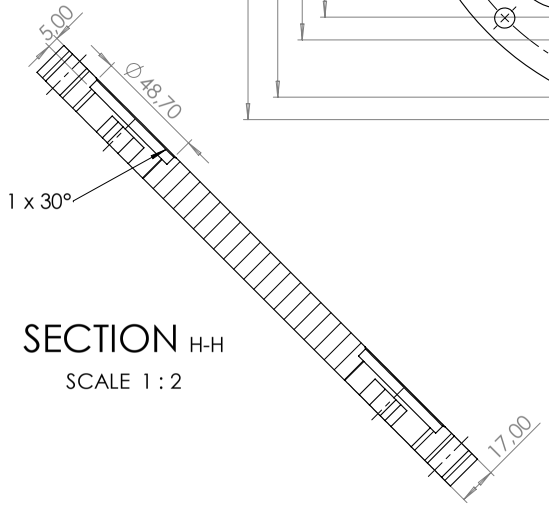

SECTION H-H
SCALE 1 : 2

UNLESS OTHERWISE SPECIFIED: DIMENSIONS ARE IN MILLIMETERS SURFACE FINISH: TOLERANCES: DIN ISO 2768-1 middle			FINISH:			DEBURR AND BREAK SHARP EDGES	DO NOT SCALE DRAWING / REVISION
							philip.e.buschmann@ntnu.no
	NAME	SIGNATURE	DATE				TITLE: Cross-talk lower
DRAWN	Buschmann						
CHK'D	Brandåstrø						
APPV'D	Moeck						
MFG							
Q.A				MATERIAL: 316 stainless steel			DWG NO. A3
				WEIGHT:			SCALE:1:2 / SHEET 1 OF 1

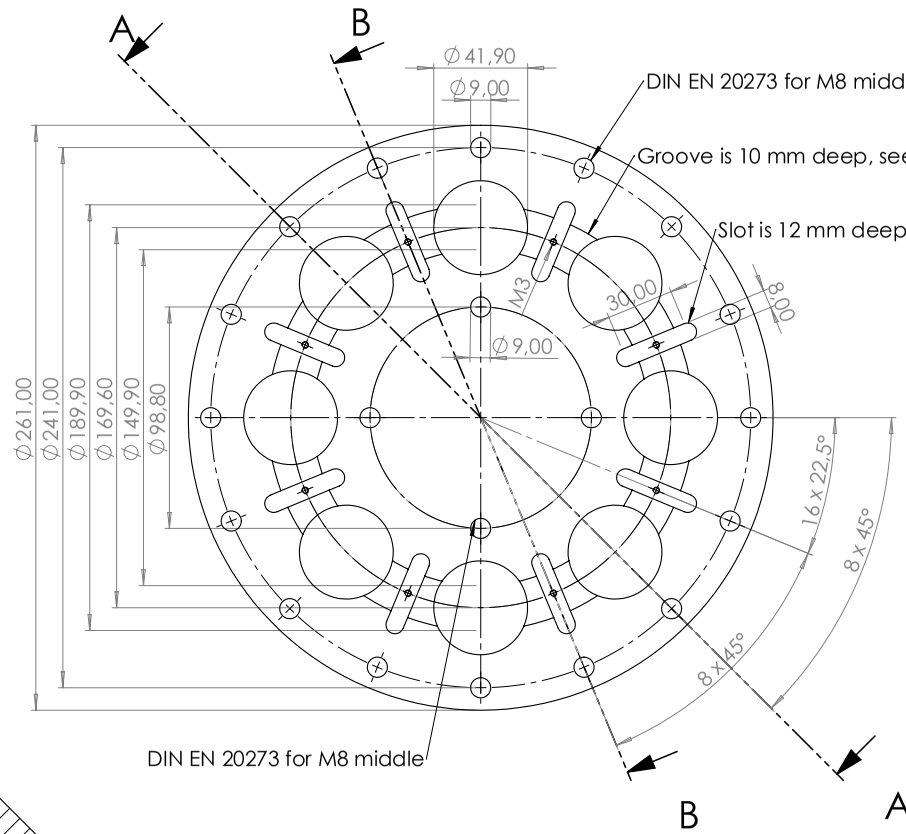

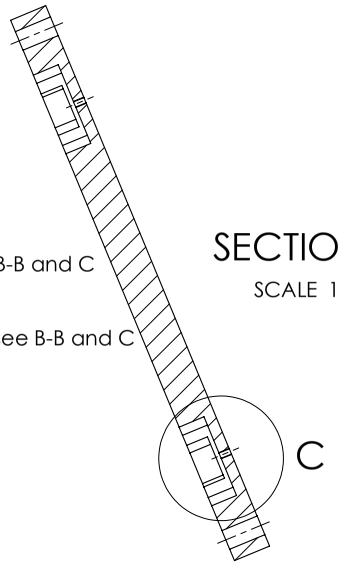

SECTION B-B
SCALE 1 : 2

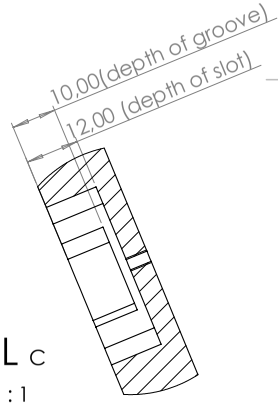

DETAIL C
SCALE 1 : 1

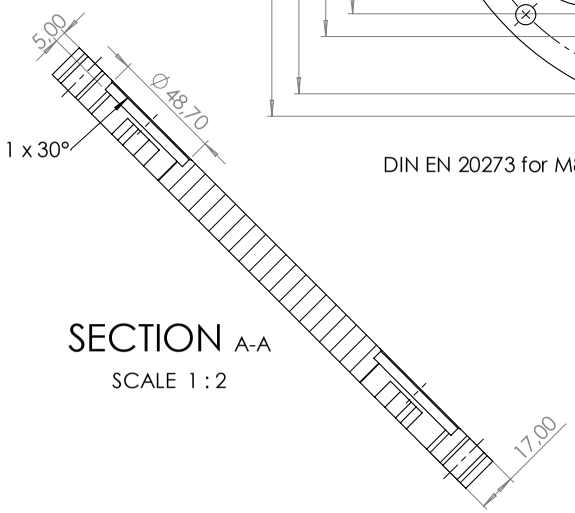

SECTION A-A
SCALE 1 : 2

UNLESS OTHERWISE SPECIFIED: DIMENSIONS ARE IN MILLIMETERS SURFACE FINISH: TOLERANCES: DIN ISO 2768-1 middle			FINISH:			DEBURR AND BREAK SHARP EDGES	DO NOT SCALE DRAWING / REVISION
							philip.e.buschmann@ntnu.no
	NAME	SIGNATURE	DATE				TITLE: Cross-talk upper
DRAWN	Buschmann						
CHK'D	Brandåstrø						
APPV'D	Moeck						
MFG							
Q.A				MATERIAL: 316 stainless steel			DWG NO. A3
				WEIGHT:			SCALE:1:2 / SHEET 1 OF 1

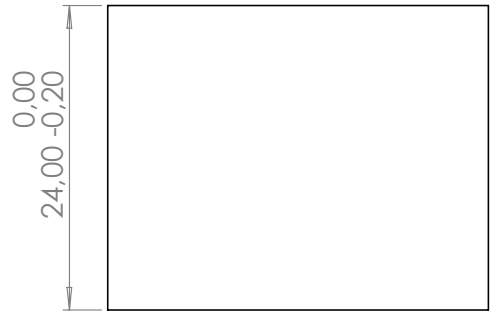

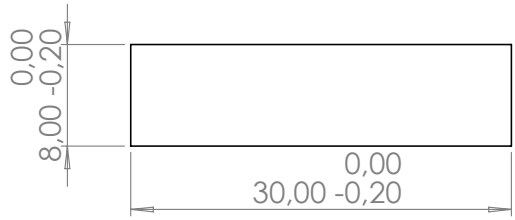

UNLESS OTHERWISE SPECIFIED: DIMENSIONS ARE IN MILLIMETERS SURFACE FINISH: TOLERANCES: DIN ISO 2768-1 middle	FINISH:	DEBURR AND BREAK SHARP EDGES	DO NOT SCALE DRAWING / REVISION

philip.e.buschmann@ntnu.no

	NAME	SIGNATURE	DATE
DRAWN			
CHK'D			
APPV'D			
MFG			
Q.A			

TITLE:

MATERIAL: 316 stainless steel

DWG NO. Blocking stone Blind

A4

WEIGHT:

SCALE:2:1

SHEET 1 OF 1

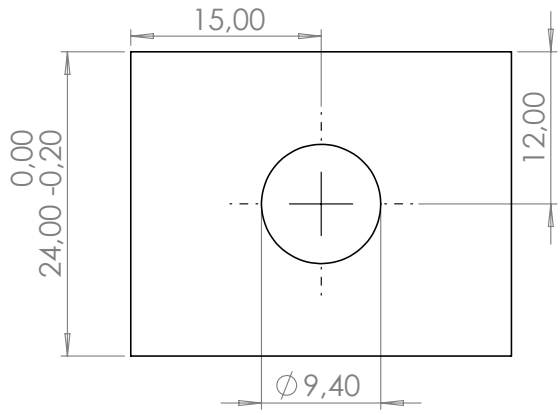

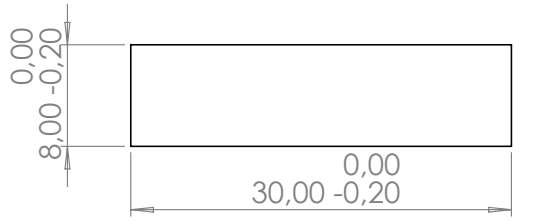

UNLESS OTHERWISE SPECIFIED: DIMENSIONS ARE IN MILLIMETERS SURFACE FINISH: TOLERANCES: DIN ISO 2768-1 middle	FINISH:	DEBURR AND BREAK SHARP EDGES	DO NOT SCALE DRAWING / REVISION

philip.e.buschmann@ntnu.no

	NAME	SIGNATURE	DATE
DRAWN			
CHK'D			
APPV'D			
MFG			
Q.A			

TITLE:

MATERIAL: 316 stainless steel

DWG NO. Blocking stone Tiny

A4

WEIGHT:

SCALE:2:1

SHEET 1 OF 1

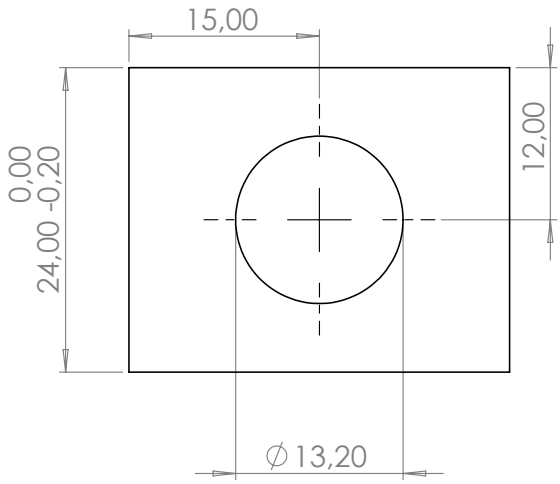

UNLESS OTHERWISE SPECIFIED: DIMENSIONS ARE IN MILLIMETERS SURFACE FINISH: TOLERANCES: DIN ISO 2768-1 middle	FINISH:	DEBURR AND BREAK SHARP EDGES	DO NOT SCALE DRAWING / REVISION

philip.e.buschmann@ntnu.no

	NAME	SIGNATURE	DATE
DRAWN			
CHK'D			
APPV'D			
MFG			
Q.A			

TITLE:

MATERIAL: 316 stainless steel

DWG NO. Blocking stone Small

A4

WEIGHT:

SCALE:2:1

SHEET 1 OF 1

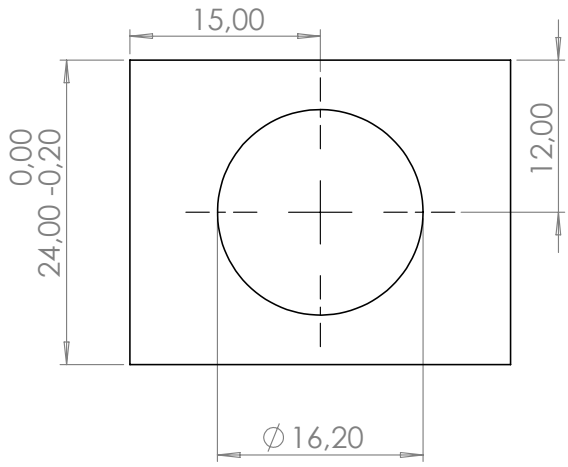

UNLESS OTHERWISE SPECIFIED: DIMENSIONS ARE IN MILLIMETERS SURFACE FINISH: TOLERANCES: DIN ISO 2768-1 middle	FINISH:	DEBURR AND BREAK SHARP EDGES	DO NOT SCALE DRAWING / REVISION

philip.e.buschmann@ntnu.no

	NAME	SIGNATURE	DATE
DRAWN			
CHK'D			
APPV'D			
MFG			
Q.A			

TITLE:

MATERIAL: 316 stainless steel

DWG NO. Blocking stone Medium

A4

WEIGHT:

SCALE:2:1

SHEET 1 OF 1

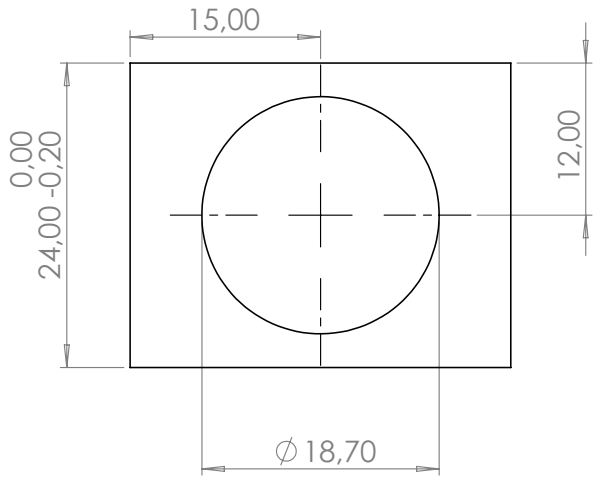

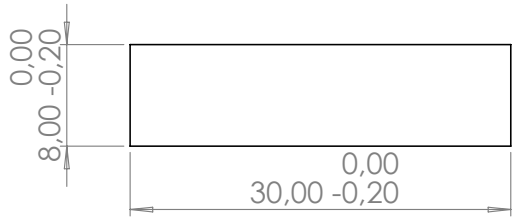

UNLESS OTHERWISE SPECIFIED: DIMENSIONS ARE IN MILLIMETERS SURFACE FINISH: TOLERANCES: DIN ISO 2768-1 middle	FINISH:	DEBURR AND BREAK SHARP EDGES	DO NOT SCALE DRAWING / REVISION

philip.e.buschmann@ntnu.no

	NAME	SIGNATURE	DATE
DRAWN			
CHK'D			
APPV'D			
MFG			
Q.A			

TITLE:

MATERIAL: 316 stainless steel

DWG NO. Blocking stone Large

A4

WEIGHT:

SCALE:2:1

SHEET 1 OF 1

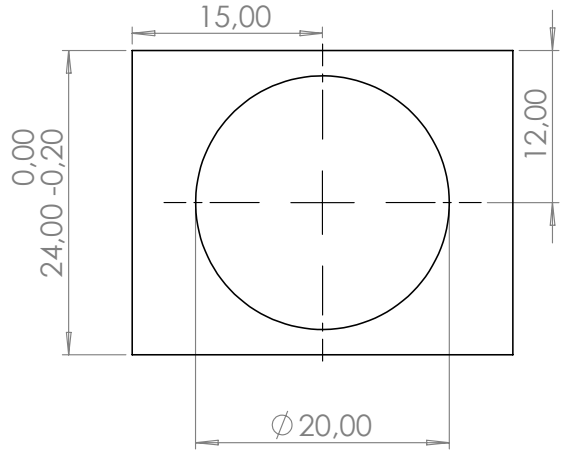

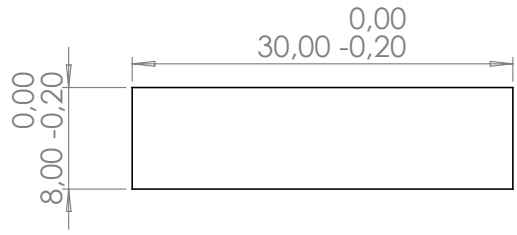

UNLESS OTHERWISE SPECIFIED: DIMENSIONS ARE IN MILLIMETERS SURFACE FINISH: TOLERANCES: DIN ISO 2768-1 middle		FINISH:		DEBURR AND BREAK SHARP EDGES		DO NOT SCALE DRAWING	REVISION
						philip.e.buschmann@ntnu.no	
	NAME	SIGNATURE	DATE			TITLE:	
DRAWN							
CHK'D							
APPV'D							
MFG							
Q.A				MATERIAL:		DWG NO.	A4
				316 stainless steel		Blocking stone Huge	
				WEIGHT:		SCALE:2:1	SHEET 1 OF 1

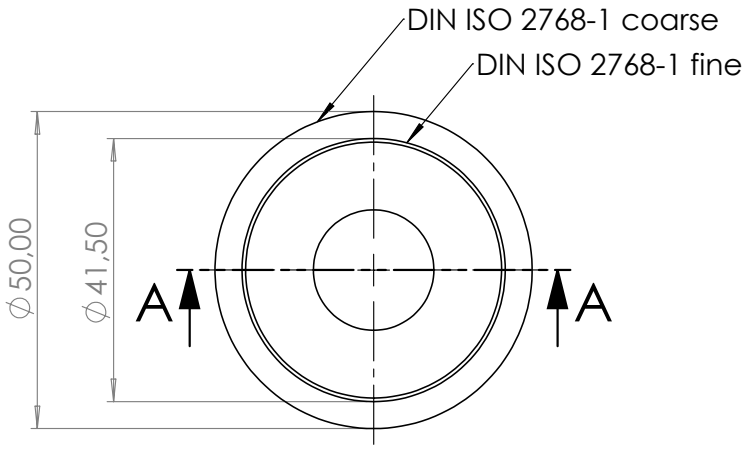

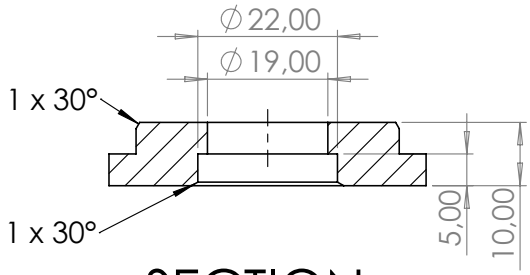

SECTION A-A

UNLESS OTHERWISE SPECIFIED: DIMENSIONS ARE IN MILLIMETERS SURFACE FINISH: TOLERANCES: DIN ISO 2768-1 middle unless otherwise specified		FINISH:				DEBURR AND BREAK SHARP EDGES	DO NOT SCALE DRAWING / REVISION
							philip.e.buschmann@ntnu.no
	NAME	SIGNATURE	DATE				TITLE:
DRAWN	Buschmann						Can holder
CHK'D	Brandåstrø						
APPV'D	Moeck						
MFG							
Q.A				MATERIAL:		DWG NO.	A4
				316 stainless steel			
				WEIGHT:		SCALE:1:1	SHEET 1 OF 1

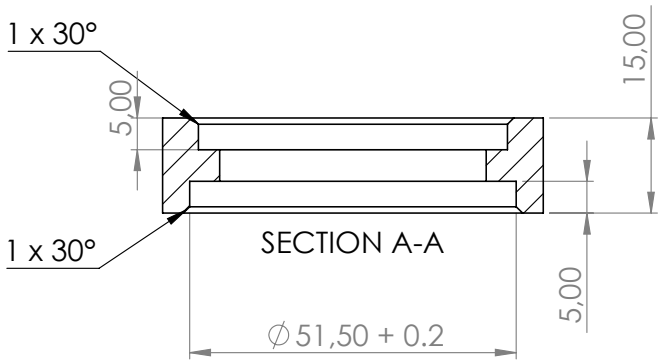

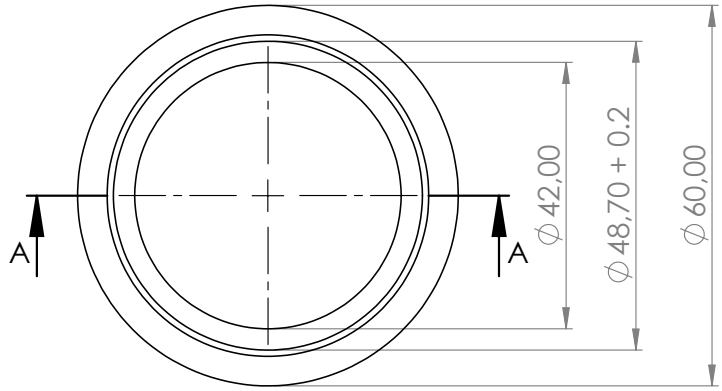

UNLESS OTHERWISE SPECIFIED: DIMENSIONS ARE IN MILLIMETERS SURFACE FINISH: TOLERANCES: DIN ISO 2768-1 middle	FINISH:	DEBURR AND BREAK SHARP EDGES	DO NOT SCALE DRAWING / REVISION

philip.e.buschmann@ntnu.no
+47 41274348

	NAME	SIGNATURE	DATE
DRAWN			
CHK'D			
APPV'D			
MFG			
Q.A			

TITLE:

MATERIAL: 316 stainless steel (or similar)

DWG NO. Adapter Quartz

A4

WEIGHT:

SCALE:1:1

SHEET 1 OF 1